

Investigation of ultra-intense laser interactions with long scale length pre-plasmas and nanowire targets via escaped fast electrons

Emma Hume

Doctor of Philosophy

University of York

Physics, Engineering and Technology

August 2023

Abstract

In this thesis the results of two experimental campaigns investigating the performance of novel nanowire targets via escaping fast electrons at the target rear surface are presented. An initial experiment was carried out to diagnose the efficiency of laser interactions with nanowire coated and planar targets using imaging of coherent transition radiation (CTR) emission induced by exiting fast electrons. This experiment was subject to an intense pre-pulse of intensity $I \sim 10^{17}$ W/cm² irradiating the targets prior to the arrival of the main laser pulse. Hydrodynamic simulations demonstrate the pre-pulse irradiation launched a shock-wave into the target, disrupting the rear surface of the thinner targets. CTR emission was still observed experimentally from these thinner targets, despite the significant target expansion. Particle-in-cell simulations are used to show the scale length of the density disruption was short enough to retain the efficient production of CTR emission in the optical regime. In addition, the hydrodynamic simulations revealed the formation of an extended pre-plasma at the front surface of the targets. This is predicted to facilitate the generation of super-ponderomotive electrons, beneficial towards the production of CTR. Remarkably, under these non-ideal conditions an increase in CTR emission was observed for a subset of shots on the nanowire coated targets compared to planar targets. This result is explained by proposing a less dense, longer scale length pre-plasma is produced from the nanowires, expediting the production of fast electrons with a greater hot electron temperature.

A subsequent experiment aimed to realise a high contrast laser interaction with nanowires through the use of a frequency doubled laser pulse. In this campaign a pepper-pot diagnostic was employed to measure the emittance of the exiting fast electron beam, a novel measurement for nanowire targets. The results indicate fast electrons with a greater emittance are obtained from the nanowire targets relative to planar targets. Particle-in-cell simulations are carried out that predict a greater transverse momenta of fast electrons from the nanowire targets, supporting this conclusion.

Contents

Abstract	2
List of Tables	6
List of Figures	7
Acknowledgements	14
Role of the Author	16
Declaration	17
1 Introduction	18
2 Theory of Laser-Plasma Interactions	27
2.1 Plasmas	27
2.1.1 Debye Length	27
2.1.2 Plasma Frequency	29
2.2 Laser-Solid Absorption	29
2.2.1 Ionisation	29
2.2.2 Critical Density	31
2.2.3 Inverse Bremsstrahlung	33
2.2.4 Resonance Absorption and Vacuum Heating	34
2.2.5 Ponderomotive Force	36
2.2.6 Ponderomotive Acceleration	37
2.2.7 Direct Laser Acceleration	38
2.3 Fast Electron Transport	39

<i>CONTENTS</i>	4
2.3.1 Return Current and Ohmic Heating	39
2.3.2 Filamentation	40
2.3.3 Divergence	41
2.3.4 Optical Transition Radiation	41
2.3.5 Sheath Field Generation	44
3 Instrumentation and Codes	46
3.1 High Power Laser Systems	46
3.1.1 Chirped Pulse Amplification	46
3.1.2 ILIL PW Laser	47
3.1.3 Laser Optics	48
3.1.4 Laser Contrast	51
3.2 Experimental Diagnostics	53
3.2.1 Optical Transition Radiation	53
3.2.2 Spectral Measurements	54
3.2.3 Time-of-Flight Detector	55
3.2.4 Fast Electron Emittance Measurements	56
3.3 EPOCH Code	58
3.3.1 Grid Resolution	60
3.3.2 Pseudoparticle Number	62
3.4 FLASH Code	65
3.4.1 Fluid Equations	65
3.4.2 Grid Structure	66
3.4.3 Laser Absorption	68
3.4.4 Limitations	70
4 Optical Transition Radiation from Preheated Planar Targets	73
4.1 Experimental Layout	74
4.1.1 Diagnostics	77
4.2 Rear Target Optical Emission	79
4.3 Ion Acceleration	87
4.4 Hydrodynamic Modelling of the Pre-Pulse	90
4.4.1 FLASH Simulation Setup	91

4.4.2	Heated Target Profiles	97
4.5	Hybrid-PIC Simulations of Fast Electron Transport	101
4.6	PIC Simulations of the Laser-Target Interactions	105
4.6.1	Pre-Pulse Interaction with Planar Target	106
4.6.2	Modelling the Effect of the Disrupted Rear Surface	111
4.6.3	Modelling the Effect of the Pre-Plasma	118
4.7	Summary and Conclusions	124
5	Optical Transition Radiation from Preheated Nanowire Targets	127
5.1	Experimental Setup	127
5.2	Rear Optical Emission	129
5.3	Proton Acceleration	131
5.4	Hydrodynamic Simulations of Pre-Pulse with Wires	134
5.5	PIC Modelling of Pre-Pulse Interaction with Nanowires	140
5.6	PIC Modelling of Main Pulse Interaction with Nanowire Pre-Plasma	144
5.7	Summary and Conclusions	148
6	Frequency Doubled Interactions with Nanowire Targets	150
6.1	Experimental Layout	150
6.2	Rear Optical Emission	152
6.3	Electron Emittance	157
6.3.1	Particle-in-Cell Simulations	166
6.4	Summary and Conclusions	170
7	Conclusions and Outlook	172
7.1	Optical Transition Radiation from Preheated Planar and Nanowire Targets	172
7.2	Emittance of Fast Electrons Generated from Nanowire Targets	174
7.3	Future Prospects	175
	List of References	176

List of Tables

3.1	Cell size and corresponding pseudoparticles per cell (ppc) used	62
3.2	Total laser energy deposited into the target, E_{depo} , as the maximum refinement level $lrefmax$ is increased. The finest grid resolution $\Delta x, y$ possible at the highest refinement level is given for each simulation.	70
4.1	Shock breakout time at the rear surface for planar targets.	97
6.1	Summary of the properties of the fundamental and frequency doubled laser pulses employed in EPOCH.	156
6.2	Description of how each term is calculated to determine an estimate of the emittance. Where applicable the number of the relevant equation in Zhang's Fermilab report is given, if the reader wishes to find more information on the derivation.	164

List of Figures

1.1	SEM image of the front surface of nanowire targets reported by Kulcsár . . .	21
2.1	Illustration of typical contributions of the pedestal, leading edge, and main pulse on the total laser profile. Contributions have been exaggerated for illustrative purposes and are not to scale.	30
2.2	Diagram to demonstrate the 1D density profile of a solid target post pre-plasma generation.	32
2.3	Strength of the laser electric field in a plasma of varying density. Dotted line indicates the position of the critical density surface.	33
2.4	Diagram to illustrate how resonance absorption is able to take place for p-polarised laser light. Note the definition of <i>p</i> -polarised means the electric field vector oscillates in the <i>plane of incidence</i> , i.e. along the light blue arrow. If the light were <i>s</i> -polarised the electric field vector would oscillate perpendicular to the plane, i.e. into and out of the page, and there would not be a component of the electric field directed into the density gradient.	35
2.5	Diagram to illustrate the ponderomotive force direction in a focused laser spot.	37
2.6	Diagram describing the trajectory and acceleration of target electrons in strong laser fields. The ponderomotive acceleration process injects bunches of electrons into the target along the <i>k</i> -vector direction.	38
2.7	Measurements of divergence angle as a function of laser intensity	40
2.8	Illustration of the production of transition radiation induced by fast electron bunches propagating through a metal-vacuum boundary.	42
2.9	Spectral properties of CTR emission	43

3.1	Illustration of the technique of chirped pulse amplification employed to produce short, high power laser pulses. © Johan Jarnestad/The Royal Swedish Academy of Sciences	47
3.2	Layout of the ILIL laser system	48
3.3	Illustration of the effect of birefringence on polarisation. Distances have been exaggerated for clarity.	50
3.4	3rd order autocorrelation trace of ILIL laser.	51
3.5	Conversion efficiency into second harmonic as a function of intensity for KDP crystals of different thicknesses.	52
3.6	(a) Optical streak image of CTR emission from the rear side of irradiated 914 μm Al foil; (b) and (c) show the integrated spectra from two shots in the same experiment. (d) CCD image of $1\omega_L$ CTR emission from the rear side of an irradiated Al/CH/Al sandwich target.	54
3.7	Experimental time-of-flight signals of accelerated ions. The <i>photopeak</i> attributed to X-ray emission and fast electrons is shown at $t = 0$	56
3.8	Illustration of pepper-pot mask and detector to demonstrate calculation of electron beam divergence from the image of the beamlet.	58
3.9	Cyclical solution of the field and particle pusher solvers implemented at each timestep in EPOCH.	59
3.10	Change in total particle kinetic energy as a function of time for varying cell size. The initial decrease in particle energy for the smallest grid sizes is attributed to energy lost to EM field fluctuations	63
3.11	Results of convergence testing for the electron pseudoparticle number per cell (ppc). (a) Total particle kinetic energy and (b) cumulative electron number counted passing through a probe plane at the rear target surface as a function of simulation time. (c) shows the variation of total particle kinetic at 78 fs with ppc, and (d) shows the variation of the total number of fast electrons counted at the probe plane.	64

3.12	Diagram of AMR functionality. The simulation initially starts with 1 block across a target with a localised region of high density. An additional block is added into the block cell containing the high density feature. Another level of refinement is then added with additional blocks inserted to gain higher resolution across the density perturbation.	67
4.1	Illustration of the laser profile implemented for the campaign to clarify the relative properties of the pre-pulse and the main pulse. The main pulse is defined to occur at a time of 0 ns, with the pre-pulse irradiating the targets -10.4 ns relative to the main pulse.	75
4.2	(a) Layout of the target chamber for the 2019 experimental campaign. (b) Details of the imaging line for the rear optical emission.	76
4.3	Image of target holder hole taken for pixel-distance calibration. Lineouts were taken (a) horizontally and (b) vertically across the image to measure the size of the central hole. The lineouts (yellow) and the respective fits (blue) are shown in (c) and (d)	78
4.4	Layout of the time-of-flight diagnostic employed in the experiment.	79
4.5	Example rear emission captured from a shot on 5 μm Ti foil. Contrast adjusted to highlight the transition radiation signal and the background.	80
4.6	Images of optical rear emission from irradiated planar targets numbered by shot number.	81
4.7	Lineouts for analysis of the total optical emission from the rear target surface.	83
4.8	Intensity of optical emission measured from the rear side of irradiated planar targets as a function of target thickness; (a) gives the total intensity, and (b) shows the intensity integrated across the peak of the emission spatial profile.	84
4.9	Total intensity of CTR emission measured from the rear side of irradiated 25 μm Ti foils as a function of target position along the laser focus axis	85
4.10	FWHM size of rear side CTR emission imaged from Ti planar targets as a function of target thickness.	86
4.11	Measured proton cut-off energies as a function of planar target thickness.	88
4.12	Measured proton cut-off energies as a function of (a) FWHM of the imaged CTR emission, and (b) intensity of CTR emission measured from the shot.	90
4.13	Power profile originally implemented in FLASH to model the pre-pulse.	91

<i>LIST OF FIGURES</i>	10
4.14 Geometry of the planar target and laser in FLASH.	92
4.15 HYADES result of pressure of a Ti target after irradiation by the pre-pulse. Each lineout represents the pressure from a mesh element.	93
4.16 Laser interaction at 50 fs with target (a) with and (b) without the exponential density profile. Both results are plotted using the same scale.	94
4.17 Parameter scan to determine an appropriate power profile for use in FLASH. (a) Maximum shock pressure obtained from FLASH simulations and (b) cor- responding energy absorption fraction relative to the actual pre-pulse energy.	95
4.18 Mass density (g/cm^3) of the Ti $12.5 \mu\text{m}$ target at (a) 0 ns and (b) 10.4 ns with no laser irradiation.	96
4.19 Mass density (g/cm^3) at 0 ns for targets of (a) $5 \mu\text{m}$, (c) $12.5 \mu\text{m}$ and (e) $25 \mu\text{m}$ thickness, and 10.4 ns after pre-pulse irradiation for (b) $5 \mu\text{m}$, (d) $12.5 \mu\text{m}$ and (f) $25 \mu\text{m}$ thickness. Lineouts of the density profiles along $r = 3 \mu\text{m}$ are shown in (g).	98
4.20 Lineout data from FLASH is shown in pink and the found fit to the pre-plasma region is shown in blue.	99
4.21 Background target temperature at 1 ps for slices taken at a target thickness of $5, 12.5$ and $25 \mu\text{m}$. First row (blue labels) is for electrons with $T_{hot} = 2 \text{ keV}$, second row (red labels) is for electrons with $T_{hot} = 15.3 \text{ keV}$. Bottom plot show the average background temperature as a function of target thickness, x	103
4.22 $x - p_x$ distribution plots of the electrons with electron number plotted as $\log_{10}(N)$. The dashed horizontal line indicates minimum particle momenta, and the sold vertical line indicates the position of the particle probe.	107
4.23 Properties of the exiting hot electrons from the pre-pulse interaction as mea- sured by the rear vacuum probe plane. (a) shows the energy spectra of elec- trons passing the probe, and (b) shows the number of electrons passing the probe as a function of time.	108
4.24 (a) E_x , (b) E_y and (c) B_z emission in the rear vacuum region at $t = 105 \text{ fs}$. For each field component the raw emission is shown, alongside the integrated Fourier spectra from the radial lineouts.	109

4.25	Properties of the exiting hot electrons from the main-pulse interaction with a planar target as measured by the probe plane. (a) is the energy spectra of electrons passing the probe; (b) is the number of electrons passing the probe as a function of time. The bunching structure around the period $t = 70 - 96$ fs is clearly seen in (c), with the corresponding calculated Fourier spectra of the peaks.	113
4.26	(a) E_y , (b) B_z and (c) E_z emission in the rear vacuum region at $t = 160$ fs. For each field component the raw emission is shown, alongside the integrated Fourier spectra from the radial lineouts. For the E_z component the radial lineouts are not shown to better see the emission.	115
4.27	Density profile output by FLASH at 10.4 ns for the 12.5 μm planar target. The shock front is well fitted by an exponential function.	116
4.28	(a) Initial density profile of the targets with an unperturbed (left) and shock disrupted (right) rear target surface. (b) E_y fields at $t = 160$ fs, (c) shows the corresponding Fourier spectra of the E_y emission.	117
4.29	Initial density profile of the pre-plasma region implemented in EPOCH.	119
4.30	Electron number density within the pre-plasma from irradiation by the main laser pulse.	120
4.31	$x - p_x$ distribution of the electrons in the pre-plasma at increasing simulation time. The solid white line at $x=50 \mu\text{m}$ indicates the probe plane position.	121
4.32	Energy spectra of the electrons passing the probe plane at $x = 50 \mu\text{m}$. Fits applied assume a Maxwell-Jüttner relativistic energy distribution.	123
4.33	Energy of ω_L (solid) and $2\omega_L$ (dashed) CTR emission as a function of target thickness for electron populations of differing temperatures.	124
5.1	(a) SEM image of the front surface of the nanowire coated targets. Lineouts selected to calculate (b) the average spacing and (c) average diameter of the wires.	128
5.2	Images of optical rear emission from irradiated planar and nanowire coated targets, numbered by shot number.	130

5.3	Intensity of CTR emission for planar and nanowire targets from (a) the total lineout and (b) the peak only as a function of target thickness. The variation of optical emission with target position along the focal axis from shots on the nanowire targets is shown in (c).	132
5.4	Proton cut-off energies measured from shots on the planar and nanowire targets as a function of total target thickness.	133
5.5	(a) Mass density of the nanowire target and (b) lineout taken across the wires at $h = 63 \mu\text{m}$, showing the density variation of the wires along r	135
5.6	Energy deposited into nanowire target as a function of peak laser power in FLASH.	136
5.7	(a) Nanostructured target and laser rays at 50 fs. Plot is reproduced in (b) and zoomed in around the interaction region.	138
5.8	Mass density of the nanowires at (a) 0 ns and (b) 10.4 ns after pre-pulse irradiation.	139
5.9	Fitting to the pre-plasma produced from pre-pulse irradiation of the nanowire targets.	140
5.10	(a) The density profile across an individual wire and (b) the full nanowire coated target modelled in EPOCH.	141
5.11	Electron number passing the probe as a function of time.	142
5.12	$x - p_x$ distribution function of electrons produced in the pre-pulse interaction with a nanowire coated target. The solid white line at $x = 10 \mu\text{m}$ indicates the position of the probe plane.	143
5.13	Initial density profile of the nanowire pre-plasma region implemented in EPOCH.	145
5.14	Electron number density at various timesteps during the main pulse interaction with the pre-plasma produced by the pre-pulse interaction with a nanowire coated target.	146
5.15	$x - p_x$ distribution function of electrons in the nanowire pre-plasma accelerated by the main pulse. The solid white line at $x = 50 \mu\text{m}$ indicates the position of the probe plane.	147
5.16	Fast electron energy spectra from the interactions of the main laser pulse with the planar pre-plasma and the nanowire pre-plasma.	148

6.1	(a) Layout of the target chamber with positioning of the relevant diagnostics indicated. The pepper-pot diagnostic was only in place for a small number of shots and was moved out the way of the optical emission imaging line when not in use. (b) Orientation of the laser fields with respect to the target. . . .	151
6.2	Pepper-pot diagnostic setup to estimate the emittance of the exiting, forward propagating fast electrons.	153
6.3	Image and spectra of optical emission measured from the rear surface of irradiated Au 1 μm targets.	154
6.4	Image and spectra of optical emission measured from the rear surface of irradiated nanowire and Ti 12.5 μm targets.	155
6.5	Energy spectrum of fast electrons recorded by the probe plane from a laser interaction at fundamental frequency, and a laser interaction with frequency doubled parameters.	156
6.6	Difference in measured signal from proton versus electron deposition in EBT3 film. This data was taken from a separate experiment at the ILIL facility, and is included for descriptive purposes only to demonstrate the different signatures of proton and electron deposition.	158
6.7	Identifying the region of interest from the pepper-pot image to analyse. . . .	160
6.8	Identifying an region of interest around the beamlets for a horizontal slice. . .	161
6.9	Identifying an region of interest to determine background intensity for a horizontal slice.	161
6.10	Background intensity after smoothing.	161
6.11	Background-corrected intensities across the beamlets.	162
6.12	Found fit to the beamlet lineout.	162
6.13	Transverse position of holes in the pepper-pot mask relative to the fitted beamlets.	163
6.14	Calculated estimates of emittance of the exiting fast electron beam for shots on planar 12.5 μm and nanowire coated targets.	166
6.15	Initial target profiles modelled in EPOCH.	167
6.16	(a) $p_x - p_y$ phase space at $t = 75$ fs of electrons generated from s - and p -polarised interactions with planar and nanowire targets. (b) Number density of electrons in the wire region at $t = 45$ fs.	168

Acknowledgments

When arriving at York in 2014 to begin my undergraduate degree I had zero idea of what a PhD was, only that it seemed like something only very clever people had and it certainly would never be open to me. Nine years later it appears I (nearly) have one, and there are a number of people who have contributed to this feat requiring a large amount of thanks.

Firstly, to my supervisor Kate Lancaster for the endless support and guidance. Every meeting has left me feeling more motivated and your positive outlook on physics and life has been so appreciated, particularly when we were met with a pandemic to navigate the project through. Your enthusiasm for lasers is completely unmatched and it has been such a joy to learn from you these past years. Thank you so much for taking me on, I will forever be a proud member of Team Lancaster!

To Petra Koester, thank you for all your help - your experimental expertise has been invaluable in both the lab and during data analysis. When travel became difficult you were incredibly accommodating in helping us get (virtual) lab time and without your efforts this thesis would look very different. To Leo Gizzi and the rest of the group at the ILIL facility, for making these nanowire experiments happen and being so welcoming to your lab.

Simulations have formed a major part of the work in this PhD, and it has been a challenging but enriching process to learn from a number of excellent scientists how to effectively run physics codes. To Robbie Scott and John Pasley for your patience in guiding me through the hydrodynamic simulations. Getting FLASH to behave was a taxing exercise I would not have achieved on my own, and I thank you both for your help and time in solving this. To Stuart Morris, Chris Ridgers, Chris Arran, and Arnaud Debayle for the question-answering on how to better run and analyse EPOCH simulations. To Alex Robinson, for the advice and comments on the hybrid-PIC simulations and for allowing the use of Zephyros.

There are a number of people I have had the pleasure of interacting with over the past few years who deserve special mention as forming an integral part of my PhD experience. To Chris Murphy; my journey in laser-plasma physics began in the final year of my degree with

a fantastic project with you, and I would not be writing this today without your throwaway comment of “Have you thought about applying to the Fusion CDT?” during one meeting (which you may not even remember!). To Christina Ingleby, Ben Harris, Harry Dudding, Andrew Malcolm-Neale, Arun Nutter, Adam Dearling, Matt Khan and Luke Thompson for all the fun in the office/at conferences/at the pub. To Koki Imada for the many tea breaks, boozy millionaire’s shortbread, and for spotting that rogue missing bracket in the Python script. To Meg, Katy, and Lyd - I have no shame in saying I am the most unaccomplished of the Heatherbank gals and you all inspire me endlessly.

To Mam and Dad for the support, particularly during the write-up period where you have provided me with copious mugs of tea and a place to live. I can’t promise you’ll understand much of this thesis - it does mention inertial confinement fusion though and you know that part now! - but it wasn’t possible without you and I appreciate you both more than you know. To Andrew, you are a model case of where hard work and dedication can get you - you have achieved, and continue to achieve, so much and I am a super proud sister. Davy (the cat) also deserves a mention here as an emotional support animal, as does the inventor of wine as another emotional support mechanism.

Finally, to Jonny for your impressive and endless supply of proud-ness. We have gone through this PhD together, and as much as I love physics it was always a highlight coming home to you at the end of the day. Thank you for all the cooking, Assassin’s Creed play-throughs, and for being a honorary laser ambassador!

Role of the Author

The author attended the experiment detailed in **Chapters 4 and 5** and aided in the execution of the optical emission imaging diagnostic. All analysis of the optical emission imaging results was carried out by the author. The time-of-flight diagnostic was operated by Alberto Fazzi and Dario Giove, with the results analysed by Martina Salvadori. HYADES simulations were carried out by John Pasley. Simulations with FLASH, Zephyros, and EPOCH were all carried out and analysed by the author.

The experiment in **Chapter 6** was operated by the experimental group at ILIL. Analysis of the experimental data and EPOCH simulations presented in this Chapter was carried out by the author.

Declaration

This thesis has not previously been accepted for any degree and is not being concurrently submitted in candidature for any degree other than Doctor of Philosophy of the University of York. This thesis is the result of my own investigations, except where otherwise stated. All other sources are acknowledged by explicit references.

Chapter 1

Introduction

Lasers can be used to deliver high energy, ultra-short pulses into solid matter, rapidly compressing and heating the target and allowing the creation of some of the most extreme environments in the Universe [1]. This field of optical laser physics dawned in 1960 following the first demonstration of a ruby laser built by Maiman [2], based on the concept of the ‘maser’ presented by Schawlow and Townes [3], and the potential of lasers was quickly acknowledged by scientists around the globe. A desire for developing high power lasers was motivated by an ambition to reach more extreme energy-density regimes; take for example the proposal of Nuckolls *et al.* [4] in 1972 of compressing hydrogen fuel with lasers in an effort to induce thermonuclear burning, sparking the research area we now know as inertial confinement fusion (ICF). At this time the peak intensity (laser power per unit area) for short pulse laser operation was severely limited by self-focusing effects in the laser amplifiers [5]. A pathway to ultra-intense ($> 10^{18}$ W/cm²) laser interactions was opened by Strickland and Mourou in 1985 when they presented the concept of chirped pulse amplification (CPA) [6], and is the basis of a number of petawatt-class lasers now existing worldwide which support a community of researchers investigating intense-laser interactions [7]. Research areas involving these interactions include, but are by no means limited to, laboratory astrophysics [8–11], ion acceleration [12,13], and X-ray sources [14,15]. One research area enjoying particular attention recently is inertial confinement fusion, with the remarkable results from the National Ignition Facility of the first demonstration of a burning plasma [16,17] and of an ignited fusion plasma [18] stimulating an invigorated activity in inertial fusion research.

One facet of high-power laser research is the irradiation of solid targets with ultra-intense

laser pulses. For the case of femtosecond-length, $> 10^{18}$ W/cm² laser pulses, the laser energy is primarily coupled into electrons at the target surface. The electrons are accelerated by the laser fields up to MeV energies, generating a population of so-called *hot* or *fast electrons* [19]. Fast electrons can propagate through the depth of the target, inducing heating of the bulk target to several eV or keV [20,21]. For sufficiently thin targets the highest energy electrons are also able to exit through the rear surface of the target; intense laser-solid interactions have therefore been suggested as a fast electron beam source. One potential application is in fast ignition [22], a variant of ICF where a fast electron beam is used to deposit energy into pre-compressed fuel and ignite a hotspot, inducing a burning plasma. The feasibility of this scheme is however strongly dependent on the ability to precisely control the energies, divergence and transport of the fast electron beam, alongside a high laser-fast electron coupling efficiency [23–26]. An additional consequence of these exiting fast electrons is the generation of an electrostatic field at the target surface due to charging of the target, which serves to accelerate protons and target ions [13,27,28]. Thus, an understanding of the laser coupling into fast electrons and the subsequent transport of the fast electron beam through the target is important for the control of the properties of the exiting fast electron beam, optimising the production of warm and hot dense matter in the bulk target, and for the generation of proton and ion beams.

The properties of the fast electrons can be influenced at the point of initial generation by the laser at the target surface, and can also be manipulated during the fast electron beam propagation through the target. To both ends, novel structured targets can be employed to control the laser-generated fast electrons. For instance, the fast electron beams are known to diverge and spread out during their propagation, posing an issue when considering the beam for practical applications which typically require a well-collimated beam. The *resistive guiding scheme* first proposed by Robinson and Sherlock [29] is based on the substitution of Ohm’s law, $\mathbf{E} = \eta\mathbf{j}$, into Faraday’s law, $\nabla \times \mathbf{E} = -\frac{\partial \mathbf{B}}{\partial t}$, to yield the driving equation behind this scheme:

$$\frac{\partial \mathbf{B}}{\partial t} = \eta \nabla \times \mathbf{j}_f + \nabla(\eta) \times \mathbf{j}_f \quad (1.1)$$

where η is the target resistivity and \mathbf{j}_f is the fast electron current density. The second term describes the generation of a magnetic field that will act to drive electrons towards regions of higher resistivity. The resistive guiding scheme therefore proposes the use of targets with an

embedded region, or regions, of a material with a higher resistivity, such that the magnetic field growth at the resistivity gradients will collimate the fast electron beam around the resistive guiding element; this scheme was demonstrated experimentally by Kar *et al.* [30] for an Al-Sn-Al sandwich target.

A suite of nanostructured targets have also been proposed in the pursuit of optimising laser coupling into solid targets. These targets are generally characterised as consisting of planar targets with a front layer of novel structures, the dimensions of which range from 10's to 100's of nm. Nanostructures presented in the literature include nanotubes [31, 32], foams [33], nanospheres [34, 35], and snowflakes [36]. The presence of these structures can increase the effective surface area for laser interaction, and act to modify the laser-target coupling; the precise impact on the interaction is dependent on the structures employed and the laser parameters.

The use of *nanowire* targets was first presented by Kulcsár *et al.* [37], where the targets are described as having a surface “resembling velvet fabric” (Figure 1.1) comprised of 10-200 nm metal fibres standing normal to an Al substrate. A factor 50 increase in emitted X-ray photon yield was reported from these ‘velvet’ targets when irradiated with a $< 9 \times 10^{16}$ W/cm², 1 ps laser pulse compared to a planar solid target. This remarkable result was attributed to an enhanced laser absorption from, in part, reduced reflection of the laser and an increased effective absorption depth. X-ray emission was again used as a figure of merit by Samsonova *et al.* [38] at a similar intensity of 5×10^{16} W/cm², but with a shorter pulse length of 60 fs. Here, a increase in the hard X-ray flux by a factor 15-22 was detected using ZnO nanowires compared to flat targets, since the nanowires facilitated a higher laser absorption and a larger plasma volume availability. Mondal *et al.* [39] explored a comparable intensity regime ($I \sim 1 \times 10^{16}$ W/cm², $\tau = 30$ fs) to irradiate Cu nanowires. The enhancement of X-ray yield was found to be sensitive to the dimensions and aspect ratio of the nanowires used, with a yield increase of a factor 14-43 measured. This result has been replicated at higher intensities too; Purvis *et al.* [40] employed a frequency-doubled laser pulse to irradiate Ni nanowires at an intensity $I = 5 \times 10^{18}$ W/cm², $\tau = 60$ fs, with a < 50 -fold increase in X-ray flux reported from the wire targets.

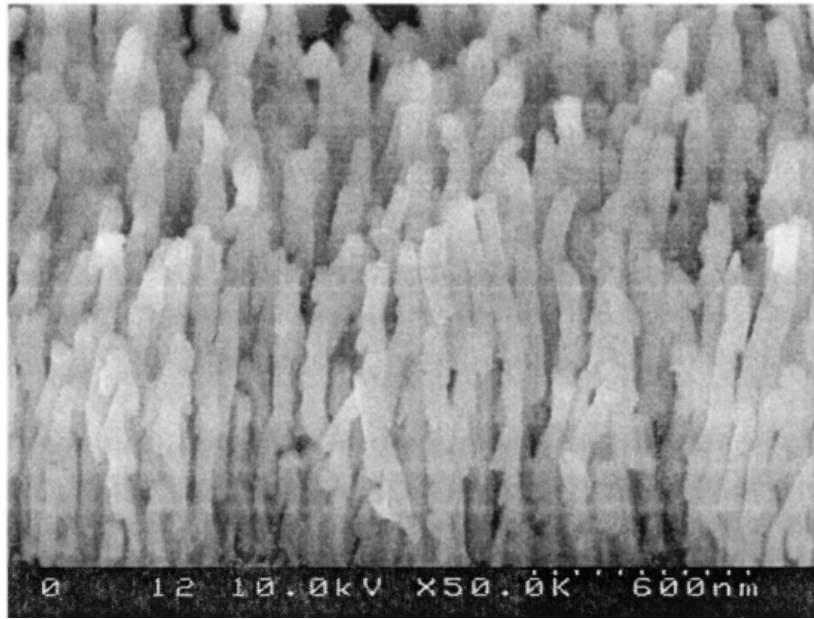


Figure 1.1: SEM image of the front surface of nanowire targets reported by Kulcsár [37].

For ultra-intense laser interactions, the laser energy will be chiefly coupled into fast electrons: for this reason, the performance of nanowire targets can therefore be explored through assessment of this hot electron population. In a study by Zhao *et al.* [41], both imaging and absolute yield of X-ray emission from the rear surface of nanowire coated targets was undertaken. A three-fold enhancement of K_α yield was observed from the nanowire target, implying an increased number and energy of the hot electrons. Additionally, the imaging of the X-ray spot revealed a comparable, even slightly reduced, FWHM spot size from the rear surface of the nanowire coated targets compared to the front surface. In contrast, the planar targets exhibited an increased X-ray FWHM spot size at the rear surface compared to the front surface, in line with a diverging fast electron beam. The authors put forward the implication that the wire structures were able to collimate the accelerated electrons. The energies of the hot electrons produced by the interaction have been measured directly via an electron spectrometer in the forward [42–44] and backward [45, 46] propagating directions: these individual studies found a hotter temperature for fast electrons produced in the nanowire interaction versus the interaction with a planar target. Studies of accelerated ions from intense laser-interactions with nanowire targets support the argument of increased coupling into hot electrons. Measurements of accelerated protons by Khaghani *et al.* [47] demonstrated an increase in proton number alongside a raised cut-off proton energy upon the use of nanowire coated targets; this result was also reported by Vallières *et al.* [48]. In

both investigations the observed improvement was ascribed to increased electron heating, facilitating the generation of a stronger accelerating sheath field at the target rear surface.

Additional studies exploring the potential of nanowire targets include the work by Curtis *et al.* [49]. Deuterated nanowires were irradiated with a 60 fs, $I = 8 \times 10^{19}$ W/cm² pulse. The exceptional volumetric plasma heating in the wires produced energetic deuteron ions at energies near the peak of the D-D fusion cross-section: the D-D produced neutrons yield exhibited a factor 500 increase compared to planar targets. The work by Mondal *et al.* [50] considered irradiated nanowires in the context of THz pulse emission. The energy of broadband THz pulses was measured from the front surface of irradiated nanorod and planar targets; the emitted pulse energy was found to be significantly greater in the case of the nanorods, with the origin of the emission attributed to coherent transition radiation from the laser-accelerated electrons.

Whilst the enhanced performance of nanowire targets is well-demonstrated, the inherent physics of the laser interaction with the wire structures and how to optimise this interaction remains a source of keen research interest. Generally, at high intensities it is suggested that the heating of electrons in the wires occurs by the laser electric field first extracting the electrons from the wires, then accelerating the electrons in the forward direction via the laser fields in the gaps between the wires [51, 52]. The size and spacing of the nanowires has been shown to influence the properties of these accelerated electrons. The use of wire structures with micro-scale dimensions (100's nm) has been found to facilitate the generation of electrons with a hotter electron temperature compared to wire targets with nano-scale dimensions (10's nm) [45]. Wires with a large spacing relative to the laser focal spot size can also be appropriate for direct laser acceleration of electrons in the wire gaps to superponderomotive energies [43, 53]. However, it is not fully apparent which choice of nanowire dimensions and laser parameters are optimal for the control of the fast electron properties.

Pre-plasma formation is an acute issue in the use of nanostructured and nanowire targets. The ASE-pedestal and the rising edge of the laser pulse can ionise and heat the surface of the nanowires before the arrival of the main laser pulse. Since the absorption of laser energy is more efficient for the nanostructured targets compared to planar targets, the intensity

threshold for significant pre-plasma generation is lowered. This was demonstrated during an intensity parameter scan by Cristoforetti *et al.* [54]: $3/2\omega_0$ emission from the front surface (an indirect signature of pre-plasma) became appreciable at a lower laser intensity for nanowire targets in comparison to planar targets. The presence of a pre-plasma can impact the interaction of the main laser pulse. One of the benefits of nanostructured targets is the increased surface area available for laser interaction, which can be reduced if pre-plasma fills the vacuum between the wires and prevents the laser pulse propagating into these gaps. In more extreme cases the wires themselves could be almost entirely ablated and the laser pulse will interact with pre-plasma only; this can add a layer of complexity when attempting to predict the electron absorption and properties of the fast electrons produced. Careful choice and control of the laser parameters is therefore crucial for a predictable and reproducible interaction with nanostructured targets. Frequency doubling has been used by Eftekhari-Zadeh *et al.* [55] to limit the lower intensity pedestal and produce a high-contrast laser pulse at a high repetition rate. In an alternative approach, Samsonova *et al.* [56] employed a long wavelength (3.9 μm) fs laser pulse to irradiate nanowire targets. The temperature of fast electrons scales with $I\lambda^2$, where I is laser intensity and λ is laser wavelength; the use of the longer wavelength laser could result in relativistic electron generation at a lower intensity than for smaller wavelength lasers (e.g. Ti:Sapphire lasers have a wavelength $\lambda = 800$ nm), and the lower laser intensity would be preferable for mitigating pre-plasma formation.

In this thesis an investigation of nanowire targets from two experimental campaigns at the ILIL facility [57] is presented, with exploration of the exiting fast electrons used to diagnose the interactions. The first experiment was carried out in 2019 and aimed to evaluate the performance of nanowire targets through imaging of the optical emission from the rear side of the irradiated targets. This was performed to measure *coherent optical transition radiation* generated by the subset of fast electrons that exit the target, a novel measurement for nanowire targets. This experiment was found to be subject to an exceptional pre-pulse of intensity $\sim 10^{17}$ W/cm², and computational studies using hydrodynamic and particle-in-cell simulations are shown to be vital in explaining the experimental measurements of transition radiation.

The outcome of hydrodynamic simulations of the pre-pulse interaction with the nanowires was the demonstration of the destruction of the wires by the time of the main pulse interac-

tion. A second experiment was therefore carried out in 2021 to achieve a frequency doubled, high-contrast laser interaction with nanowire targets. In this instance the key diagnostic employed was measurements of the *emittance* of the exiting fast electron beam using a pepper-pot diagnostic. The structure of the thesis describing these experiments is outlined as follows:

Chapter 2: Theory of Laser-Plasma Interactions

The main theory relevant to the investigations presented in this thesis is introduced. This includes the interaction of a high-intensity laser with solid targets, absorption into fast electrons, the transport of the fast electron population through the bulk solid target, and the consequences of the fast electron transport, e.g. ion acceleration and the emission of transition radiation.

Chapter 3: Instrumentation and Codes

The work presented in this thesis consists of both experimental and computational studies of laser-solid interactions. The instrumentation in the high power laser at the ILIL facility is outlined, as are the diagnostic methods implemented to diagnose the properties of the fast electrons generated in the interaction. In addition, the particle-in-cell code approach to modelling laser-solid interactions and codes to model the hydrodynamic behaviour of the heated targets are described.

Chapter 4: Optical Transition Radiation from Preheated Planar Targets

Chapters 4 and 5 are concerned with understanding data obtained during the experiment in 2019 where planar and nanowire coated Ti targets were irradiated with a $\sim 10^{20}$ W/cm² laser pulse, preceded 10.4 ns before by a $\sim 10^{17}$ W/cm², 10's fs pre-pulse. Chapter 4 addresses first the results obtained from the planar targets. An enhancement in both the intensity of coherent optical transition radiation and proton cut-off energy is observed from shots on 25 μ m Ti targets compared to shots on thinner Ti targets. These results are explained through a consideration of the pre-plasma formation at the front surface, bulk target expansion, and the disruption of the target rear surface from shock-wave breakout. These studies reveal the density gradient at the shock front is steep enough to sustain efficient transition radiation in the optical regime, and the pre-plasma conditions are appropriate to facilitate the generation

of super-ponderomotive electrons from the main pulse interaction.

Chapter 5: Optical Transition Radiation from Preheated Nanowire Targets

Within the same experiment, a subset of shots on nanowire coated targets displayed a greatly enhanced intensity of coherent optical transition radiation compared to planar targets of comparable thickness, despite the extensive disruption to the target structures from the pre-pulse interaction. Hydrodynamic simulations of the pre-pulse interaction with the nanowires suggest a lower density, longer scale-length pre-plasma is produced from this interaction compared to the pre-pulse interaction with the planar foil targets. Particle-in-cell simulations are then used to propose how the presence of this pre-plasma could explain an enhanced yield of coherent transition radiation formation.

Chapter 6: Frequency Doubled Interactions with Nanowire Targets

Following the pre-pulse experiment a separate campaign was carried out in 2021 with a frequency doubled laser pulse to ensure a high contrast, high intensity interaction with the nanowires. This chapter presents experimental data obtained using a pepper-pot diagnostic to estimate the emittance of the exiting fast electron beam. The use of a pepper-pot to measure fast electrons in a laser-solid interaction is an extremely novel measurement, and is certainly unique to intense interactions with nanowires. Preliminary results indicate an increase in electron emittance for the nanowire targets, an important discovery if considering these nanowire coated targets for use as a fast electron beam source.

Chapter 7: Conclusions and Outlook

In this chapter the results presented in the thesis are reviewed and further discussed in the context of the literature. Experimental and computational work has been undertaken to explore and further understanding of coherent transition radiation from pre-heated targets, and contribute towards the interpretation and feasibility of CTR measurements in future laser-solid experiments. The presence of a pre-plasma during intense laser-solid interactions has also been addressed with respect to CTR production. With respect to nanowire targets, the emittance of the fast electron beam generated from the nanowires has been estimated experimentally. The implications of this measurement on the use of nanostructured targets are discussed and also on the use of a pepper-pot diagnostic in laser-solid interactions more

broadly.

Chapter 2

Theory of Laser-Plasma Interactions

The work in this thesis is concerned with the interaction of *high-intensity* lasers with solid targets. During this interaction a *plasma* is formed at the front surface, facilitating the generation of fast electrons, accelerated ions, radiation emission, and the creation of additional plasma material as a consequence of fast electron propagation through the target. In this chapter the relevant theory regarding the definition of a plasma, the behaviour of plasmas, how high-intensity lasers couple their energy into solid material, and fast electron transport through the target, is outlined.

2.1 Plasmas

Plasmas are often referred to as the “fourth state of matter” and are essentially created by sufficiently ionising a given material. For the material to be defined as a plasma there are a set of criteria that need to be met regarding the collective behaviour of the ions and electrons.

2.1.1 Debye Length

Imagine an electric field with a potential $\phi(x)$ is applied to a plasma with an average ionisation of 1 ($n_e = n_i = n_0$) in a 1D geometry. The ions will be attracted towards to the negative ‘side’, and the electrons towards the positive ‘side’. Consider first the electron response; since electrons are light they will be readily accelerated by the field, and as such the

local electron density will be a function of the potential, $n_e = n_e(\phi)$, with the electron energy related to the potential by $E = \frac{1}{2}m_e v^2 - e\phi$. If the electron distribution can be described as a *Maxwellian* population, the electron distribution function can be written as

$$f_e(v) = \frac{n_0}{(2\pi v_{th})^{3/2}} \exp\left[\frac{-E}{2k_B T}\right] \quad (2.1)$$

$$\rightarrow f_e(v) = \frac{n_0}{(2\pi v_{th})^{3/2}} \exp\left[\frac{-1}{2k_B T} \left(\frac{1}{2}m_e v^2 - e\phi\right)\right]. \quad (2.2)$$

The electron density in the potential is found by integrating Equation 2.2 across velocity space, giving the density as

$$n_e(\phi) = n_0 \exp\left[\frac{e\phi}{k_B T}\right]. \quad (2.3)$$

The ions remain relatively stationary in response to the electric field meaning the ion density across the potential is the same as the initial ion density, $n_i = n_0$. Poisson's equation can then be used to relate the electrostatic potential and find the charged particle densities:

$$\frac{d^2\phi}{dx^2} = -\frac{\rho}{\epsilon_0} \quad (2.4)$$

$$= -\frac{e}{\epsilon_0} [n_i - n_e] \quad (2.5)$$

$$\frac{d^2\phi}{dx^2} = \frac{en_0}{\epsilon_0} \left[\exp\left(\frac{e\phi}{k_B T}\right) - 1 \right]. \quad (2.6)$$

Take the case far from the peak potential where $e\phi/k_B T \ll 1$, allowing the exponential to be approximated by a Maclaurin series as

$$\exp\left(\frac{e\phi}{k_B T}\right) \approx 1 + \frac{e\phi}{k_B T} + \dots \quad (2.7)$$

Putting this expansion into Equation 2.6 gives

$$\frac{d^2\phi}{dx^2} \approx \frac{en_0}{\epsilon_0} \left[1 + \frac{e\phi}{k_B T} - 1 \right] \approx \frac{e^2 n_0}{\epsilon_0 k_B T} \phi. \quad (2.8)$$

A solution for ϕ can be found using an exponentially decaying function,

$$\phi(x) = \phi_0 \exp\left[-\frac{x}{\lambda_D}\right], \quad (2.9)$$

where we have defined the term λ_D , or the *Debye length*, as

$$\lambda_D = \sqrt{\frac{\epsilon_0 k_b T}{n_e e^2}}. \quad (2.10)$$

Physically, the Debye length can be interpreted as the length over which a DC potential is screened by (predominantly) electrons in a plasma. It shows that a higher electron density and a lower temperature will result in a more effective shielding of applied potential.

2.1.2 Plasma Frequency

Consider an electric field applied to a plasma. Since the ions possess a much greater mass than the electrons they remain relatively stationary. In contrast, the electrons, being more mobile, will be displaced by the external field. The collective motion of the electrons will build up a potential difference across the bulk plasma, inducing an electric field proportional to the electron number density. This leads the electrons to feel a restoring force, with the electrons collectively oscillating at a characteristic frequency known as the *plasma frequency* [58]

$$\omega_{pe} = \sqrt{\frac{n_e e^2}{m_e \epsilon_0}}, \quad (2.11)$$

where n_e is the electron number density, e is the electron charge, and m_e is the electron mass. When a wave of frequency ω encounters a plasma, it will only be able to propagate through the plasma under the condition $\omega > \omega_{pe}$. If the plasma frequency is greater, then the plasma is able to respond to the perturbations induced by the EM wave and prohibit the propagation of the wave.

2.2 Laser-Solid Absorption

2.2.1 Ionisation

For an ideal laser-target interaction the target will be irradiated with a single, clean laser pulse. In reality, there are contributions from amplified spontaneous emission in the gain media [59] which acts to produce a *pedestal* of constant low-level intensity light. In addition, the laser pulse has a *leading edge* of rising intensity rather than an abrupt ‘spike’ of intensity. An example laser profile is illustrated in Figure 2.1 to demonstrate the effect of the pedestal and leading edge on the total laser profile. Note, the precise characteristics of the intensity

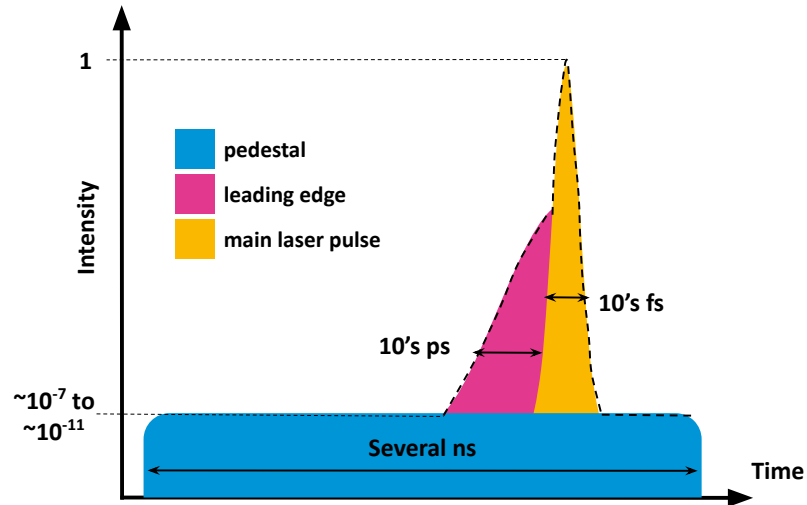


Figure 2.1: Illustration of typical contributions of the pedestal, leading edge, and main pulse on the total laser profile. Contributions have been exaggerated for illustrative purposes and are not to scale.

and temporal ratios are dependent on each laser system, so the values given in the Figure are purely indicative.

The pedestal and leading edge of the laser pulse are able to couple energy into the solid target and generate a *pre-plasma* at the front surface through ionisation of the target material, prior to the arrival of the main laser pulse. In these extreme laser conditions the photon flux is so great that statistically negligible mechanisms can become more meaningful, and the strong electric fields involved relax energy restrictions such that we can obtain sufficient ionisation to produce a plasma.

There are three main field ionisation mechanisms that are important in this regime. Firstly, *multiphoton ionisation*, where the target electron absorbs multiple photons in quick succession to reach the required energetic threshold for ionisation [60]. Secondly, on occasion electrons are able to pass, or tunnel, through the atomic Coulomb potential barrier and escape from the atom without the need of obtaining the ‘full’ ionisation energy. In the presence of a strong electric field (such as a laser field) the potential barrier will be deformed, making this process of *tunneling ionisation* more probable [61]. The Keldysh parameter [62],

given by

$$\gamma_K = \sqrt{\frac{2m_e\omega^2 I_0}{e^2 E_0^2}} = \sqrt{\frac{I_0}{2\phi_p}}, \quad (2.12)$$

compares the *ponderomotive potential* of the laser, ϕ_p , (see Section 2.2.5) and the ionisation potential, I_0 , to determine the dominant ionisation process. If $\gamma_K \ll 1$ then tunneling ionisation will dominate; conversely, if $\gamma_K \gg 1$ then multiphoton ionisation will dominate. Finally, there is the case where the laser field is so strong the potential barrier is suppressed sufficiently such that an electron is able to escape classically, termed *barrier suppression ionisation*. It is estimated that a laser pulse of length 10's fs - 1 ps and peak intensity $> 10^{12-14}$ W/cm² is required for the observation of this ionisation [63]; these conditions are met for our ultra-intense lasers.

The interaction of the pedestal and leading edge of the main laser pulse causes the target to be pre-heated, and a *pre-plasma* is generated at the front surface of the solid target prior to the arrival of the high intensity 'main' laser pulse. This pre-plasma expands into the vacuum at a velocity equal to the ion acoustic velocity

$$v_s = \sqrt{Z_i T_e / m_i} \quad (2.13)$$

as presented in Ref. [64]. An example of the density profile of a solid target with a pre-plasma is shown in Figure 2.2. The resultant pre-plasma is characterised by a density *scale length*, L_s , given by

$$L_s = \frac{n}{dn/dx}, \quad (2.14)$$

with the pre-plasma typically possessing a density profile of the form

$$n_e(x) = A \exp(-x/L_s). \quad (2.15)$$

2.2.2 Critical Density

The dispersion relation of a electromagnetic wave of the form $E(x, t) = E_0 \exp[i(kx - \omega t)]$ in a plasma can be derived as [65]

$$\omega_0^2 = \omega_{pe}^2 + k^2 c^2 \quad (2.16)$$

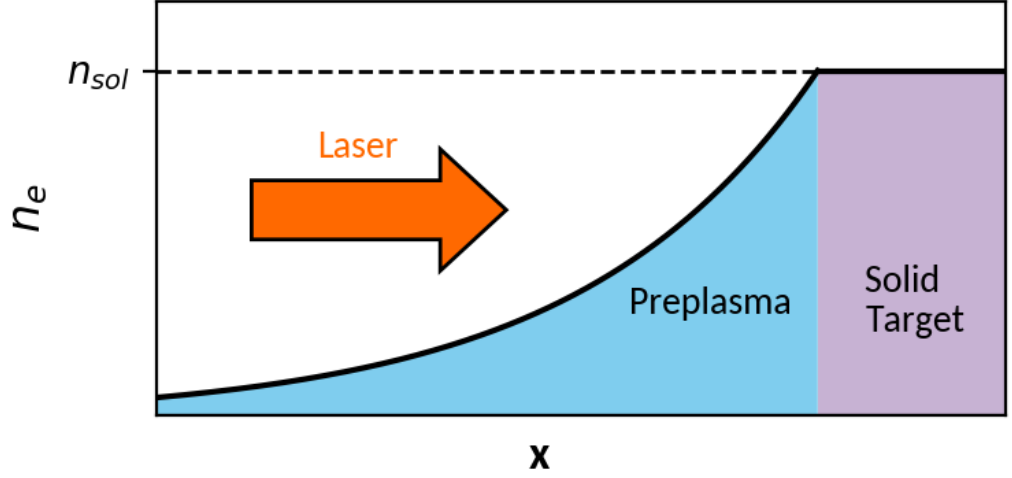


Figure 2.2: Diagram to demonstrate the 1D density profile of a solid target post pre-plasma generation.

where ω_{pe} is the plasma frequency, ω_0 is the angular frequency of the incoming EM wave in vacuum, and k is the modified wavevector of the EM wave in the plasma. We can see that a laser wave is able to propagate through a plasma given $\omega_0 > \omega_{pe}$. For the special case where $\omega_0 = \omega_{pe}$ we obtain $k = 0$, indicating the point at which the laser can no longer propagate inside the plasma and is instead reflected. This occurs at an electron density

$$n_{crit} = \frac{4\pi^2 c^2 m_e \epsilon_0}{e^2 \lambda^2} = \frac{1.1 \times 10^{21}}{\lambda_{\mu m}^2} \text{ cm}^{-3}, \quad (2.17)$$

more commonly referred to as the *critical density*. Solid metals have electron densities $\sim 10^{22-23} \text{ cm}^{-3}$, prohibiting the propagation of optical lasers through the bulk target.

Beyond the critical density surface the laser is able to propagate a short distance into the over-critical material. Here, $\omega_0 < \omega_{pe}$ which yields an imaginary k -value. The laser electric field in the over-critical target is now described by $E(x, t) = E_0 \exp(-|k|x - i\omega t)$. The field will exhibit an evanescent decay into the target, with the over-critical depth over which the electric field decays over given by the *collisionless skin depth*,

$$\lambda_{sd} = \frac{c}{\omega_p}. \quad (2.18)$$

For very intense ($a_0 > 1$) laser interactions, where a_0 is defined in Equation 2.33, rela-

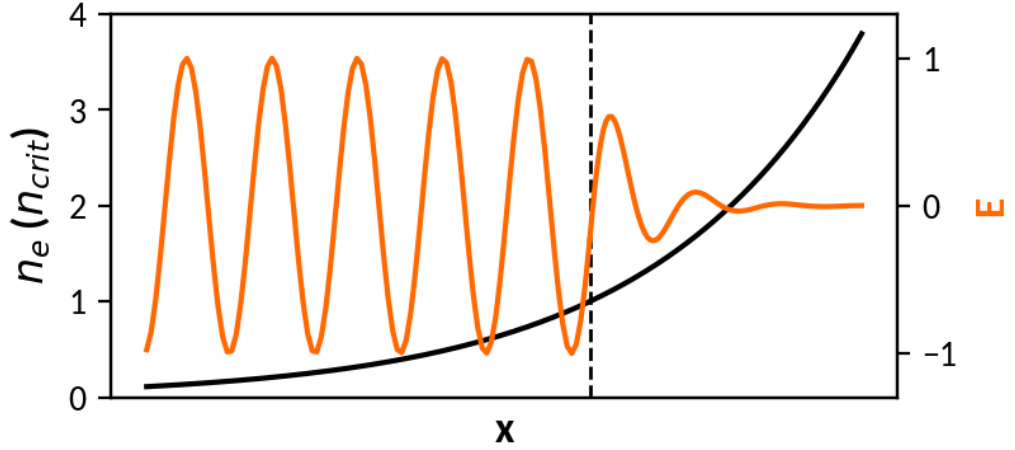


Figure 2.3: Strength of the laser electric field in a plasma of varying density. Dotted line indicates the position of the critical density surface.

tivistic electrons can be created. The electron mass will increase at these relativistic energies, affecting the ability of the plasma to reflect the laser light [66]. Reflection of the laser light will then occur at a relativistically-corrected critical density of [67]

$$n_{crit,rel} = \gamma_{rel} n_{crit} \quad (2.19)$$

where γ_{rel} is the relativistic factor

$$\gamma_{rel} = \sqrt{1 - \frac{v^2}{c^2}}. \quad (2.20)$$

2.2.3 Inverse Bremsstrahlung

The process of *inverse bremsstrahlung*, or free-free absorption, involves the excitation of a free electron by absorption of a laser photon whilst the electron is in the field of an ion [68]. The energetic electron can then lose this gained energy via collisions with ions, causing a heating of the bulk plasma [67]. The efficiency of the inverse bremsstrahlung absorption process is consequently dependent on ν_{ei} , the electron-ion collisionality, in the plasma. The exact scaling of the collisional absorption with ν_{ei} is dependent on the density profile of the plasma. As an example, for a plasma with an exponential density profile the absorption is

described by Kruer as [65]

$$f_A = 1 - \exp\left(-\frac{8 \nu_{ei}^* L_s}{3c} \cos^3 \theta\right) \quad (2.21)$$

where f_A is the fractional absorption, ν_{ei}^* is the electron-ion collision frequency at the critical density, L_s is the decay length of the exponential profile, and θ is the angle of laser incidence. The rate of electron-ion collisions at n_{crit} can be described as

$$\nu_{ei}^* \propto \frac{n_{crit} Z^*}{T_e^{3/2}} \quad (2.22)$$

where Z^* is the average ionisation. From assessment of these two equations we can see inverse bremsstrahlung absorption is maximised in plasmas with large density scale lengths, higher values of Z and n_{crit} , and a lower temperature.

2.2.4 Resonance Absorption and Vacuum Heating

Consider p -polarised laser light incident onto a target at an angle θ , resulting in a component of the electric field being directed into the target. As presented earlier, the laser field can propagate into a plasma up to the critical density before undergoing an evanescent decay into the over-dense plasma. For irradiation at an angle, the dispersion relation of the laser EM wave in the plasma given in Equation 2.16 is modified to account for the directional wave components,

$$\omega_0^2 = \omega_{pe}(x)^2 + c^2(k_x^2 + k_y^2) \quad (2.23)$$

$$\omega_0^2 = \omega_{pe}(x)^2 + c^2(k_x^2 + k_0^2 \sin^2 \theta). \quad (2.24)$$

Reflection of the wave ($k_x = 0$) will occur when the plasma frequency satisfies

$$\omega_{pe}^2 = \omega_0^2 - c^2 k_0^2 \sin^2 \theta \quad (2.25)$$

$$\omega_{pe}^2 = \omega_0^2 (1 - \sin^2 \theta) \quad (2.26)$$

$$\omega_{pe}^2 = \omega_0^2 \cos^2 \theta. \quad (2.27)$$

From Equation 2.11 we know $\omega_{pe} \propto \sqrt{n_e}$; combining this with the knowledge that the critical density occurs where $\omega_0 = \omega_{pe}$, we arrive at the conclusion that the laser is reflected

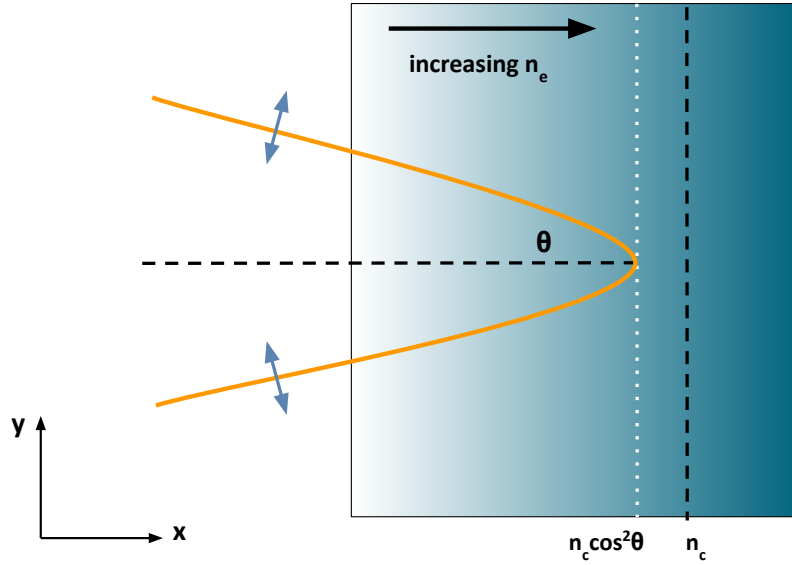


Figure 2.4: Diagram to illustrate how resonance absorption is able to take place for p-polarised laser light. Note the definition of *p*-polarised means the electric field vector oscillates in the *plane of incidence*, i.e. along the light blue arrow. If the light were *s*-polarised the electric field vector would oscillate perpendicular to the plane, i.e. into and out of the page, and there would not be a component of the electric field directed into the density gradient.

at an electron density

$$n_e = n_c \cos^2 \theta. \quad (2.28)$$

The electric field is able to propagate to the critical density, allowing the excitation of electron plasma waves. At the critical surface, where the frequency of the laser-driven oscillations matches that of the critical density plasma, the amplitude of these electron plasma waves will grow rapidly [69]. This growth is not infinite; the electron wave will eventually be damped through wave breaking, convection or collisional effects [70]. The resonant absorption mechanism produces a non-Maxwellian tail of hot electrons, the temperature of which was predicted theoretically by Forslund *et al.* [71] to scale with laser intensity as

$$T_{hot} \approx 14(I_{10^{16}} \lambda_{\mu m}^2 T_{keV})^{1/3} \text{ keV}, \quad (2.29)$$

where $I_{10^{16}}$ is laser intensity in 10^{16} W/cm^2 , λ is laser wavelength in μm , and T is the background electron temperature in keV.

Resonance absorption takes place for laser interactions with a longer scale length pre-

plasma. An associated mechanism also occurs for a steep density gradient where the plasma scale length is smaller than the amplitude of the electron oscillation. Brunel [72] first detailed the process of ‘not-so-resonant, resonant absorption’, generally referred to as *vacuum heating* or *Brunel heating*. In this scenario, electrons are pulled into vacuum by *p*-polarised laser light when the electric field is directed away from the target on one half-cycle. In the next half-cycle, the electrons are accelerated back into the target as the electric field is directed into the target. This process occurs once per laser cycle, injecting electron bunches into the target at a periodicity equal to the laser frequency ω_L . Gibbon and Bell [73] demonstrated this vacuum heating mechanism is dominant over resonant absorption for a laser pulse with intensity $I \sim 10^{14-18}$ W/cm² interacting with a short density scale length plasma with $L/\lambda < 0.1$.

2.2.5 Ponderomotive Force

An electron in the presence of the laser electric field will experience a *ponderomotive force*, given by [74]

$$f_P = -\frac{e^2}{2m_e\omega_0^2}\nabla E^2, \quad (2.30)$$

where ω_0 is the laser frequency and ∇E is the gradient of the laser electric field. One can also express this ponderomotive force in terms of a *ponderomotive potential*, ϕ_p :

$$f_p = -\nabla\phi_p, \quad \phi_p = \frac{e^2}{2m_e\omega_0^2}E^2. \quad (2.31)$$

In high-power laser applications a focused laser beam is used with a spatially varying focal spot described by a Gaussian profile. The intensity is at a peak at the centre of the focal spot and rapidly reduces with radius, thus establishing an E-field gradient. Following Equation 2.30, the ponderomotive force will act to drive electrons to regions of lower electric field strength. Since the strength of the laser electric field has a temporal dependence given by $E = E_0 \sin(\omega_0 t)$, the final result is an oscillation of the electron at a frequency $2\omega_0$, with the magnitude of E^2 reaching a maxima twice per laser cycle.

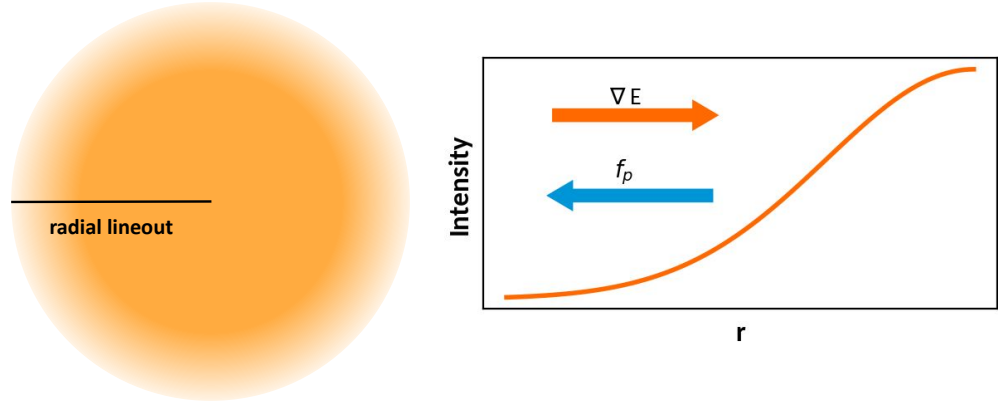


Figure 2.5: Diagram to illustrate the ponderomotive force direction in a focused laser spot.

2.2.6 Ponderomotive Acceleration

There is, of course, a magnetic field component of the wave to acknowledge, directed perpendicular to the \mathbf{E} field. The ponderomotively-driven electron motion and magnetic field produces a $e\mathbf{v} \times \mathbf{B}$ Lorentz force pointing perpendicular to the \mathbf{E} and \mathbf{B} fields, i.e. in the k -vector direction of wave propagation. The result is a ‘figure-of-eight’ motion of an electron in a EM field, with oscillations in the \mathbf{E} and k -vector directions. A full derivation of this result (see Ref. [68]) reveals a net velocity of the electron in the direction of the EM wave propagation,

$$v_d = \frac{e^2 E_0^2}{4m_e^2 \omega_0^2 c}. \quad (2.32)$$

This is otherwise known as *ponderomotive acceleration* [75].

In the context of laser-plasma interactions this ponderomotive acceleration becomes appreciable at ultra-intense laser intensities. The threshold can be described using the normalised vector potential, a_0 , given as

$$a_0 = \frac{eE_0}{m\omega_0 c} = \sqrt{\frac{I\lambda_{\mu m}^2}{1.37 \times 10^{18}}} \quad (2.33)$$

where E_0 is the peak laser field value. When a_0 exceeds 1 ($I\lambda_{\mu m}^2 > 1.37 \times 10^{18} \text{ W/cm}^2$), the quiver motion and subsequent ponderomotive acceleration force can become great enough to overcome the ponderomotive potential. The electrons are able to escape the laser fields and are injected into the target along the laser k -vector at a frequency $2\omega_0$, with a hot

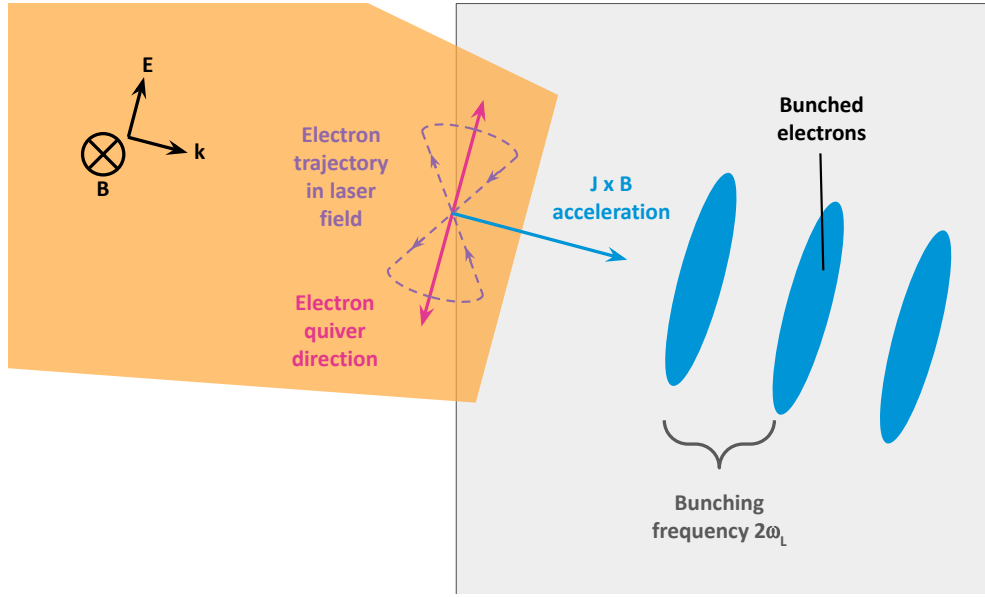


Figure 2.6: Diagram describing the trajectory and acceleration of target electrons in strong laser fields. The ponderomotive acceleration process injects bunches of electrons into the target along the k -vector direction.

electron temperature estimated by Wilks *et al.* as [76]

$$T_{hot} \approx \left(\sqrt{1 + \frac{I\lambda_{\mu m}^2}{2.8 \times 10^{18}}} - 1 \right) 0.511 \text{ MeV}. \quad (2.34)$$

The Wilk's scaling estimates the electron temperature as the energy of the electron oscillations in the laser electric field, E_{osc} . Later work by Sherlock [77] proposed the electron energy distribution is better described as an average energy

$$E_{avg} \approx 0.6E_{osc} \quad (2.35)$$

where a reduction in energy is predicted due to work done in drawing the return current (see Section 2.3.1).

2.2.7 Direct Laser Acceleration

Within the ultra-intense regime there exists scenarios where the electrons are able to be accelerated to super-ponderomotive energies under *direct laser acceleration* (DLA). If energetic electrons are confined within some static electric or magnetic field they will undergo betatron oscillations in the static field. Provided this betatron frequency is close to the

laser frequency (in the frame of the relativistic electron), and the electrons are oscillating in the vicinity of the laser fields, there can be an additional energy coupled from the laser into the electrons, with these electrons accelerated in resonant bunches at $2\omega_0$ [78]. One situation this may occur is in an intense laser interaction with an under-critical density, long scale length plasma: the ponderomotive force in the intense, focused laser beam can expel electrons in the undercritical plasma outwards, creating a positively charged *plasma channel* with a charge-separation electric field in the transverse direction [79, 80]. Electrons can be confined in this channel whilst undergoing oscillations across the channel, and subsequently experience additional acceleration [81, 82].

2.3 Fast Electron Transport

2.3.1 Return Current and Ohmic Heating

The fast electron beam will possess a current density \mathbf{j}_f . The electron numbers and energies produced from intense laser interaction result in high currents, with this current generated in a small localised region approximately the size of the focal spot. From Ampère-Maxwell's law we know a magnetic field is produced in the presence of a current density. Calculations by Bell *et al.* [83] estimated an energy ~ 5 kJ in this magnetic field for a fast electron beam produced from a 10^{18} W/cm², 1 ps interaction. This is energetically impossible - the energy contained in such a laser pulse is the order 10's J - and the conclusion is drawn that the fast electrons must either (a) be confined to the front of the target (since the energy in the magnetic field scales with penetration depth), or (b) the fast electron current is balanced by a *return current*, \mathbf{j}_b , provided by the background target plasma. It follows that

$$\mathbf{j}_f + \mathbf{j}_b \approx 0, \quad (2.36)$$

with the fast electron beam only able to propagate through the target if the target material has the ability to generate a locally balancing return current. From Ohm's Law, an electric field

$$\mathbf{E} \approx -\eta(T) \mathbf{j}_f \quad (2.37)$$

where η is the temperature-dependent resistivity of the background plasma, is required to draw this return current. Work is done by the thermal electrons against this electric field

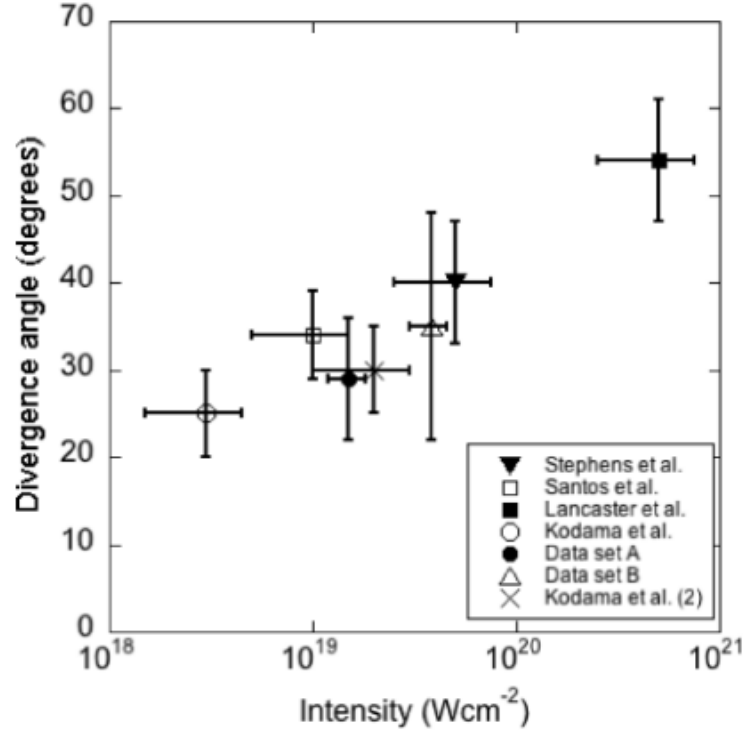


Figure 2.7: Measurements of divergence angle as a function of laser intensity [88]

in the form

$$W = \mathbf{E} \cdot \mathbf{j} \cdot dx. \quad (2.38)$$

The consequence of this is *Ohmic heating* of the target by the return current, with the heating rate given by [84]

$$\frac{\partial T}{\partial t} = \frac{\eta(T) \mathbf{j}_f^2}{C_v}. \quad (2.39)$$

2.3.2 Filamentation

The propagation of the electron beam through a plasma leaves it susceptible to instabilities that can cause the beam to undergo *filamentation*, first observed experimentally in an exiting electron beam by Wei *et al.* [85]. These instabilities work in tandem to cause the fast electron beam to break up into distinct filamentary structures. There are three main instability modes to consider: Weibel [86], filamentation and two-stream instabilities [87]. In a nutshell, these instabilities are the growth of unstable electromagnetic (Weibel and filamentation) or electrostatic (two-stream) modes and can be amplified by the interaction of the forward propagating fast electron current and backward propagating return current.

2.3.3 Divergence

A well-known feature of a laser-solid generated fast electron beam is that it is *divergent* at a half-angle $\theta_{1/2}$ [89–91]. Particle-in-cell simulations by Adam *et al.* [92] suggested the electron beam divergence is seeded in magnetic field fluctuations in the laser-target interaction region deflecting the energetic electrons. Work by Debayle *et al.* [93] built on this further, proposing that there are two components contributing to the total divergence: the angular dispersion of the fast electrons due to the small scale magnetic fields formed due to the Weibel instability, and an additional radial deviation due to the laser ponderomotive force. This divergence of the fast electron beam has been seen in experimental observations to increase with laser intensity as reported by Green *et al.* [88], as demonstrated in Figure 2.7. Later work by Armstrong *et al.* [94] measured the spatial profile of X-ray bremsstrahlung emission from the rear surface of irradiated targets. It was shown that there were a duo of electron sources contributing to the X-ray emission region: a central source from high-energy electrons, and a secondary source of broader emission induced by refluxing electrons, thus showing the picture of divergence scaling with laser intensity is more complex than first suggested.

2.3.4 Optical Transition Radiation

Fast electrons produced in intense-laser solid interactions will propagate through the target material. As the electrons traverse the target there will be a polarisation of the dielectric material due to the local electric field associated with the electrons. In homogeneous material (e.g. the target bulk), this transient polarisation has no additional effects. However, the situation changes when we consider the case of fast electron propagation through the target surface and into vacuum. Using Maxwell’s equations, the wave equation can be solved in the target and vacuum regions to show that the inhomogeneous solution from the electron fields is not sufficient to ensure continuity of the electric displacement field \mathbf{D} and the electric field \mathbf{E} . To satisfy the continuity boundary condition, an additional homogeneous solution is required which is associated with radiators in the target. This produces a radiation field that is dubbed *transition radiation* [95,96]. This radiation is emitted from polarised atoms at the target boundary in response to the inequality of fields in the target and in vacuum.

The intensity and spectra of the transition radiation emission is dependent upon properties of the fast electrons. In high intensity regimes electrons are predominantly accelerated

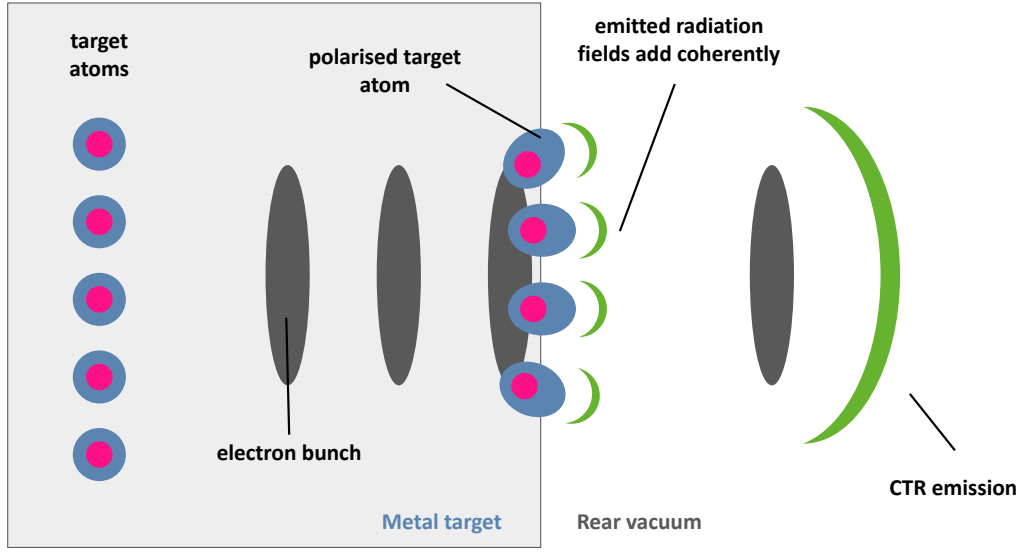


Figure 2.8: Illustration of the production of transition radiation induced by fast electron bunches propagating through a metal-vacuum boundary.

in bunches, resulting in the emitted radiation adding coherently to form *coherent transition radiation* (CTR). For a beam of electrons comprised of n_b bunches emitted at a frequency $1/\Delta t$, the CTR energy W emitted per unit angular frequency and solid angle is related to the fast electrons by [97]

$$\frac{d^2W}{d\omega d\Omega_{CTR}} \propto \underbrace{\frac{e^2 N(N-1)}{4\pi^2 c n_b^2 u_t^6}}_{(1)} \underbrace{\frac{\sin^2(n_b \omega \Delta t / 2)}{\sin^2(\omega \Delta t / 2)}}_{(2)} \underbrace{\exp(-k_{\perp}^2 \sigma^2)}_{(3)} \quad (2.40)$$

where N is electron number per bunch, u_t is target temperature, and σ is the variance of the spatial distribution of the bunch. The numbered terms in Eqn. 2.40 indicate characteristic properties of CTR emission. Firstly, Term (1) shows the energy emitted has a quadratic scaling with the number of electrons, demonstrated experimentally for a wakefield-accelerated electron beam passing through a thin metal foil [99]. Secondly, Term (2) indicates the emission energy will be maximised at harmonics of the bunching frequency, meaning the CTR spectral profile is inherently linked to the laser frequency ω_0 since electron bunches will be accelerated at either ω_0 or $2\omega_0$ [100]. Figure 2.9 shows the spectrum predicted for a bunching frequency ω_0 . Finally, Term (3) accounts for a drop in the efficiency of the production of CTR due to dephasing of the electron bunches. Experiments measuring CTR emission as a function of target thickness verify this prediction [101, 102].

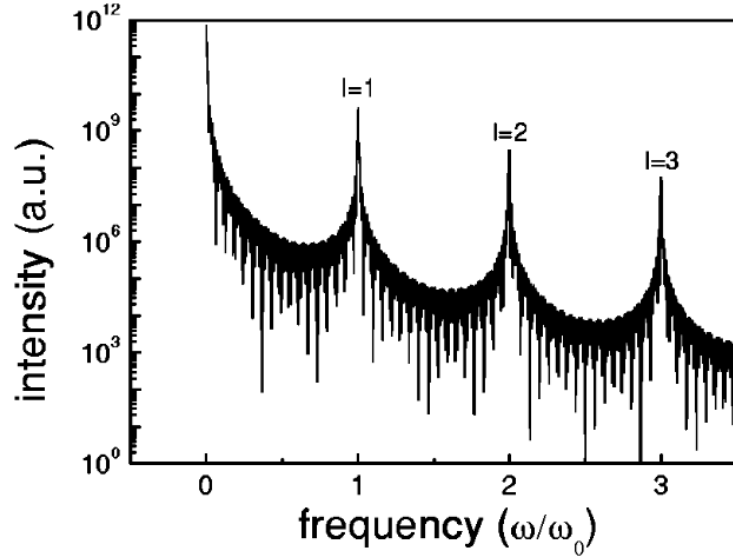


Figure 2.9: Spectral properties of CTR emission [98].

The total emitted transition radiation spectra contains an additional incoherent component [95],

$$\frac{d^2W}{d\omega d\Omega}_{ITR} = \frac{e^2 N}{\pi^2 c} \left[\langle \epsilon_{\parallel}^2 \rangle + \langle \epsilon_{\perp}^2 \rangle \right], \quad (2.41)$$

where $\langle \epsilon_{\parallel} \rangle$ and $\langle \epsilon_{\perp} \rangle$ are the amplitudes of the electric fields generated by the electron in the radiation plane or perpendicular to the radiation plane, respectively. The key feature to note in Equation 2.41 is the linear scaling of the intensity of emission with N . For a large number of fast electrons we would expect CTR, with a quadratic dependence on electron number, to dominate.

This transition radiation is produced most efficiently over a region called the *formation zone*. Generally, the length of the formation zone is given by [103]

$$L_f = \frac{c}{\omega} \frac{\beta}{\left[1 - \beta (\epsilon_r - \epsilon_r \sin^2 \theta)^{1/2} \right]}, \quad (2.42)$$

where β is the speed of the particle relative to the speed of light (v/c), ϵ_r is the dielectric constant of the material, and θ is the angle of observation. In the discussion of transition radiation formation at the solid-vacuum interface there are two formation lengths to consider, since ϵ_r differs between the media. In the plasma the dielectric constant is described by

$\epsilon_r = 1 - (\omega_p/\omega)^2$, and the length of the formation zone can be written as [97]

$$L_f \simeq \frac{c}{\omega_p} \frac{1}{\cos\theta}, \quad (2.43)$$

where ω_p is the plasma frequency. At $\theta = 0^\circ$ the formation length reduces to the expression for the plasma skin depth; electrons beyond the skin depth should not significantly contribute to the formation of CTR. Along the direction of propagation of the exiting fast electron(s) the *formation length* in vacuum can be given as [104]

$$L_f \simeq \frac{c}{\omega} \gamma^2, \quad (2.44)$$

where ω is the angular frequency of the radiation and γ is the Lorentz factor of the fast electron, since $\epsilon_r = 0$. The relationship can be reduced to a function of the wavelength of the radiation and the kinetic energy of the electron using $\gamma = \frac{\text{KE}}{m_e c^2} + 1$:

$$L_f \simeq \frac{\lambda_{\mu m}}{2\pi} [(1.951 \times \text{KE}_{\text{MeV}}) + 1]^2 \mu m. \quad (2.45)$$

From Equations 2.43 and 2.45 one can appreciate that whilst the formation length in plasma is very short for solid targets, where the skin depth is to the order of a few nm's, the formation length in the vacuum can be relatively long for high energy electrons and extend to the order of μm 's.

2.3.5 Sheath Field Generation

As the fast electrons propagate through the target and exit into the vacuum, a sheath electric field grows at the rear surface of the target. This sheath field extends over a Debye length and acting to recirculate lower energy electrons back into the target [105]. The strength of the sheath field is sensitive to the properties of the fast electron population: for example, Ridgers *et al.* [106] showed the sheath potential is dependent on the average energy of the fast electrons.

The potential in the sheath field is strong enough to rapidly ionise target material at the back, and subsequently accelerate these ions in a direction normal to the surface of the target. This mechanism, known as *target normal sheath acceleration* (TNSA), was first formally

described in the work by Wilks *et al.* [107]. The presence of water and hydrocarbon contaminants on material surfaces means protons are commonly detected in experiments with energies higher than the target ions, due to their higher charge-mass ratio. Maximum ion energies due to TNSA have been found to be sensitive to the fast electron temperature [108], and also to the thickness of the target employed and laser pulse length [109].

Irradiation by an intense laser can result in rapid energy deposition and heating at the front surface, launching a shock-wave into the bulk target [110]. If this shock is sufficiently strong, or the target sufficiently thin, this shock-wave can break out at the rear surface of the target before or during the main laser interaction, disrupting the rear surface. This has been shown in previous works to be detrimental to the efficiency of TNSA, with lower proton cut-off energies measured when a scale length pre-plasma is present at the rear surface [111,112].

Chapter 3

Instrumentation and Codes

3.1 High Power Laser Systems

3.1.1 Chirped Pulse Amplification

The basis of most modern high power laser systems is the concept of chirped pulse amplification (CPA) [6]. During the pulse amplification stage there are non-linear effects that come into play when the intensity becomes too great, distorting the spatial and temporal profile of the laser pulse and potentially damaging the amplifier(s). This places a limit on the pulse intensity that can feasibly be reached inside the amplifying media. In the CPA technique, the initial pulse is first stretched using pairs of diffraction gratings, where the first grating creates angularly dispersed light depending on the wavelength, and the second will refocus the dispersed light spatially. The light will however not be refocused *temporally* due to the path difference between red and blue light, creating a chirped, temporally stretched pulse. This lower power pulse can be amplified via passage of the pulse through a solid state amplifier whilst maintaining a relatively low intensity. After amplification the pulse can be compressed again using diffraction gratings to obtain a high power pulse with a short duration. The Nobel-Prize winning approach allows laser pulses to be amplified to several Joules, whilst limiting the aforementioned unfavourable non-linear effects in the amplifying media such as self-focusing.

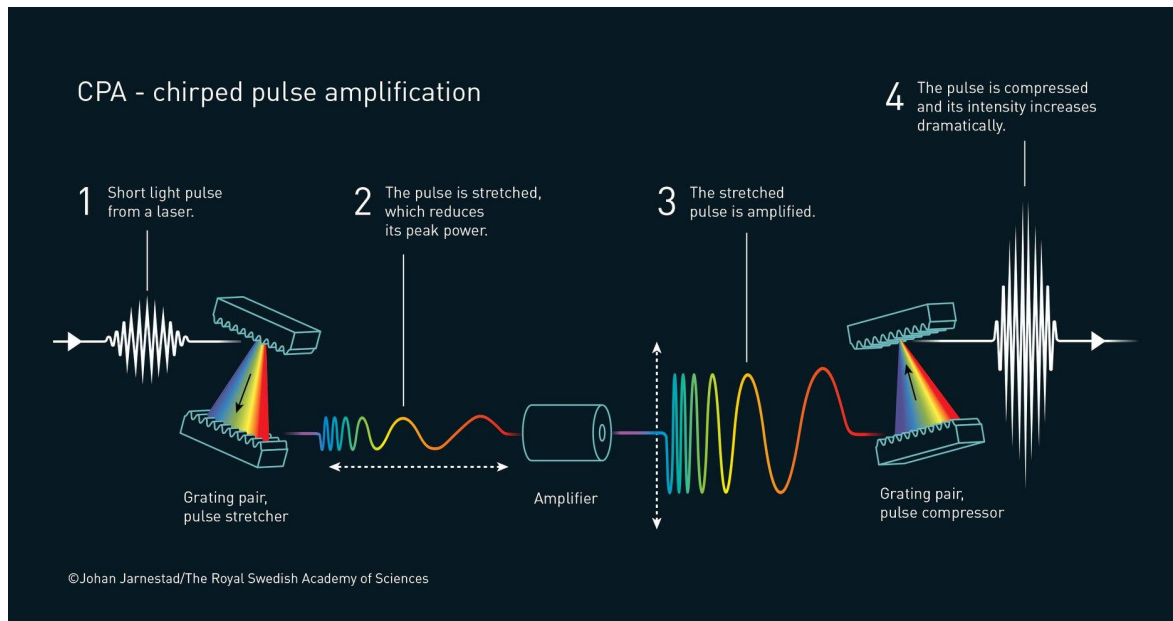


Figure 3.1: Illustration of the technique of chirped pulse amplification employed to produce short, high power laser pulses. © Johan Jarnestad/The Royal Swedish Academy of Sciences

3.1.2 ILIL PW Laser

The experimental data presented in this thesis was obtained at the Intense Laser Irradiation Laboratory (ILIL), Pisa. The following description of the ILIL-PW Ti:Sapphire laser system has been adapted from Ref. [57].

An initial train of 6 nJ, 15 fs laser pulses at 74 MHz is generated by a Ti:Sapphire oscillator. A booster module is used which includes a 14-pass amplifier to increase pulse energy to the order of 10 μ J before pulses are selected at a rate of 10 Hz from the oscillator output. An Öffner-type stretcher is used to create chirped 300 ps pulses. Several amplification stages are employed in the laser system to create < 8 J pulses. First, a regenerative amplifier is used resulting in pulse energies of \sim 0.6 mJ, followed by a 5-pass pre-amplifier to further increase the energy to 30 mJ. To prevent optical damage from high fluences the beam is then expanded to a diameter of 10 mm with a telescope. The enlarged beam passes through a 4-pass amplifier and gains energy up to 600 mJ. As before, the beam is again expanded to a diameter of 36 mm, before being sent to the final amplification stage where a 4-pass amplifier increases the pulse energy to a maximum of < 8 J. Here, monitoring of the pulse energy is also carried out through measurements of the energy leaking through the last turning mirror after the final amplifier, with shot-to-shot energy fluctuations previously inferred

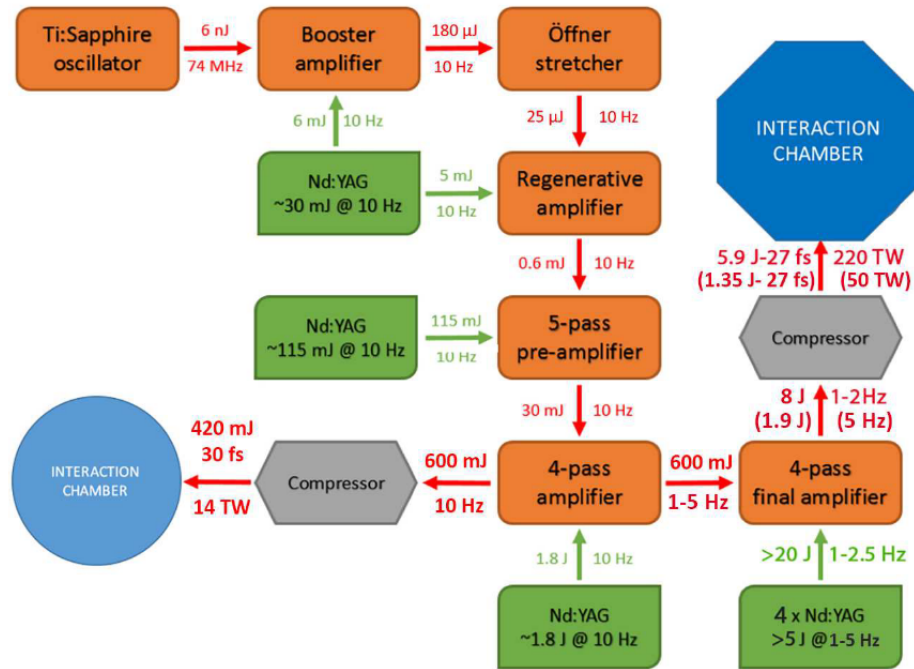


Figure 3.2: Layout of the ILIL laser system. Taken from Ref. [57].

as $< 2\%$ root mean square. Finally, temporal compression of the full energy pulse to < 27 fs is achieved using 4 gratings in a folded configuration. Conversion efficiency is 75%, resulting in a final peak power of 220 TW. Figure 3.2 summarises the layout of the ILIL laser, with the PW line target chamber indicated by the hexagon shape.

3.1.3 Laser Optics

The creation of a high quality, high intensity laser pulse is only possible with the inclusion of additional optics in the laser chain. Here we introduce the specific complementary optics in place at the ILIL laser facility.

Saturable absorber

For an amplifying medium to be able to lase it needs to be pumped with energy (e.g. from a flash lamp or another laser) to produce a population inversion. However, a side effect is that the amplifying medium will then be able to radiate spontaneous emission which can be subsequently amplified, known as *amplified spontaneous emission* (ASE). The random nature of this emission results in a constant, low level light which presents as a *pedestal* on which any laser pulses sit atop.

This ASE is mitigated through the use of a *saturable absorber* at the booster amplifier. A saturable absorber exhibits a varying level of absorption depending on the fluence of the incoming light; lower energy light will be absorbed, whilst higher energy light will saturate the absorber and can propagate through. In laser applications, this means the lower energy pedestal will be absorbed and removed whereas the higher energy pulses can continue on, yielding a ‘cleaned’ laser profile.

Pulse Shaping

As the pulse travels through the laser system it is subject to dispersion and phase distortions. The *group delay* is a time delay experienced by a light pulse as it propagates through an optical element. The group delay is dependent on the frequency of light; since the pulse contains a spread of wavelengths, this results in a broadening of the pulse in time termed *group delay dispersion*. An acousto-optic programmable dispersive filter (AOPDF) [113] named the Fastlite *Dazzler* is placed after the stretcher to apply phase corrections and pre-compensate this distortion prior to amplification.

Gain narrowing can occur during amplification, where the centre of the optical spectrum experiences greater amplification than the spectral wings. The Fastlite *Mazzler* is an acousto-optic programmable gain filter (AOPGF) which is placed in the regenerative amplifier to compensate for this. It ensures the bandwidth of the pulse is maintained between entering and exiting the regenerative amplifier. Use of the *Mazzler* also results in a flatter spectrum, allowing for optimal compression.

Pockels Cell

The ILIL laser initially generates pulses from the oscillator at a rate of 75 MHz, with the rate dropping to 10 Hz when exiting the booster amplifier. This pulse rate reduction is not due to pulses spontaneously ‘disappearing’ during the laser chain, but is down to the use of *Pockels cells* as a pulse picker.

In essence a Pockels cell acts as a voltage-controlled wave plate. It can be explained by the Pockels effect, where a change in the birefringence of an electro-optic crystal is observed

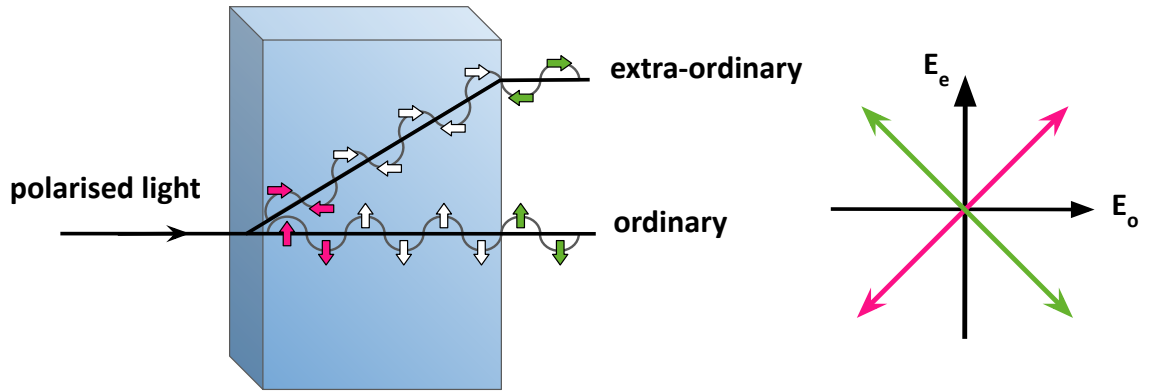


Figure 3.3: Illustration of the effect of birefringence on polarisation. Distances have been exaggerated for clarity.

under an applied potential difference. When light impinges on the crystal it is described by two components: the ordinary component with polarisation perpendicular to the optical axis, and the extra-ordinary component with polarisation parallel to the optical axis. The ordinary and extra-ordinary waves will experience different refractive indices and propagate at different velocities; this is the property of birefringence. When a voltage is applied the birefringence becomes considerable enough to induce a non-negligible phase shift between the ordinary and extra-ordinary components. Figure 3.3 illustrates how the phase shift results in a rotation of polarisation.

The Pockels cell setup is completed by the placement of a *polariser* after the crystal to only permit the passage of light with polarisation matching that imposed by the activated Pockels cell. When unactivated, the polarisation of the light will not change and will simply reflect from the polariser. Pockels cells are in use at the ends of the booster and regenerative amplifiers to restrict leakage of pulses after every pass of the cavity. Alignment of the crystal is critical to the performance of the Pockels cell; if the optical axis of the crystal is misaligned it can cause the pulse to be partially polarised even without an applied voltage, leading to unwanted pulses passing through.

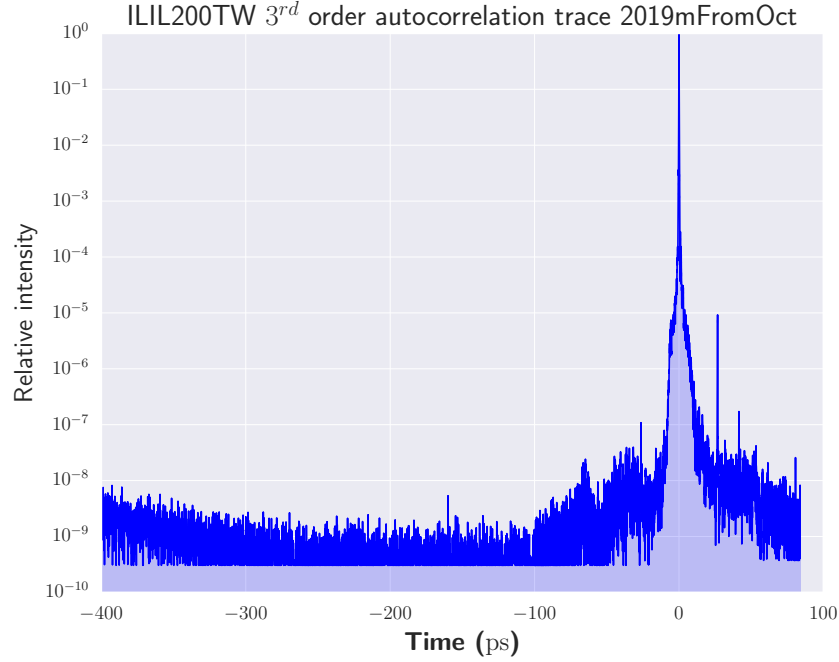


Figure 3.4: 3rd order autocorrelation trace of ILIL laser.

3.1.4 Laser Contrast

For the ILIL PW laser, background ASE arises dominantly from the final amplifier and has a contrast better than 10^{-8} as measured by a Sequoia third-order cross-correlator (Figure 3.4). A larger divergence of the ASE with respect to the main beam means the focal position is 250-300 μm away from the main pulse focus, leading to an on-target intensity of $\sim 10^9$ W/cm^2 . As such, the ASE interaction can be assumed to be negligible when compared to the main pulse intensity of $\sim 10^{21}$ W/cm^2 . Furthermore, low intensity pulses, or pre-pulses, can arrive at the target arising from Pockels cell leaks. These pre-pulses can be of significant intensity if the timing coincides with the pumping of amplifiers further down the laser chain.

The laser contrast refers to the ratio of the ASE or pre-pulse intensity or energy relative to the main pulse. Additional optics can be placed at the end of the laser chain to remove any residual ASE or pre-pulses and improve the contrast. This is not always necessary, but can be helpful as an assurance in instances where a high contrast is critical to the success of the interaction. Plasma mirrors [114] consisting of glass slabs with an anti-reflection coating on the front can be used - however, traditional plasma mirrors are by design single use and not practical for experiments carried out at high repetition rate.

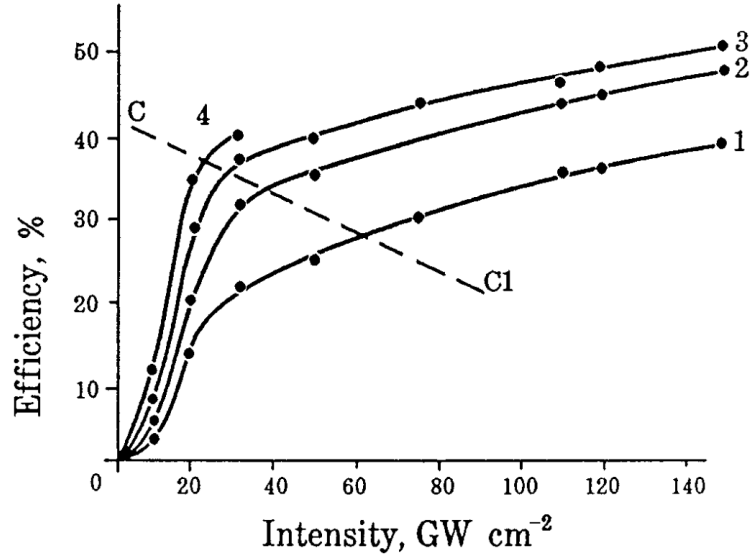


Figure 3.5: Conversion efficiency into second harmonic as a function of intensity for KDP crystals of different thicknesses. Reprinted with permission from [115] © The Optical Society

Alternatively, second harmonic generation (SHG) produced in non-linear crystals can be exploited to clean the laser profile. When light propagates through a uniaxial (possessing no inversion symmetry) crystal material such as KDP [116] it is able to induce a second order polarisation determined by

$$\mathbf{P}^{(2)}(t) = 2\epsilon_0\chi^{(2)}EE^* + \left(\epsilon_0\chi^{(2)}E^2e^{-i2\omega t}\right) \quad (3.1)$$

where $\chi^{(2)}$ is the second-order susceptibility term and E is the laser electric field [117]. The second term in Eqn. 3.1 results in the launching of a wave with a frequency twice that of the incoming wave. The intensity of the frequency doubled wave is then given by

$$S = 2\pi cP^2(k_{2\omega}/\Delta k)^2 \sin^2(\Delta kx) \quad (3.2)$$

$$\Delta kx = |k_{2\omega} - 2k_\omega| \quad (3.3)$$

where k_ω and $k_{2\omega}$ are the wavevectors of the incident and frequency doubled light respectively and P is the magnitude of the polarisation [118]. From assessment of Equations 3.1 and 3.2 we can see the intensity of second harmonic light scales *quadratically* with the intensity of the incoming laser light, since \mathbf{P} scales with laser intensity ($I \propto E^2$) and the intensity of the subsequent 2ω light scales with P^2 . This means lower intensity laser light

(such as from a prepulse or pedestal) will be substantially less efficiently converted to 2ω compared to the higher intensity main laser pulse. Remaining fundamental frequency light can be filtered out, and the 2ω light with an improved contrast used to irradiate the target.

3.2 Experimental Diagnostics

3.2.1 Optical Transition Radiation

A consequence of laser-generated fast electrons exiting the target material is the emission of *transition radiation*. If the fast electrons are propagating in bunches this radiation adds coherently to form *coherent transition radiation*, with spectral peaks at the electron bunching frequency (ω_L or $2\omega_L$). When using a Ti:Sapphire laser ($\lambda = 800$ nm) the second harmonic will be at 400 nm, which lies in the visible optical regime. Experimentally, imaging can be implemented to capture CTR emission from the target surface at typically the first and second laser harmonics. This can be achieved with a CCD camera or a digital camera if spatial resolution is required, or a streak camera to obtain spectral and/or temporal information on the emission. Alongside CTR there will also be a contribution from incoherent TR (ITR): there is no frequency dependence on the incoherent emission spectrum so the ITR emission intensity should be uniform across all wavelengths, including the optical regime. The intensity of ITR is proportional to the fast electron number N , whereas the intensity of CTR is proportional to N^2 , so the intensity of ITR will be relatively low for large fast electron numbers. Figure 3.6 shows examples from the literature of experimental results of optical transition radiation emission using streak camera, spectrometer, and CCD measurements.

Images of optical transition radiation can be used to indirectly infer information on the fast electrons. Analysis of the images can be carried out to measure the intensity of the OTR emission: the intensity scales with electron number, so a greater emission intensity can imply a greater number of fast electrons at the target surface. Transition radiation is produced in the direct vicinity of the fast electrons at the target surface. Imaging of OTR using a CCD or digital camera allows spatial information on the OTR emission, and thus on the fast electron beam. OTR imaging has previously revealed filamentation of the fast electron beam [120] and fast electron beam divergence [121].

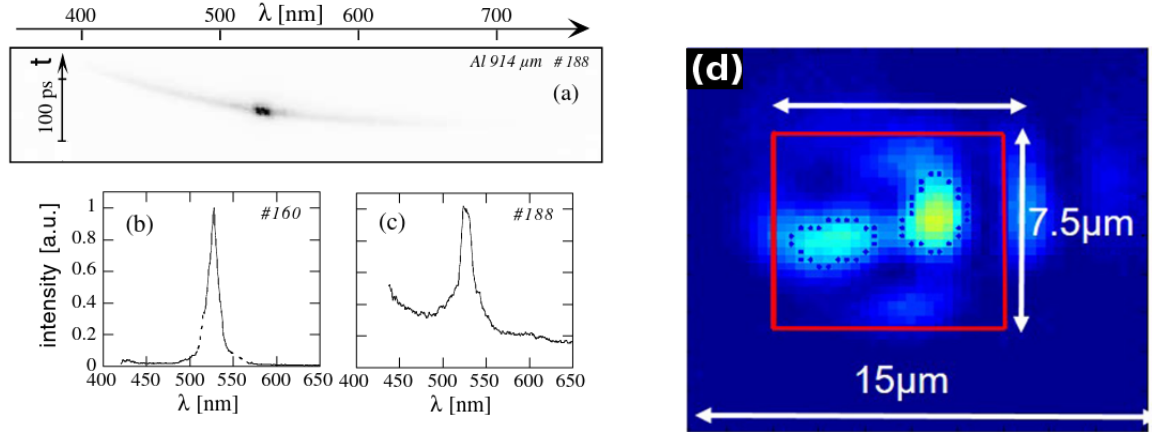


Figure 3.6: (a) Optical streak image of CTR emission from the rear side of irradiated $914 \mu\text{m}$ Al foil presented in [101]; (b) and (c) show the integrated spectra from two shots in the same experiment. (d) CCD image of $1\omega_L$ CTR emission from the rear side of an irradiated Al/CH/Al sandwich target presented in [119].

3.2.2 Spectral Measurements

Spectral measurements of emitted light from the surface of the irradiated target can allow us to uncover more information on the target behaviour. An *optical spectrometer* can be used to obtain this spectrum. The components of a spectrometer are relatively uncomplicated, consisting of a diffraction grating to split the light into its constituent wavelengths and a CCD array to collect the dispersed light. Coupling a fibre to the entrance of the spectrometer can increase the amount of light collected and allow more flexibility when positioning the spectrometer.

For the laser-solid interactions reported here, there is interest in characterising the light emitted from the front and rear surfaces of the target. From the rear surface the focus is on understanding the emission of coherent transition radiation. As laid out in Section 2.3.4 the spectrum will display peaks at harmonics related to the bunching frequency of the electrons. Identifying the wavelengths of these peaks allows the inference of the electron bunching frequency, and hence the laser absorption mechanism dominant in the interaction.

In addition, obtaining the spectrum from the front surface of the target can shed more light on the initial laser-target interaction. The amount of reflected light at the laser wavelength can be used as a coarse measurement of the laser absorption fraction [122]; this needs

to be taken with a pinch of salt however as the reduction of measured light could be due to enhanced scattering rather than increased absorption of the laser light. An additional outcome of measuring the front surface emission spectra is the ability to monitor for pre-plasma formation. The pedestal, prepulses and the leading edge of the main pulse can pre-ionise the target prior to the arrival of the main pulse, forming a lower density expanded plasma in front of the above-critical target. The main pulse interacts with a sub-critical plasma where the Two Plasmon Decay (TPD) and Stimulated Raman Scattering (SRS) parametric instabilities can occur near $n_c/4$, producing plasmons. The resultant plasmons can couple with laser photons to form light at $3/2\omega$. Detecting $3/2\omega$ light in the front surface spectra can consequently serve as an indirect indicator of pre-plasma [123, 124].

3.2.3 Time-of-Flight Detector

The act of forward propagating fast electrons exiting the target will lead to the formation of a sheath field at the rear surface, resulting in the acceleration of ions lying on the surface. The ion flux and energies are sensitive to the properties of the fast electrons (e.g. temperature and current density) as this dictates the strength of the sheath field formed. Ion measurements can hence function as a complementary diagnostic when investigating fast electrons. A *time-of-flight detector* can be used to measure the energies of these accelerated ions at a high repetition rate [125, 126]. In this approach, the velocity of an accelerated ion is inferred through measuring the time taken for the ion to traverse from the rear target surface to the detector. The detector used can vary depending on the temporal/energy resolution and sensitivity requirements, with common options including diamond [127] or silicon carbide [128] semiconductor devices, or scintillators [129].

A typical signal recorded by a time-of-flight detector is shown in Figure 3.7. A key feature to highlight is an initial, sharp peak named the *photopeak*. This is not the detection of ions, but instead the detection of X-rays and fast electrons emitted during the laser interaction. The photopeak is used as a reference signal to identify a ‘zero-time’, t_{ph} . Ions are then detected at a given time t_{ion} . The distance between the target and the detector, d_{TOF} , is easily known from the experimental setup. From this information it is possible to infer the

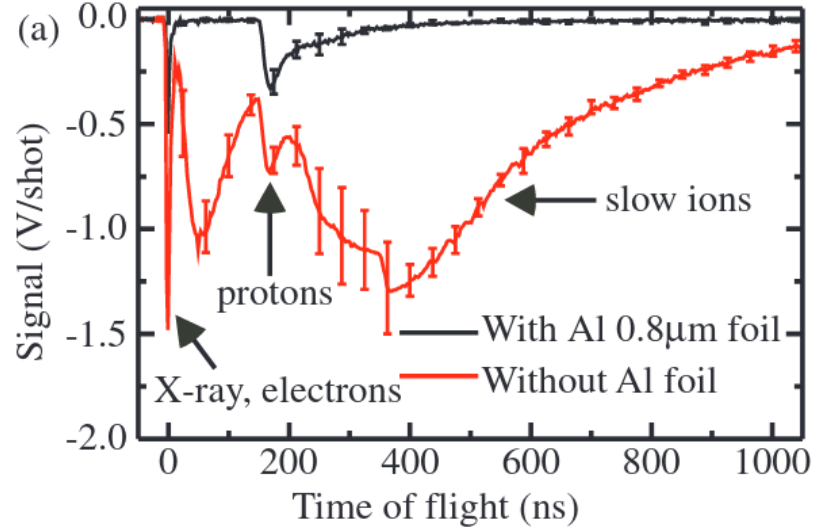


Figure 3.7: Experimental time-of-flight signals of accelerated ions. The *photopeak* attributed to X-ray emission and fast electrons is seen at $t = 0$. Taken from [129].

time-of-flight of each ion as

$$t_{TOF} = t_{ion} - \left(t_{ph} - \frac{d_{TOF}}{c} \right). \quad (3.4)$$

Assuming the particle is travelling at an approximately constant velocity to the detector, the average velocity of the ion is found by $v_{TOF} = d_{TOF}/t_{TOF}$. Finally, the kinetic energy of the ion can be calculated as $KE_{ion} = (\gamma - 1)m_i c^2$. In this way an energy spectra of the accelerated ion species can be constructed from the time-of-flight data.

3.2.4 Fast Electron Emittance Measurements

The *emittance* of a particle beam is defined as the area of position-momentum space occupied by the particles. Emittance is a figure of merit more commonly encountered in the accelerator community [130,131] where a beam with a small emittance is seen as favourable, but can also be considered when characterising fast electron beams generated in laser-solid interactions.

A measure of the emittance of an electron beam can be realised through the use of a *pepper-pot* diagnostic. A pepper-pot mask made of a plate with a grid of holes is placed directly in the path of the electron beam. The electrons that pass through the pepper-

pot will form a *beamlet* from each hole. These electron beamlets can be captured using a detector behind the pepper-pot mask. The positioning and divergence of each beamlet can be related to the transverse momenta of the electrons passing through the corresponding hole. Coupling this with the known positions of the holes and beamlets, we can obtain a value for the transverse emittance of the beam using measurements of the beamlets from a lineout across x [132]:

$$\epsilon_x^2 \approx \frac{1}{N^2} \left\{ \left[\sum_{j=1}^p n_j (x_{hj} - \bar{x})^2 \right] \left[\sum_{j=1}^p \left[n_j \sigma_{x'_j}^2 + n_j (\bar{x}'_j - \bar{x}')^2 \right] \right] - \left[\left(\sum_{j=1}^p n_j x_{hj} \bar{x}'_j \right) - N \bar{x} \bar{x}' \right]^2 \right\} \quad (3.5)$$

with the parameters defined as:

- p = number of holes,
- x_{hj} = position of the hole,
- n_j = number of electrons within the beamlet,
- N = total number of electrons, $\sum_{j=1}^p n_j$
- \bar{x} = mean position of all beamlets,
- \bar{x}'_j = mean divergence of j-th beamlet,
- \bar{x}' = mean divergence of all beamlets,
- $\sigma_{x'_j}$ = mean r.m.s spot size of j-th beamlet at the j-th hole.

Most of these values can be retrieved directly from the beamlet images, i.e. beamlet position, intensity and r.m.s spot size. The mean divergence here refers to the average ‘shift’ of the beamlet and is not the beamlet spot size. To obtain the mean divergence, consider the setup outlined in Figure 3.8 which generates several beamlets, each originating from a different subset of the full electron beam. The transverse momenta, p_x , of each electron results in a shift of the position in x whilst propagating from the pepper-pot hole to the detector. Under the assumption that the divergence angle is small ($\tan(\theta) \approx \theta$), the mean divergence of the beamlet due to the transverse momenta of the electrons can be calculated through

$$\bar{x}'_j = \frac{\bar{X}_j - x_{hj}}{L} \quad (3.6)$$

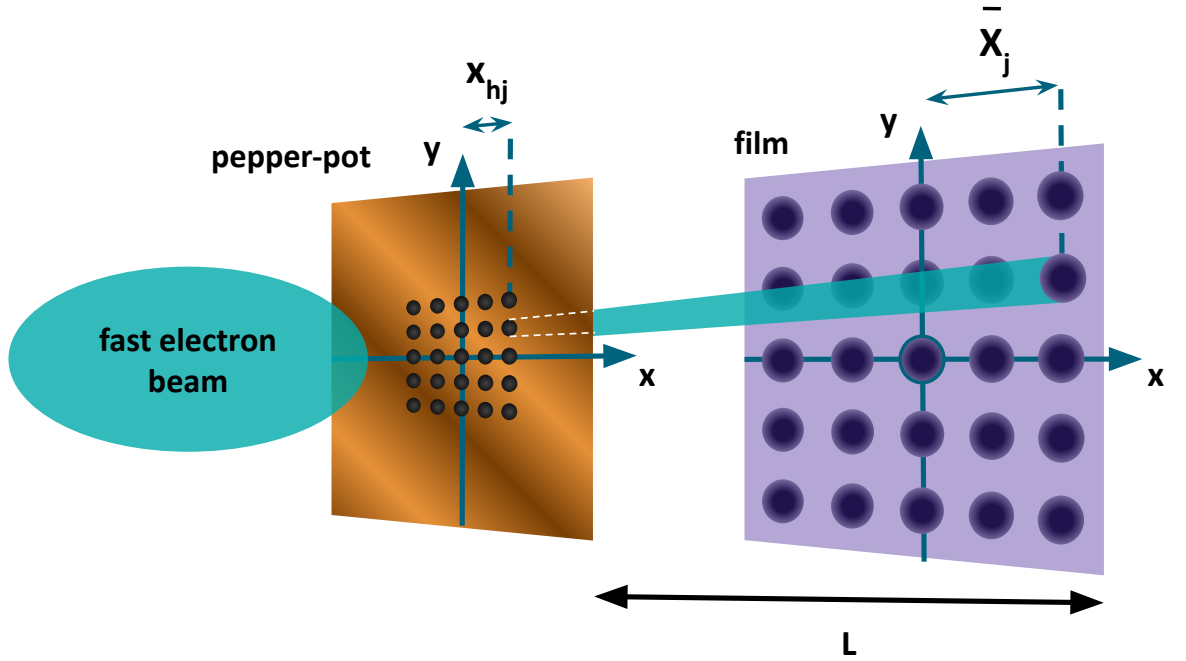


Figure 3.8: Illustration of pepper-pot mask and detector to demonstrate calculation of electron beam divergence from the image of the beamlet.

where \bar{X}_j is the mean position of the beamlet and L is the distance between the pepper-pot mask and detector. The divergence is given in units of radians.

3.3 EPOCH Code

The *particle-in-cell* (PIC) code EPOCH [133] has been used in this thesis to model the laser-target interactions and track the initial behaviour of the fast electron population. A particle-in-cell code fundamentally works by dividing the simulation domain into a grid and populating each grid cell with a number of *pseudoparticles*, each representing a larger number of real target species such that the plasma is literally reproduced via particles in cells. Using a kinetic treatment rather than a fluid treatment allows for deviations away from purely Maxwellian populations, allowing PIC codes to capture electron acceleration to energies at the tail of a Maxwellian distribution in the laser-plasma interaction.

EPOCH utilises two coupled solvers to resolve the laser-plasma interaction: a *field solver* that uses Maxwell's equations to solve for the local EM fields, and a *particle pusher* that

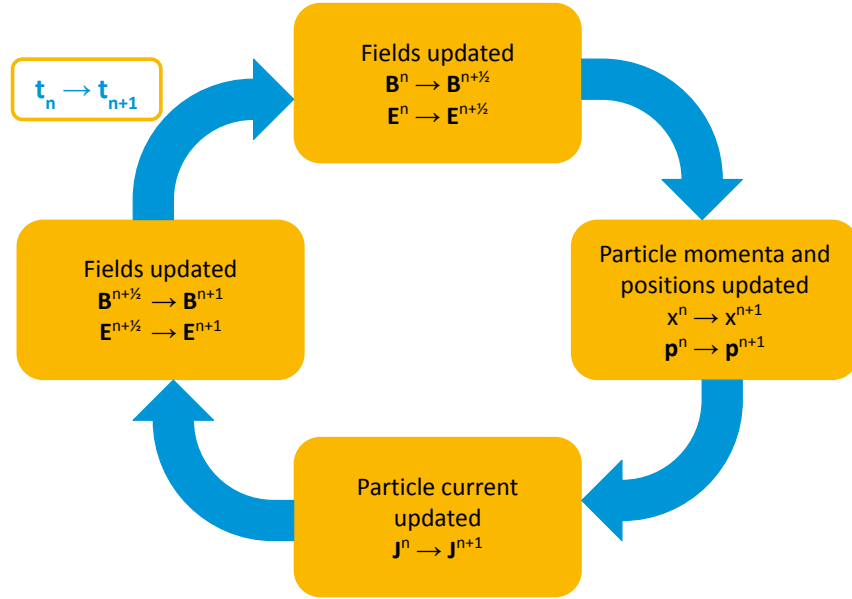


Figure 3.9: Cyclical solution of the field and particle pusher solvers implemented at each timestep in EPOCH.

solves for the new particle position and updates the currents. These solvers are implemented at each timestep to progress from t_n to t_{n+1} as follows, where n is the timestep number. The EM fields are advanced one half timestep using a discretised form of Maxwell's equations (meaning the derivatives can be approximated as a finite step e.g. $\partial x/\partial t \rightarrow \Delta x/\Delta t$):

$$\mathbf{E}^{n+1/2} = \mathbf{E}^n + \frac{\Delta t}{2} \left(c^2 \nabla \times \mathbf{B}^n - \frac{\mathbf{J}^n}{\epsilon_0} \right) \quad (3.7)$$

$$\mathbf{B}^{n+1/2} = \mathbf{B}^n - \frac{\Delta t}{2} \left(\nabla \times \mathbf{E}^{n+1/2} \right) \quad (3.8)$$

to give the EM fields at the grid points. The particle pusher then works to solve for the new momenta for each particle under the Lorentz force:

$$\mathbf{p}_\alpha^{n+1} = \mathbf{p}_\alpha^n + q_\alpha \Delta t \left[\mathbf{E}^{n+1/2} \left(x_\alpha^{n+1/2} \right) + \mathbf{u}_\alpha^{n+1/2} \times \mathbf{B}^{n+1/2} \left(x_\alpha^{n+1/2} \right) \right]. \quad (3.9)$$

Note the solution to Equation 3.9 requires knowledge of the \mathbf{E} and \mathbf{B} fields at the particle position rather than at the grid points; this is obtained through interpolation of field contributions from neighbouring cells.

Particle position is updated to x_α^{n+1} using the velocity \mathbf{u}_α^{n+1} calculated from the momenta

\mathbf{p}_α^{n+1} . Updating of the current from $\mathbf{J}^n \rightarrow \mathbf{J}^{n+1}$ is carried out using the Esirkepov current density decomposition scheme [134]. The EM fields can then be updated to complete the timestep:

$$\mathbf{B}^{n+1} = \mathbf{B}^{n+\frac{1}{2}} - \frac{\Delta t}{2} (\nabla \times \mathbf{E}^{n+\frac{1}{2}}) \quad (3.10)$$

$$\mathbf{E}^{n+1} = \mathbf{E}^{n+\frac{1}{2}} + \frac{\Delta t}{2} \left(c^2 \nabla \times \mathbf{B}^{n+\frac{1}{2}} - \frac{\mathbf{J}^{n+1}}{\epsilon_0} \right). \quad (3.11)$$

This cyclical iteration of solvers is summarised in Figure 3.9 and is repeated every timestep until the simulation time ends. Timestep size Δt can be chosen by the user with the stipulation that it must satisfy the Courant-Friedrichs-Lewy, or CFL, condition [135]:

$$\Delta t \leq \frac{\Delta x}{c} \quad (3.12)$$

where Δx is the mesh size and c is the speed of light. This ensures information from a cell (particle or wave) can only travel to its nearest neighbour cell between timesteps.

3.3.1 Grid Resolution

The choice of grid resolution is important with respect to resolving both physics and numerical effects. Grid size must be chosen carefully to limit the phenomena of *numerical heating*. If the cell size is too coarse compared to the Debye length, λ_D , we encounter the growth of instabilities from numerical modes (aliases) destabilizing plasma oscillations, leading to an artificial gradual heating of the plasma [136]. Choosing a grid size that is comparable to λ_D can diminish the instability growth to negligible levels [137]. An additional mitigation is to model the pseudoparticles as being spread over a finite volume as opposed to a point particle, with the distribution described by a *particle shape function*. This has the equivalent effect of averaging the fields over a few nearby cells. In practice EPOCH will interpolate from the shape function to get the current at each grid position, and inversely interpolate from the grid points to the shape function to get the EM fields at the particle centre. Higher order shape functions have been found to be useful in reducing the effect of numerical heating, with a fifth-order “b-spline” shape function strongly recommended for laser-solid interactions [133].

For the work presented in this thesis the intention is to model the interaction of intense lasers with cold, solid targets, with a view of studying the fast electrons and subsequent transition radiation generated. To limit numerical heating there must be sufficient resolution of the Debye length of the plasma, which for a $\lambda = 800$ nm laser can be reduced to

$$\lambda_D = \sqrt{\frac{\epsilon_0 k_B T}{n_e e^2}} \quad (3.13)$$

$$= \sqrt{\frac{(8.85 \times 10^{-12})(1.38 \times 10^{-23})(11.6 \times 10^{-3})}{(1.72 \times 10^{27})(1.6 \times 10^{-19})^2}} \sqrt{\frac{T_{eV}}{A}} \quad (3.14)$$

$$\lambda_D = 0.179 \times \sqrt{\frac{T_{eV}}{A}} \text{ nm} \quad (3.15)$$

for a target at temperature T_{eV} and electron density $An_{crit} \text{ m}^{-3}$. The skin depth additionally needs to be resolved, both for accurately representing the laser absorption and for modelling transition radiation emission (the formation zone size is comparable to the skin depth). The skin depth can be given in a similar representation as

$$L_s = \frac{c}{\omega_p} = c \sqrt{\frac{\epsilon_0 m_e}{e^2 n_e}} \quad (3.16)$$

$$= \sqrt{\frac{(3 \times 10^8)^2 (8.85 \times 10^{-12}) (9.11 \times 10^{-31})}{(1.6 \times 10^{-19})^2 (1.72 \times 10^{27})}} \sqrt{\frac{1}{A}} \quad (3.17)$$

$$L_s = 128 \times \sqrt{\frac{1}{A}} \text{ nm}. \quad (3.18)$$

An example target of solid Ti ($\rho = 4.506 \text{ g/cm}^{-3}$) with an average ionisation $Z_{bar} = 10$ yields an electron density of $5.67 \times 10^{29} \text{ m}^{-3}$, or $300 n_{crit}$. Assuming a cold, unheated target at $T = 1 \text{ eV}$, this gives length scales of $\lambda_D = 0.01 \text{ nm}$ and $L_s = 7.39 \text{ nm}$. A cell size $\Delta x, y < 10 \lambda_D$ is required to mitigate numerical heating, placing an upper limit of $\Delta x, y \lesssim 0.1 \text{ nm}$. The domain is required to be large enough in x to encapsulate the front vacuum, target thickness and rear vacuum, and also large enough in y to capture any outgoing EM emission. A domain size of 10's μm in x and y is necessary to fulfill these requirements. Whilst the aforementioned grid resolution is possible in EPOCH, it would not be feasible for the scale of simulation intended here as the runtime would be entirely impractical. To relax the restrictions on cell size, the targets are instead modelled with a reduced electron density and an increased initial temperature, realising an increased Debye length and skin depth that can be more easily resolved. With respect to modelling transition radiation, a PIC simulation

$\Delta_{x,y}$ (nm)	Ti ppc	e^- ppc
1	1	10
2	4	40
5	25	250
10	100	100
15	225	2250
25	625	6250

Table 3.1: Cell size and corresponding pseudoparticles per cell (ppc) used

study by Ding *et al.* [138] saw no observable difference in the generation of THz emission from coherent transition radiation when using a target density of $10 n_{crit}$ or $110 n_{crit}$, so the reduced target density should not impact the formation of transition radiation.

Testing is carried out to establish these changes are appropriate to resolve the Deybe length with a more coarse grid resolution. A small domain of size $1 \times 1 \mu\text{m}$ is created and populated with pseudoparticles representing the proposed target material with $n_e = 20 n_{crit}$, $n_i = n_e/10$ and $T = 1 \text{ keV}$. Boundaries are set to reflective in x and y to prevent particle loss through the domain boundaries. No laser was used for these simulations. Simulations are established with varied cell size ranging from 1 - 25 nm, with the number of pseudoparticles per cell scaled to keep the total pseudoparticle number constant; Table 3.1 details the grid size and pseudoparticles per cell for each case. Each simulation is run up to 150 fs and the total kinetic energy of the particles output as a function of time. Figure 3.10 shows that as grid size becomes smaller the heating rate (given by the gradient) reduces as expected. Above a grid resolution of 10 nm we see the numerical heating rate begins to increase slightly; when modelling solid targets we therefore aim to use a grid resolution finer than 10 nm.

3.3.2 Pseudoparticle Number

For a laser-plasma interaction to be sufficiently resolved there needs to be an adequate number of pseudoparticles to correctly reproduce the collective plasma behaviour. The number of real particles represented by a pseudoparticle is referred to as the *weighting* of the pseudoparticle. When modelling solid density targets we can expect a high pseudoparticle number will

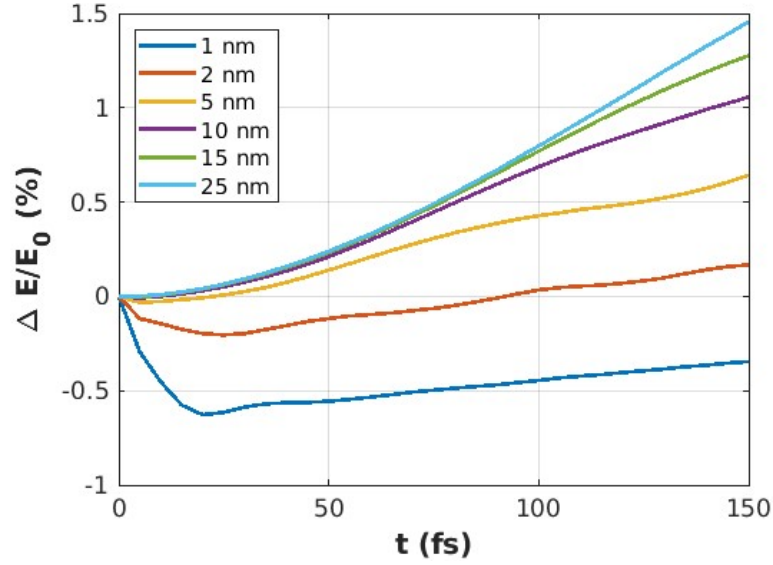


Figure 3.10: Change in total particle kinetic energy as a function of time for varying cell size. The initial decrease in particle energy for the smallest grid sizes is attributed to energy lost to EM field fluctuations [139].

be needed for an appropriate weighting. Moreover, laser acceleration will only involve a small number of the target electrons, so a large number of pseudoparticles is required to allow representation of the fast electron population whilst minimising statistical noise. On the other hand, using more pseudoparticles increases the memory and runtime of the code with each particle adding approximately 10 B to the total memory. The user is therefore presented with a balancing act: use enough pseudoparticles to accurately represent the physics, but not so many that the code takes an exorbitant amount of time and resources to run.

Convergence testing is carried out to identify a suitable number of electron pseudoparticles to implement in the simulations presented in the Results chapters. A simulation domain of size $10 \times 20 \mu\text{m}$ with a grid resolution of $\Delta x, y = 4 \text{ nm}$ is established. A $5 \mu\text{m}$ thick Ti target is set up with an average ionisation of 10, and an electron density $n_e = 20 n_{crit}$. The electron pseudoparticle number per cell is varied from 10 to 640, with the corresponding Ti pseudoparticle number per cell a factor 10 lower (1 - 64). Figure 3.11(a) shows the change in total particle kinetic energy as a function of time. As the laser energy is coupled into the target the kinetic energy of the electrons increases, with a slight decrease observed after 80 fs as a fraction of the fast electrons exit the simulation domain. The total energy then begins to plateau after 90 fs, coinciding with the time the laser fields are turned off. The simulations

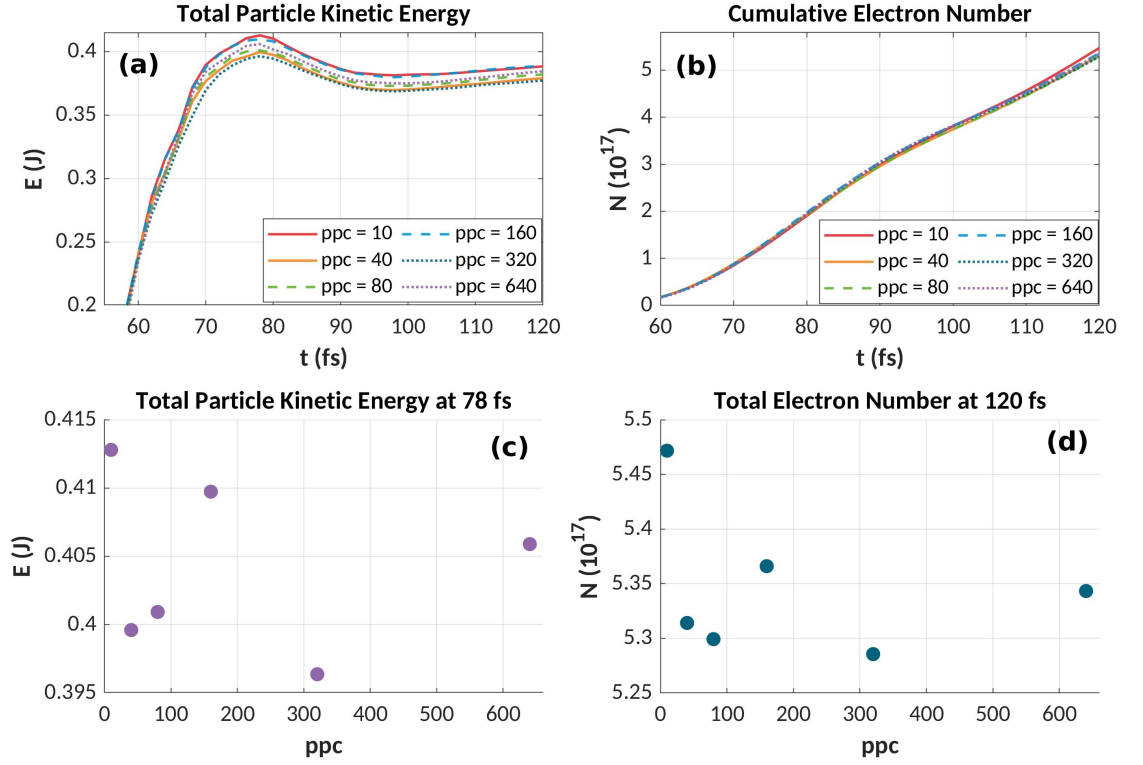


Figure 3.11: Results of convergence testing for the electron pseudoparticle number per cell (ppc). (a) Total particle kinetic energy and (b) cumulative electron number counted passing through a probe plane at the rear target surface as a function of simulation time. (c) shows the variation of total particle kinetic at 78 fs with ppc, and (d) shows the variation of the total number of fast electrons counted at the probe plane.

with different numbers of pseudoparticles per cell (ppc) demonstrate very similar profiles. As a figure of merit the peak total particle kinetic energy at $t = 78$ fs is taken from each simulation and plotted in Figure 3.11(c). The total energy is 0.404 ± 0.006 J, corresponding to a fluctuation of ± 1.6 % across ppc values of 10 - 640.

Since the studies addressed in this thesis are concerned with physics induced at the rear target surface by propagating fast electrons, another figure of merit to judge the convergence of pseudoparticle number is the number of fast electrons reaching the rear surface. To extract this information a probe plane is placed at $x = 4.5 \mu\text{m}$ which measures pseudoparticles representing fast electrons with energy > 100 keV propagating through the probe plane. Figure 3.11(b) shows the cumulative electron number as a function of time for simulations with varying numbers of electron pseudoparticles per cell. As was the case for the total particle kinetic energy, there is little effect with changing the electron pseudoparticle num-

ber. Figure 3.11(d) shows the final electron number counted at the probe as a function of electron ppc. The result for electron ppc = 10 shows an increased count compared to the simulations with a higher ppc, an indication that the weighting is too great and a higher number is required for convergence. The average electron number is $(5.32 \pm 0.03) \times 10^{17}$ electrons, corresponding to a fluctuation of $\pm 0.6\%$. These results indicate the simulations rapidly reach convergence with electron pseudoparticle number, with very little change in the final properties of the fast electrons achieved with increasing the electron pseudoparticle number beyond 40 ppc.

3.4 FLASH Code

The Eulerian hydrodynamic code FLASH [140] is employed to model the effect of the laser interaction on the target structures over ns timescales. Several example problems are included with FLASH to demonstrate the various capabilities of the code. The example *LaserSlab* problem was used as a basis for this work which models a laser irradiating an Al disc.¹ This simulation was then adapted to model our specific problem, with the details outlined in Section 4.4.1.

3.4.1 Fluid Equations

The evolution of a plasma can be described macroscopically as a fluid governed by the values of velocity (\mathbf{u}), density (ρ) and pressure (P) using the following forms of the Euler equations:

$$\frac{\partial \rho}{\partial t} + \nabla \cdot \rho \mathbf{u} = 0 \quad (3.19)$$

$$\rho \left(\frac{\partial \mathbf{u}}{\partial t} + \mathbf{u} \cdot \nabla \mathbf{u} \right) = -\nabla P \quad (3.20)$$

$$\frac{\partial}{\partial t} (\rho E) + \nabla \cdot [(\rho E + P) \mathbf{u}] = Q_{las} - \nabla \cdot \mathbf{q} \quad (3.21)$$

where E is the total specific energy, Q_{las} is the energy added by laser heating per unit volume, and \mathbf{q} is the total heat flux. These equations describe the conservation of mass, conservation of momentum, and conservation of energy respectively. In laser-driven plasmas the ions, electrons and photons are not in thermal equilibrium with each other. Equation 3.21

¹Further details on the *LaserSlab* problem can be found in Section 34.7.5 of the FLASH user manual (Version 4.6.2).

can therefore be written for the ions, electrons and photons separately, with each population described by an individual temperature. This is known as a *single fluid, three temperature (3T)* treatment.

Euler’s equations are closed by the *equation of state (EOS)* which connects the internal energy, temperature and pressure of a given species. Here we used a tabulated EOS generated by PrOpacEOS [141]. The user sets the range of density and temperature values to solve over, and PrOpacEOS calculates the specific internal energy and pressure for each electron density/temperature pair requested.

In addition, PrOpacEOS calculates terms required to determine the overall opacity of each material. A *Planck mean opacity* is applicable when the plasma is optically “thin”, i.e. where the radiation mean free path is greater than the scale length of the system, is taken here for the absorption and emission terms. For an optically “thick” plasma, where the radiation mean free path is smaller than the scale length of the system, a *Rosseland mean opacity* is more justifiable [142] and is used here for the transport term.

In situations where there is a broad range of photon energies, taking a value for the opacity at each wavelength is not most practical approach. In this case it is more convenient to consider the opacity terms for different groups of photon energies, referred to as a *multigroup diffusion approximation*. Values for these opacity terms are therefore calculated for each density/temperature pair supplied by the user, and also for distinct energy groups where the opacity term is averaged over the frequency range encompassed by each group.

3.4.2 Grid Structure

In solving hydrodynamic simulations the target material is initially discretized into smaller fluid elements using a user-defined grid or mesh. The continuity equation, Equation 3.19, outlines the condition that the change in mass within a given fluid element must equal the flow of mass into or out of the element. In the *Lagrangian* scheme the continuity equation is instead written as

$$\frac{\partial \rho}{\partial t} + \rho \nabla \cdot \mathbf{u} = 0 \quad (3.22)$$

with the consequence of allowing no mass diffusion out of a fluid element. Each mesh

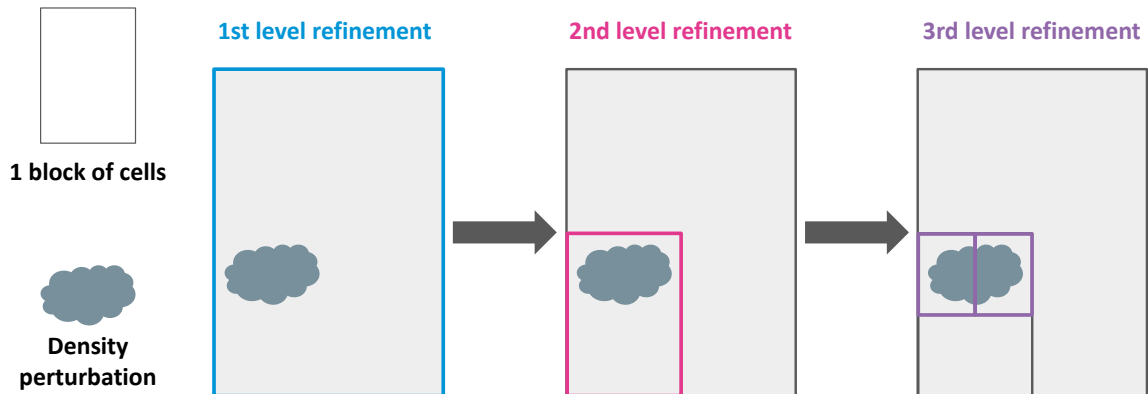


Figure 3.12: Diagram of AMR functionality. The simulation initially starts with 1 block across a target with a localised region of high density. An additional block is added into the block cell containing the high density feature. Another level of refinement is then added with additional blocks inserted to gain higher resolution across the density perturbation.

element follows the evolution of the material contained inside it, with the mesh free to move such that the mass contained inside remains constant. Over long timescales Lagrangian meshes are prone to “bow-tie” in 2D configurations when moving over large spatial scales or trying to track swirling regions of fluid, often leading to the code “crashing” [143]. At this time it can be possible for the mesh to be re-zoned and the code restarted, but this can be a laborious process and not guaranteed for all codes.

In the *Eulerian* scheme the grid is fixed with the mass able to flow through the grid, and so the bow-tie problem is avoided. Use of an Eulerian grid however has the disadvantage of potentially overestimating the diffusion of a material if there is insufficient grid resolution since the mass is spread evenly over a fluid element. Additional resolution is accomplished in FLASH using PARAMESH [144], a block-structured *adaptive mesh refinement* (AMR) scheme. Rather than having fine resolution across the whole domain, PARAMESH works to instead add additional grid cells into an existing fluid element depending on the modified local second-order derivative of the chosen refinement criteria (density, temperature etc.) [145]. Figure 3.12 shows how additional blocks are added by PARAMESH where there is a feature to be resolved. In this way, additional grid cells are reserved only for regions that require finer resolution, saving computational cost.

3.4.3 Laser Absorption

Incident laser beams are modeled using *2D-in-3D ray tracing*. The laser is represented as a set of rays originating from a lens outside the domain, that are then traced through the domain towards a defined target region (typically the laser focal spot) at every timestep. To calculate the power loss from each ray into the target FLASH assumes an inverse bremsstrahlung model:

$$\frac{dP}{dt} = \frac{4}{3} \left(\frac{2\pi}{m_e} \right)^{1/2} \frac{Ze^4 \ln\Lambda[\mathbf{r}_0]}{n_{crit} k_B^{3/2}} \frac{n_e(\mathbf{r}_0)^2}{T_e(\mathbf{r}_0)^{3/2}} \frac{(1 + Ut + Rt^2)^2}{(1 + Wt + St^2)^{3/2}} P \quad (3.23)$$

where Z is the average ionisation, $\ln\Lambda$ is the Coulomb logarithm, n_{crit} is the critical density, k_B is Boltzmann's constant, n_e is the local electron density, T_e is the local electron temperature, P is the power of the ray, and \mathbf{r}_0 is the initial position of the ray. The terms U, R, W , and S collectively describe the evolution of the ray in time and are defined as:

$$U = \frac{\nabla n_e(\mathbf{r}_0) \cdot \mathbf{v}_0}{n_e(\mathbf{r}_0)} \quad R = -\frac{c^2 \nabla n_e(\mathbf{r}_0) \cdot \nabla n_e(\mathbf{r}_0)}{4n_e n_e(\mathbf{r}_0)} \quad (3.24)$$

$$W = \frac{\nabla T_e(\mathbf{r}_0) \cdot \mathbf{v}_0}{T_e(\mathbf{r}_0)} \quad S = -\frac{c^2 \nabla T_e(\mathbf{r}_0) \cdot \nabla T_e(\mathbf{r}_0)}{4n_e T_e(\mathbf{r}_0)} \quad (3.25)$$

where \mathbf{v}_0 is the initial ray velocity. At each timestep each ray is moved through the domain, with the ray position and velocity updated at each cell and used to calculate the power loss. This iterates through until every ray has either been absorbed by the target material or has exited the domain. For a set target we can see from Equations 3.24 and 3.25 that the power loss at each cell is dictated by the electron temperature and density values and their respective local gradients, and scales with the power possessed by the ray.

When carrying out initial simulations it was found that this inverse bremsstrahlung model was unsuitable for our laser regime ($I \approx 10^{17}$ W/cm², $\tau = 35$ fs) with the energy deposited into the target found to be virtually zero. To compensate for this a benchmarking simulation using the 1D Lagrangian radiation hydrodynamics code HYADES [146] was carried out at early times (< 100 ps) to determine a more realistic energy deposition value. HYADES models absorption of a laser incident on an over-critical target via the Fresnel reflection model; this model is justified since there is little plasma expansion and a negligible change in plasma density over the laser pulse time [147]. The target density and laser power profiles were then modified in FLASH to reach the desired energy absorption. A detailed explanation on this

process is provided in Section 4.4.1.

Testing is carried out to identify the maximum level of grid refinement required to resolve the laser absorption in the laser-target interaction considered in this work. The laser profile is modelled with a FWHM pulse length of 35 fs, a peak power of 1×10^{15} W, and a HWHM spot size of $2 \mu\text{m}$. The target considered is Ti at solid density, $\rho = 4.5 \text{ g cm}^{-3}$, with an exponential density profile of scale length 15 nm on the front surface. The full details and motivation for establishing the simulation in this way are addressed in Section 4.4. The simulation domain is in a cylindrical geometry and of size $25 \times 125 \mu\text{m}$. The domain is represented by 1 block in r and 5 blocks in h , with each block consisting of 10×10 cells. For the testing the maximum level of refinement was varied. The methodology used by PARAMESH means the spatial extent of each “child” block must be half the spatial extent of the “parent” block where additional refinement is required. So, each level of refinement results in a factor 2 finer grid resolution in the region where the next “child” block is placed.

The results of the total energy deposited in a set of simulations increasing levels of refinement are shown in Table 3.2. It can be seen that a maximum refinement level, $lrefmax$, of 2-5 yields an energy deposition significantly lower than that achieved with $lrefmax = 6$. The exponential density layer has an initial thickness of approximately 200 nm, and the minimum grid size achieved with $lrefmax = 6$ is 78 nm. Whilst the layer is not particularly well resolved, the grid size is sufficiently small to resolve the local density gradient and substantially increase the energy absorption (following Equation 3.24) by over a factor 10 compared to $lrefmax = 5$. A simulation was carried out with $lrefmax = 7$ to further improve the resolution, but the simulation failed to run after several attempts due to segmentation faults that were unable to be fixed. For the simulations the maximum refinement level was therefore set to 6, corresponding to a minimum grid size of 78 nm.

The FLASH simulations are also run over longer times, up to 10.4 ns, to model the shock wave launched by this target heating. Good spatial resolution is also required to accurately reproduce the propagation of the shock through the target. However, the minimum grid size is severely restricted by the requirements for the laser absorption, and it is not possible to carry out specific testing for the shock resolution that is decoupled from the laser absorption

lrefmax	Minimum $\Delta x, y$ (nm)	E_{depo} ($10^{-7} J$)
2	1250	26.9
3	625	26.9
4	312.5	211.8
5	156.25	184.9
6	78.13	2268.8
7	39.06	-

Table 3.2: Total laser energy deposited into the target, E_{depo} , as the maximum refinement level $lrefmax$ is increased. The finest grid resolution $\Delta x, y$ possible at the highest refinement level is given for each simulation.

since the refinement level is fixed for the entire simulation. For these simulations the grid resolution is therefore dictated by the requirements to resolve the laser-target interaction.

3.4.4 Limitations

As with all codes, FLASH cannot model all of the physics involved in a laser-plasma interaction across different regimes. For example, the only laser-plasma absorption process modelled in FLASH is inverse bremsstrahlung. Laser energy can also be coupled into hot electrons through resonance absorption and/or vacuum heating, an absorption process that is present in the range $I\lambda^2 = 10^{15-18}$ W/cm² and is not currently modelled by FLASH. In the regime $I\lambda^2 > 10^{18}$ W/cm² there can be the generation of fast electrons via ponderomotive acceleration, with the fast electron population described by a temperature greater than the bulk. Hydrodynamic codes cannot account for these electrons as they assume local thermodynamic equilibrium of a fluid in a cell. The code also does not capture effects due to the fast electron transport through the target e.g. Ohmic heating.

An interaction of a laser with a target can result in the excitation of parametric instabilities such as stimulated Raman scattering (SRS), stimulated Brillouin scattering (SBS), and two plasmon decay (TPD). The SRS and SBS instabilities scatter laser light, reducing the coupling efficiency into the target. The TPD instability generates electron plasma waves, which dependent on the plasma conditions can either result in the generation of suprathermal electrons or contribute to local heating of the plasma [148]. These parametric instabilities

are not modelled by FLASH, and can lead to an inaccurate estimate of the laser coupling into the target.

There exists formulae that define the threshold intensity for appreciable growth of the laser plasma instabilities. These are summarised by Montgomery [149] as

$$I_{\text{threshold,SRS}} > \frac{4 \times 10^{17}}{L_{\mu\text{m}} \lambda_{\mu\text{m}}} \text{ W/cm}^2 \quad (3.26)$$

$$I_{\text{threshold,SBS}} > \frac{7 \times 10^{15} T_{\text{keV}}}{L_{\mu\text{m}} \lambda_{\mu\text{m}}} \cdot \frac{n_{\text{crit}}}{n_e} \text{ W/cm}^2 \quad (3.27)$$

$$I_{\text{threshold,TPD}} > \frac{5 \times 10^{15} T_{\text{keV}}}{L_{\mu\text{m}} \lambda_{\mu\text{m}}} \text{ W/cm}^2 \quad (3.28)$$

These formulae demonstrate that the onset of these instabilities occurs more readily for plasmas with a longer scale length and a higher temperature. For the work here the pre-pulse laser profile has a laser intensity of $1 \times 10^{17} \text{ W/cm}^2$ and a laser pulse length is 35 fs. Whilst the pulse length is too short for an appreciably long density scale length plasma to form during the laser pulse, the intensity threshold for TPD in particular is low enough that appreciable TPD can be induced in these interactions. For example, the work by Veisz *et al.* [150] studied the onset of TPD for femtosecond interactions for steep density scale lengths in the range $L/\lambda = 1 - 7$. The measured TPD signal was found to increase rapidly beyond a scale length of $L/\lambda = 1.5$, or $L = 1.2 \mu\text{m}$. In addition, in an experimental study by Cristoforetti *et al.* [54] an intensity threshold of $I\lambda^2 = 3.5 \times 10^{17} \text{ W}\mu\text{m}^2\text{cm}^{-2}$ was revealed for 40 fs pulse irradiation of planar targets. This was for the case where the pre-plasma was generated by the ASE pedestal only. Thus, if the ASE pedestal or earlier pre-pulses are intense enough to preform even a short scale length pre-plasma prior to the arrival of the “main” pre-pulse, there is potential for the non-negligible production of TPD in this intensity regime that is not accounted for here in the hydrodynamic modelling.

With respect to the importance of the SBS and SRS instabilities, the intensity threshold formulae can be referred to once more. The intensity threshold for SBS in Eqn. 3.27 shows a dependence on the electron density. For the pre-pulse interaction the target may have a shorter scale length pre-plasma preformed in advance, but the bulk plasma will be above critical density and so the intensity threshold is raised. In addition, the respective formula for SRS in Eqn. 3.26 shows the intensity threshold is 2 orders of magnitude greater than for

TPD or SBS. Thus, the main instability of concern in this regime is TPD.

Chapter 4

Optical Transition Radiation from Preheated Planar Targets

The use of nanowire targets in intense-laser interactions is relatively novel and work is ongoing in the high power laser community to characterise the performance of nanowire targets in different regimes (wire dimensions, laser properties etc.). An experiment was carried out in 2019 at the ILIL facility, Pisa, using nanowire coated targets in an ultra-intense regime ($I \approx 10^{20}$ W/cm², $\tau = 27$ fs). The aim was to assess the performance of the nanowire targets through the forward accelerated fast electrons. In particular, imaging of optical transition radiation emission from the rear target surface is used as the chief diagnostic. In this regime the main OTR component will be coherent transition radiation, induced by bunches of fast electrons: the intensity of CTR scales quadratically with electron number, N^2 , and so measuring the optical emission can serve as an indirect indicator of the number (or temperature) of the fast electrons produced in the interaction (e.g. Ref. [151]).

To benchmark the performance of the nanowire targets, a number of shots were taken on planar Ti foil targets in the same experiment. The emission of coherent optical transition radiation was measured from shots on the planar targets of varying thicknesses, to serve as a reference dataset from which to benchmark the performance of the nanostructured targets. By taking these measurements the effect of the presence of the nanowires at the front surface of the target on the fast electron production can be evaluated.

In 2020 a particularly energetic pre-pulse of intensity $I \approx 10^{17}$ W/cm² was discovered during work on another experiment at the facility, which was also present for our campaign. Fully understanding the experimental results requires an appreciation of the effect of this exceptional pre-pulse on the target structures, particularly for the nanowire targets where pre-plasma formation has been identified as an acute concern. Considering the impact of the pre-pulse was not a trivial exercise; hydrodynamic modelling showed extensive deformation of the targets at both the front and rear surface, which has an effect on both the main laser interaction with the target and on the coherent transition radiation production at the rear surface.

This Chapter will present results of the experimental measurements from the planar targets only. Within this Chapter the effect of the pre-pulse on the foil targets is considered through the use of hydrodynamic modelling, and particle-in-cell modelling is used to understand the effect of the target deformation on the production of coherent transition radiation. Through the experimental data and the interpretative simulation studies, the fundamental production of coherent transition radiation in the case of pre-heated targets is explored. In Chapter 5 the results from the nanowire targets are presented and explained following the findings from this Chapter. In this way the data from the experiment is presented first by explaining the results from the planar targets, which is not straightforward in light of the pre-pulse, then explaining the results from the nanowire targets where the presence of the front surface structures adds another parameter towards the interpretation of the data.

4.1 Experimental Layout

The TW beamline at ILIL was utilised at a 15° angle of incidence, with focusing achieved with an $f/ \sim 4.5$ (effective focal length 450 mm) silver-coated OAP mirror. Energy in each pulse was 5.40 ± 0.04 J with 60% of the energy on target, of which 60% was contained within the focal spot. Pulse duration was 27 fs and focal spot waist size was measured as 4.0×4.1 μm , leading to an on-target intensity within the focal spot of 5.7×10^{20} W/cm².

After the experiment a misalignment of the Pockels cell at the exit of the regenerative amplifier was identified. This misalignment permitted the partial leakage of pulses out of the

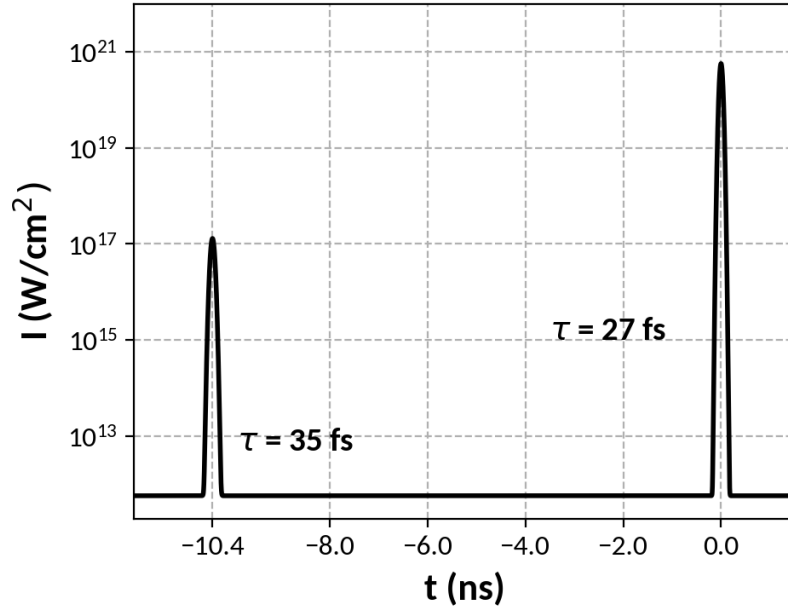


Figure 4.1: Illustration of the laser profile implemented for the campaign to clarify the relative properties of the pre-pulse and the main pulse. The main pulse is defined to occur at a time of 0 ns, with the pre-pulse irradiating the targets -10.4 ns relative to the main pulse.

regenerative amplifier at time periods equal to the amplifier round trip time of 10.4 ns (i.e. at times -10.4, -20.8, -31.2 ns etc. relative to the main pulse). Timing of the pump lasers meant only the pre-pulse at 10.4 ns before the main pulse was amplified to an appreciable level. Characterisation of the pre-pulse energy was carried out by the ILIL laser team and concluded an energy contrast of 3×10^{-4} . The pre-pulse was focused at the same position as the main pulse and had a pulse duration of 35 fs, resulting in a pre-pulse intensity of 1.3×10^{17} W/cm². Figure 4.1 summarises the laser profile implemented considering both the main pulse and the pre-pulse.

The targets used are nanowire coated targets comprised of 6 μm long nanowires sitting normal to a 5 μm thick Ti substrate, and Ti foils of 5, 12.5, and 25 μm thickness to provide comparison data to assess the performance of the nanostructured targets. The targets are mounted on a target holder to allow multi-shot data collection. The main diagnostic to be discussed is imaging of optical emission from the rear surface of the irradiated targets. The results of a time-of-flight (TOF) diagnostic to detect accelerated ions are briefly presented; the TOF diagnostic was operated by A. Fazzi and D. Giove from INFN-Milan Section. The

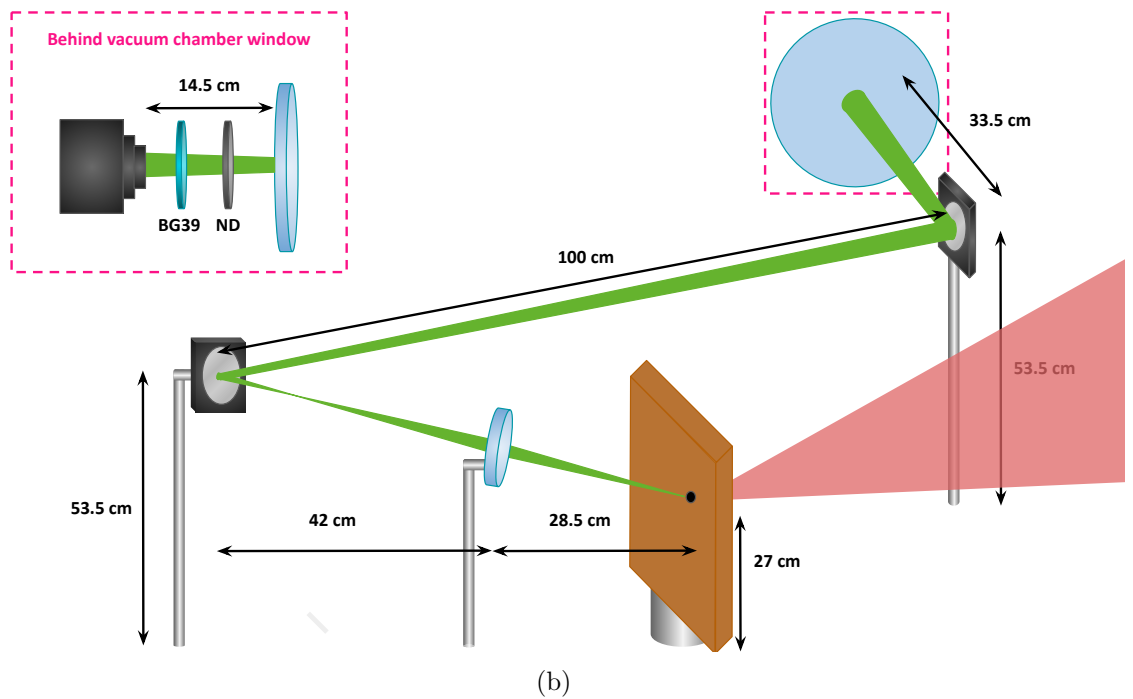
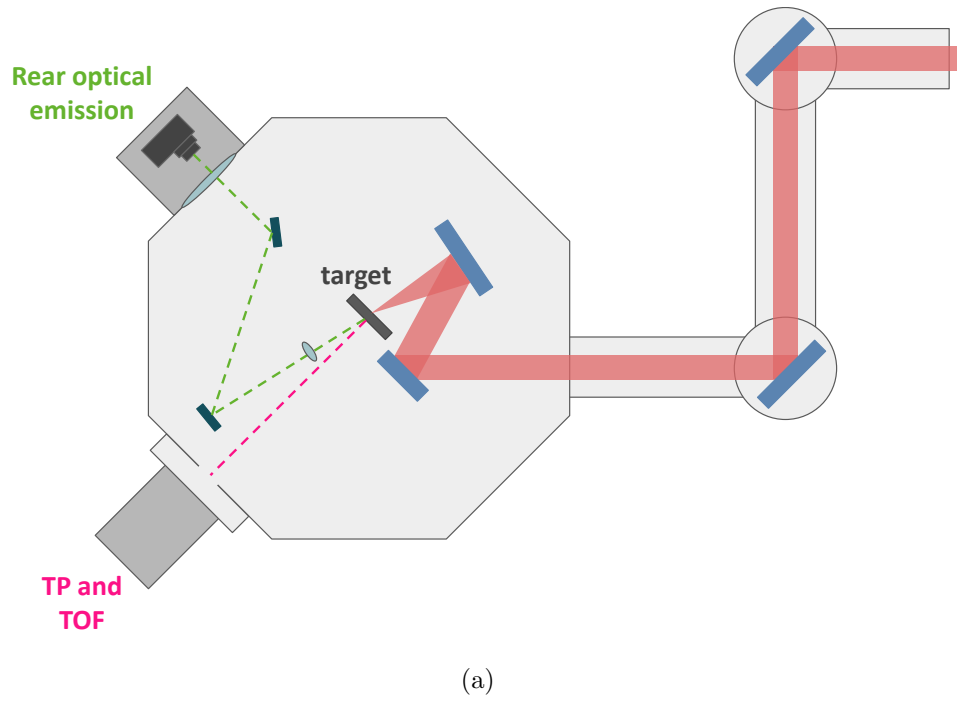


Figure 4.2: (a) Layout of the target chamber for the 2019 experimental campaign. (b) Details of the imaging line for the rear optical emission.

positioning of these diagnostics with respect to the targets is illustrated in Figure 4.2(a).

4.1.1 Diagnostics

An imaging line was established to view the optical emission from the rear target surface. A lens of focal length $f = 27$ cm was used to focus an image of the rear side of the target. Mirrors were placed to establish an imaging path to a Pentax K200D camera placed outside the target chamber as shown in Figure 4.2(b). In order to avoid disturbing the path of TNSA-generated ions, the imaging line was vertically displaced to be out of the plane of the target normal. Using the heights of the target holder and the first mirror (27 and 52.5 cm respectively) and the horizontal distance between them (70.5 cm), the angle of observation was calculated as $\theta = 20.6^\circ$. An ND filter was used for each shot which has the effect of reducing the intensity by a factor 10 to the power of the ND number (e.g. an ND3 filter will reduce the intensity by a factor 10^3) in order to avoid saturation of the image. A BG39 bandpass filter was used with transmission of $> 1\%$ for wavelengths $\sim 320 - 700$ nm.

To determine the pixel-distance conversion, images are taken of the target holder when illuminated by light from a torch. The targets were mounted on the front side of the target holder (i.e. the side facing the laser) with the camera imaging the rear side of the target holder. The target and therefore the source of the rear optical emission will be in the plane of the target holder front side. Accordingly, evaluation of the pixel-distance conversion is carried out for the central darker hole corresponding to the hole facing the laser. Lineouts are taken horizontally and vertically across the hole using *ImageJ* software, with a line thickness of 100 pixels. A fit is applied to the lineouts of the form

$$I = mx + c + A \exp \left[- \left(\frac{x - x_0}{\sqrt{2}\sigma} \right)^{16} \right], \quad (4.1)$$

incorporating a straight line fit to account for the background light, and a SuperGaussian to describe the hole where A is the height of the peak, x_0 is the central position of the distribution and σ is the standard deviation of the distribution. Optimal parameters for

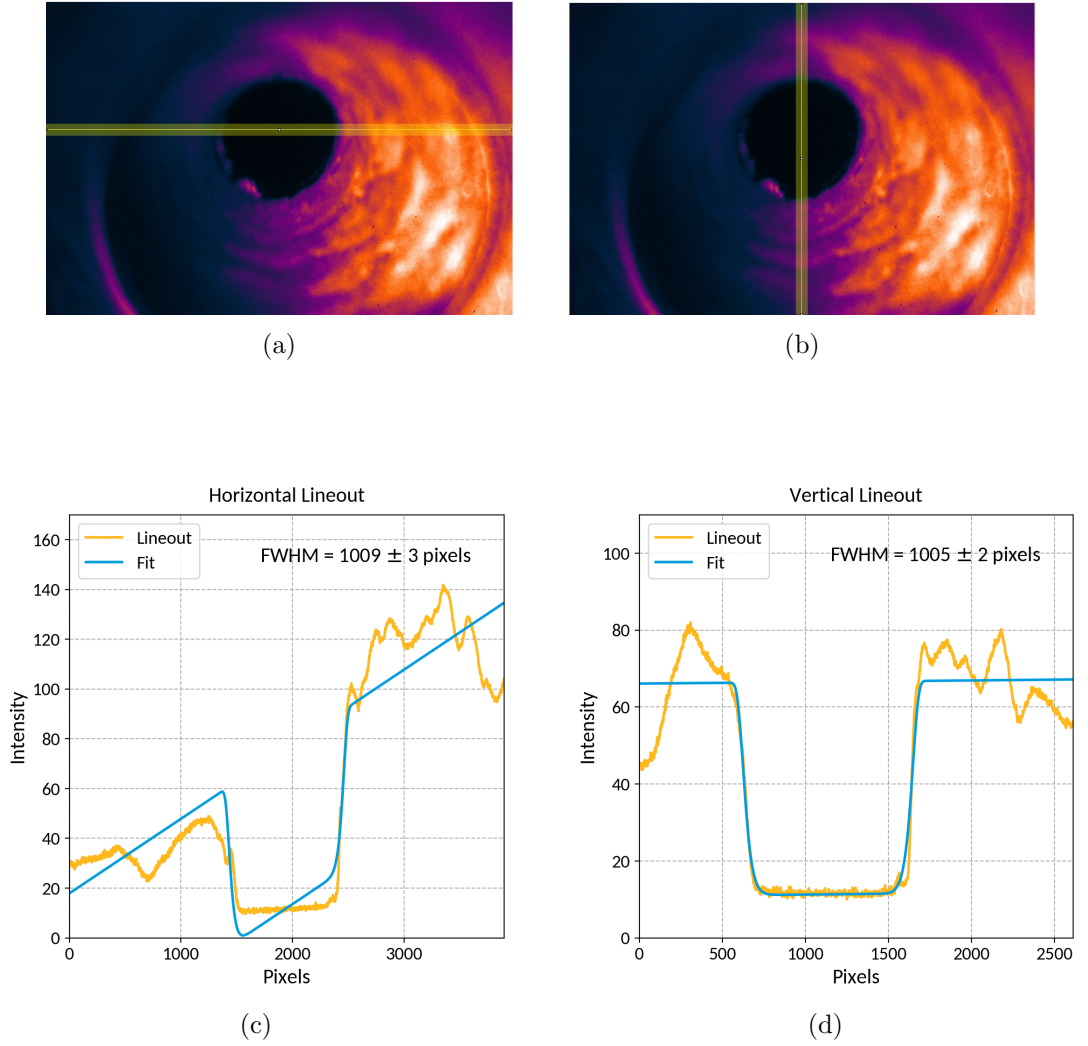


Figure 4.3: Image of target holder hole taken for pixel-distance calibration. Lineouts were taken (a) horizontally and (b) vertically across the image to measure the size of the central hole. The lineouts (yellow) and the respective fits (blue) are shown in (c) and (d)

each lineout fit is found using the `curve_fit` function from the SciPy library on Python:

$$I_{\text{horz}} = 0.03x + 18 - 64 \exp \left[- \left(\frac{x - 1946}{\sqrt{2} \times 365} \right)^{16} \right] \quad (4.2)$$

$$I_{\text{vert}} = 0.0004x + 66 - 55 \exp \left[- \left(\frac{x - 1136}{\sqrt{2} \times 363} \right)^{16} \right]. \quad (4.3)$$

The FWHM of the target holder hole in pixels is then calculated from the values of

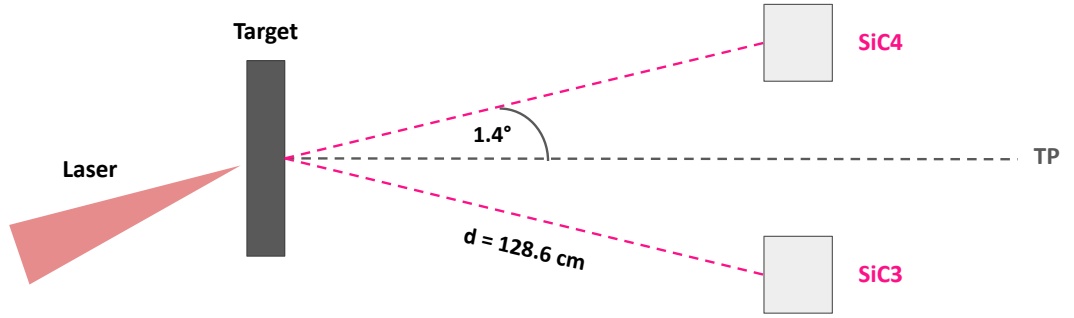


Figure 4.4: Layout of the time-of-flight diagnostic employed in the experiment.

standard deviation, σ , from each fit:

$$\text{FWHM} = 2\sqrt{2} \times \sigma \times (\log 2)^{1/16} \quad (4.4)$$

$$\text{FWHM}_{\text{horz}} = 2\sqrt{2} \times 365 \times (\log 2)^{1/16} = 1009 \pm 3 \quad (4.5)$$

$$\text{FWHM}_{\text{vert}} = 2\sqrt{2} \times 363 \times (\log 2)^{1/16} = 1005 \pm 2 \quad (4.6)$$

with the error on each value given as the error output by the *curve_fit* routine. The diameter of each target hole is 1 mm, meaning each pixel is equal to $\sim 1 \mu\text{m}$.

Rear-accelerated ions were detected with the use of a time-of-flight diagnostic. Two SiC detectors were placed a distance of 1286 mm away from the rear target surface, at an off-axis angle of $\pm 1.4^\circ$ as illustrated in Figure 4.4. The path along the target normal direction was left clear for the Thomson parabola diagnostic, the results of which are not presented in this thesis. To make clear, the TOF diagnostic was not operated or analysed by the author. We however present the TOF data to complement our optical imaging diagnostics, since both diagnostics are concerned with measurements from the rear target surface.

4.2 Rear Target Optical Emission

Images of the optical emission from the rear target surface were taken for each shot. Figure 4.5 shows an example image obtained during the campaign. The images generally presented a small, intense, filamented area of emission, surrounded by a larger diffuse ‘halo’ of emission. The brighter, intense region of emission is thought to be from coherent optical transition radiation induced by the propagating fast electrons. The larger, dimmer area is thought to be late-time recombination emission, thermal emission, or perhaps incoherent transition

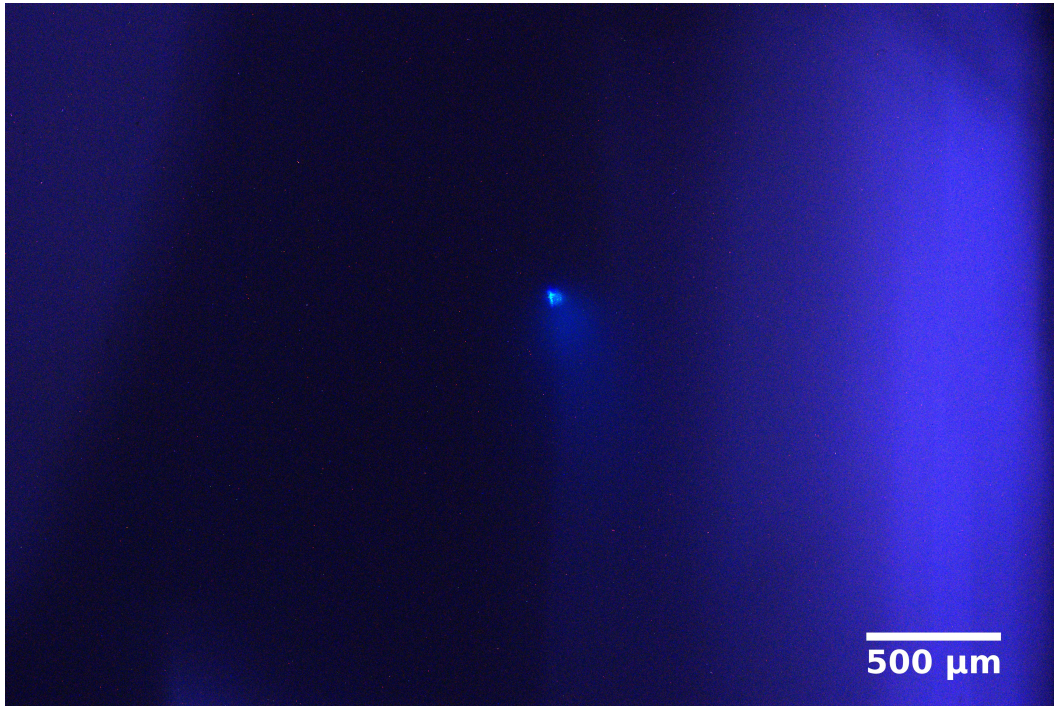


Figure 4.5: Example rear emission captured from a shot on $5 \mu\text{m}$ Ti foil. Contrast adjusted to highlight the transition radiation signal and the background.

radiation. Since the images are temporally and spectrally integrated it is difficult to uncover which is dominant here. To assess the CTR emission further, all images are cropped to a region of size $250 \times 250 \mu\text{m}$, around the bright region of interest. The resulting images are displayed in Figure 4.6 and divided according to the target type, with shots on Ti foils of thicknesses 5, 12.5 and $25 \mu\text{m}$ shown in columns 1, 2 and 3 & 4 respectively. The brightness and contrast settings are equivalent for each image.

ImageJ software is used to process the dataset and assess the measured intensities of the bright region optical emission imaged. Due to the irregular shape of the emission it was decided to analyse the emission in both the horizontal and vertical directions. For each image a rectangular ROI centred around the emission of size 1000×100 pixels is selected. The thickness of 100 pixels is chosen so the lineout will completely encompass the bright spot emission for all targets. A lineout of the intensity as a function of distance is taken, with the intensity averaged in the normal direction (e.g. for the horizontal lineout the intensity is vertically averaged). To account for background light, the ROI is displaced by 100 pixels downwards for the horizontal case and 100 pixels to the right for the vertical case, and

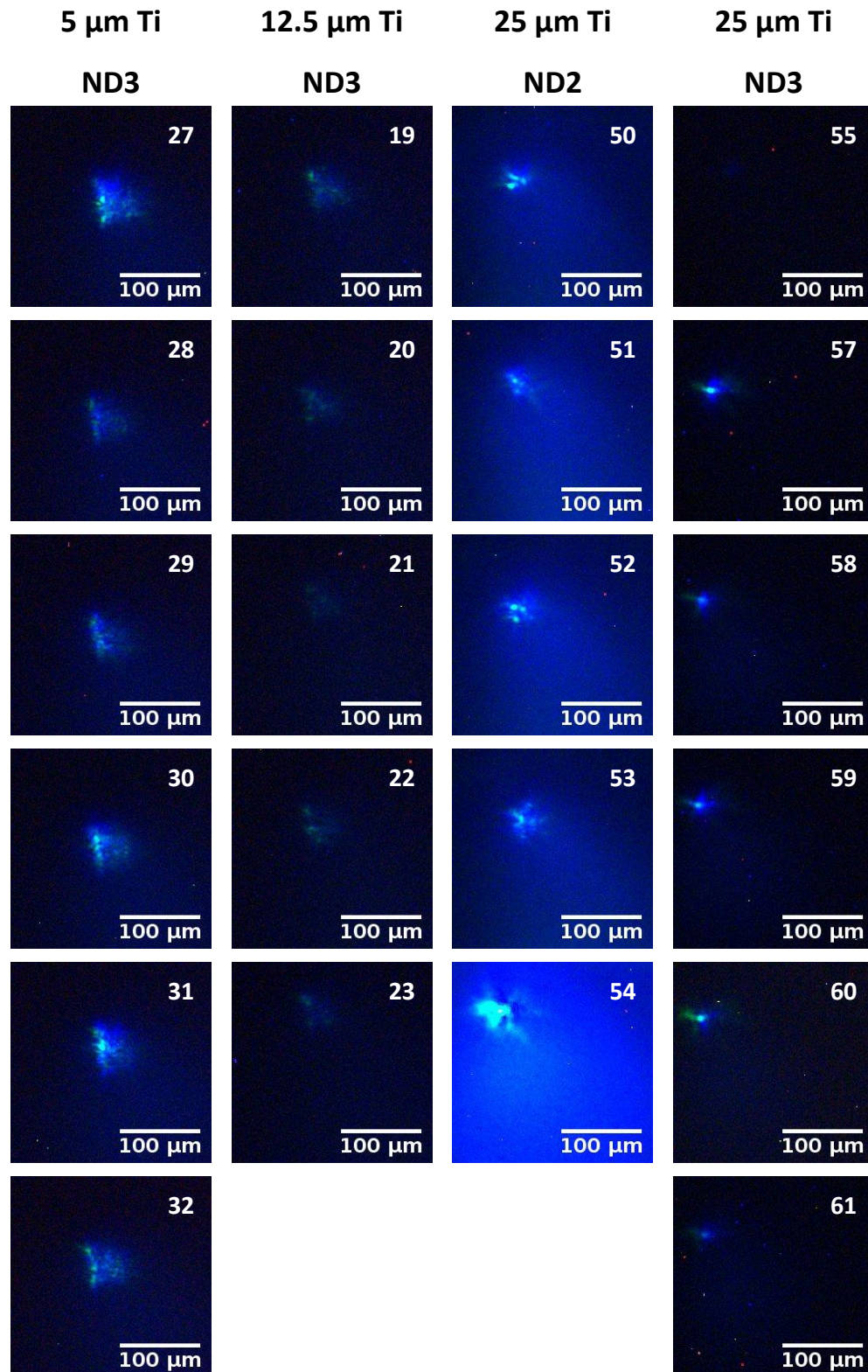


Figure 4.6: Images of optical rear emission from irradiated planar targets numbered by shot number.

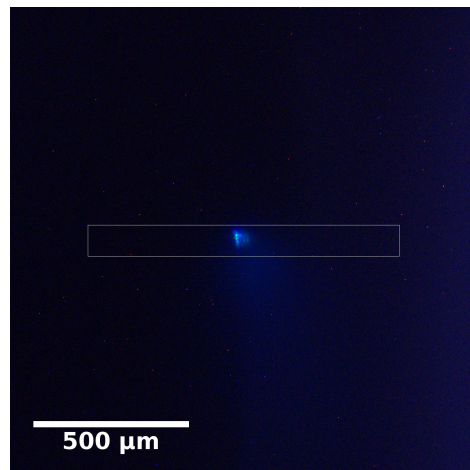
a lineout obtained from this position. This offset is selected to be as close as possible to the emission region, whilst not including any of the bright optical emission within the ROI. Background correction is carried out by subtracting this background lineout from the lineout across the optical emission. An example of the lineouts obtained from shot 30 on 5 μm Ti foil is shown in Figure 4.7. The background corrected intensity shows the emission presents a roughly Gaussian spatial profile. A Gaussian fit is therefore applied to the corrected intensity lineout with optimal parameters found using the SciPy *curve_fit* function. Finally, the effect of the use of an ND filter is accounted for by multiplying intensity by

$$I = I_{corr} \times 10^{ND} \quad (4.7)$$

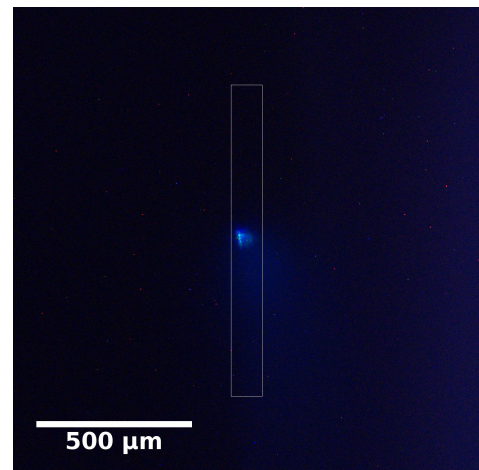
where ND is the number of the ND filter used.

The total intensity of the optical emission is retrieved using the SciPy's *integrate.simps* package, employing Simpson's rule to integrate the corrected intensity across the whole lineout. For each shot the average intensity from the horizontal and vertical lineouts is found, and these total intensities as a function of target thickness are displayed in Figure 4.8(a). To confirm the total intensity value is not influenced by saturated pixels far from the optical emission or additional light not captured by the background lineout, the total intensity of rear optical emission from each target is additionally obtained by integrating across the peaked region only. The peak region is determined from the Gaussian fit, with the integration limits taken as the x -positions where the Gaussian profile was reduced to 1% of the maximum height. The plotted error bars on each intensity value is calculated by considering the standard error from summation of the intensity values across the analysis region, $SE = \sigma/\sqrt{N}$, where σ is the standard deviation of the intensity values and N is the number of points in the lineout used for analysis. The error on the target thickness is $\pm 10\%$ as quoted by the target manufacturer, Goodfellows.

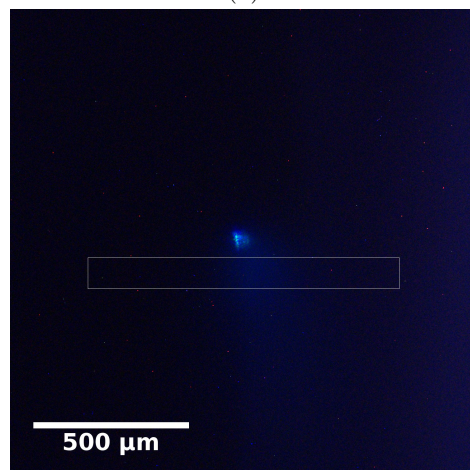
The total intensity of CTR emission integrated across the peaked region is shown in Figure 4.8(b). It can be seen that the most intense emission is obtained from shots on 5 μm Ti, with a marked decrease in intensity from shots on 12.5 μm Ti. For the shots on 25 μm Ti with an ND3 filter the intensity appears to exhibit a slight *increase in optical emission*



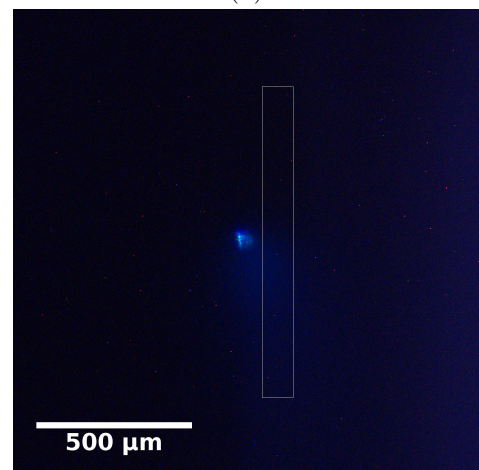
(a)



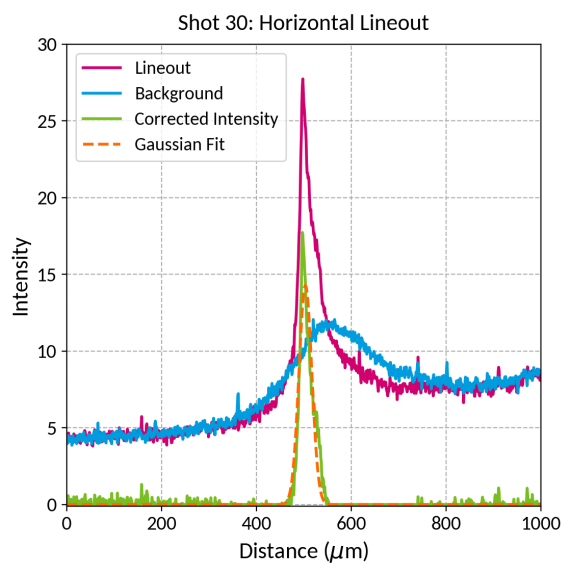
(b)



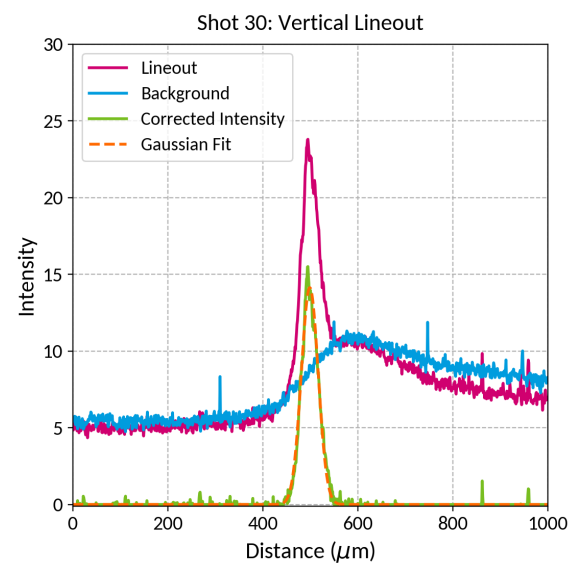
(c)



(d)



(e)



(f)

Figure 4.7: Lineouts for analysis of the total optical emission from the rear target surface.

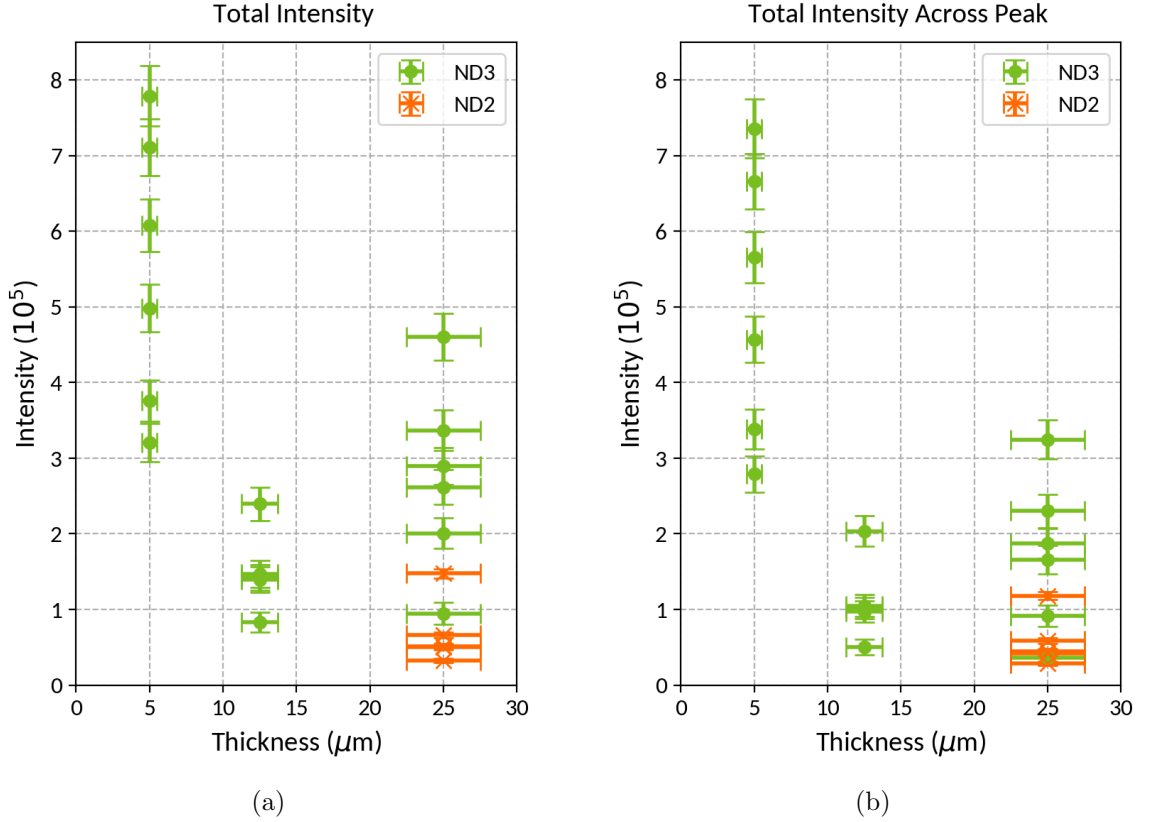


Figure 4.8: Intensity of optical emission measured from the rear side of irradiated planar targets as a function of target thickness; (a) gives the total intensity, and (b) shows the intensity integrated across the peak of the emission spatial profile.

intensity. Previous experiments have observed a decrease in CTR intensity with thickness of target foils, e.g. [100,152], in-line with theory outlined in the paper by Bellei *et al.* [120] that states that increased de-phasing of electron bunches in thicker targets reduces the efficiency of CTR production, and collisional effects can also prove detrimental to the intensity of CTR emission from thicker targets.

The use of an ND filter should not in itself affect the results, especially since the intensity has been corrected to account for the filtering during analysis. The difference in results between ND2 and ND3 filtered shots on 25 μm Ti could be explained by the position of the target along the laser axis. During the experiment the target holder position was varied along z , the laser focal axis, to find the best focal position. All reported shots on Ti 5 and 12.5 μm data were obtained at a focal position of 75 μm . Figure 4.9 shows the measured CTR intensities as a function of the scanned positions. Error on each position is $\pm 5 \mu\text{m}$,

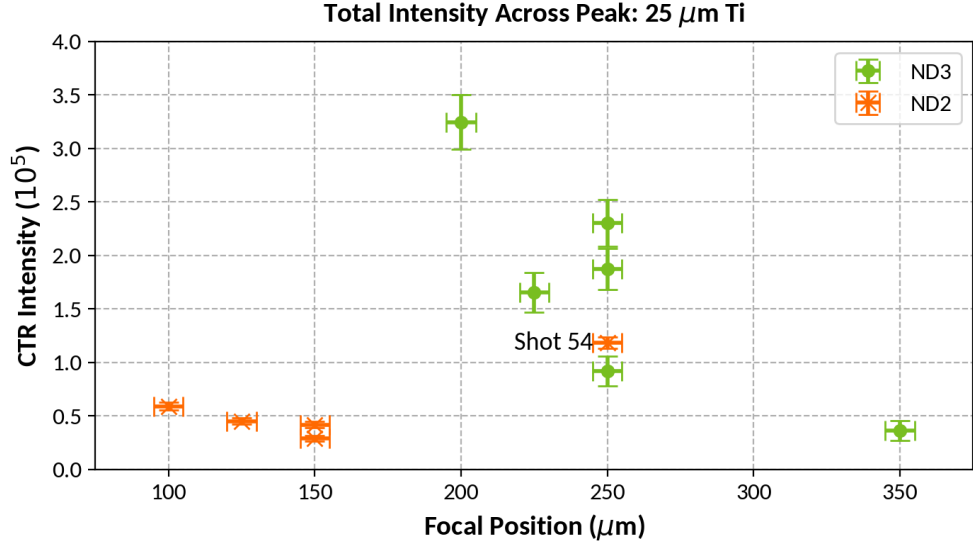


Figure 4.9: Total intensity of CTR emission measured from the rear side of irradiated $25 \mu\text{m}$ Ti foils as a function of target position along the laser focus axis

determined from the known error on the motorised stage used to move the target holder¹. Initial shots on $25 \mu\text{m}$ Ti were taken at a position $z \sim 125 \mu\text{m}$ with an ND2 filter. For shot 54 a large step in position along the focal axis was taken to $z = 250 \mu\text{m}$, at which point a sharp increase in intensity of optical emission and proton cut-off energy was observed. The filtering was increased to ND3 as the image appeared saturated. The following shots (55 and 56) were carried out at a focal position $z = 350$ and $z = 300 \mu\text{m}$ respectively, but resulted in lower proton cut-off energies and dimmer optical emission². Target position was therefore reverted to the position from shot 54, and the remainder of the shots taken around this position. The majority of shots with the ND3 filter were consequently taken around best focus, and explains why the shots on Ti $25 \mu\text{m}$ foil with an ND3 filter exhibited more intense emission.

The size of the CTR emission region is obtained from the fit applied to the lineouts. The standard deviation, σ , of the Gaussian fit is used to calculate the FWHM from each shot as

$$\text{FWHM} = 2\sqrt{2 \ln 2} \sigma. \quad (4.8)$$

¹Private communication, Petra Koester 2023

²Low optical signal meant analysis was not able to be carried out on shot 56.

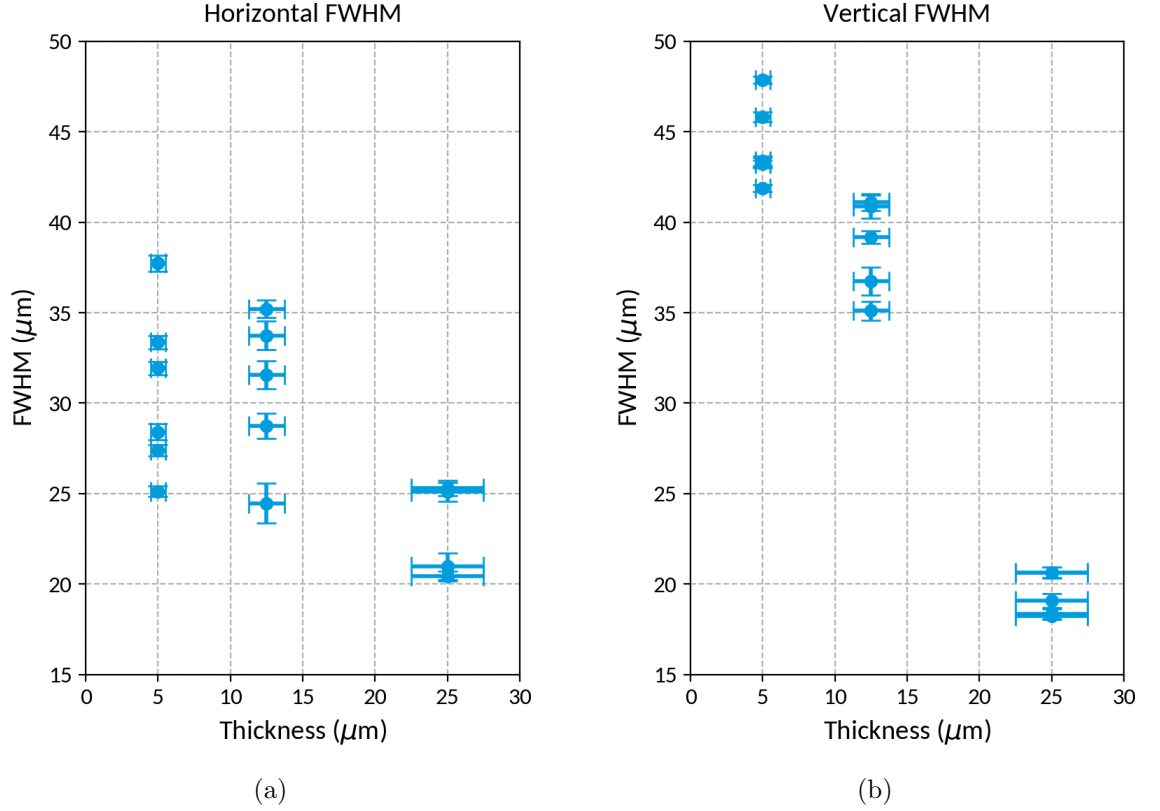


Figure 4.10: FWHM size of rear side CTR emission imaged from Ti planar targets as a function of target thickness.

The error in the emission size is calculated using the error in c output by the fitting function. Figure 4.10 shows the emission size in the horizontal and vertical direction as a function of target thickness, including only shots taken at best focus with ND3 filter for 25 μm Ti targets. Error on each target thickness is $\pm 10\%$. The emission size *decreases with target thickness* in both the horizontal and vertical direction, with a more pronounced decrease in emission size observed in the vertical direction. In work presented by Santos *et al.* the size of the optical emission region was measured from the target rear surface, and found the emission size to be approximately the same for targets of thickness 10 and 20 μm [121].

In summary, these experimental measurements of the optical rear surface emission have revealed smaller, intense regions of emission attributed to coherent optical transition radiation. The intensity of the CTR region was measured for the planar targets. A reduction in intensity was observed between target thicknesses of 5 and 12.5 μm , but interestingly a slight increase was measured from the 25 μm targets, in disagreement to what is expected

from theory and previous experimental measurements. In addition, the FWHM size of the CTR emission was found to decrease with target thickness. Since CTR is emitted in a region very close to the propagating fast electrons, one might expect an increase in emission size with target thickness from the divergent fast electron beam traversing a greater distance. At this stage the effect of the atypical pre-pulse encountered in this experiment and the influence on the target structure has not been considered; the referenced works all concern CTR emission from solid metal foils. It is apparent the effect of the pre-pulse must be taken into consideration when endeavouring to explain the results here: as Bellei identifies in Ref. [120], the efficiency of CTR production does have a dependence on the target properties. Before this consideration, the results obtained from the TOF diagnostic are examined to explore the laser-target interactions with respect to the rear-accelerated ions.

4.3 Ion Acceleration

Analysis of the TOF data was completed by M. Salvadori. The output of each SiC detector is coupled to an oscilloscope to record the accelerated proton signal at the detector as a function of time. Each trace was analysed to infer the energies of the protons from the time taken to travel to the detector. For each shot the maximum, or “cut-off”, energy of the proton spectra is acquired. The error on value of the cut-off energy is calculated from the oscilloscope sampling rate. For a more accurate estimate of the error, one would need to take into consideration the response of the detector: at this time the precise details of the detectors are not known (e.g. detector thickness, charge collection efficiency) and so the detector error can not be quantified.

The cut-off proton energy is plotted against planar target thickness in Figure 4.11 as measured by the two detectors. The lowest ion energies are measured from the 5 μm targets, with a slight increase in ion energy from shots on 12.5 μm targets. A marked enhancement in ion cut-off energy is then observed from the 25 μm targets. The energies from rear-side protons have been shown previously to reduce with target thickness [153], which disagrees with our observations. However, we must take into consideration the effect of the intense pre-pulse. Kaluza *et al.* [112] investigated the effect of ASE-produced pre-plasma on proton cut-off energies from thin targets, and found the energy increased with target thickness up

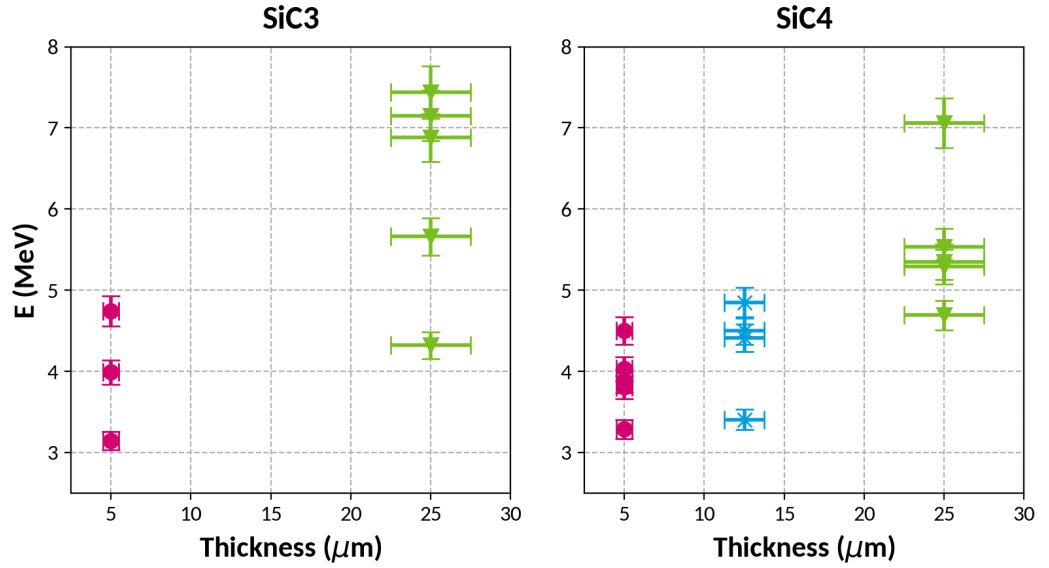


Figure 4.11: Measured proton cut-off energies as a function of planar target thickness.

to an optimal thickness dependent on the properties of the pre-pulse. Two sources of accelerated protons were identified in this regime: (1) protons accelerated from the front surface by a sweeping potential in the pre-plasma region [109], and (2) rear surface protons accelerated via the TNSA mechanism. The trend of increasing ion cut-off energy was explained by a consideration of both front and rear side acceleration. Work by Mackinnon *et al.* [111] demonstrated an ultra-short density scale length is required at the rear surface for efficient TNSA acceleration; a plasma of scale length $100 \mu\text{m}$ added to the rear surface was shown to severely degrade the efficiency of proton acceleration by orders of magnitude compared to an unperturbed rear surface. Thinner targets were found to be more susceptible to rear surface deformation from a shockwave induced by the pre-pulse and radiative heating, and therefore presented reduced TNSA energies; on the other hand, there is less target material for front surface-accelerated protons to be stopped by, and thus front surface protons can be detected from the thinnest targets.

A later experiment at ILIL measured accelerated proton cut-off energies for intense laser interactions with planar foils of different thicknesses [154]. This campaign was subject to the same pre-pulse conditions as for our experiment, and was compared to results without the pre-pulse. They discovered an enhancement in proton energies for shots on Ti $25 \mu\text{m}$ planar foil with the pre-pulse, a result which was not reproduced for thinner targets where

the proton energies with the pre-pulse were equivalent to, or lower than, the case without the pre-pulse. This is in agreement with the result reported here. Following modelling they concluded that whilst the presence of pre-plasma can enhance the laser coupling into fast electrons, in the case of the thinner targets the shock wave launched by the pre-pulse heating reaches the rear surface before the arrival of the main pulse, disrupting the sheath field that serves to accelerate the protons.

The proton cut-off energies are also considered with respect to the results from the optical rear emission. Cut-off energy is shown as a function of the size of CTR emission in Figure 4.12(a). As the size of the rear CTR emission region increases, the proton cut-off energy decreases. A recent study by Takagi *et al.* [155] used a statistical approach to predict a maximum ion energy scaling with fast electron density as

$$E_{max}(MeV) \propto \left(\frac{n_f}{n_c} \right)^{0.31}, \quad (4.9)$$

where n_f is the fast electron density. CTR emission is directly related to the passage of fast electrons; it could then be inferred that a smaller emission size is related to a higher fast electron density, and hence a greater ion cut-off energy. Finally, the cut-off energies are plotted against the measured intensity of optical emission in Figure 4.12(b). There is an overall trend of a *reduction in proton cut-off energy with increasing rear emission intensity*. This correlation is, at this stage, unexplained. Exploring this relationship further is beyond the scope of this work, but is the focus of continuing investigation.

The results of the experimental TOF data are consistent with the optical rear emission data regarding the observation of an enhanced performance from 25 μm thick targets compared to thinner targets. According to the work presented by Gizzi *et al.* [154], a similar pre-pulse was able to launch a shock wave disrupting the rear surface of targets thinner than 25 μm . The effect of the pre-pulse is clearly not negligible and we need to account for it accordingly to understand our optical emission data; if shock breakout is indeed present here, this will have an impact on the ability of the target rear surface to generate optical transition radiation emission. We therefore look to model the effect of the pre-pulse heating for our targets and assess the extent of deformation to the rear target surface for the different

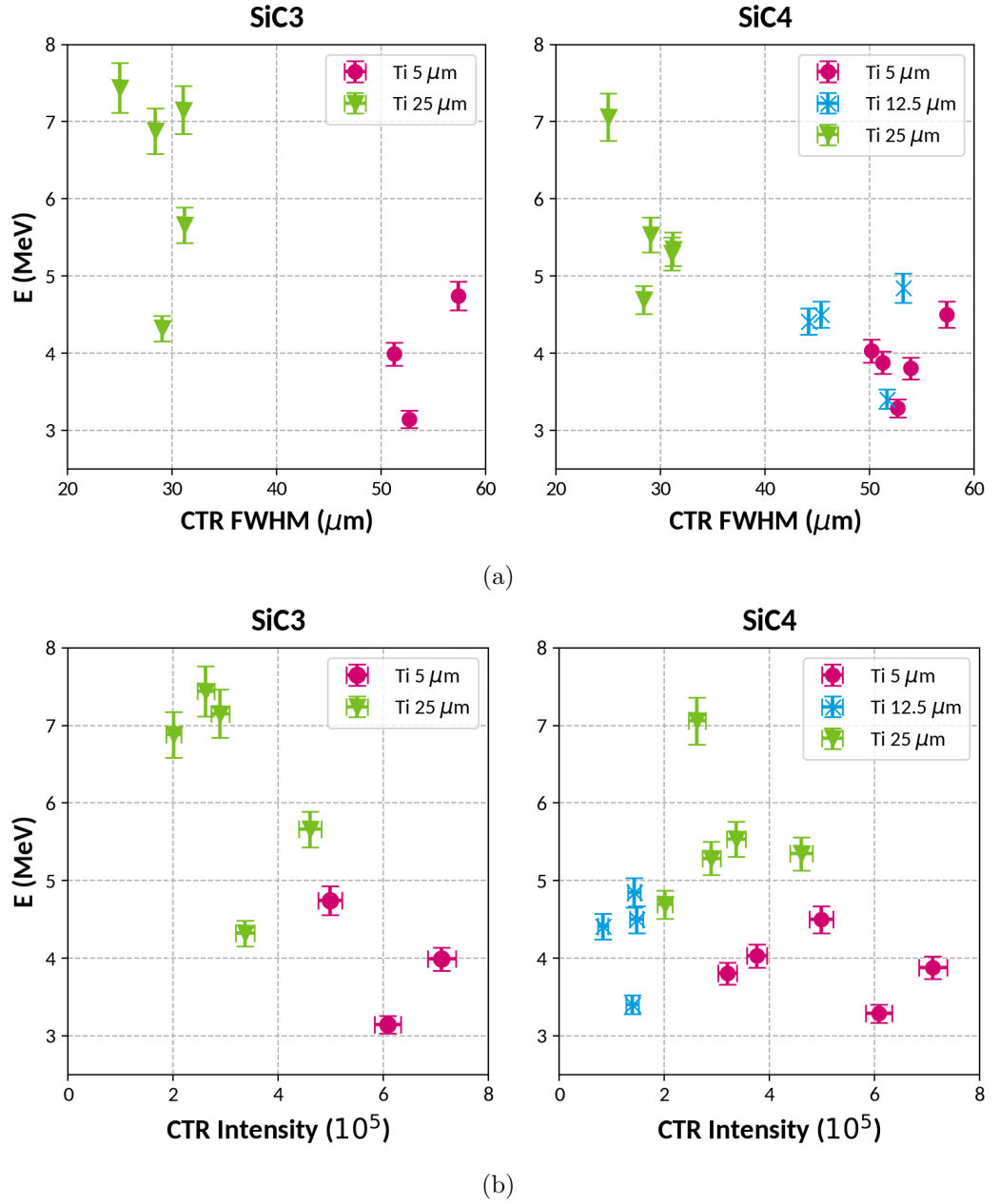


Figure 4.12: Measured proton cut-off energies as a function of (a) FWHM of the imaged CTR emission, and (b) intensity of CTR emission measured from the shot.

targets employed.

4.4 Hydrodynamic Modelling of the Pre-Pulse

The targets were subject to an intense, $I \sim 10^{17}$ W/cm² pre-pulse irradiating the targets 10.4 ns before the main pulse arrival. It is anticipated that the target structures will be affected

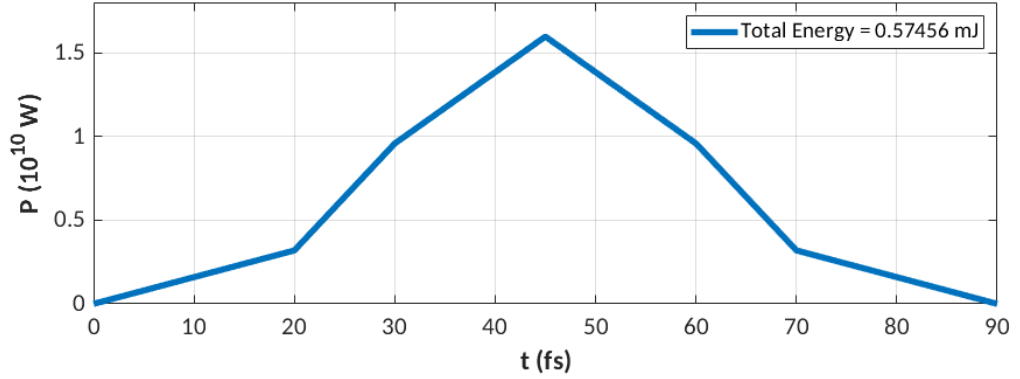


Figure 4.13: Power profile originally implemented in FLASH to model the pre-pulse.

by this pre-pulse. A pre-plasma will be formed from heating and expansion of the target, leading to a longer scale length plasma at the front surface. Rapid energy deposition from a laser pulse can also lead to the formation of a shock wave which can subsequently propagate through and disrupt the bulk target [156]. When considering the effect of the pre-pulse in the context of our experiment we come into relatively unexplored territory. Experimental pre-pulses tend to be of much lower intensity, with the pedestal and the leading edge of the main pulse typically governing pre-plasma formation. Prior investigations considering the interaction of a ~ 10 's fs, $I \sim 10^{17}$ W/cm² laser pulse on a solid target are limited: short laser pulses are typically coupled with higher intensities $I \geq 10^{18}$ W/cm² to optimise collisionless absorption, and lower intensity regimes of $I \leq 10^{15}$ W/cm² are achieved with longer pulses where collisional absorption is dominant. To clarify the effect of our pre-pulse on the target structures we therefore needed to use the hydrodynamic code *FLASH* to model the hydrodynamic motion of the targets.

4.4.1 FLASH Simulation Setup

A $50 \mu\text{m} \times 125 \mu\text{m}$ ($r \times h$) simulation domain was set up in a cylindrical geometry. Blocks of 10×10 cells were established and initially distributed with 2 blocks in the r direction and 5 in h . Maximum refinement level was set to 6, with the finest grid resolution possible being 78 nm, and the refinement parameters to be used by PARAMESH set as electron temperature, electron pressure, mass density, and boundary cells. EOS tables were calculated for Ti target material using PrOpacEos, with 25 values of temperature spaced logarithmically from 2.0 - 2.0×10^5 eV and 25 values of electron density spaced logarithmically from 1.0×10^{16}

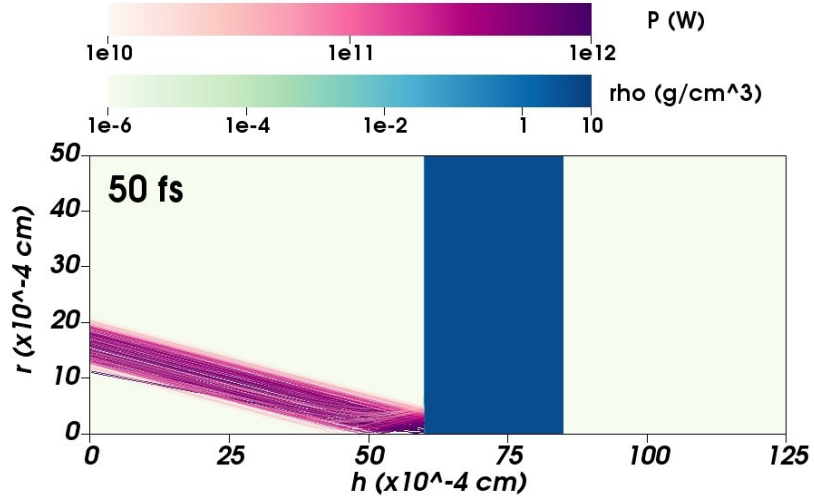


Figure 4.14: Geometry of the planar target and laser in FLASH.

- $1.0 \times 10^{24} \text{ cm}^{-3}$. The Ti target was initially set at a solid density $\rho = 4.5 \text{ g/cm}^3$ and temperature $T_{ion,ele,rad} = 290.1 \text{ eV}$. Chamber material was set as He gas at an initial density $\rho = 1 \times 10^{-5} \text{ g/cm}^3$ and temperature $T_{ion,ele,rad} = 290.1 \text{ eV}$.

To recreate the pre-pulse, a power profile was constructed with a Gaussian temporal profile of FWHM = 35 fs and a peak power of $1.6 \times 10^{10} \text{ W}$ as shown in Figure 4.13. The total energy in the pulse is 0.57 mJ, as calculated from the main pulse focal spot energy of 1.9 J and the energy contrast between pre- and main pulses of 3×10^{-4} . The laser rays are set to focus at the front surface of the target at $h = 60 \text{ }\mu\text{m}$ at an incidence angle of 15° . The focal spot has a Gaussian spatial profile of e-folding length $r_e = 2.41 \text{ }\mu\text{m}$, with the laser region extending out to a maximum radius $r_{max} = 5.2 \text{ }\mu\text{m}$. The geometry of the incoming laser rays focused onto the target is shown in Figure 4.14. The simulation is run up to 100 fs with a timestep of 0.01 fs, then restarted to run up to 10.4 ns with a timestep of 1 ps.

An initial simulation using the laser profile indicated in Figure 4.13 on a $12.5 \text{ }\mu\text{m}$ thick Ti target resulted in 3 nJ of energy absorbed, or an absorption fraction of 1×10^{-5} . To determine if this low absorption fraction is reasonable for our conditions, the 1D code HYADES is used to model the pre-pulse interaction and early hydrodynamic response up to 100 ps. It has been previously observed that HYADES is capable of matching absorption and resul-

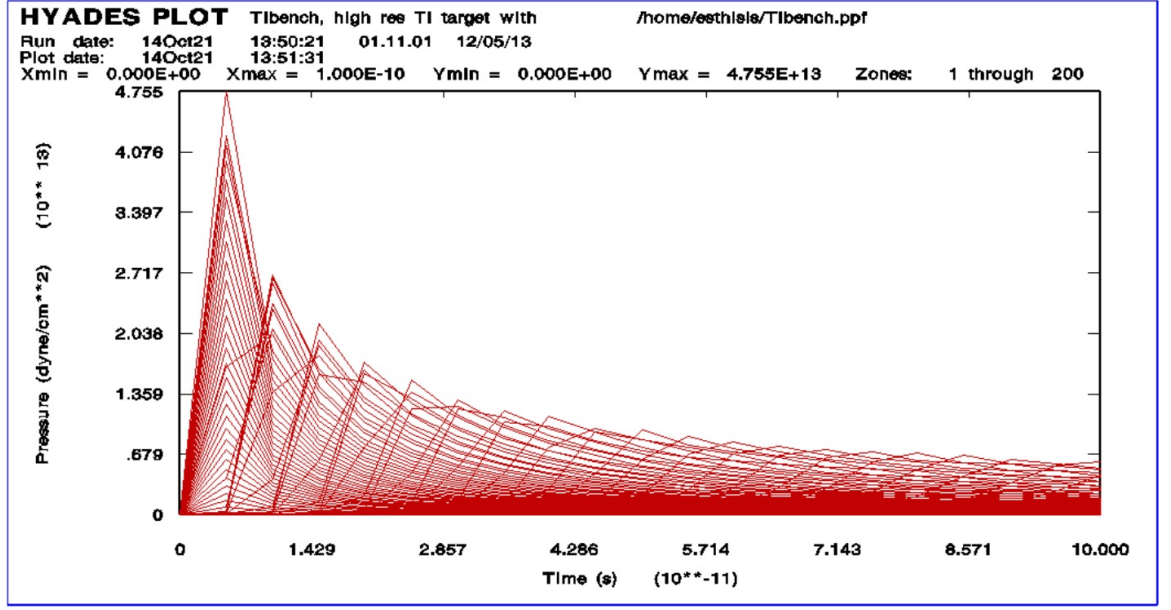


Figure 4.15: HYADES result of pressure of a Ti target after irradiation by the pre-pulse. Each lineout represents the pressure from a mesh element.

tant hydrodynamics to experimental results with pulses of this intensity and duration³. The maximum pressure was taken at each timestep (Figure 4.15) which should correlate with the peak pressure in the shock. Pressures taken from the FLASH simulation reached a maximum of 10^{-3} MBar, compared to shock pressures obtained with HYADES of 1-10 MBar across the same time period. The difference in results between HYADES and FLASH is suggested to be from HYADES having a substantially higher energy deposition into the electrons, resulting in a stronger shock wave being launched. This implies the energy absorption in FLASH is too low and needs to be addressed.

FLASH models energy deposition using an inverse bremsstrahlung model and has a dependence on local electron density and electron temperature gradients as shown in Equations 3.24 and 3.25. To boost the energy deposition an exponentially decaying density profile was added at the target front surface of the form

$$\rho = 4.5 \times \exp\left(\frac{-(60 - h_{\mu m})}{0.015}\right) \quad (4.10)$$

where ρ is mass density. The exponential decay length of 15 nm was chosen so that the same

³Private communication, John Pasley, 2021.

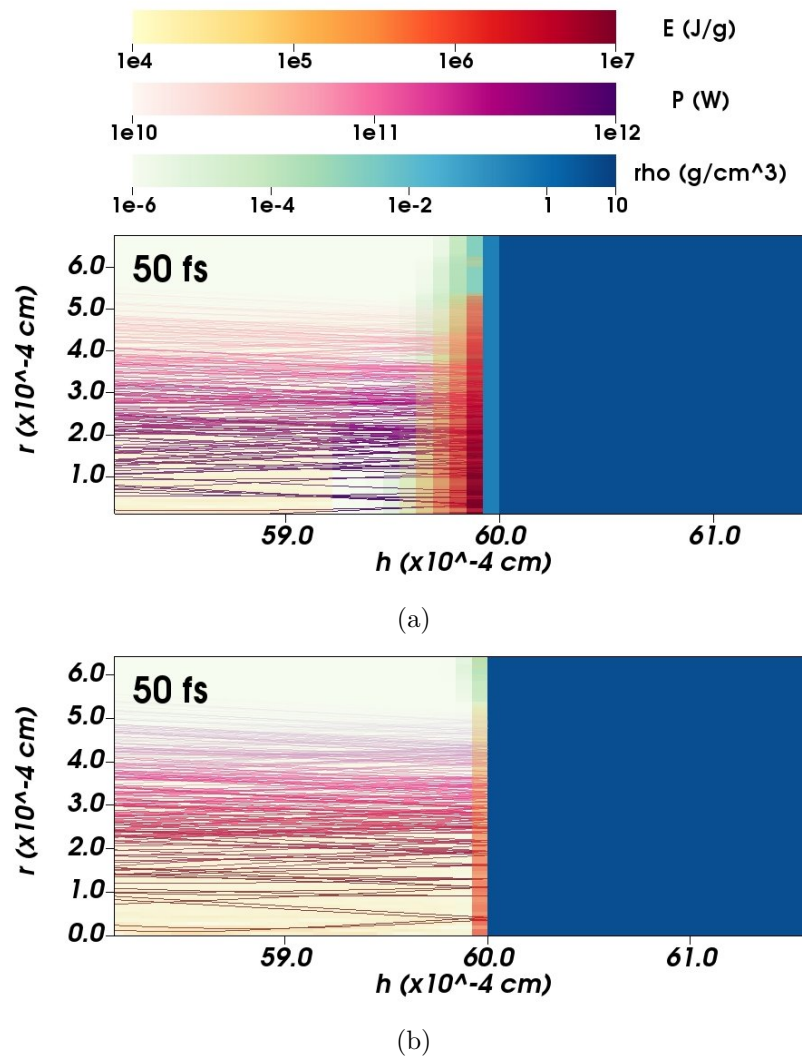


Figure 4.16: Laser interaction at 50 fs with target (a) with and (b) without the exponential density profile. Both results are plotted using the same scale.

density profile could be replicated around the wires when modelling the nanostructured targets in Chapter 5, as the wires have an average diameter and gap size of 400 nm. This scale length is sufficiently short that it will have little impact on the final density profiles. Plots of the interaction both with and without the exponentially decaying region are shown in Figures 4.16(a) and (b) respectively. It can be seen that the presence of the decaying plasma facilitates a much greater energy deposition into a larger region compared to the steep density profile. The majority of the energy is being delivered into a thin layer of the exponentially decaying density region, but still close to the bulk target.

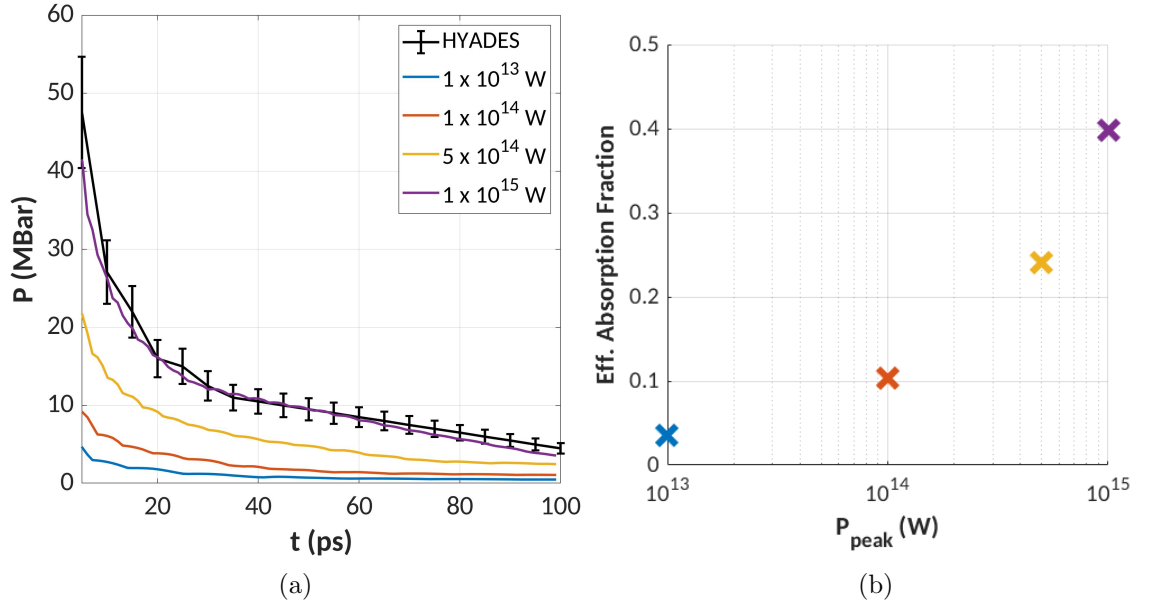


Figure 4.17: Parameter scan to determine an appropriate power profile for use in FLASH. (a) Maximum shock pressure obtained from FLASH simulations and (b) corresponding energy absorption fraction relative to the actual pre-pulse energy.

It appears FLASH is not best suited for accurately modeling the absorption of 10's fs pulses, and so a benchmarking exercise was carried out to determine the energy absorption. The energy input at the target surface was established using HYADES, matched in FLASH, and then FLASH was employed to tackle the longer time-scale hydrodynamics. Energy deposition per ray scales with the ray power, so to tailor the total energy deposited the laser power profile was scaled to increase the power of the rays. A parameter scan was carried out in FLASH using the same laser profile as shown in Figure 4.13, but uniformly scaled up by different scaling factors. The other simulation parameters are the same as described in Section 4.4.1.

The maximum shock pressure from the FLASH simulations at early times < 100 ps was used as a figure of merit and benchmarked against the HYADES output to infer when a satisfactory initial energy deposition had been reached. Figure 4.17(a) shows the HYADES output is matched to within 15% when using a laser profile with a peak power $P_{peak} = 1 \times 10^{15}$ W. The *LaserDeposition* module in FLASH outputs the amount of energy deposited by the laser and can be used to calculate an “absorption fraction” relative to the actual pre-pulse energy of 0.57 mJ for each case. Figure 4.17(b) shows the absorption fraction scales with the laser power as expected from Equation 3.24. For the laser profile with $P_{peak} = 1 \times 10^{15}$

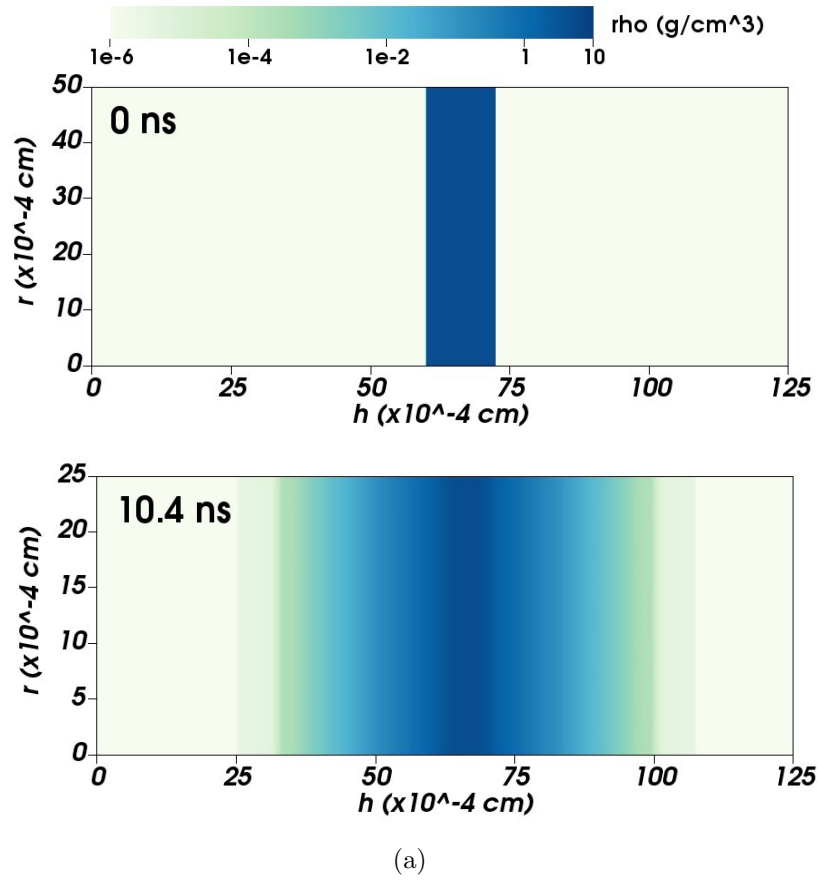


Figure 4.18: Mass density (g/cm^3) of the Ti $12.5 \mu\text{m}$ target at (a) 0 ns and (b) 10.4 ns with no laser irradiation.

W the absorption fraction is ~ 0.4 . As mentioned earlier, work is limited in this regime, but previous work has shown absorption fractions of between 0.15 [122] and < 0.67 [157].

The simulations are initialised with a central slab of Ti at solid density, with He gas above and below to represent vacuum. The code does not explicitly see the Ti as consisting of solid material possessing properties such as surface tension and material strength. Instead, the whole domain is assumed to be a plasma. The initial strong pressure gradients at the material interfaces will lead to a non-physical expansion of the target into the vacuum material. This occurs even when there is no laser irradiation or energy deposition as demonstrated in Figure 4.18. To rectify this the target surfaces were ‘fixed’ by setting the front and rear layers of cells as a domain boundary, preventing the hydro solvers being explicitly solved across the target surfaces. Laser rays are set to reflect at boundaries, so the front surface was only fixed for a radius $r > 8 \mu\text{m}$ to allow energy deposition into the target. The rear 100 nm of

Target Thickness (μm)	Shock Breakout Time (ns)
5	0.6
12.5	4.2
25	> 10.4

Table 4.1: Shock breakout time at the rear surface for planar targets.

the target thickness was set to be fixed boundary cells.

4.4.2 Heated Target Profiles

With an appropriate laser deposition determined and the artificial target expansion reduced, full simulations are carried out to determine the evolution of the planar targets between the pre-pulse and main pulse irradiation time. A simulation is set up for each target and run up to 10.4 ns, the main pulse interaction time. In initial runs it is observed that the shock wave launched from the laser heating reflected at the rear surface boundary cells used to limit the artificial target expansion. Test runs are carried out to determine the shock breakout time at the rear surface as recorded in Table 4.1. A condition is then set to relax the rear boundary at a time of 0.1 ns before the shock breakout time in order to allow the shock to exit the target.

The main objective from these hydrodynamic simulations is to determine the extent of target deformation as a result of the pre-pulse interaction. Figures 4.19(b), (d), and (f) show the mass density profiles of the planar targets at the time of the main pulse interaction. All targets show pre-plasma formation at the front surface as a result of the laser heating. The repercussions of the pre-plasma on the main laser interaction will be dependent on the pre-plasma scale length. The scale length at the front of the 25 μm target is estimated at 10.4 ns [based upon Figure 4.19(f)]. The front surface density profiles are similar across the different thicknesses⁴ so we only need to carry out a fit to one target type. A lineout was taken at $r = 3 \mu\text{m}$ along $h = 0 - 60 \mu\text{m}$ in order to characterise the pre-plasma. The lineout data was converted to electron number density by multiplying the mass density values by $Z_{Ti}N_A/M_R$. It can be seen that the critical density surface now lies at $h = 34.8 \mu\text{m}$, around 25 μm away from the original target surface at $h = 60 \mu\text{m}$. Fitting was done to this lineout using a power

⁴This is to be expected since the target thickness shouldn't impact the front surface interaction

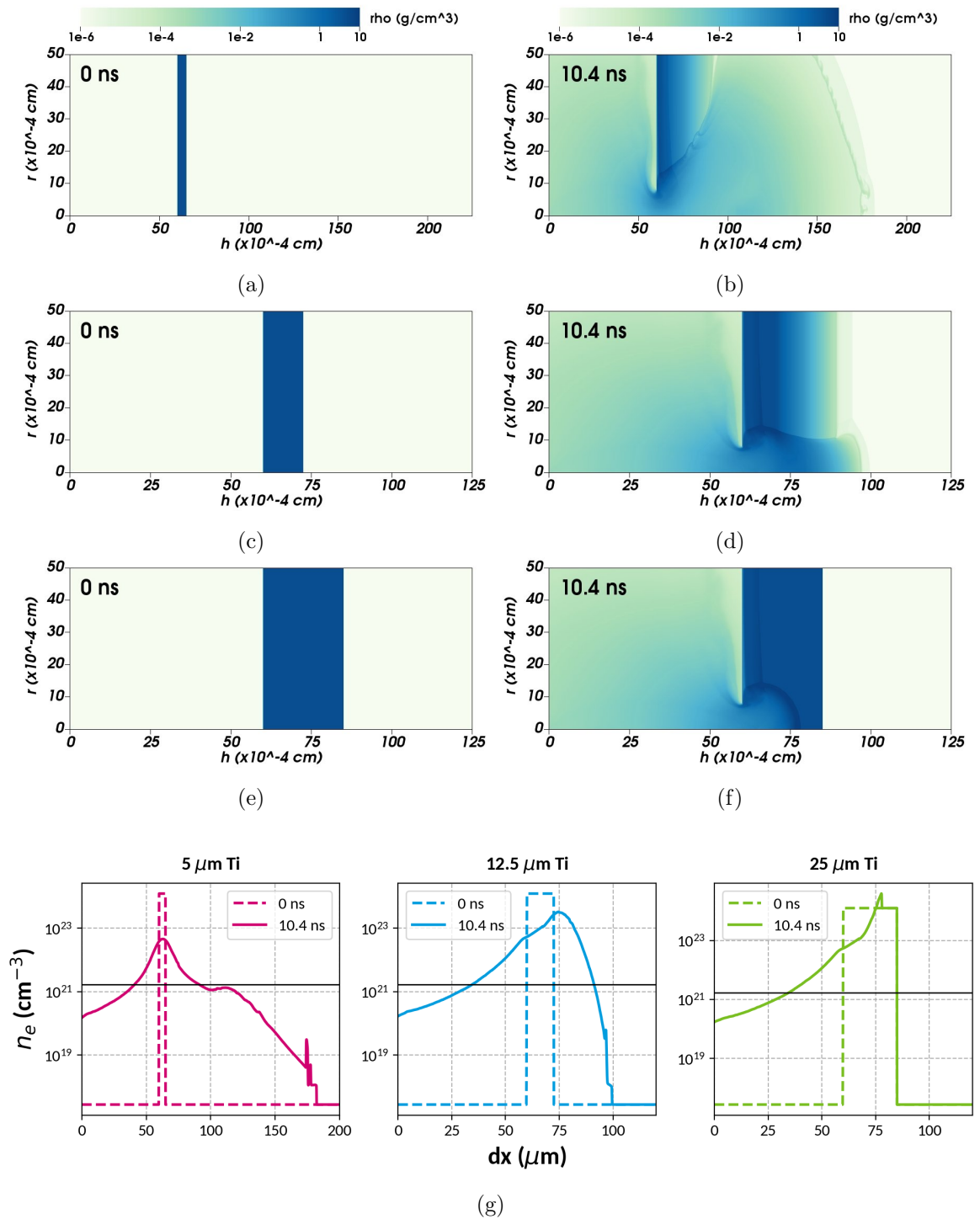


Figure 4.19: Mass density (g/cm³) at 0 ns for targets of (a) 5 μm , (c) 12.5 μm and (e) 25 μm thickness, and 10.4 ns after pre-pulse irradiation for (b) 5 μm , (d) 12.5 μm and (f) 25 μm thickness. Lineouts of the density profiles along $r = 3 \mu\text{m}$ are shown in (g).

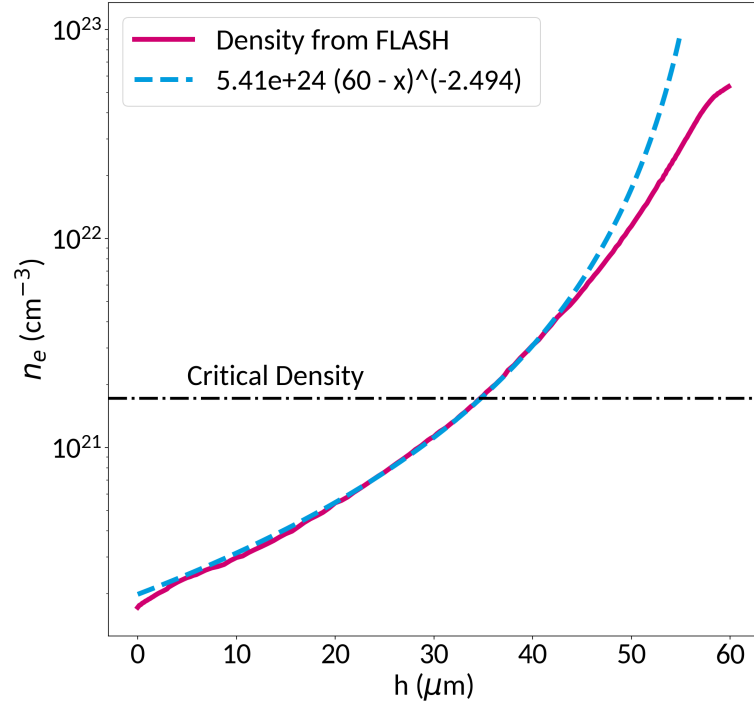


Figure 4.20: Lineout data from FLASH is shown in pink and the found fit to the pre-plasma region is shown in blue.

law function of the form $n_e = A(B - h)^{-C}$ similar to the work by Scott *et al.* [158] with the best fit displayed in Figure 4.20(b). The scale length is non-uniform across the pre-plasma and is described by the function

$$L_{pp}(h) = \frac{n}{dn/dh} = \frac{1}{2.494} (60 - h_{\mu m}) \mu m. \quad (4.11)$$

Use of Equation 4.11 yields a scale length at the critical density surface ($h = 34.8 \mu m$) of $10.1 \mu m$.

The properties of the rear target-vacuum boundary for each target are also of interest for interpreting the rear surface optical emission data. For optimal CTR generation a steep density gradient is required to establish a large change in dielectric constant. Shock breakout, however, perturbs the rear surface for the 5 and 12.5 μm targets resulting in an extended density profile as opposed to a sharp ‘step’ in density. Lineouts were taken at $r = 3 \mu m$ for each target at 10.4 ns to evaluate the rear density profiles, and are shown in Figure 4.19(g). For the 25 μm target the rear surface is undisrupted, with the shock front remaining in the bulk target. In contrast, the profiles for the thinner targets present an

extended density profile from shock propagation into vacuum, with the shock front clearly visible at $h \sim 160 \mu\text{m}$ for the $5 \mu\text{m}$ target. The shocks originating from the thinner targets do exhibit a discontinuity in density, changing by ~ 2 orders of magnitude across a few μm , but the gradients are not as substantial as the solid density-vacuum interface of the $25 \mu\text{m}$ target.

Shock breakout by the main pulse irradiation time from the thinner targets has created a more complex environment within which to analyse the rear optical emission data. The main pulse interaction with the pre-plasma has to be considered thoroughly in terms of the fast electron population produced; the number, energy and bunching of the electrons is sensitive to the properties of the pre-plasma with consequences on later transition radiation emission. Target expansion has changed the effective target thicknesses employed in the experiment. The distance between the critical density surface at the front and the rear target surface is now greatest for the Ti $5 \mu\text{m}$, but the average target density is much lower than for the Ti $12.5 \mu\text{m}$. The reduced density gradient at the shock front, as opposed to the steep density gradient of the undisrupted target-vacuum boundary, may reduce the intensity of transition radiation produced for the thinner targets [159]. The undisrupted rear surface of the $25 \mu\text{m}$ target may still allow for substantial CTR generation from the main pulse interaction however. On the other hand, the interaction of the high intensity pre-pulse with the unheated targets may generate enough fast electrons to be a significant source of TR emission also. Results of the hydrodynamic simulations alone are not sufficient to judge which interaction is dominant here, and further investigation is required to elucidate the contribution of each interaction.

As a final note, the effect of this pre-pulse on planar targets has also been investigated by Gizzi *et al.* [154] using the 2D Eulerian hydrocode POLLUX [160]. Whilst their experimental work was carried out independently of this campaign, it was still subject to the same pre-pulse and thus their results can be referred to as a comparison. They found the rapid heating by the pre-pulse resulted in a shock being launched into the $25 \mu\text{m}$ target with an estimated velocity of $1.5 \mu\text{m}/\text{ns}$. This shock speed leads to the conclusion that shock breakout at the rear surface has occurred by the time of main pulse irradiation for the thinner 5 and $12.5 \mu\text{m}$ targets but not for the $25 \mu\text{m}$ target, in agreement with our analysis.

4.5 Hybrid-PIC Simulations of Fast Electron Transport

The investigation with FLASH has allowed exploration of the effect of the shock wave from the pre-pulse interaction on the target structure, and provided information on the pre-plasma formation and rear target disruption. An additional aspect to consider is the population of pre-pulse-generated hot electrons with respect to their potential to heat the bulk target through collisions or Ohmic heating. This has motivated an investigation into the extent of heating possible from the pre-pulse interaction, in an effort to further characterise the effect of the pre-pulse on our targets prior to the main pulse interaction.

To simulate the fast electron transport through the foil targets the hybrid-PIC code ZEPHYROS is employed. The target and laser parameters are defined following the experimental pre-pulse conditions. The laser is set with an intensity of 1.3×10^{17} W/cm² and a laser spot of radially varying intensity according to

$$I = I_{peak} \exp \left[-\frac{r^2}{2r_{spot}^2} \right]. \quad (4.12)$$

Here, r_{spot} is set to $1.697 \mu\text{m}$ corresponding to a HWHM of $2 \mu\text{m}$, and extends out to a maximum radius of $5.15 \mu\text{m}$ (where intensity has dropped to 1% I_{peak}). The laser injects fast electrons into this region over a time period of 35 fs in a top-hat temporal profile, i.e. the laser intensity does not vary with time. The simulation domain consists of $(tx \times 100 \times 100)$ cells of dimensions $(0.1 \times 1 \times 1) \mu\text{m}^3$, where tx is the target thickness in μm . Each cell is set to represent solid Ti with an initial ion density $n_i = 5.67 \times 10^{28} \text{ m}^{-3}$ and initial temperature $T_b = 0.1$ eV under the assumption that the target has undergone minimal to no bulk heating prior to the pre-pulse irradiation. Boundaries are set to reflective in x, y, and z directions.

ZEPHYROS does not model the laser-plasma interaction and absorption - for this a full particle-in-cell code would be required - and as such the user must define appropriate parameters to represent the fast electron population. Absorption fraction is set to 0.4 as guided by the hydrodynamic simulation work. Previous work could not be found regarding measurements of the divergence of the fast electron beam at this intensity and pulse length. The experimental trend reported by Green *et al.* [88] estimates a divergence angle $\theta_{1/2} \sim 20^\circ$ at an intensity of 1×10^{18} W/cm²; the divergence angle is thus set to 20° . An

estimate of the fast electron temperature is obtained from theory. The pre-pulse intensity lies in a ‘crossover’ region where the primary absorption mechanism transitions from resonance absorption to ponderomotive acceleration. From resonance absorption the expected fast electron temperature is estimated by the scaling provided by Wilks and Kruer [67], $T_{hot} \approx 10[T_{keV}I_{15}\lambda_{\mu m}^2]^{1/3} \approx 2$ keV, where T_{keV} is target temperature. If ponderomotive acceleration is dominant then the fast electron temperature can be approximated as being close to the ponderomotive potential energy, $U_p = m_e c^2 \left(\sqrt{1 + (I_{18}\lambda^2/1.37)} - 1 \right) = 15.3$ keV. Since we cannot say with confidence which mechanism is dominant here, we model cases for the two fast electron temperature estimates of 2 keV (resonance absorption) and 15.3 keV (ponderomotive acceleration). A total of 1×10^6 macroparticles are used to represent this fast electron population.

The background temperature at the rear surface of the targets of different thicknesses is shown in Figure 4.21. Heating from hot electrons with a temperature following the resonance absorption scaling ($T_{hot} = 2$ keV) is shown in the first row with blue labelling, and heating from hot electrons with a ponderomotive temperature scaling ($T_{hot} = 15.3$ keV) is shown in the second row with red labelling. For the RA electron case the heating at the rear surface is negligible compared to the background temperature. These electrons are highly collisional and readily deposit their energy close to the front of the target. Even at a depth of $x = 5$ μm the heating has rapidly dropped off; at a depth of $x = 25$ μm there is essentially no heating observed at the rear surface. For the ponderomotive electron case the higher energy electrons are stopped less from drag or scattering, and are able to propagate deeper into the target. Greater heating is observed than from the RA case, but the magnitude of the heating remains small. The highest temperature reached is ~ 0.11 eV - compared to the initial temperature of 0.1 eV this is a very small amount of heating.

Based on these simulations carried out with ZEPHYROS, the energy of the pre-pulse-accelerated electrons is not great enough to induce significant heating of the target prior to the main pulse irradiation. These results indicate that the keV-level electrons heat the target primarily within the first few μm of the target thickness, and heating at the rear target surface is marginal. Concerning the experimental measurements of optical emission, this suggests appreciable heating and thermal emission from the rear surface is unlikely from

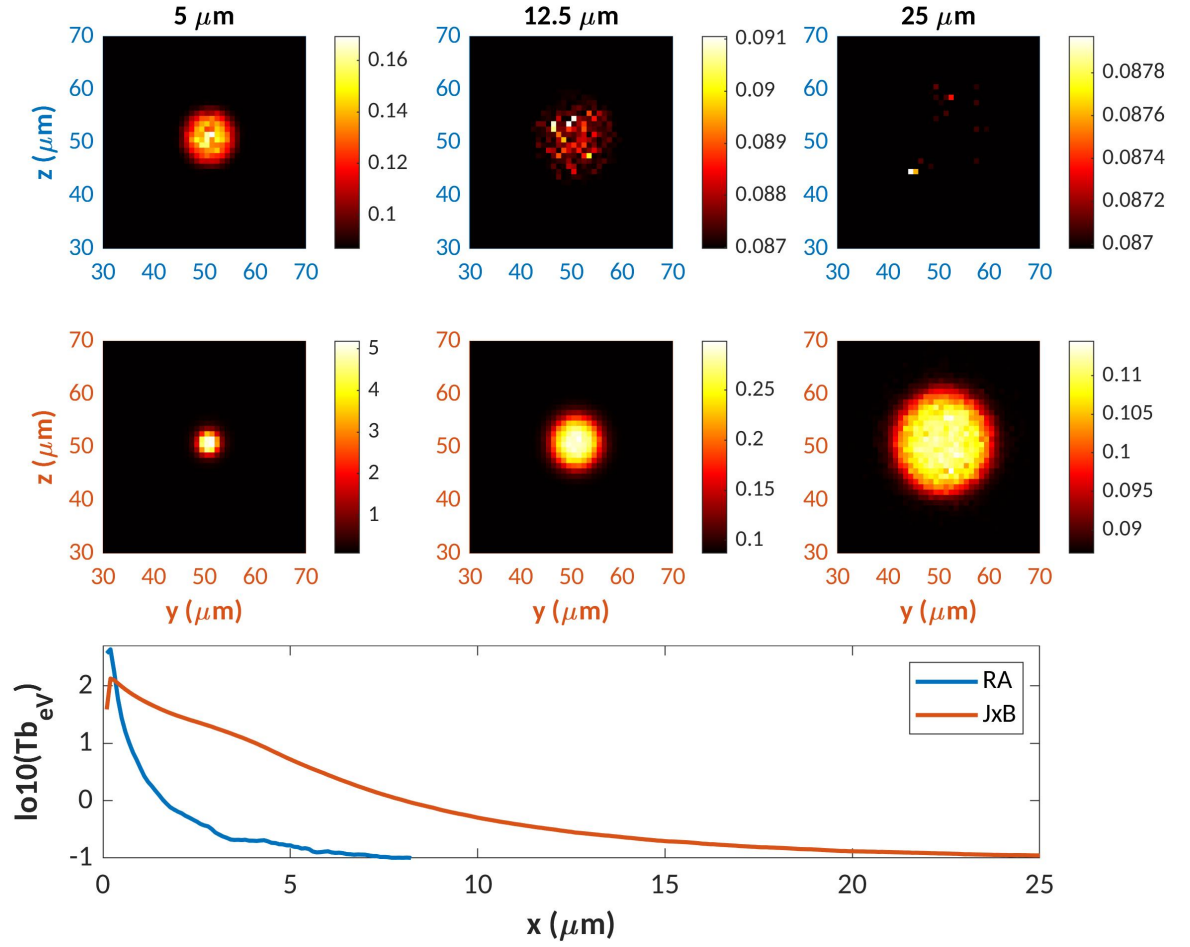


Figure 4.21: Background target temperature at 1 ps for slices taken at a target thickness of 5, 12.5 and 25 μm . First row (blue labels) is for electrons with $T_{hot} = 2$ keV, second row (red labels) is for electrons with $T_{hot} = 15.3$ keV. Bottom plot show the average background temperature as a function of target thickness, x .

the pre-pulse interaction. Moreover, the low background heating results suggest that at the target rear surface there is either (a) a low number of electrons to deposit energy through drag and collisions or (b) there is a low electron current to induce significant Ohmic heating. Either way, this suggests there are a low number of electrons reaching the target surface, and any bunching structure is likely to be vastly reduced after the transport through the target. This implies that observable coherent transition radiation emission is unlikely; incoherent transition radiation is still possible, but again there is a low electron number at the rear surface, and since the power of ITR emission scales linearly with electron number the emission is expected to be small.

A second source of fast electrons is from the main pulse interaction with the expanded

targets. There lies the possibility that the fast electrons generated from this interaction, with a higher current density, could induce a measurable amount of thermal emission in the optical regime. Since our experimental measurements are spectrally and temporally integrated, it is possible that this emission could form a contribution to our measured signal. Whilst it would be informative to model the transport of these electrons through the targets as for the pre-pulse interaction, this exercise is not simple. The lineouts of the density profiles obtained from FLASH at the time of the main pulse irradiation in Figure 4.19(g) indicate a $35 \mu\text{m}$ thick layer of under-critical pre-plasma at the front surface. The background density must be higher than the fast electron density in order to provide a sufficient return current for current neutralisation and allow the fast electron beam to propagate into the target [161]. For an ultra-intense laser interaction with under-critical plasma this is not necessarily satisfied. In addition, changes in the density of the background electrons due to the presence of the fast electrons are not captured in hybrid-PIC codes. Consequently, in the hybrid-PIC simulation the injected fast electron beam will be unable to travel into the target and will be confined to the front surface; simulations are therefore restricted to those with a density $\geq n_{crit}$. Whilst one could run the simulation for the overdense region only, such as in the study by Honrubia *et al.* [162], for the thinner foils the target is mostly underdense - for Ti $5 \mu\text{m}$ there is $50 \mu\text{m}$ overdense material out of a total thickness of $180 \mu\text{m}$. This includes underdense material at the rear surface; we would therefore be omitting the most crucial region of the target and the results of the simulation will not be hugely informative.

Hybrid-PIC modelling was carried out to evaluate whether target heating induced by the fast electron transport could form an appreciable contribution to the measured optical emission in this experiment. The results presented here suggests the hot electrons generated in the pre-pulse interaction with the target do not have a high enough current density to induce significant heating at the rear surface of the targets. The hot electron temperature has a clear impact on the ability of the electrons to induce bulk heating at the rear surface of the targets. Electrons with a hot electron temperature following a resonance absorption scaling are effectively stopped before reaching the rear surface, particularly for the thickest target ($25 \mu\text{m}$). If the hot electrons have a temperature guided by ponderomotive scaling there is a more substantial region of heating induced at the rear surface, but even this is estimated to only heat the region by $\sim 0.01 \text{ eV}$ and will be unobservable. The main pulse interaction

with the expanded target profiles was unable to be modelled here. Previous work can be used as a guide to determine whether substantial heating is possible. Work presented by Green *et al.* [163] included simulations of the induced heating at the rear surface of 50 μm Al foils due to the transport of fast electrons generated by a laser with comparable parameters to our main laser pulse. They found the bulk temperature was raised by a maximum of approximately 0.7 eV, again a relatively small amount of heating. From both the pre- and main pulse laser interactions the rear surface heating is predicted to be marginal, and is unlikely to be a source of bright optical emission at the target rear surface.

4.6 PIC Simulations of the Laser-Target Interactions

The hybrid-PIC and hydrodynamic simulations both required assumptions to be made about the laser absorption mechanism at play and about the properties of the fast electron population. Within this experiment we encountered atypical laser-target interactions that are not as well-understood as a “standard” intense laser-solid interaction, and it would be wise to explore these interactions more thoroughly. Particle-in-cell simulations are able to model the fundamental interaction and coupling of the laser into the target electrons. Furthermore, PIC simulations are able to capture transition radiation generated by the passage of charged particles (electrons) propagating through the target-vacuum boundary, a feature that is not resolved by either hydrodynamic nor hybrid-PIC simulations. A computational study using the PIC code EPOCH was executed to address the fast electron and transition radiation generation in our experiment. This is considered in a multi-stage process. Firstly, the interaction of the pre-pulse with the planar target is modelled to estimate the hot electron energies and optical transition radiation emission induced by the interaction. Secondly, the main pulse interaction with the expanded targets is considered. Ideally the entire density profile obtained from FLASH would be input as the starting target density in EPOCH, ready for irradiation from the main pulse. However, a fine cell size is required to well resolve any optical emission in the rear vacuum, which will not be feasible for the larger domain size ($\sim 200 \mu\text{m}$) needed to replicate the heated density profile. The decision was made to opt for a decoupled approach, with one study looking at the effect of an increasingly disrupted rear surface on the formation of transition radiation, and one looking at the properties of fast electrons produced from the main pulse interaction with the extended pre-plasma. This will

allow the study of both aspects of the main pulse interaction, without having to compromise between resolution of emitted radiation and modelling of a realistic expanded density profile.

4.6.1 Pre-Pulse Interaction with Planar Target

The computational study begins by considering the case of a laser representing the laser pre-pulse interacting with a solid planar target. The target is set as $2.5 \mu\text{m}$ thick Ti with an average ionisation $Z_{bar} = 10$, electron density $n_e = 20n_{crit}$, and a temperature of 1 keV. Grid resolution was set to 1 nm in both x and y. Each cell is populated with 1 pseudoparticle to represent Ti ions, and 10 pseudoparticles to represent electrons. A laser is set with a Gaussian spatial profile of $\text{FWHM} = 4 \mu\text{m}$ irradiating the front surface of the target at an incidence angle of 15° . The laser intensity is set to $1.3 \times 10^{17} \text{ W/cm}^2$ with a FWHM pulse length of 35 fs. To permit laser absorption it was found that a short scale length pre-plasma is required at the front of the target. It is anticipated that at the pre-pulse intensity the primary absorption mechanisms will be resonance absorption and/or vacuum heating. These take place at the critical density; in reality the rising edge of the pulse and the pedestal will create a pre-plasma encompassing the critical density surface, but the simulations here do not capture this and the laser would mostly interact with overdense material. To compensate for this, an exponentially decaying density profile is added to the front surface of the target with a scale length of 15 nm. To diagnose the exiting fast electrons a probe is placed at $x = 4 \mu\text{m}$, in the rear target vacuum. The probe is set to only record pseudoparticles representing electrons that pass in the +ve x -direction. The simulation is run up to a simulation time of 150 fs.

Plots of the $x - p_x$ distribution of the electrons in the whole simulation domain are shown in Figure 4.22 to understand the acceleration of electrons into the target. Only a small number of electrons are accelerated into the target, and do not reach energies much greater than the initial target temperature of 1 keV. These hot electrons do not present a clear indication of acceleration in bunches, with no bunched structures apparent in the $x - p_x$ distribution. An energy spectra of exiting fast electrons is constructed in *Matlab* from the probe outputs to more precisely characterise the electrons produced. Kinetic energies are calculated using the momenta of each passing pseudoparticle recorded by the probe, and a histogram is created with bins in 1 keV increments. The resultant electron energy spectra

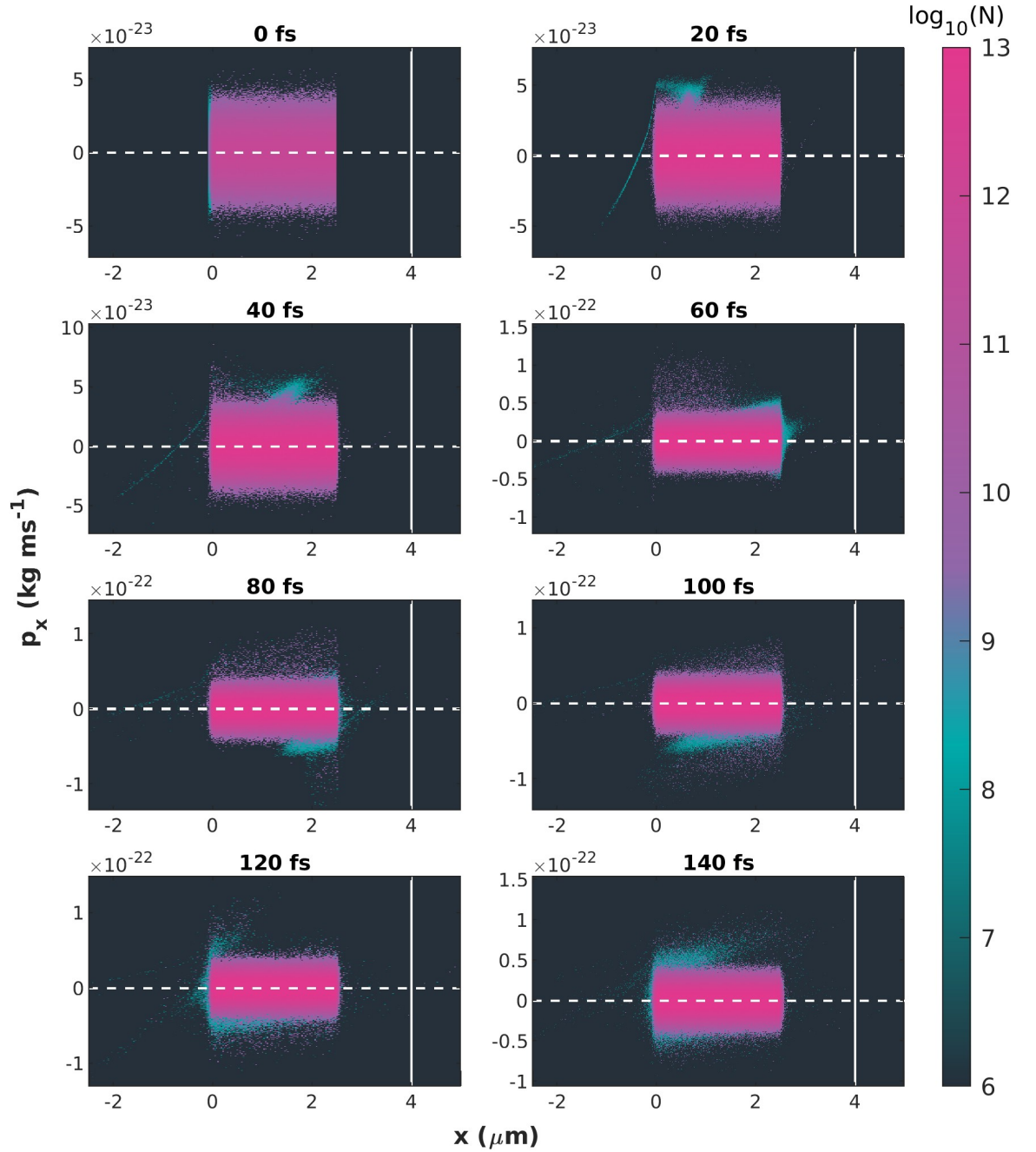
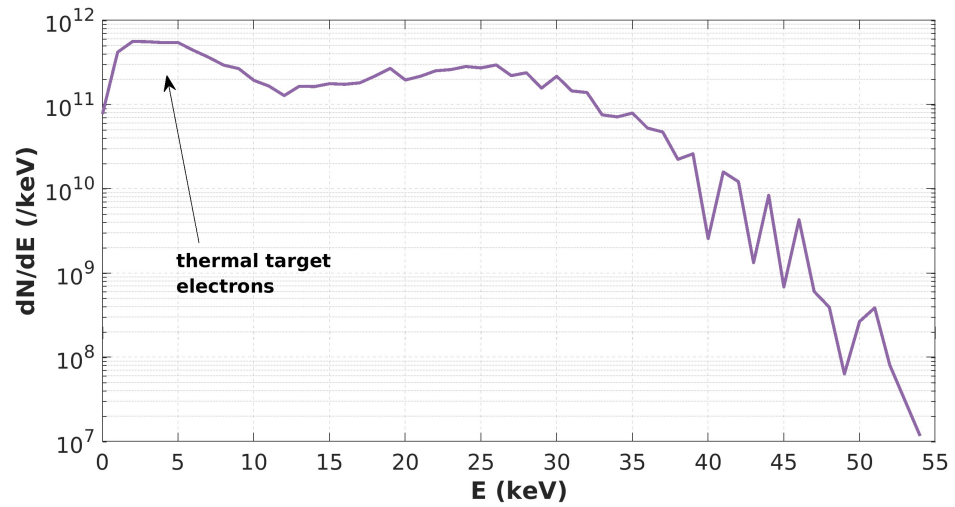
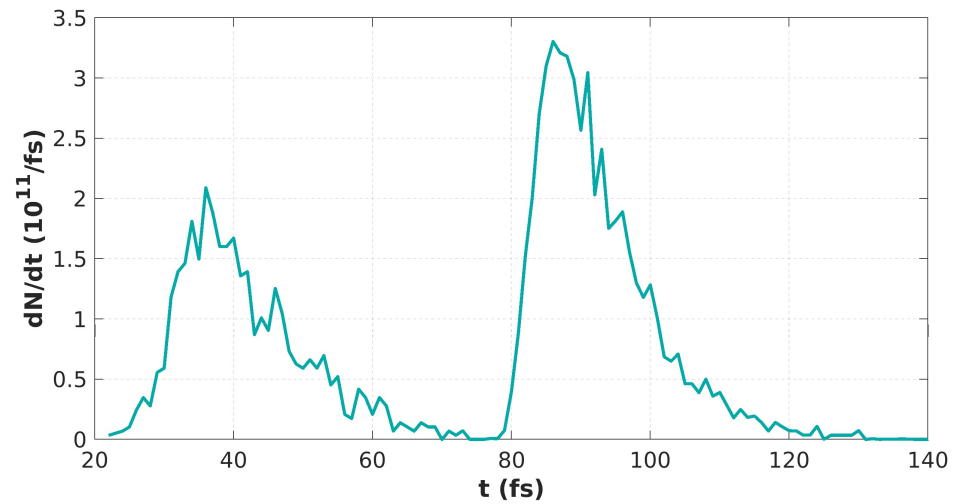


Figure 4.22: $x - p_x$ distribution plots of the electrons with electron number plotted as $\log_{10}(N)$. The dashed horizontal line indicates minimum particle momenta, and the solid vertical line indicates the position of the particle probe.

is shown in Figure 4.23(a). There is a peak in the spectra in the range 0 - 10 keV; it is likely this is a contribution from target pseudoparticles drifting from the rear surface ($T_{\text{targ}} = 1$ keV). The hot electrons reach a maximum energy of ~ 54 keV, which is rather low (by relativistic laser interaction standards). At these energies one would expect the electrons to



(a)



(b)

Figure 4.23: Properties of the exiting hot electrons from the pre-pulse interaction as measured by the rear vacuum probe plane. (a) shows the energy spectra of electrons passing the probe, and (b) shows the number of electrons passing the probe as a function of time.

be relatively collisional as they propagate through the solid target. Recall a target of $2.5 \mu\text{m}$ thickness is modelled here, and in the experiments the maximum target thickness was $25 \mu\text{m}$; the flux of these electrons leaving the rear target surface in the thicker targets in the experiment will be low.

To capture transition radiation in the rear vacuum, an output needs to be selected at a time when the hot electrons have exited the rear target surface. Temporal information on

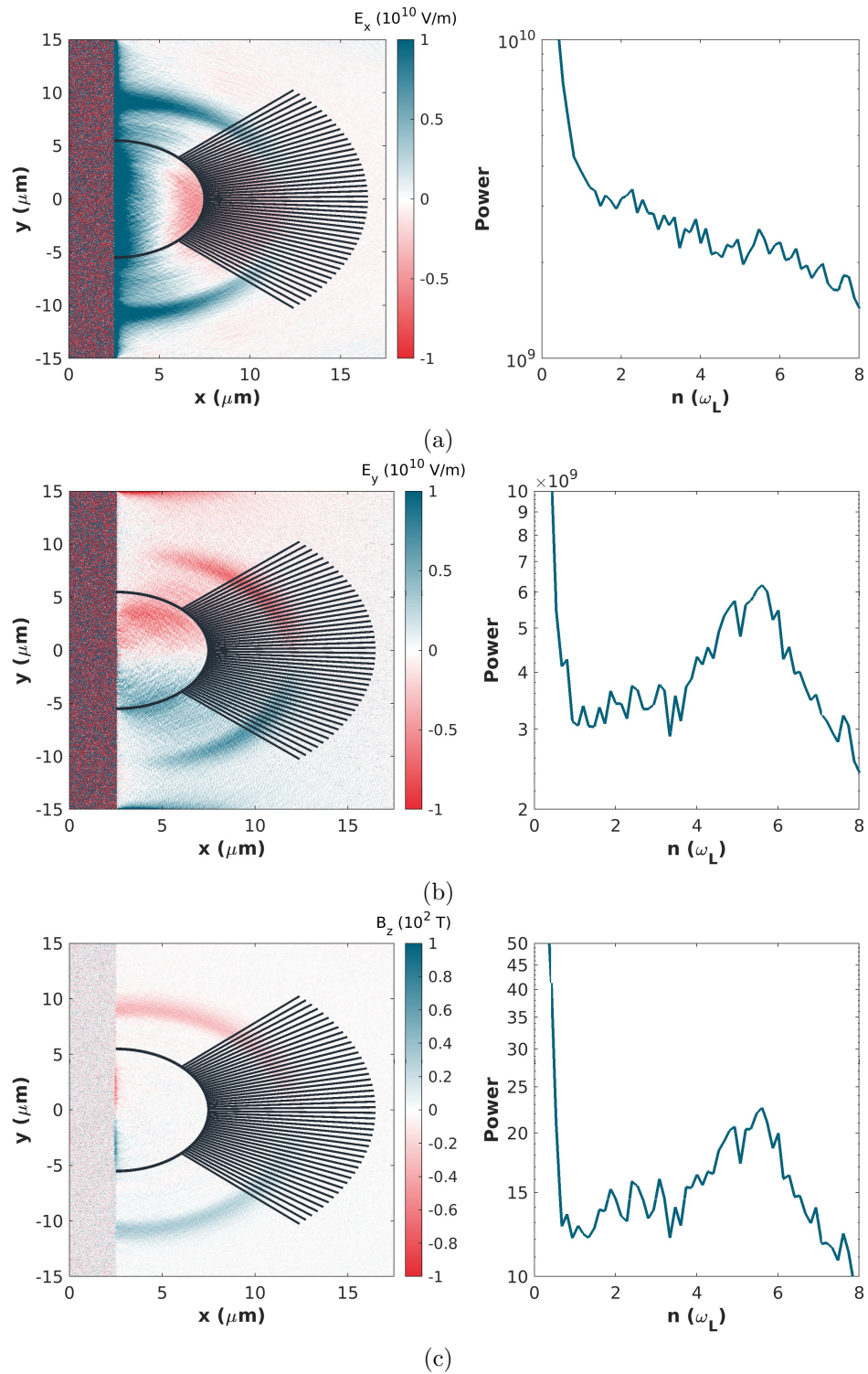


Figure 4.24: (a) E_x , (b) E_y and (c) B_z emission in the rear vacuum region at $t = 105$ fs. For each field component the raw emission is shown, alongside the integrated Fourier spectra from the radial lineouts.

the exiting hot electrons can be extracted from the probe plane in EPOCH⁵. A histogram is created with time bins of 1 fs precision, and the electron number taken as the sum of the pseudoparticle weightings within each bin. The resultant histogram is presented in Figure 4.23(b). Two distinct populations are detected, with one group measured at $t = 20 - 60$ fs and a second group measured at $t = 80 - 120$ fs. In the plots of the $x - p_x$ distribution function in Figure 4.22 the laser accelerated electrons, seen in blue in the $+ve p_x$ region, do not exit the target until $t = 60$ fs. Ergo, the early detected electrons are not thought to be from laser-accelerated hot electrons, and instead are from the population of thermal target electrons drifting from the rear target surface. The later electrons are the hot electrons, with the bulk detected in the rear vacuum by $t \approx 100$ fs.

The passage of the hot electrons through the target rear surface has the potential to induce transition radiation. To determine whether this is possible from the pre-pulse interaction, the E_x , E_y , and B_z field components plotted in the left-hand side of Figure 4.24 are used to search for any transition radiation emission. Analysis is carried out at $t = 105$ fs as at the next output the fields had exited the simulation domain. For each field component radial lineouts are drawn in the rear vacuum region in the angular range -45° to 45° in 2° intervals. A 1D fast Fourier transform is performed for each lineout to obtain the frequency spectra of the field component.

The plots in the right-hand side of Figure 4.24 show the Fourier spectra produced by integrating the spectras from each lineout. Each spectra shows a large contribution near zero frequency, which can be attributed to static fields. For example, a rear target electrostatic sheath field is generated in the direction normal to the target surface (x -direction), present in the E_x field component in 4.24(a). The measured spectras do not present any clear harmonic peaks, suggesting there is not significant production of CTR that can be resolved in the PIC simulation. For the lower order harmonics $\leq 4\omega_L$ there is a relatively flat spectra observed in the E_y and B_z field components. One would expect incoherent transition radiation to be uniform as a function of k_x , so this could be ITR. Above $\sim 4\omega_L$ there is an increase in the intensity of the emission spectra. For a target density $n_e = 20n_{crit}$ the plasma frequency is approximately $\omega_{pe} \sim 4.4\omega_L$. The emission above $4\omega_L$ could therefore originate from the

⁵As of EPOCH-v4.19.0

front surface of the target, or from the bulk target plasma rather than from the rear surface.

In summary, the EPOCH simulations here looked at the pre-pulse interaction from the perspective of the laser-accelerated electrons and the rear EM emission. The electrons are predicted to have relatively low energies of 10's keV, and are not generated in high numbers. Analysis of the EM emission did not yield any signs of appreciable CTR emission. In practice, for the thicker targets these electrons are likely to be stopped through collisions with the solid density material. It is proposed that it is highly unlikely the experimentally observed optical emission originates from transition radiation generated from the pre-pulse interaction, since the electron numbers and energies are low and any bunching will be severely impacted by collisions when propagating through the target, resulting in highly inefficient CTR generation.

4.6.2 Modelling the Effect of the Disrupted Rear Surface

The main effect of the pre-pulse encountered in this experiment was to disrupt the target structure, both at the front and rear surface. For the thinner targets the shock-wave launched by the pre-pulse interaction has been shown by the hydrodynamic simulations to have broken out at the time of main-pulse irradiation: however, CTR emission was clearly observed in the experiment. The purpose of this section is to decide whether the shock wave launched by the pre-pulse has disrupted the surface to the extent that the production of CTR is no longer possible, or whether a steep enough density gradient is retained to allow observable CTR emission.

To successfully detect and isolate coherent transition radiation in the simulation attention must be paid to other sources of harmonic generation in relativistic solid interactions. Harmonics can be generated at the target front surface via the relativistic oscillating mirror (ROM) [164], coherent wake emission (CWE) [165], and coherent synchrotron emission (CSE) [166] mechanisms. Experimentally, observation of these harmonics from the rear surface is not expected: the electron density and subsequent plasma frequency of the solid targets is high enough to limit the propagation to higher order harmonics. In PIC simulations of laser-solid interactions it is however typical to implement a reduced density in order to increase the grid resolution required to resolve the Debye length. A simulation target

electron density $n_e = 20 n_{crit}$, as employed for modelling the pre-pulse interactions, corresponds to a plasma frequency $\omega_{pe} \approx 4.4\omega_L$. To permit the identification of rear surface CTR emission $< 8\omega_L$ with limited contributions from other mechanisms the target electron density implemented in this simulation was therefore raised to $n_e = 77 n_{crit}$. In addition, a thin target is modelled in the PIC simulations and the laser field may be able to pass through the target thickness; the laser electric field was therefore set to be polarised in the z -direction, i.e. oscillating in and out of the plane of the simulation (x, y) , so any propagating laser fields will not impact the radiation spectra in the rear vacuum.

An EPOCH simulation is set up with a $2.5 \mu\text{m}$ thick Ti planar target of average ionisation $Z_{bar} = 10$ and an electron density $n_e = 77 n_{crit}$. The simulation domain is set to dimensions $(40 \times 80) \mu\text{m}$. Grid resolution is set to 4 nm , a compromise between resolution of the plasma skin depth, for resolving both the laser interaction volume and the CTR formation length in the plasma, and computational run-time. Each grid cell is populated with 16 Ti^{10+} pseudoparticles and 160 electron pseudoparticles. Laser intensity is set to $5.7 \times 10^{20} \text{ W/cm}^2$ with a FWHM pulse length of 27 fs , irradiating the target at normal incidence. At non-normal incidence, there can be injection of electron bunches due to ponderomotive acceleration along the laser propagation axis at $2\omega_L$, and vacuum heating can inject electrons into the target normal direction at ω_L . Choosing normal incidence forces the primary absorption mechanism to be ponderomotive acceleration, and ensures the electron bunches are injected down one axis only (target normal). This will improve the outlook of modelling CTR emission alongside a well-defined bunching frequency at the rear surface of the target. Field outputs are set to be averaged over 10 timesteps ($\sim 0.09 \text{ fs}$) to reduce noise. A probe plane to measure the fast electrons is placed at the rear target surface at $x = 2.5 \mu\text{m}$; a study by Rusby *et al.* [167] demonstrated that the sheath field formed at the rear surface for relativistic interactions is strong enough to significantly affect the energies of the exiting electrons, so the probe was placed before the sheath field. To reduce contributions from the bulk target electrons, a lower limit on the kinetic energy is imposed such that the particle's kinetic energy must exceed 100 keV to be recorded by the probe.

In order for coherent transition radiation to be produced there is a necessity for the fast electrons to be bunched temporally. To confirm this condition is satisfied the probe output

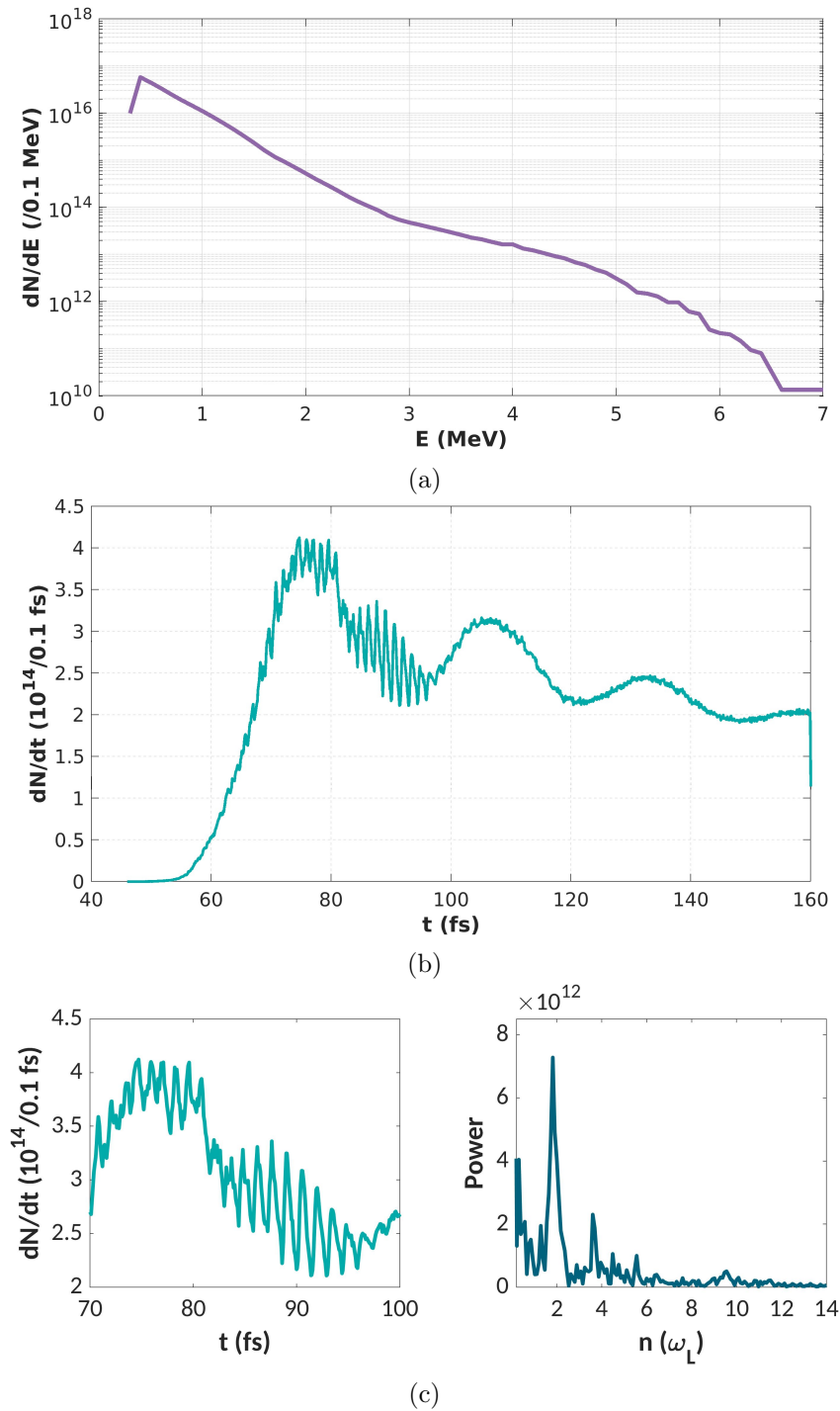


Figure 4.25: Properties of the exiting hot electrons from the main-pulse interaction with a planar target as measured by the probe plane. (a) is the energy spectra of electrons passing the probe; (b) is the number of electrons passing the probe as a function of time. The bunching structure around the period $t = 70 - 96$ fs is clearly seen in (c), with the corresponding calculated Fourier spectra of the peaks.

is analysed to extract temporal information on the fast electrons. The time at which a pseudoparticle passes the probe plane at the rear target surface is recorded and used to construct a histogram of electron number as a function of time, shown in Figure 4.25(b). In the period $t = 70 - 100$ fs there is clear evidence of electron bunch production. There are broader, less clearly bunched electrons detected at later times, which are ascribed to refluxing electrons. For this time period $t = 70 - 100$ fs a Fourier transform is carried out using the Matlab *Fast Fourier transform* algorithm. The frequencies are plotted in units of the laser frequency, ω_L , in 4.25. A clear peak is evident at $2\omega_L$. This is evidence of ponderomotive acceleration of electron bunches into the target and across the rear surface boundary, rendering CTR production possible at the rear of the target.

The E_y and B_z field components are processed to identify low-order harmonics. The output at 160 fs is analysed, by which time clear radiation fields have formed as shown in the left plots of Figures 4.26(a) and (b). Radial lineouts are taken in the angular range -45° to 45° in 2° intervals. For each lineout a 1D fast Fourier transform is performed, and a frequency spectra obtained. The spectra shown in the right plots of Figures 4.26(a) and (b) show the integrated spectra across all lineouts for the E_y and B_z fields respectively. These spectra show a clear peak at $2\omega_L$, and additional peaks at even harmonics $4\omega_L$ and $6\omega_L$.⁶ As described in Equation 2.40, the CTR spectrum will be maximised at harmonics of the bunching frequency. The probe output in Figure 4.25 clearly demonstrates electron bunches at $2\omega_L$ are propagating through the rear target surface. This suggest the even harmonics in the PIC spectra can be attributed to CTR emission at the rear surface. The rear field emission for the E_z field component, i.e. in the plane of laser polarisation, is also presented in Figure 4.26(c) as a useful exercise in demonstrating the importance of the choice of laser polarisation and target density. Odd harmonics are present either from the propagation of laser fields or the propagation of higher order harmonics from the front side of the target with $\omega > \omega_{pe}$. By setting the polarisation in the z -direction these emissions have been isolated from those in the $x - y$ plane where the CTR emission exists.

With a comparative case established, the next step is to model the impact of the shock breakout on the CTR emission. The density profile outputs from FLASH are used to deter-

⁶A peak is also apparent at $8\omega_L$; at this frequency we are approaching $\omega > \omega_{pe}$ and thus cannot be so assured this emission is from the rear target.

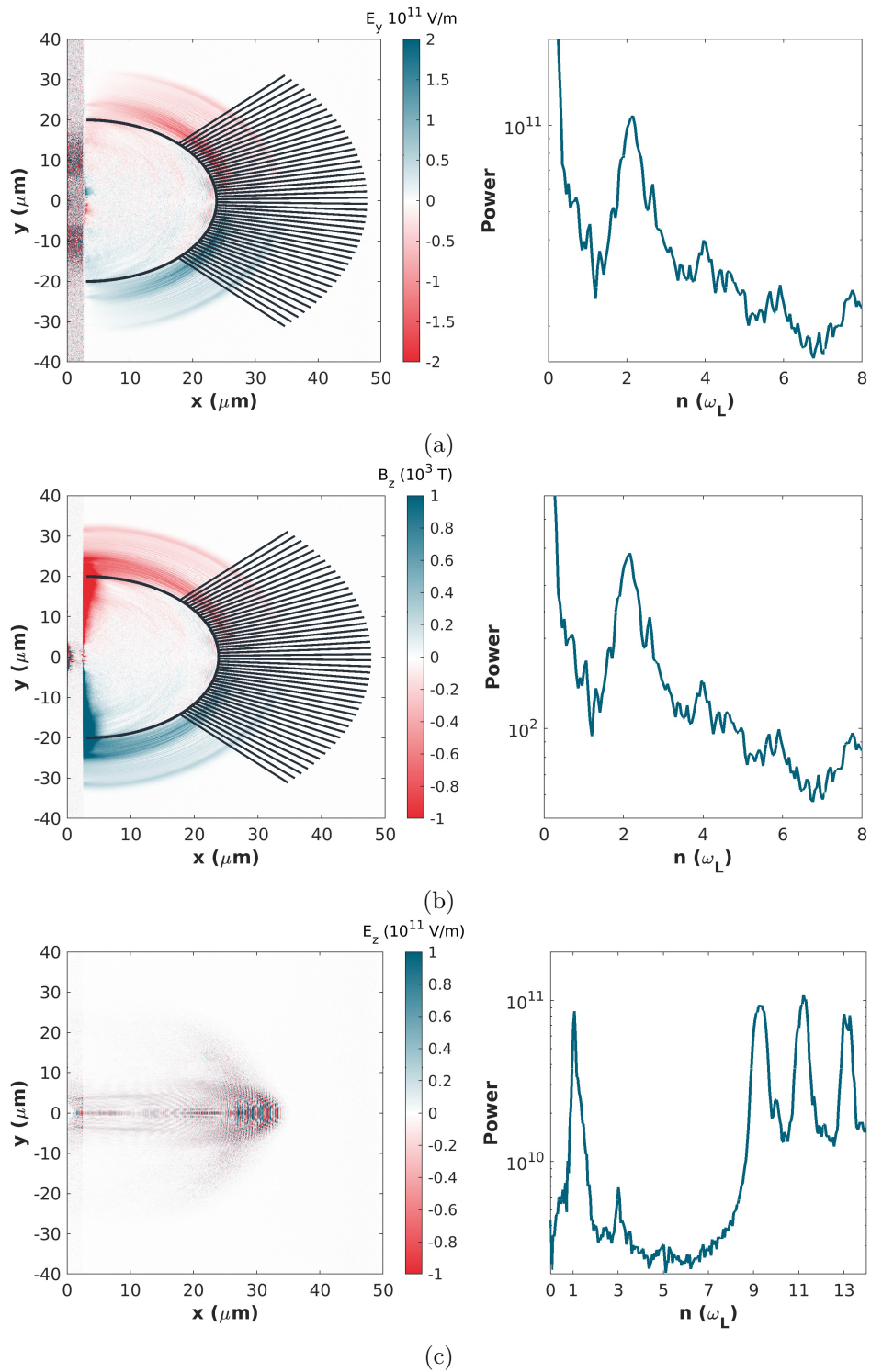


Figure 4.26: (a) E_y , (b) B_z and (c) E_z emission in the rear vacuum region at $t = 160$ fs. For each field component the raw emission is shown, alongside the integrated Fourier spectra from the radial lineouts. For the E_z component the radial lineouts are not shown to better see the emission.

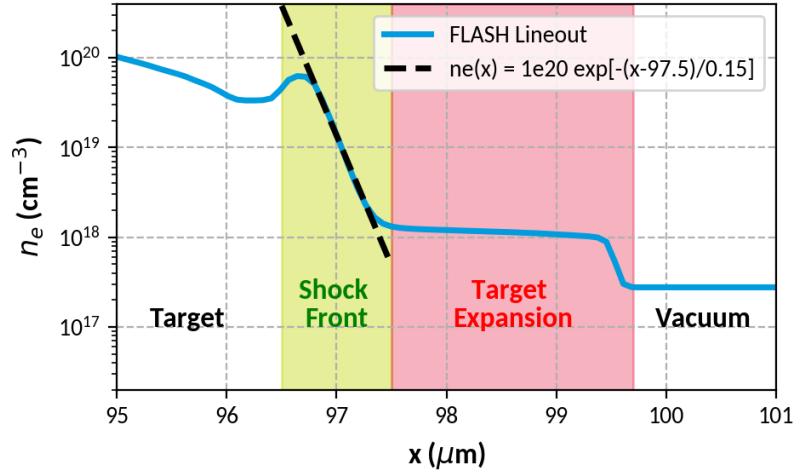


Figure 4.27: Density profile output by FLASH at 10.4 ns for the 12.5 μm planar target. The shock front is well fitted by an exponential function.

mine appropriate rear density profiles to model in EPOCH. Figure 4.27 shows the density profile around the rear target boundary for the expanded Ti 12.5 μm planar target at 10.4 ns. The shock front can be seen indicated in green, sitting atop a shelf-like density profile indicated in red. Whilst setting up FLASH it was noted that the target material would artificially “bleed” into the vacuum material, with the fix being that the rear target surface was set as a domain boundary and unset within ~ 0.1 ns of shock breakout. The target is able to expand slightly between the time of boundary un-setting and shock breakout; this shelf-like density region is therefore designated as a numerical artefact from the artificial target expansion. When estimating the rear profile this region, shown in Figure 4.27 with red shading, is disregarded. The density profile of the shock front, indicated in green shading, can then be represented with an exponential decaying profile of decay length 150 nm.

To replicate the shock-disrupted rear surface an exponentially decaying profile is placed at the rear surface. The decay length of the rear surface density profile is set to 150 nm following fitting to the results from FLASH. The resultant initial density profile of the target is shown in Figure 4.28(a). All other simulation settings are identical to those used for the unperturbed rear surface simulation. Analysis is performed on the E_y field emitted into the rear vacuum region at $t = 160$ fs, shown in Figure 4.28(b). The ellipsoidal region and rays used to take lineouts for Fourier analysis are consistent with that used for the analysis on the “ideal” target in Figure 4.26(a).

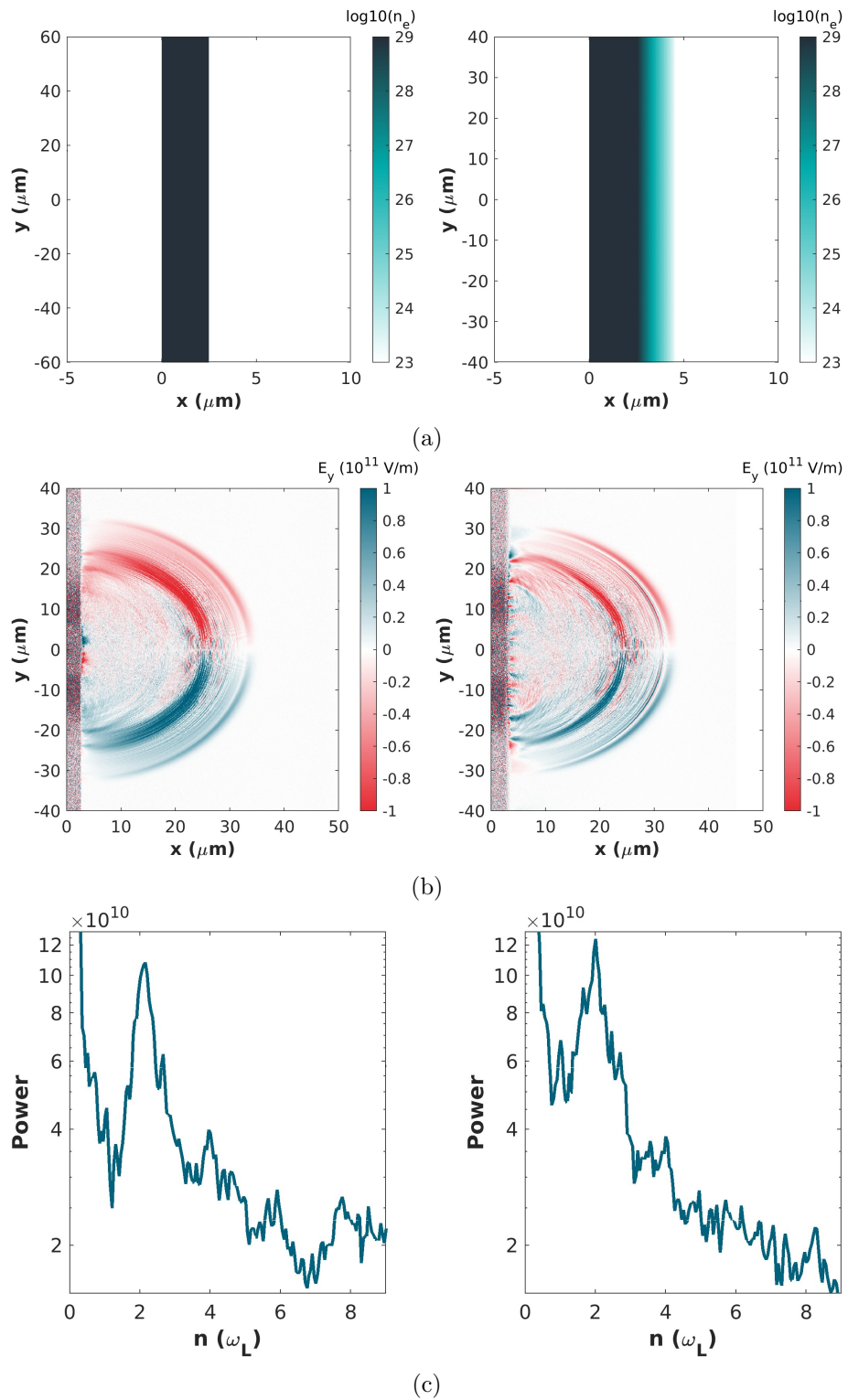


Figure 4.28: (a) Initial density profile of the targets with an unperturbed (left) and shock disrupted (right) rear target surface. (b) E_y fields at $t = 160$ fs, (c) shows the corresponding Fourier spectra of the E_y emission.

The Fourier spectra obtained from the simulation modelling shock-breakout at the rear surface is remarkably similar to the unperturbed case. Clear peaks at $2\omega_L$ and $4\omega_L$ are present and are a comparable power to that from the unperturbed rear surface. A peak at $6\omega_L$ was previously observable - the application of the exponential density profile on the rear surface has obscured the peak at this higher harmonic. Osipov *et al.* [159] used a theoretical approach to explore the effect of a blurred rear target boundary on the spectrum of transition radiation. A decrease in the amplitude of higher order harmonics was predicted when the scale of the inhomogeneity is greater than λ/π^2 , where λ is the radiation wavelength. It is therefore anticipated that lower order harmonics, with longer wavelengths, will be less sensitive to a given density profile disruption, in agreement with the results from PIC simulation shown here. The experimental results measured the optical emission, i.e. emission around $2\omega_L$. The outcome of these simulations suggests the shock front is steep enough to permit the efficient production of CTR in this optical region.

The aim of this particle-in-cell simulation study was to evaluate whether coherent optical transition radiation can be formed efficiently under conditions where the density profile at the target surface is disrupted. An “ideal” undisrupted planar target was modelled in EPOCH to demonstrate the modelling of CTR emission in a PIC code, and to find the expected spectra around the optical region. A spectra with peaks at even laser harmonics was found, in-line with the theory that states that the spectral emission of CTR will peak at harmonics of the electron bunching frequency $2\omega_L$. Upon disrupting the rear target surface it has been demonstrated here that the emission profile is remarkably similar around the optical regime, and $2\omega_L$ CTR emission is of a comparable power compared to an steep density profile at the rear surface. With respect to the experimental measurements of optical transition radiation, the outcome of the PIC simulations suggest the observed emission can originate from the *main pulse interaction*, even in the case of the thinner planar targets where the rear target surface has been disrupted.

4.6.3 Modelling the Effect of the Pre-Plasma

In the previous section the effect of the disrupted rear surface on the formation of CTR was explored for the main pulse interaction with a planar front surface. The output of the FLASH simulations demonstrated not only a deformed rear surface from shock breakout, but also

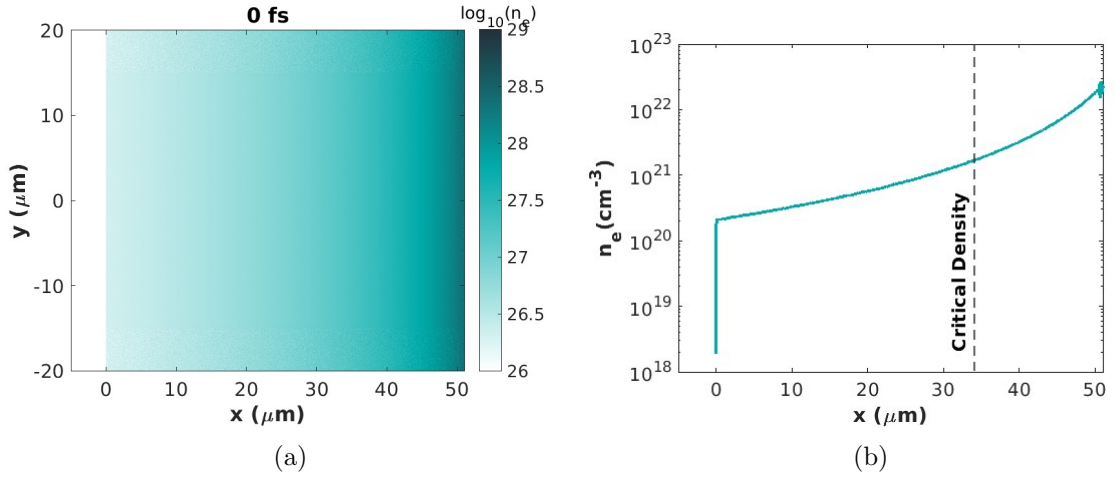


Figure 4.29: Initial density profile of the pre-plasma region implemented in EPOCH.

the formation of an extended, long scale length pre-plasma on the front surface. The presence of the pre-plasma will undoubtedly influence the laser coupling into the electrons in the plasma. The effect of the pre-plasma on the properties of the fast electrons is now considered.

2D simulations are carried out using EPOCH to evaluate the effect of the pre-plasma on the main laser interaction. The pre-plasma is defined using the output of the Ti 25 μm FLASH hydrodynamic simulation. The density profile along the target thickness is extracted at 10.4 ns, and a fit of the form $n_e = 5.41 \times 10^{24} \times (60 - x_{\mu\text{m}})^{-2.494} \text{ cm}^{-3}$ was found to closely reproduce the pre-plasma region (Figure 4.20). This density profile is used to populate a domain of size $51 \times 40 \mu\text{m}$ as displayed in Figure 4.29. Cell size is set to $20 \times 20 \text{ nm}$, and each cell is populated with 286 pseudoparticles to represent electrons and 13 pseudoparticles to represent Ti^{22+} ions. Initial target temperature was set to 1 keV. A focusing laser profile was established with a FWHM spot size of $4 \mu\text{m}$ at best focus and a maximum intensity of $5.7 \times 10^{20} \text{ W/cm}^2$, delivered under a Gaussian temporal profile of 27 fs FWHM. The position of best focus is set to $x = 30 \mu\text{m}$. To measure the energies of the fast electrons, a probe plane is again implemented, placed at $x = 50 \mu\text{m}$.

The target electron density is shown in Figure 4.30 to explore the response of the electrons in the plasma to the incoming laser. The formation of a plasma channel in the pre-plasma is clearly seen from electron displacement by the ponderomotive force of the laser. This channel is present throughout the underdense plasma. The $x - p_x$ distribution is plotted in Figure

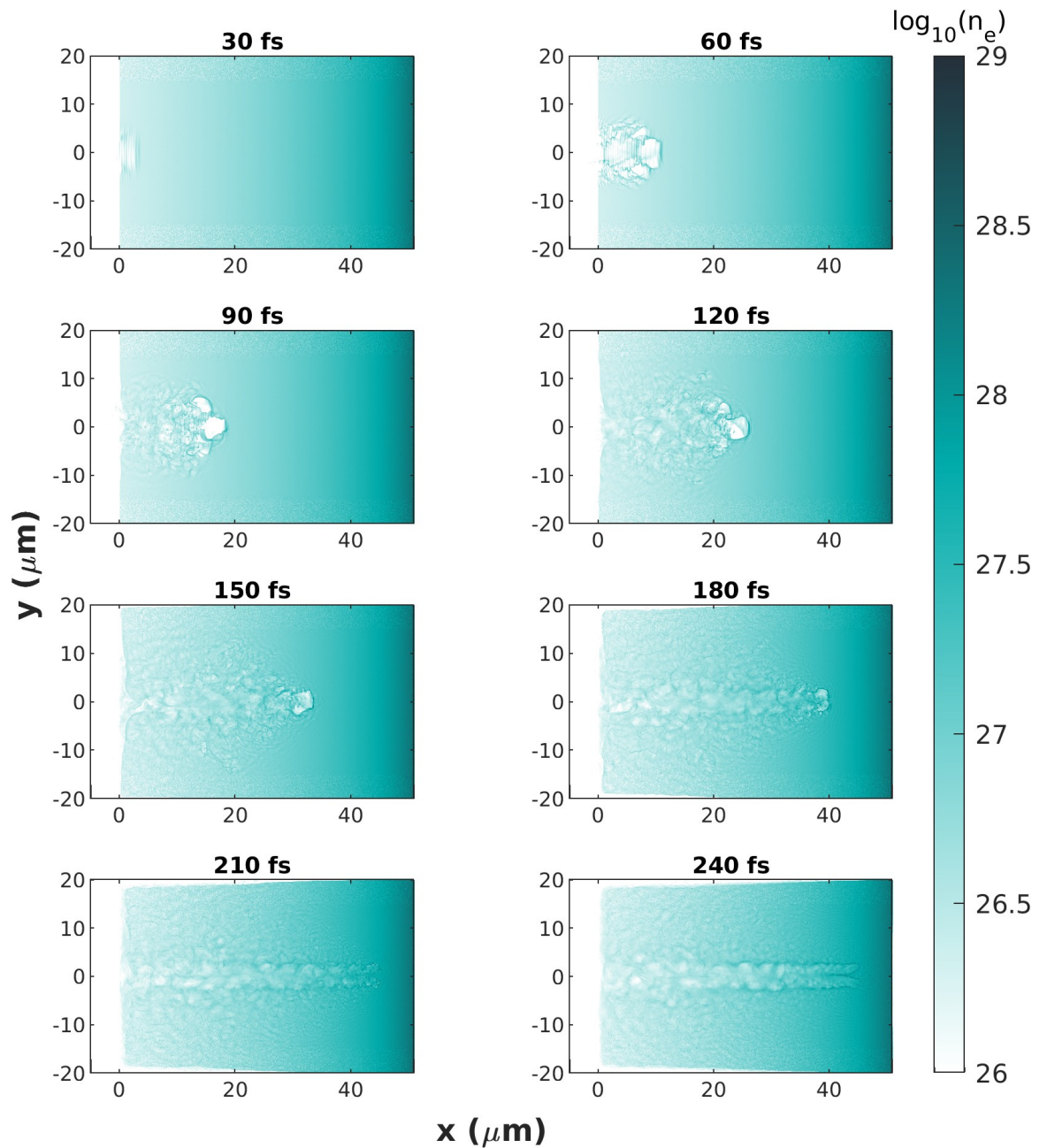


Figure 4.30: Electron number density within the pre-plasma from irradiation by the main laser pulse.

4.31 at various times to inspect the acceleration of these electrons into the bulk target. At each time the x -axis has been truncated around the region of accelerated electrons, allowing spatial features to be identified more clearly. At 30 fs the fast electrons present clear periodic structures, with 400 nm spacing between peaks. This is a signature of fast electron acceleration at a frequency $2\omega_L$. As the high energy electrons are accelerated into the target they

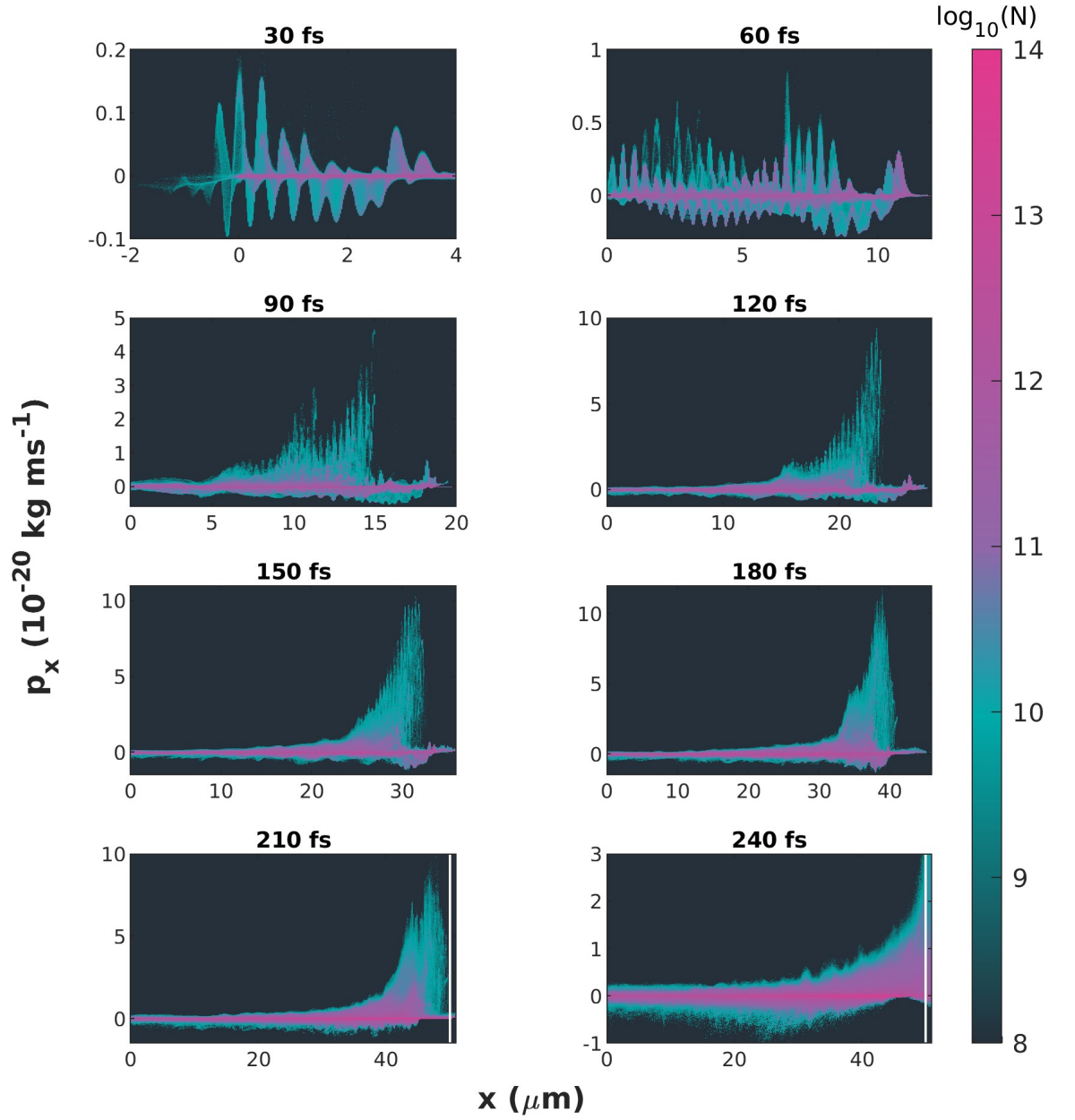


Figure 4.31: $x - p_x$ distribution of the electrons in the pre-plasma at increasing simulation time. The solid white line at $x = 50 \mu\text{m}$ indicates the probe plane position.

retain these distinct bunched structures; the presence of the pre-plasma therefore does not inhibit the formation of electron bunches, and CTR emission remains possible under these conditions.

The plots of the $x - p_x$ distribution function also reveal information on the acceleration mechanism at play during the laser interaction. The energies of the bunched electrons

increase as they are injected along the x -direction and remain under the influence of the laser fields, producing a “swept” profile of electrons in the distribution function evident at $t = 120$ and $t = 150$ fs. Results of PIC simulations by Shaw *et al.* [168] revealed a linear increase in electron energy as a function of propagation distance through an under-dense plasma, and are quite distinct from those generated by a LWFA mechanism. These electrons were deemed as having undergone direct laser acceleration, and also exhibited bunching structures as seen in the results here. The characteristic “swept” profile of electrons is also reported by Levy *et al.* [169]. Here, the argument is given that “the direct laser acceleration experienced by these electrons is evidenced by their $\lambda/2$ ($0.4 \mu\text{m}$) modulations and their maximum momentum ($p_{x,max}/m_e c \approx 180$), consistent with the prediction $p_{x,max}/m_e c = a_0^2/2$ for a single particle in an electromagnetic plane wave in vacuum.” For the PIC simulations performed here the corresponding maximum momenta predicted from this calculation is $p_{x,max} = 3.64 \times 10^{-20} \text{ kg m s}^{-1}$ for $a_0 = 16.32$. This value is actually exceeded in the $x - p_x$ distribution plots at $t = 120 - 210$ fs; this could be due to relativistic self-focusing in the under-critical density plasma increasing the local intensity and thus the predicted $p_{x,max}$ value. The plots in Figure 4.31 therefore demonstrate signatures of *direct laser acceleration* of the electrons.

The fast electron energy spectra is constructed from the time-integrated output of the probe plane at $x = 50 \mu\text{m}$ and plotted in Figure 4.32. The relativistic electrons are assumed to be described by a Maxwell-Jüttner energy distribution function

$$f_h(E, T_{hot}) = \frac{\gamma p}{A} \exp\left(-\frac{E}{k_B T_{hot}}\right), \quad (4.13)$$

where γ is the Lorentz factor, p is particle momenta, A is a normalisation constant, E is electron energy and T_{hot} is hot electron temperature [170]. A fit with an average hot electron temperature $T_{hot} = 17 \text{ MeV}$ is found to describe the population of higher energy electrons well, although does underestimate the number of lower energy electrons ($> 40 \text{ MeV}$). At the laser intensity of $5.7 \times 10^{20} \text{ W/cm}^2$ the ponderomotive scaling gives a hot electron temperature $T_{hot} = 5.34 \text{ MeV}$; as evident in Figure 4.32 this temperature is not appropriate for this population. An investigation by Peebles *et al.* [171] was subject to a longer scale length pre-plasma comparable to ours ($L_{pp} = 10 \mu\text{m}$), but with a longer pulse length of 180 fs for a

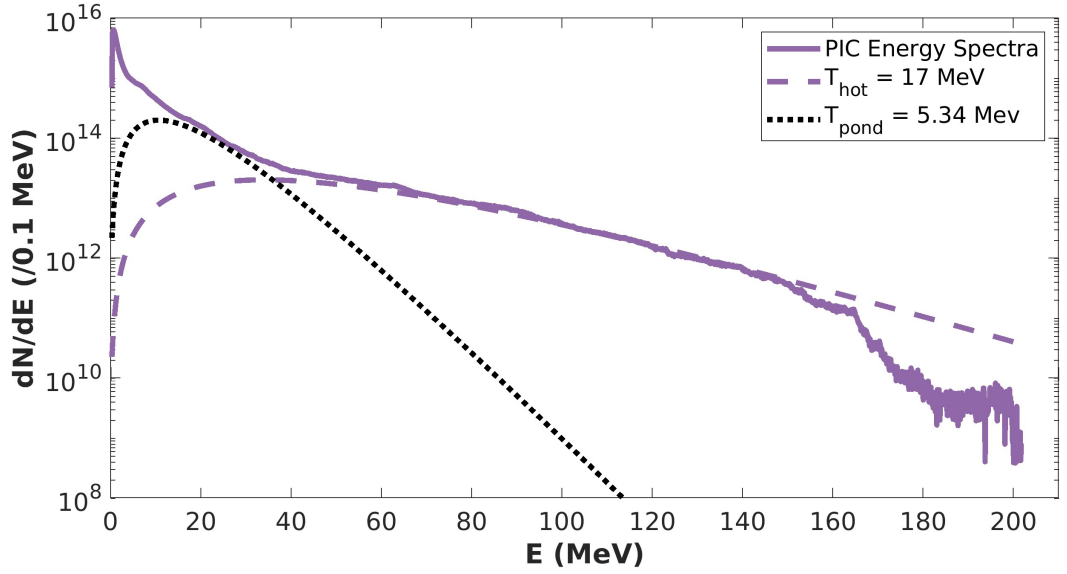


Figure 4.32: Energy spectra of the electrons passing the probe plane at $x = 50 \mu\text{m}$. Fits applied assume a Maxwell-Jüttner relativistic energy distribution.

main laser intensity $3 \times 10^{20} \text{ W/cm}^2$. Their simulations showed the fast electrons could be described by a temperature $T_{hot} = 8.6 \text{ MeV}$, closer to the ponderomotive scaling. However, it is worth noting these simulations were in 1D: in this regime the transverse motion of the electrons is important (e.g. Figure 4.30 shows the formation of a plasma channel) and must be captured for a full evaluation of the electron response to the laser fields.

The PIC simulations exhibit the generation of super-ponderomotive electrons in the under-critical pre-plasma, indicating a direct laser acceleration mechanism is possible for this interaction. With respect to the understanding of our experimental results, a drop of measured CTR intensity with target thickness is associated with a dephasing of the electron bunches as they traverse the target thickness. An electron population with a greater temperature is less susceptible to this de-phasing effect, with Figure 4.33 showing the variation of total harmonic energy emitted as a function of thickness for electrons with different temperatures. The electron bunches produced, as predicted by the PIC simulation, are less susceptible to dephasing as they propagate through the target, even for the expanded, pre-heated targets encountered in our experiment.

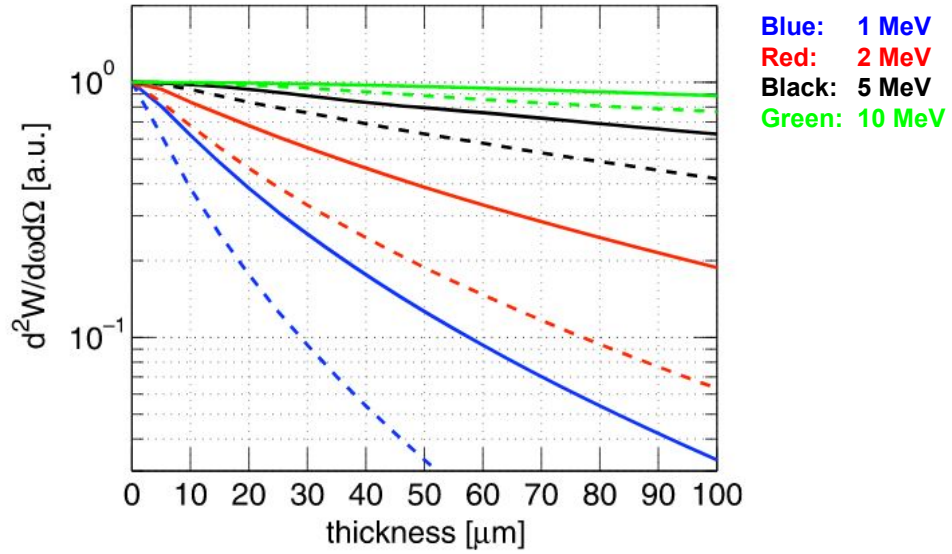


Figure 4.33: Energy of ω_L (solid) and $2\omega_L$ (dashed) CTR emission as a function of target thickness for electron populations of differing temperatures. Taken from [97].

4.7 Summary and Conclusions

Experimental measurements of optical transition radiation were taken from the rear surface of irradiated Ti planar targets. The intensity of the measured emission was found to decrease from a target thickness of $5 \mu\text{m}$ to $12.5 \mu\text{m}$, but was surprisingly found to increase slightly at a target thickness of $25 \mu\text{m}$. The FWHM size of the emission was found to decrease as a function of target thickness, again in contrast to results reported elsewhere in the literature. Results from the time-of-flight diagnostics provided an additional unexpected result, with an exceptional proton cut-off energy realised with the $25 \mu\text{m}$ target compared to the thinner targets. One would typically expect thinner targets to yield higher proton energies, as a larger electron current reaches the rear surface of thinner targets to generate the accelerating sheath field.

Taking into account the effect of the pre-pulse on the target structure has proved pivotal in interpreting our results. Hydrodynamic modelling using the code FLASH revealed the pre-pulse interaction resulted in the formation of a longer scale length pre-plasma at the front surface. In addition, a strong shock-wave was launched into the targets. For the 5 and $12.5 \mu\text{m}$ planar targets this shock-wave broke out at the rear surface before the main pulse

irradiation, disrupting the rear surface boundary. The expansion of these thinner targets meant the effective target thickness was much greater than the original target thickness. The 25 μm target however retained the solid, steep rear density gradient. Hybrid-PIC and PIC simulations have been used to deduce that the main effect of the pre-pulse was to disrupt the target structures; any contributions of thermal emission from fast electron transport or OTR production are proposed to be negligible.

For high intensity interactions we anticipate the production of *coherent* optical transition radiation, since the electrons will predominantly be accelerated in bunches, at harmonics related to the electron bunching frequency. The production of CTR is complex and has several dependencies on the fast electron and target properties. To fully understand the expected CTR production from our pre-pulse afflicted targets we will review the findings in order of the journey of the fast electrons: generation at the front surface, propagation through the heated targets, and exiting through the rear surface.

1. **Effect of the pre-plasma:** The interaction of the main laser pulse interacting with the pre-plasma profile predicted by FLASH, with a scale length $L_{pp} \sim 10 \mu\text{m}$ at the critical surface, was modelled and the generation of a population of high-energy, $T_{hot} \sim 17 \text{ MeV}$ bunched electrons was discovered. Part of the expected decrease of CTR production with target thickness is dephasing of the electrons bunches with distance: for higher temperature electrons this effect becomes less significant, even over distances $\sim 100 \mu\text{m}$. Thus, the pre-plasma is predicted to facilitate the injection of electrons which will be more resilient against dephasing as they propagate through the target.
2. **Effect of the target expansion:** The pre-plasma formation and shock-wave break-out results in an increase in the effective target thickness. Considering the distance between the critical density surface and the shock front/rear target surface, the new effective target thicknesses for the 5, 12.5 and 25 μm targets are ~ 140 , 60, and 50 μm respectively. This can explain the observed decrease in optical emission size observed with increasing (original) target thickness, since the fast electron beam is divergent and will increase in spot size as it propagates through the effective target thickness. In the previous point we propose the electron energies produced in the pre-plasma imply dephasing of the propagating electron bunches is not a major consideration. Collisions, however, can still play a role in ‘smearing’ the electron bunches. The thickness

of *overdense* material of the 12.5 μm target is larger than for the 5 μm target, so electrons have a longer distance over which to undergo collisions. The thickness of overdense material is slightly larger for the 25 μm target compared to a target of 12.5 μm thickness.

- 3. Effect of the shock breakout:** Whilst the thickness of overdense material is greatest for Ti 25 μm targets, they have the advantage of a rear surface unperturbed by shock breakout. PIC simulations showed that the *scale length* of the density perturbation at the rear surface of the thinner targets was sufficiently short to produce a similar power of CTR emission at $2\omega_L$. However, the electron density at the Ti 25 μm rear surface (solid density) is greater than for the thinner targets at the shock front (i.e. their target rear surface) by over 2 orders of magnitude. CTR production is most efficient for a greater change in dielectric constant. The dielectric constant in a plasma is dictated by the plasma frequency, which is related to the electron density; thus, the difference in dielectric constant at the target-vacuum interface will be significantly greater for Ti 25 μm compared to the thinner targets. This property can aid in explaining why the CTR emission at the rear surface was brighter for the Ti 25 μm targets.

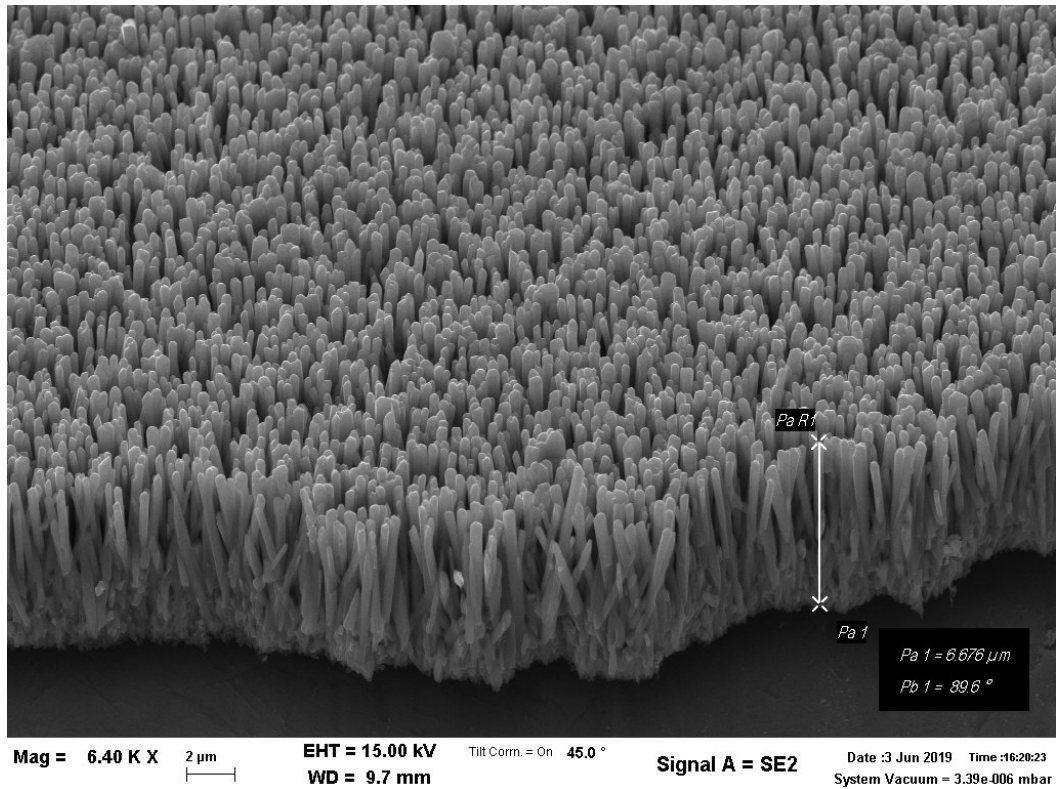
Chapter 5

Optical Transition Radiation from Preheated Nanowire Targets

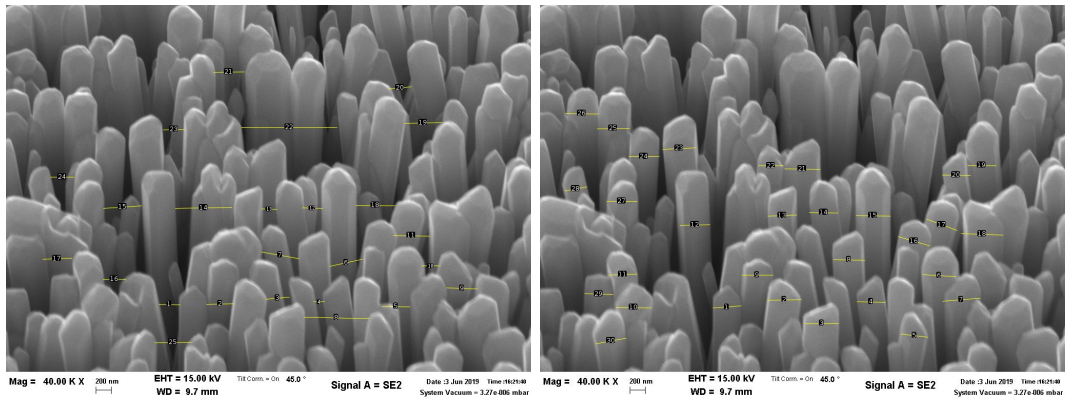
For this experiment the planar foils were not the main focus; the key aim was to explore the use of *nanowire coated targets*, with the shots on planar targets to be used as a “control” dataset to benchmark the performance of the nanowire targets against. In fact, the planar targets served an additional purpose in helping to identify the presence of the intense pre-pulse and to approximate the timing of shock breakout at the rear surface. In this Chapter experimental data obtained from the nanowire targets, the impact of the pre-pulse on the nanowire target structure, and results from particle-in-cell simulations performed in an effort to explain the experimental measurements are presented.

5.1 Experimental Setup

The nanostructured targets employed in this campaign consisted of a Ti planar foil substrate coated with a layer of nanowires directed normal to the target surface, as imaged in Figure 5.1(a). The nanowires were made of ZnO and grown via chemical bath deposition onto the 5 μm thick Ti substrate [172]. The diameter and spacing of these wires is found from SEM images taken at a higher magnification; *ImageJ* software is used to place lines across a selection of gaps between wires [Figure 5.1(b)] and the wires themselves [Figure 5.1(c)] and the lengths of each line measured. The 200 nm reference line at the bottom of the images is used to calculate the pixel-distance conversion, and is measured to be 32 pixels long (1 pixel \approx 6.25 nm). The average diameter of the wires is found to be 390 ± 50 nm, with the



(a)



(b)

(c)

Figure 5.1: (a) SEM image of the front surface of the nanowire coated targets. Lineouts selected to calculate (b) the average spacing and (c) average diameter of the wires.

average spacing being more variant at 400 ± 200 nm.

The experimental conditions are identical to that outlined in the previous chapter (see Section 4.1) as the shots on nanostructured targets were taken during the same day as for the planar targets, but will be summarised again here for convenience. The nanostructured

targets are irradiated on the nanowire side at an incidence angle of 15° by a laser with a pre-pulse of intensity 1.3×10^{17} W/cm² and a pulse length of 35 fs, followed 10.4 ns later by the main pulse of intensity 5.7×10^{20} W/cm² and a pulse length of 27 fs. The focal spot size is measured to be 4 μm FWHM for both pulses.

5.2 Rear Optical Emission

Rear surface optical emission (i.e. emission from the rear of the planar substrate) was imaged for each shot. All images were taken with an ND3 filter and a BG39 filter to remove fundamental laser light. The images obtained are displayed in Figure 5.2. Images of the rear emission captured for 5 and 12.5 μm thick Ti are shown alongside the nanostructured results for comparison; as the expectation is for the intensity of the emission to reduce with target thickness the comparison to planar targets is restricted to these two thicknesses closest to the total thickness of the nanostructured targets (11 μm).

The smaller, bright regions of emission are believed to be from coherent optical transition radiation emitted when the fast electrons exit the target. The total intensity of this imaged CTR emission is acquired for each shot on the nanostructured targets using the same method as for the planar targets. For each image a lineout with a length of 1000 pixels and thickness of 100 pixels is drawn in both the horizontal and vertical direction, centred on the region of bright emission. The intensity averaged over the thickness is measured, resulting in a 1000 pixel-long lineout across the emission region. Background correction is achieved through subtracting the average intensity of a equivalent lineout taken at a slight displacement such that the bright emission is not included within the background lineout. To find the total intensity a Gaussian fit is applied to the background-corrected lineout which well describes the emission spatial profile, and the total intensity calculated by integrating across the Gaussian fit. The found values of emission intensity for the nanowire coated targets are plotted alongside the intensities measured for 5 and 12.5 μm thick planar Ti targets in Figure 5.3(a). The error on the target thicknesses are given as $\pm 10\%$. To ensure the integrated intensity value is not influenced by saturated pixels or random scattered light far from the emission region, the total intensity is also measured by integrating across the Gaussian peak

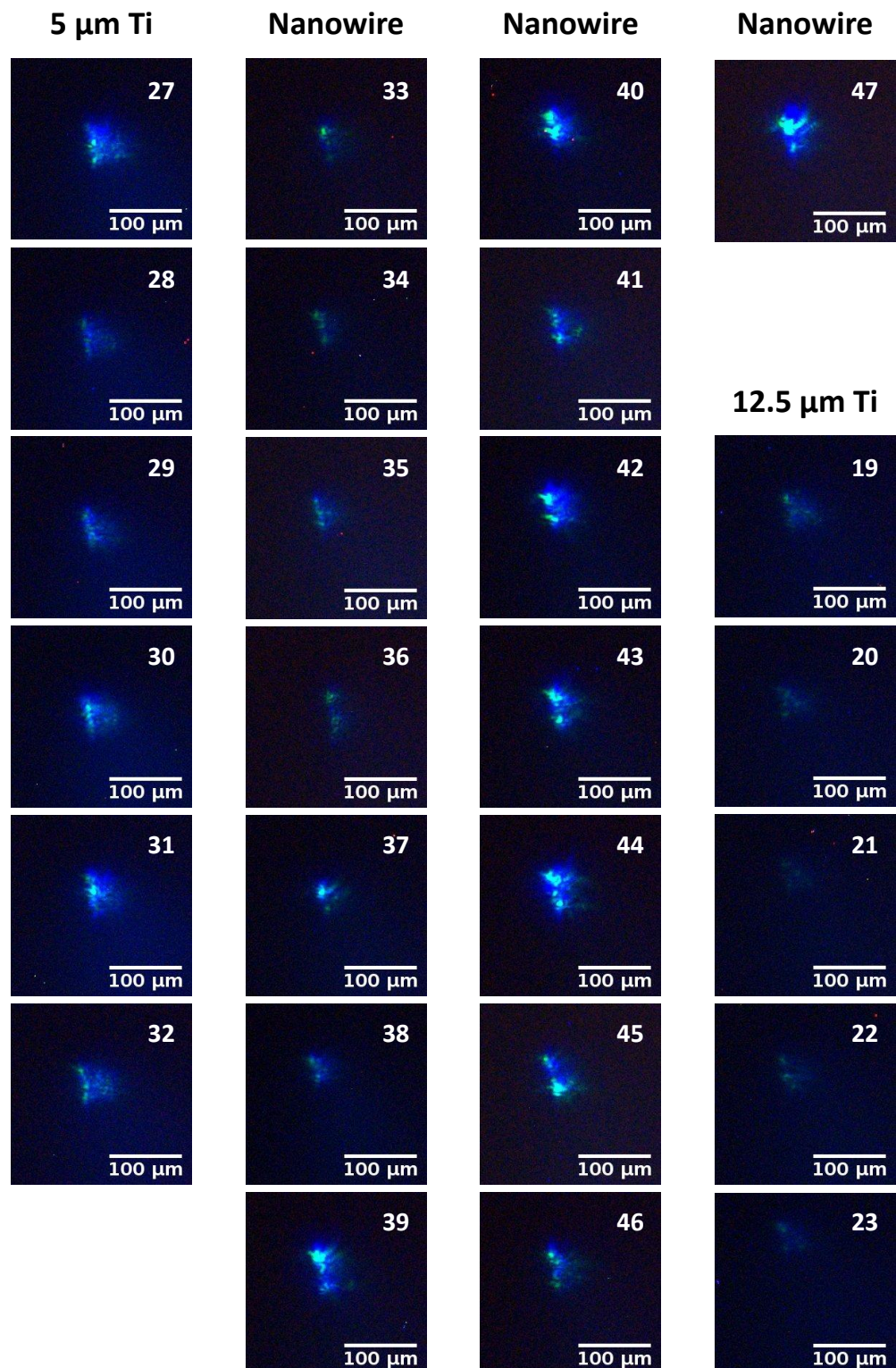


Figure 5.2: Images of optical rear emission from irradiated planar and nanowire coated targets, numbered by shot number.

only, using the 1% peak values as integration limits; these intensities are plotted in Figure 5.3(b).

The measured CTR emission intensities displayed in Figure 5.3 reveal a subset of shots on the nanowire coated targets that follow the expected trend of reduced intensity with target thickness, fitting well with the results from the planar targets. However, the results also show a number of shots on nanowire targets which yielded intensities that *exceeded* that measured from even the 5 μm thick planar targets. These well-performing shots were taken by rastering over the same nanowire target sample as the other shots (shooting on a “fresh” area each time), and laser conditions were said to be consistent shot-to-shot. At the beginning of the shots on nanowire targets, a scan of target position along the laser focal axis was carried out to determine the position of best focus. Figure 5.3(c) shows the CTR intensity is, on average, greatest at $z = 100 \mu\text{m}$, but there were also shots producing less intense optical emission at that position, so the enhanced performance cannot be attributed to target position along the focal axis alone.

From the investigations presented in Chapter 4 it is proposed that the observed CTR emission originates from the main pulse interaction with the targets, which have undergone substantial target expansion due to heating and shock wave propagation arising from the pre-pulse interaction. The nanowire targets were subject to the same intense pre-pulse and are susceptible to target deformation also. If we adhere to the argument that the CTR emission originates from the main pulse interaction, this raises the hypothesis that the nanowire targets can be a more efficient producer of transition radiation at the target rear surface *even after significant target disruption from the pre-pulse*. To understand how this is possible, hydrodynamic simulations are used to evaluate the effect of the pre-pulse on the nanowire target structure (Section 5.4) and particle-in-cell simulations to explore the following interaction of the main laser pulse (Section 5.6).

5.3 Proton Acceleration

Cut-off energies of accelerated protons were measured for the shots on nanowire targets, and the proton energies obtained from these shots are compared to the results from shots on

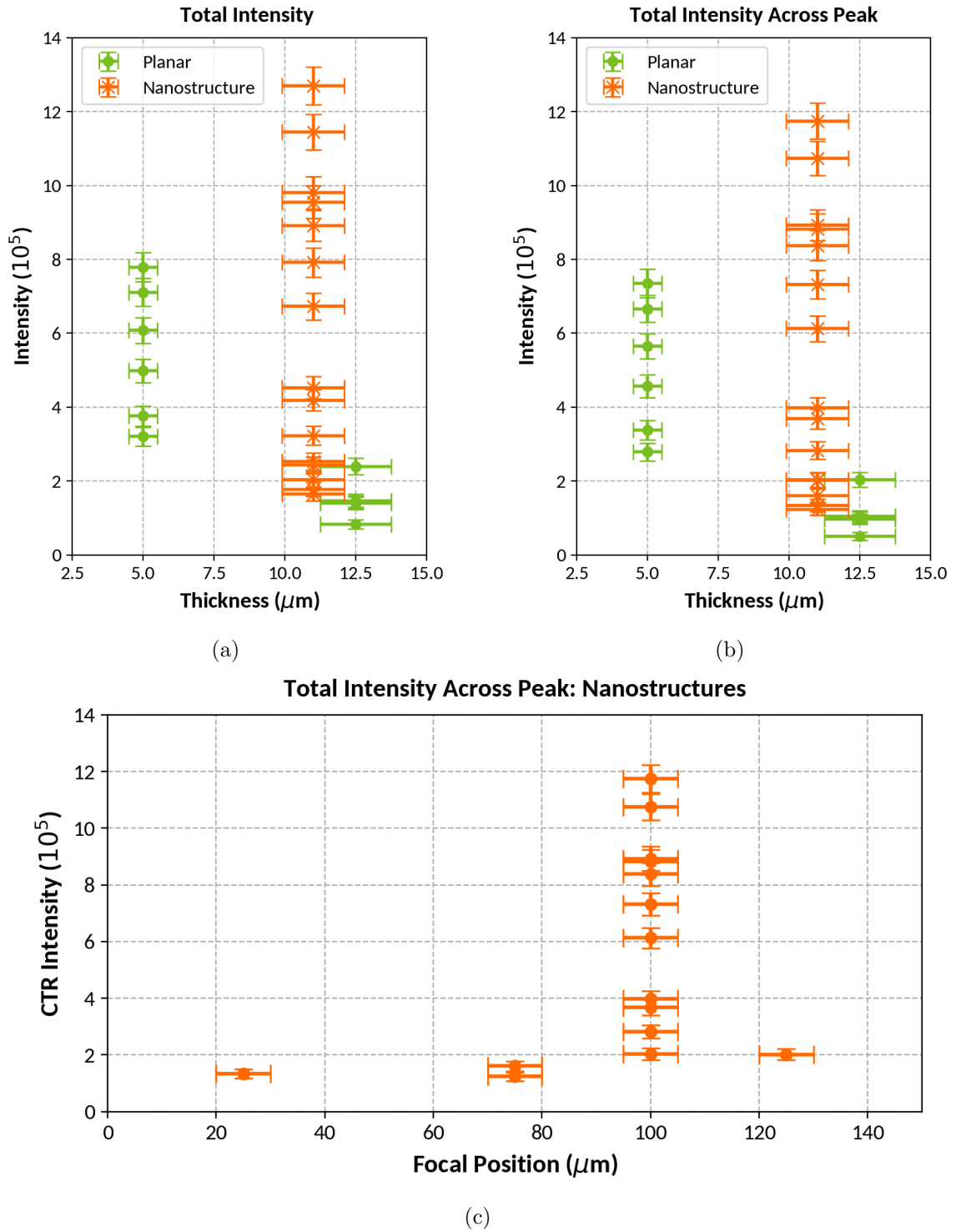


Figure 5.3: Intensity of CTR emission for planar and nanowire targets from (a) the total lineout and (b) the peak only as a function of target thickness. The variation of optical emission with target position along the focal axis from shots on the nanowire targets is shown in (c).

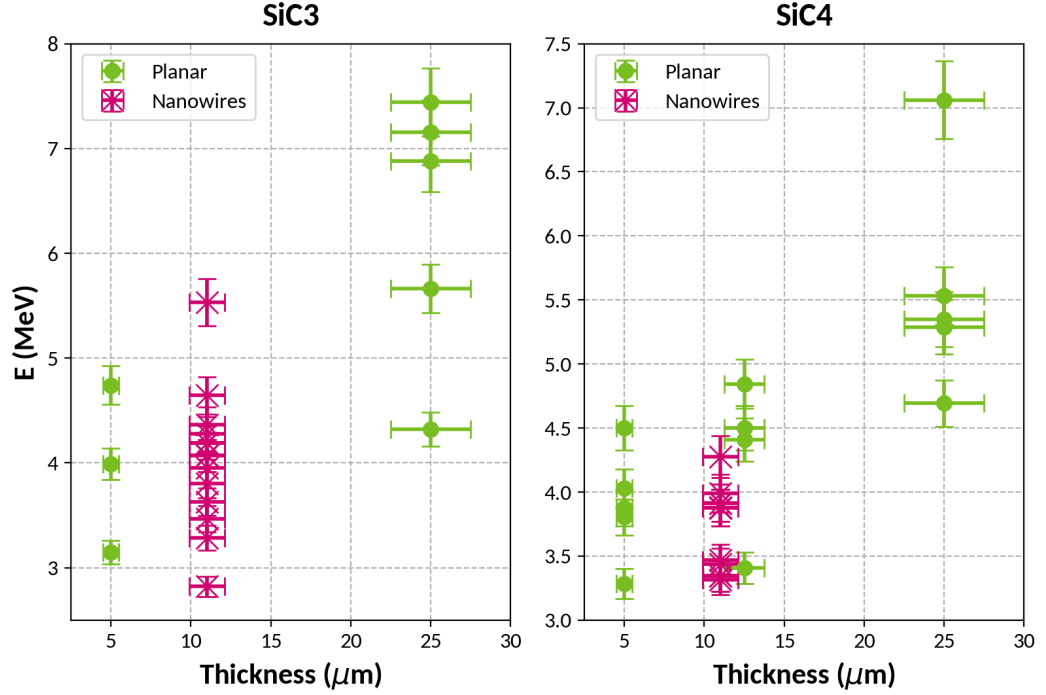


Figure 5.4: Proton cut-off energies measured from shots on the planar and nanowire targets as a function of total target thickness.

planar foil targets in Figure 5.4. The measured proton energies from the nanowire targets are comparable to those from irradiated $5 \mu\text{m}$ thick targets, and lower than those from $12.5 \mu\text{m}$ thick targets. Previous work with structured targets reports similar observations of no improvement in cut-off energy. In a study by Sedov *et al.* [173], irradiated microstructured targets produced greater accelerated particle numbers than irradiated flat targets, yet the cut-off proton energy remained equivalent. Bailly-Grandvaux *et al.* [174] found that whilst the presence of front structures increased the accelerated proton yield by a factor 5, the cut-off energy did not see a similar enhancement and was in fact similar to the cut-off energy from shots on flat targets. Complementary PIC simulations inferred this was due to shuttering from pre-plasma filling the gaps between the structures, limiting the laser propagation to the tips of the wires and increasing the distance between the fast electron generation position and the rear target surface. Of course, these studies were not subject to the same pre-pulse as encountered in our experiment, and so we cannot compare these results directly. Overall, it appears the presence of the nanowire structures has not impacted the measured proton cut-off energies.

5.4 Hydrodynamic Simulations of Pre-Pulse with Wires

Previous work investigating nanostructured targets for use in intense laser interactions has emphasised the importance of considering the effect of pre-pulse. For example, the study by Cristoforetti *et al.* [54] inferred ASE-produced pre-plasma was formed at a lower intensity threshold compared to planar targets due to a higher absorptivity. The small spacing between the nanostructures means the gaps will quickly fill with pre-plasma, and any structured target features will become obsolete. Whilst ASE-produced pre-plasmas from nanostructured targets have been previously considered, the hydrodynamic behaviour of nanowire targets irradiated by a fs-scale pulse has not been addressed. It would be reasonable to assume the structures have been affected by our experimental pre-pulse, but we cannot say what the precise outcome would be. It is possible only a small portion of the wires had been ablated, with the gaps partially filled with a low density pre-plasma and a structured density profile remaining; equally, the wires may have been completely destroyed and a homogeneous plasma formed, reducing the main pulse interaction to an intense interaction with a longer scale length plasma on the front surface rather than with a structured target.

To evaluate the significance of the pre-pulse interaction on the integrity of the nanostructures, simulations are carried out using the 2D hydrodynamic code FLASH. A simulation domain of size $50 \times 125 \mu\text{m}$ is set up in a 2D cylindrical geometry, comprised of 2×5 blocks. Each block consists of 10×10 cells with a maximum refinement level of 6 during the simulation. To observe a reasonable laser absorption it was required to model the nanowires with an exponentially decaying front surface. The wires are represented as $6 \mu\text{m}$ long central spikes of density spaced 800 nm apart. The central, peak density $\rho = 12.3 \times \text{solid Ti density}$, with the central spikes surrounded by an exponentially decaying density profile with a scale length of 15 nm . Figure 5.5 shows the mass density of the resulting wire structures. The increased central density is used so the total mass within the wire is equivalent to the mass of a full-sized wire at solid density, and the short scale length of the decaying region ensures gaps of approximately 400 nm size are retained between the wires. A planar Ti slab of thickness $5 \mu\text{m}$ at solid density is placed behind the wires to represent the solid substrate.

It is noted here that the use of a 2D cylindrical geometry means wires are not modelled in this scenario, and instead the target consists of concentric ringed structures at the front

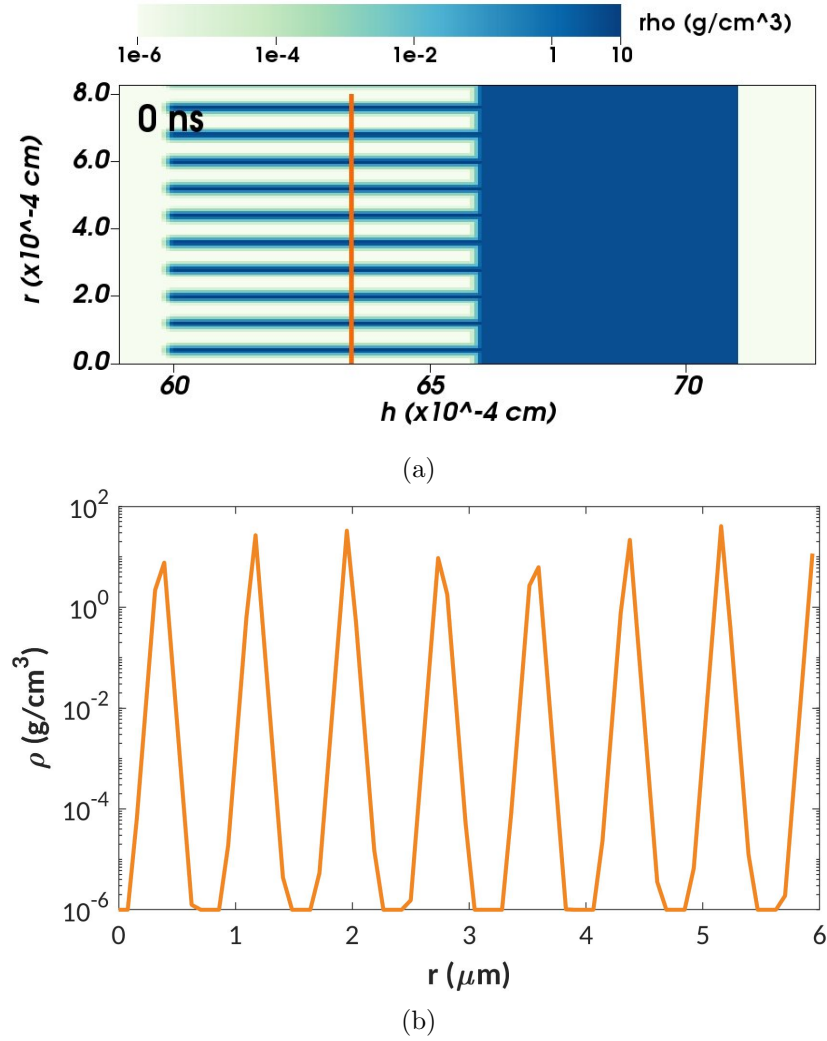


Figure 5.5: (a) Mass density of the nanowire target and (b) lineout taken across the wires at $h = 63 \mu\text{m}$, showing the density variation of the wires along r .

surface. The intention of these simulations is to assess the integrity of the nanostructures and whether the structures survive after irradiation by the pre-pulse. To answer this the filling of the gaps between the wires by the expanding heated plasma and the plasma expansion away from the target need to be resolved. Both of these effects can be captured through the use of these concentric ring structures, and will equally apply for the nanowires.

As discussed previously, FLASH has been shown to not be the most suitable for modelling the absorption of 10's fs pulses (see Section 4.4.1), and when using a power profile equivalent to the power of the experimental pre-pulse the energy absorbed is incredibly low. In a similar fashion to the simulations modelling the planar targets, a parameter scan is carried out to

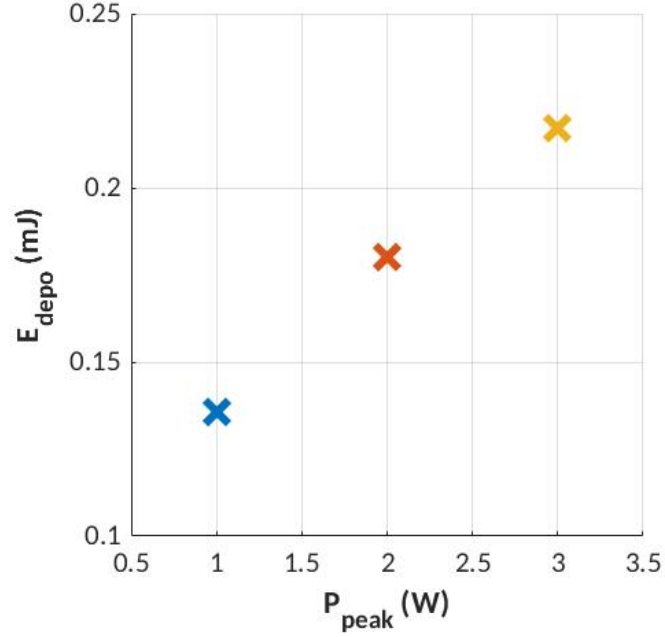


Figure 5.6: Energy deposited into nanowire target as a function of peak laser power in FLASH.

determine an appropriate power profile to deliver a reasonable amount of laser energy to the nanowires. A power profile that results in ~ 0.23 mJ of energy deposited is aimed for, which is equivalent to that used for the planar targets - this will provide a “best-case” scenario for assessing the extent of deformation to the wire targets. It is appreciated that prior studies have demonstrated an improved energy absorption for nanowires; for example an increased in absorption by a factor ~ 2 was reported by Eftekhari-Zadeh *et al.* [55]. However, this was at a vastly greater laser intensity and it is not possible to predict the expected improvement in absorption for the experimental conditions here.

The laser is set with a Gaussian focal spot of e-folding length $r_e = 2.41 \mu\text{m}$, irradiating the target at an angle of 15° and focused onto the tips of the nanowires at $h = 60 \mu\text{m}$. The laser power profile has a Gaussian temporal profile with a FWHM of 35 fs. To determine a suitable peak power to implement, simulations are carried out with different peak powers. FLASH simulations are run up to 100 fs and the total energy deposited is obtained for each power profile. The resulting power scan is displayed in Figure 5.6. A laser profile with a peak power 3×10^{12} W yields a total energy deposition of ~ 0.22 mJ, close to the energy deposition for the planar targets. This peak power is substantially lower than that

implemented for the planar target ($P_{peakPlanar} = 1 \times 10^{15}$ W), with the total amount of energy deposited seen to increase much more rapidly with peak laser power than for the planar target [Figure 4.17(b)]. To explain this drastic difference, the energy deposition per cell was plotted at the time of peak laser irradiation; see Figure 5.7. The rays representing the laser enter the vacuum gaps between the wire. Since they are incident at an angle, the rays interact with the side of a wire and are able to deposit energy into the corresponding cell. For an individual ray-target cell interaction the fraction of energy deposited is expected to be similar to that for the planar target, since the target front surface layer is established in an identical way. However, for the nanowire case the ray then reflects down the gap, interacting with the neighbouring wire surface and depositing additional energy. Each ray is able to ricochet down the wire gaps to carry out many energy deposition events, resulting in an enhanced energy deposition compared to the planar targets. In reality the interaction of a laser with nanowires is more complex; a laser delivers EM waves of radiation that are able to interfere with each other and are subject to additional effect such as a diffraction. The extreme increase in absorption is attributed to the ray approach of modelling the laser, where in reality the wave nature of the laser will have a significant effect. The hydrodynamic simulations are not being carried out as a means to meticulously reproduce the laser absorption, and so the use of a lower power to compensate for this will be sufficient. The following full simulations implement the power profile with a peak power $P_{peak} = 3 \times 10^{12}$ W.

A full run over 10.4 ns to model the hydrodynamic expansion up to the main pulse irradiation time can now be carried out. When running over longer timescales the target material is subject to artificial expansion into the vacuum “material”. This expansion can be prevented by setting the rear target cells as boundary cells, thereby fixing their positions. However, this also prevents shock wave propagation through the target rear surface, and as such the boundary cell assignment needs to be relaxed just before the shock wave reaches the rear surface. A preliminary simulation showed shock breakout from the nanowire targets has occurred by 1 ns after laser irradiation, so the back cells are set to be released at 0.9 ns.

The subsequent density profiles at 0 ns and 10.4 ns of the nanowires after pre-pulse irradiation are shown in Figure 5.8. Shock propagation and thermal expansion around the target irradiation region has resulted in the loss of wire structures up to $r \sim 25 \mu\text{m}$. The wire gaps

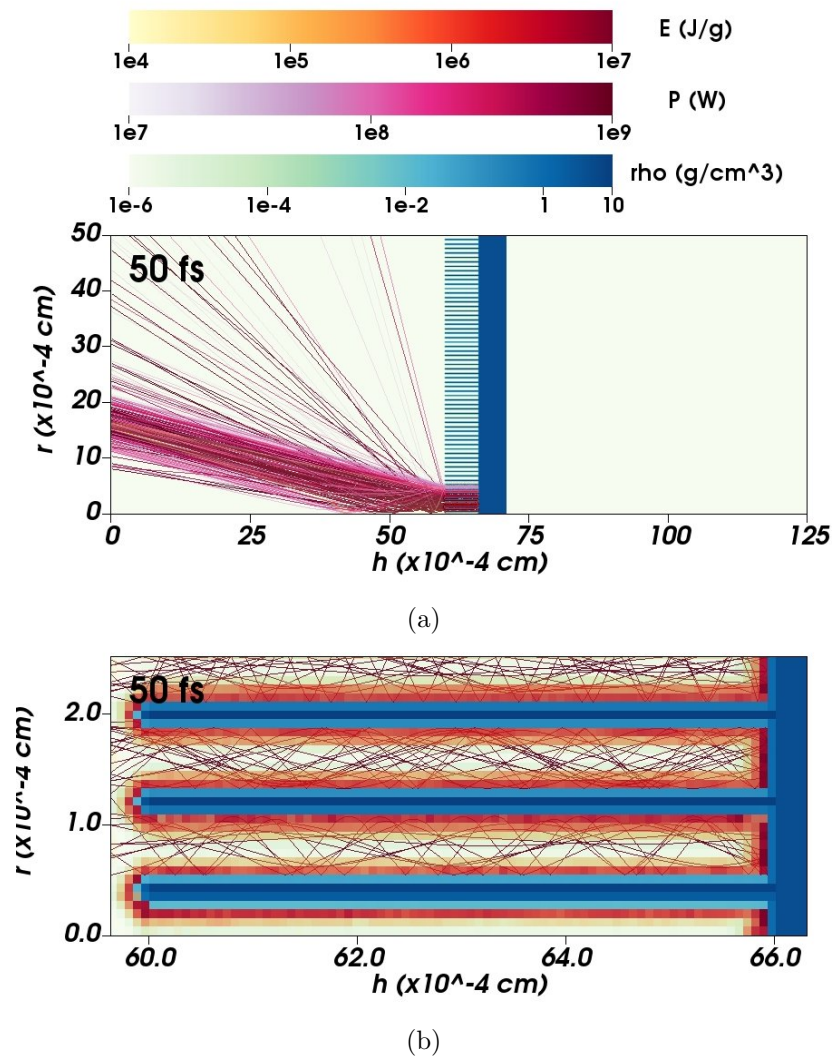


Figure 5.7: (a) Nanostructured target and laser rays at 50 fs. Plot is reproduced in (b) and zoomed in around the interaction region.

have been filled by target material and the density profile has become essentially uniform. Beyond $r = 25 \mu\text{m}$ indistinct wires do remain visible; the extensive blurring of these wires is caused by the aforementioned artificial expansion, and without this effect there would likely be wires remaining. It is possible the pre-plasma extending out into the front vacuum will have filled the residual vacuum gaps in any case, so we cannot comment further on the integrity of these wires further from the laser interaction site.

The output of the hydrodynamic simulations show that the main pulse will interact with an extended pre-plasma. To characterise the pre-plasma region, a density lineout is taken

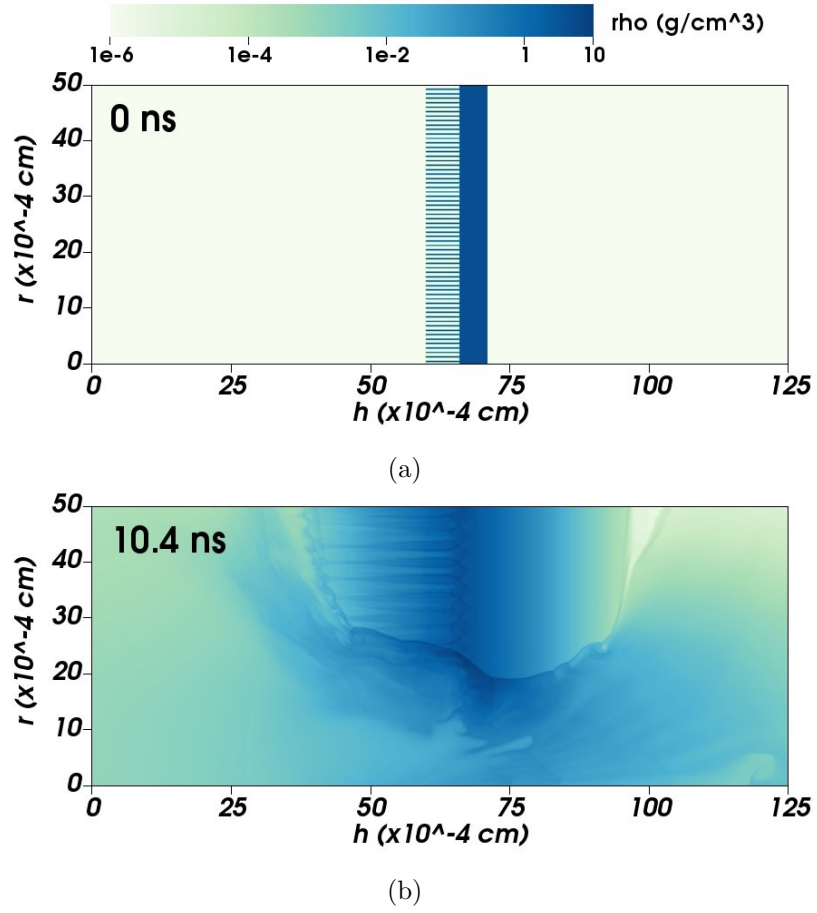


Figure 5.8: Mass density of the nanowires at (a) 0 ns and (b) 10.4 ns after pre-pulse irradiation.

at constant $r = 3 \mu\text{m}$ along $h = 0 - 60 \mu\text{m}$. A fit is applied of the form $n_e = A(B - h)^{-C}$ following the function described in Ref. [158], and the found fit is displayed in Figure 5.9. The exact scale length varies with distance due to the nature of the function used and is given by

$$L_{pp}(h) = \frac{n}{dn/dh} = \frac{1}{1.755}(60 - h_{\mu\text{m}}) \mu\text{m}. \quad (5.1)$$

Use of Equation 5.1 yields a scale length of the pre-plasma at the critical density surface ($h = 37.5 \mu\text{m}$) of $12.8 \mu\text{m}$. Similar fitting to the results for the irradiated planar targets returned a scale length at the respective critical density surface of $10.1 \mu\text{m}$. The results of the hydrodynamic simulations therefore indicate a *longer scale length pre-plasma* is obtained from the pre-pulse irradiated nanowire targets compared to the planar targets.

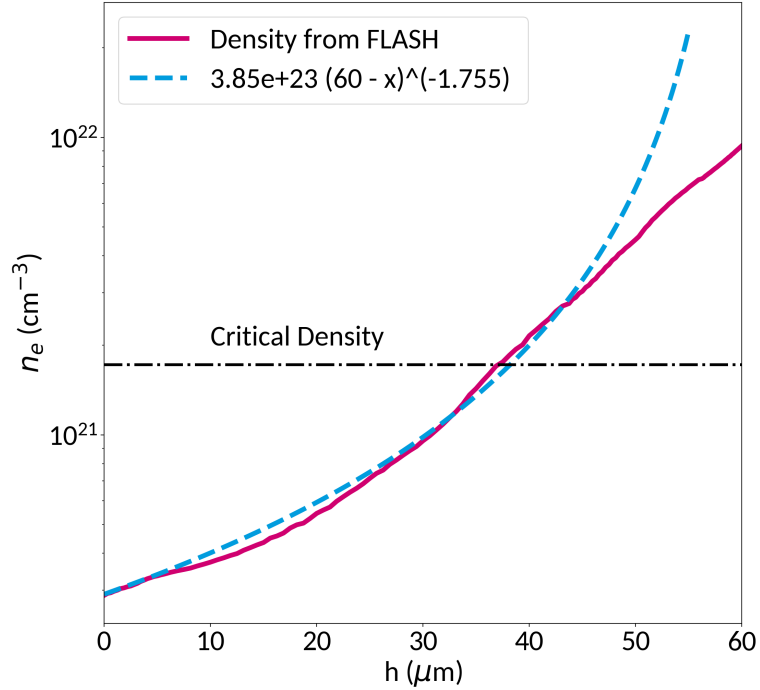


Figure 5.9: Fitting to the pre-plasma produced from pre-pulse irradiation of the nanowire targets.

5.5 PIC Modelling of Pre-Pulse Interaction with Nanowires

Whilst the main laser pulse is interacting with a more homogeneous, longer scale length pre-plasma, the pre-pulse is able to interact with the wire structures. The assumption for the hydrodynamic simulations was that an equivalent amount of pre-pulse energy was deposited into the wires compared to the planar targets. Previous work by Ovchinnikov *et al.* [175] indirectly inferred enhanced coupling into nanorod targets at a similar intensity ($\sim 10^{17}$ W/cm²) through an observed increase in K_α emission. The interaction of the fs pre-pulse with the nanowires is modelled here to investigate the pre-pulse interaction with the nanowires in contrast to the pre-pulse interaction with a planar target, and identify if a difference in absorption is to be expected for our experimental conditions.

The interaction of the pre-pulse with the nanowire coated targets is modelled in 2D EPOCH. In the experimental campaign the nanostructures were composed of wires with an average diameter of 400 nm, with 400 nm spacing between wires. As established when modelling the pre-pulse interaction with planar targets, to permit absorption of the fs, 10^{17} W/cm² laser pulse into solid target it was found necessary to add a short scale length pre-

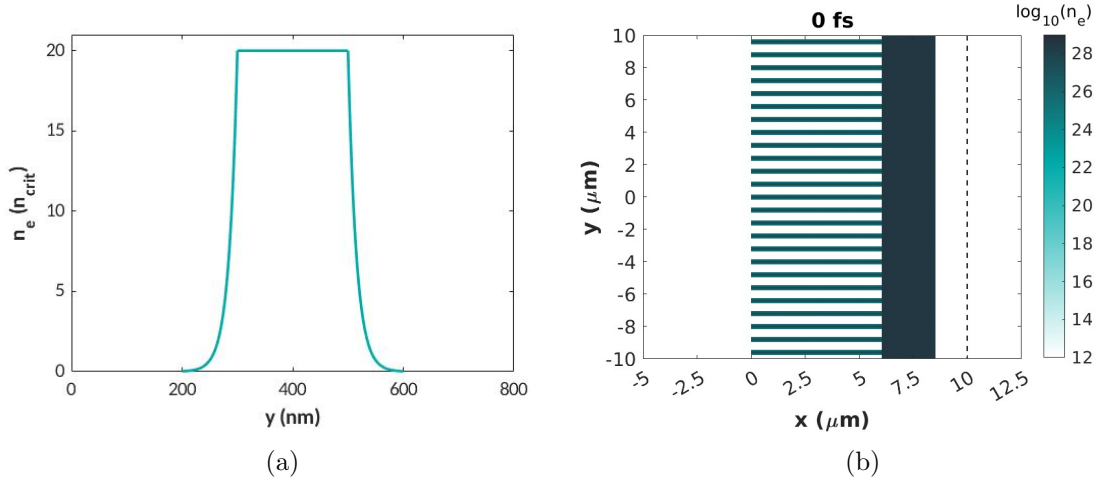


Figure 5.10: (a) The density profile across an individual wire and (b) the full nanowire coated target modelled in EPOCH.

plasma on the front surface of the target. This was to create some plasma of density $\leq n_{crit}$ for the laser to interact with, which would be produced in practice by the ASE pedestal or other pre-pulses. For the nanowires this is realised by modelling each wire at a constant density $n_e = 20 n_{crit}$ for the central 200 nm. The 100 nm at each side is then modelled with a radial exponentially decaying density profile with a decay length of 15 nm. This produces wires with under-critical plasma at the edges, whilst retaining a steep density profile with the bulk of the wire at 20 n_{crit} . The density profile across one of these wires is shown in Figure 5.10(a). Adding the short scale length pre-plasma to wires ensures that the front surface conditions are consistent between the planar and nanowire targets. The nanowires are modelled as 6 μm long in x , and are mounted on a planar 2.5 μm thick substrate at 20 n_{crit} [Figure 5.10(b)]. The initial target temperature is set as 10 eV to reduce the number of thermal electrons rapidly filling the vacuum gaps during the total laser irradiation time of 90 fs. Cell size is set as 1×1 nm across a total domain size of 17.5×20 μm . Electron pseudoparticle number is set to 10 per cell, and ion pseudoparticle number is set to 1 per cell to represent Ti^{10+} ions.

The total number of injected electrons accelerated during the laser interaction with the nanowires can be estimated from the output of a probe plane placed at $x = 10$ μm . There was a lower kinetic energy limit of 2 keV imposed on the probe output from the nanowire target to restrict contributions from the thermal target electrons ($T_{targ} = 10$ eV). A lower energy limit was not placed on the probe for the planar target; Figure 4.23 shows the energy spectra

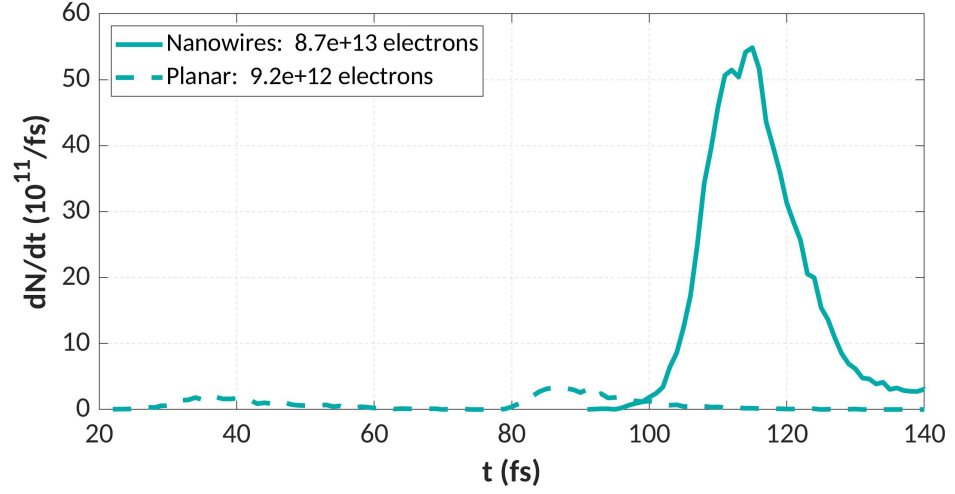


Figure 5.11: Electron number passing the probe as a function of time.

of the electrons collected by the probe from the planar target case and demonstrated the numbers of electrons with energies < 2 keV are a minimal contributor to the total electron number. Thus, the lack of a lower energy limit on the planar case will not have a significant influence on the probe output. The integrated pseudoparticle weightings of electrons passing the probe are given as a function of time in Figure 5.11. There are a greater number of fast electrons recorded exiting the rear target surface for the nanowire case with respect to the planar case, with an increase of total electron number by a factor 9.

The $x - p_x$ distribution function of the electrons in the pre-pulse irradiated nanowire targets are displayed in Figure 5.12. The wires extend across the range $x = 0 - 6 \mu\text{m}$, and the substrate extends across $x = 6 - 8.5 \mu\text{m}$. There is heating of the electrons along the wire up to $x = 6 \mu\text{m}$, with no clear production of electron bunches. The increase in accelerated electron number in Figure 5.11 could be explained by the increased target area of which the laser fields can interact, along the length of wires, rather than being limited to the skin depth of the plasma.

Whilst the production of CTR is unlikely due to the absence of electron bunches, the emission of the incoherent component may be more intense from the nanowires. However, the number of fast electrons do remain low compared to a more intense laser interaction. Take for example the modelling of the main pulse interaction with a planar target in Figure 4.25: there the probe was recording $\sim 10^{14}$ electrons per 0.1 fs, compared to 10^{12} electrons

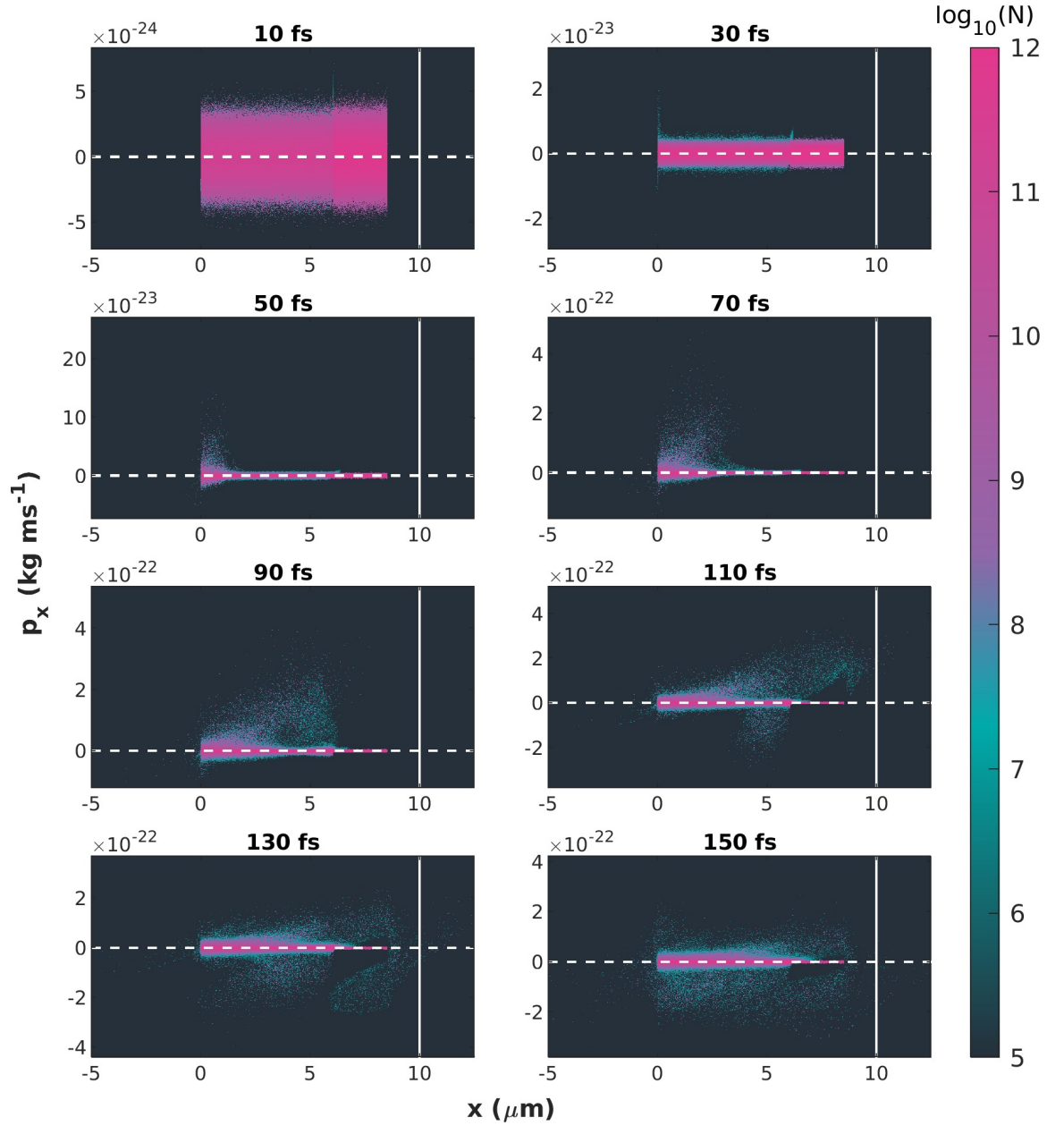


Figure 5.12: $x - p_x$ distribution function of electrons produced in the pre-pulse interaction with a nanowire coated target. The solid white line at $x = 10 \mu\text{m}$ indicates the position of the probe plane.

per 1 fs for the pre-pulse with the nanowires. A similar conclusion can be drawn here as for the planar targets: the hot electrons generated by the pre-pulse are not in sufficiently high numbers to induce appreciable incoherent transition radiation, and electron bunching is not present which suggests coherent transition radiation is also improbable.

Within the discussion we must take a moment to appreciate the limitations of the

modelling of nanowires. In a 2D simulation setup the nanostructures appear identical to nanochannel or nanogroove targets. In reality we are dealing with a 3-dimensional problem, and the laser-target interaction will differ between target types. Wires will be present in the z -direction (directed into and out of the page) which are not able to be captured here. The electrons may interact with these additional wires, by collisions for example, affecting the energy spectra of the electrons exiting the rear surface.

5.6 PIC Modelling of Main Pulse Interaction with Nanowire Pre-Plasma

The outcome of the EPOCH investigation in Chapter 4 indicates the observed optical transition radiation emission originates from the main pulse interaction with the expanded targets. This is a particularly striking result for the nanowire targets, where a number of shots yielded a substantial increase in OTR emission intensity relative to shots on planar targets of comparable thickness. Hydrodynamic simulations with FLASH (Section 5.4) suggest a longer scale length pre-plasma is produced from the pre-pulse interaction with the nanowires compared to planar targets. A particle-in-cell study is implemented here to confirm whether the change in pre-plasma conditions present for planar and nanowire targets could contribute to the observed differences in OTR emission intensity from the perspective of fast electron generation.

The interaction of the main pulse with pre-plasma generated from the pre-pulse-planar target interaction has been modelled in Section 4.6.3; the setup used here is identical aside from the use of a different density profile. To summarise, a simulation domain of size $51 \times 40 \mu\text{m}$ is established, comprised of cells of size $20 \times 20 \text{ nm}$. The target density profile is taken as the found fit to the FLASH output at 10.4 ns, given as $n_e = 3.85 \times 10^{23} \times (60 - x_{\mu\text{m}})^{-1.755} \text{ cm}^{-3}$ as presented in Figure 5.9. Each cell is initially populated with 286 pseudoparticles to represent target electrons, and 13 pseudoparticles to represent Ti^{22+} ions. The target is irradiated with a focusing laser of spot size $4 \mu\text{m}$ FWHM at the best focus position of $x = 30 \mu\text{m}$ and has a Gaussian temporal profile of 27 fs, resulting in a maximum intensity of $5.7 \times 10^{20} \text{ W/cm}^2$ to reproduce the experimental main pulse. The simulation is run up to 300 fs.

To characterise the acceleration of electrons into the target we look at the target electron

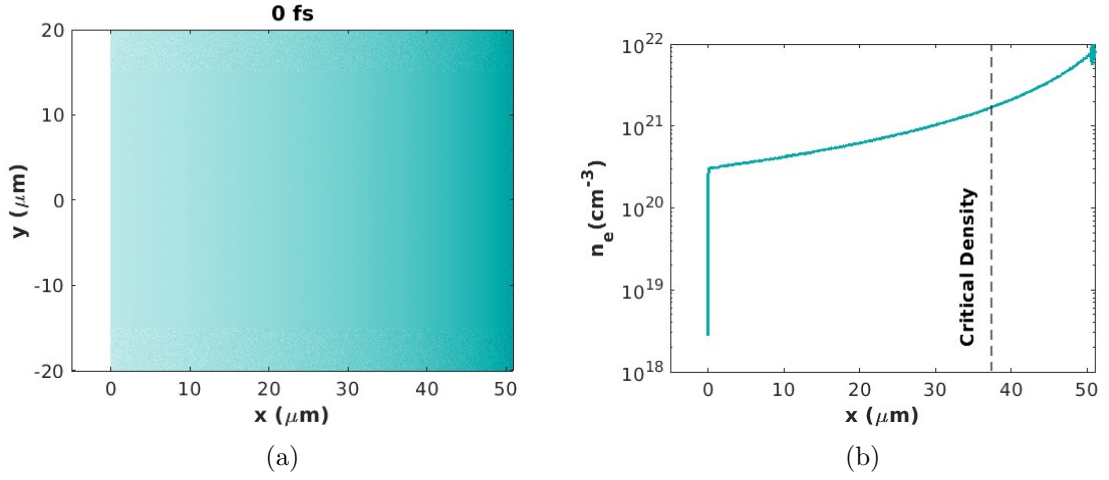


Figure 5.13: Initial density profile of the nanowire pre-plasma region implemented in EPOCH.

number density (Figure 5.14) and the $x - p_x$ distribution function (Figure 5.15) during the laser-plasma interaction. In the plot of electron number density we observe significant displacement of the electrons via the ponderomotive force of the laser, forming cavities within the plasma. This permits exceptional acceleration of the target electrons. The $x - p_x$ distribution function in Figure 5.15 shows electron acceleration in distinct bunches of spacing ~ 400 nm ($2 \omega_L$). The electron bunching and the increasing energy with propagation distance into the under-critical plasma, alongside the channel formation, all indicate a direct laser acceleration mechanism as discussed in Section 4.6.3.

The final energy spectra for the nanowire (pre-plasma) interaction is shown in Figure 5.16. As for the planar pre-plasma, the main laser interaction with the nanowire-generated pre-plasma is capable of producing super-ponderomotive electrons. The electron energy spectra from the planar interaction is shown for comparison. The spectra for electrons with energies < 100 MeV look remarkably similar. However, the energy spectra reveals the number of $E > 100$ MeV electrons are greater for the nanowire pre-plasma interaction. Fitting to the spectra suggests a hot electron temperature of 19 MeV can reproduce the spectra of the fast electrons accelerated in the nanowire pre-plasma well, compared to a temperature of 17 MeV from the planar pre-plasma. The difference between the planar and nanowires is the scale length of the pre-plasma, with the nanowire target exhibiting a lower density, longer scale length pre-plasma, suggesting a dependence of the production of the highest

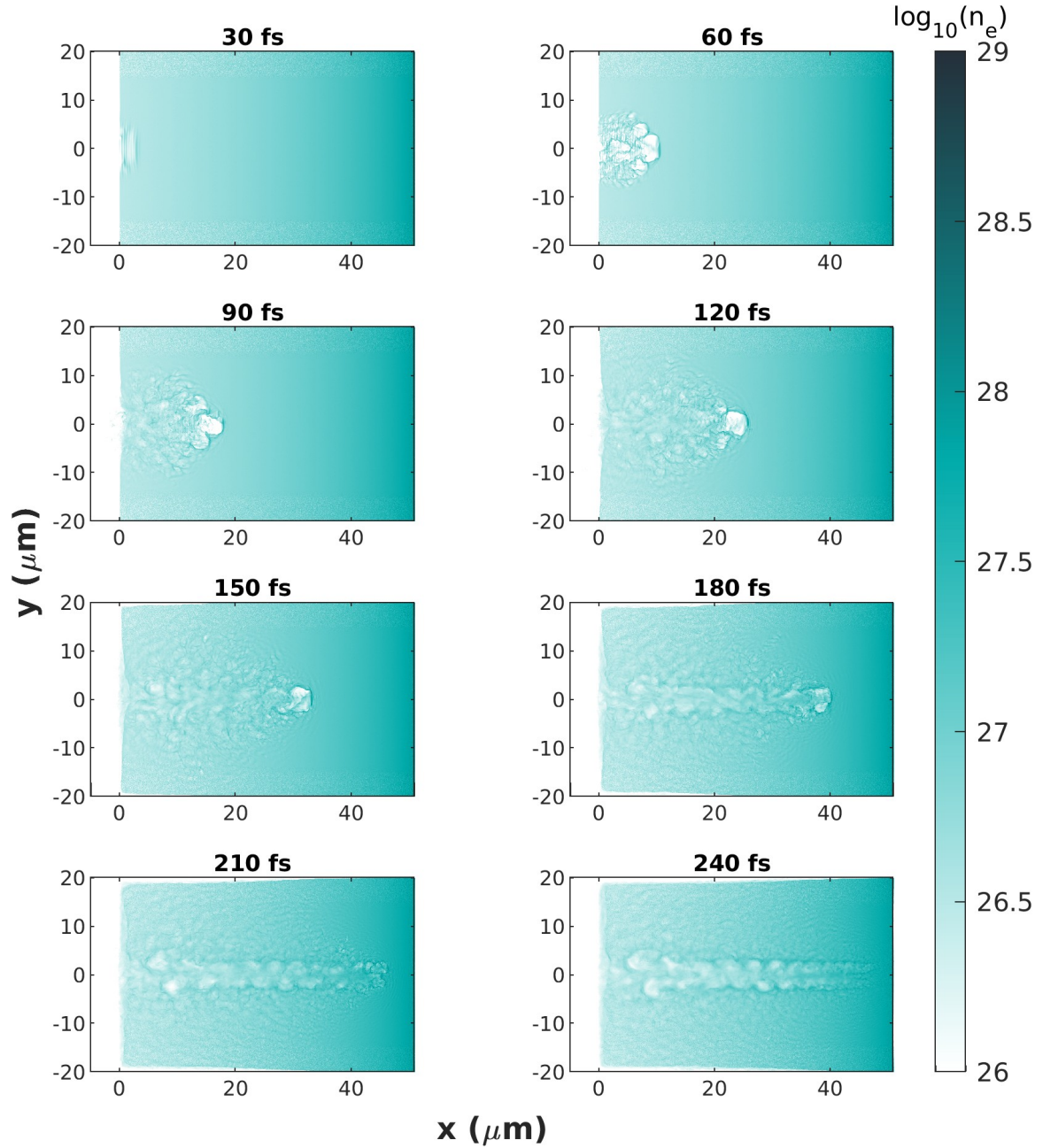


Figure 5.14: Electron number density at various timesteps during the main pulse interaction with the pre-plasma produced by the pre-pulse interaction with a nanowire coated target.

energy electrons on the pre-plasma density profile. Other groups have studied this interaction (intense laser incident on a longer scale length pre-plasma). Higginson *et al.* [176] studied the energies of electrons produced in cone-wire targets with differing scale lengths of pre-plasma. As the scale length of the pre-plasma was increased ($\leq L_{pp} = 5 \mu\text{m}$) the total laser absorption was found to increase, attributed to a longer distance over which the laser

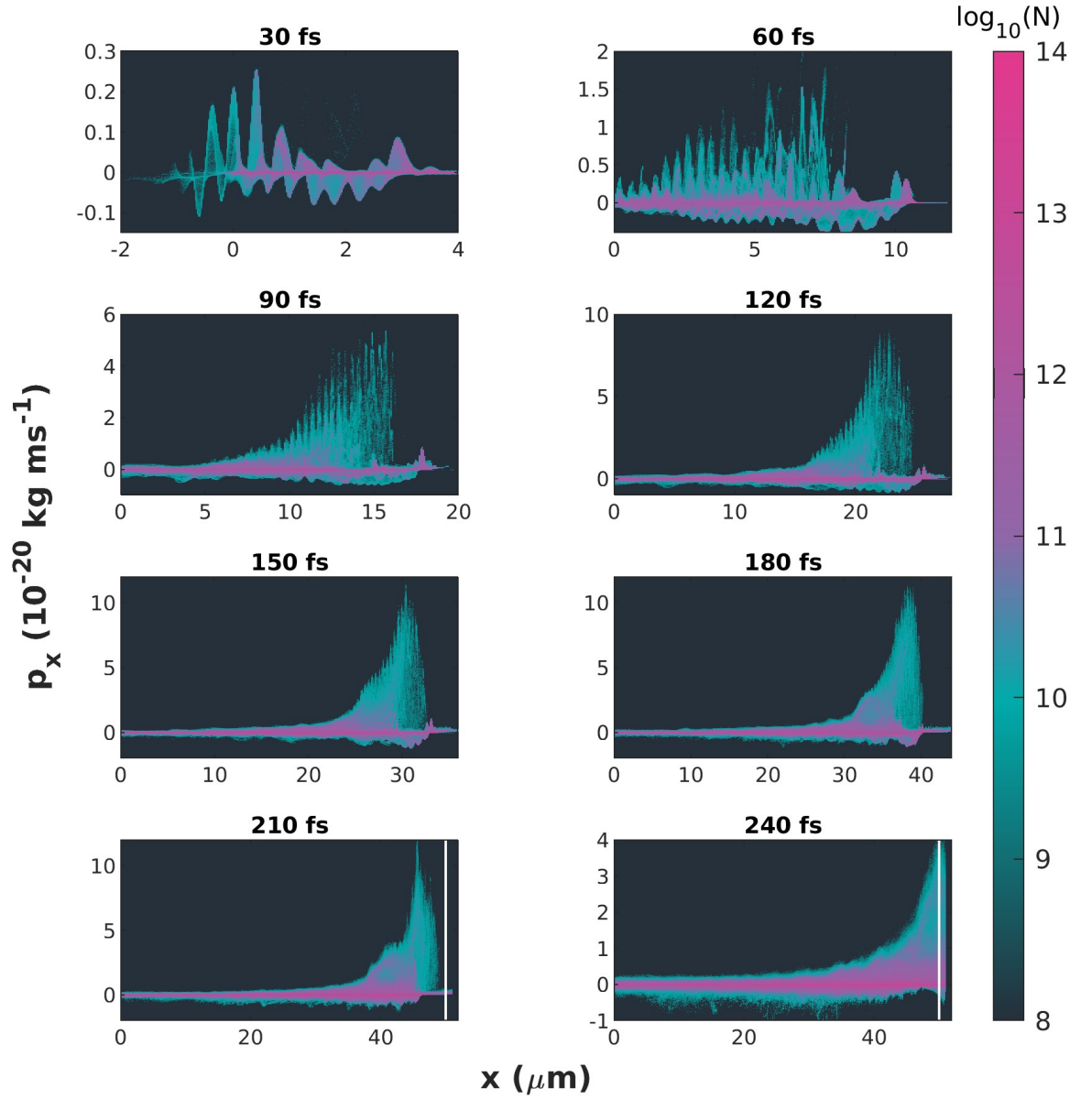


Figure 5.15: $x - p_x$ distribution function of electrons in the nanowire pre-plasma accelerated by the main pulse. The solid white line at $x = 50 \mu\text{m}$ indicates the position of the probe plane.

can interact with and accelerate electrons, and a corresponding increase in electron mean energy was also discovered. A study by Hussein *et al.* [177] demonstrated a dependence of the energy of DLA-accelerated electrons on the density of the pre-plasma in both experiment and simulations.

As discussed for the results in Chapter 4, an electron population with a hotter temperature will be less sensitive to dephasing as it propagates through the target thickness. Here,

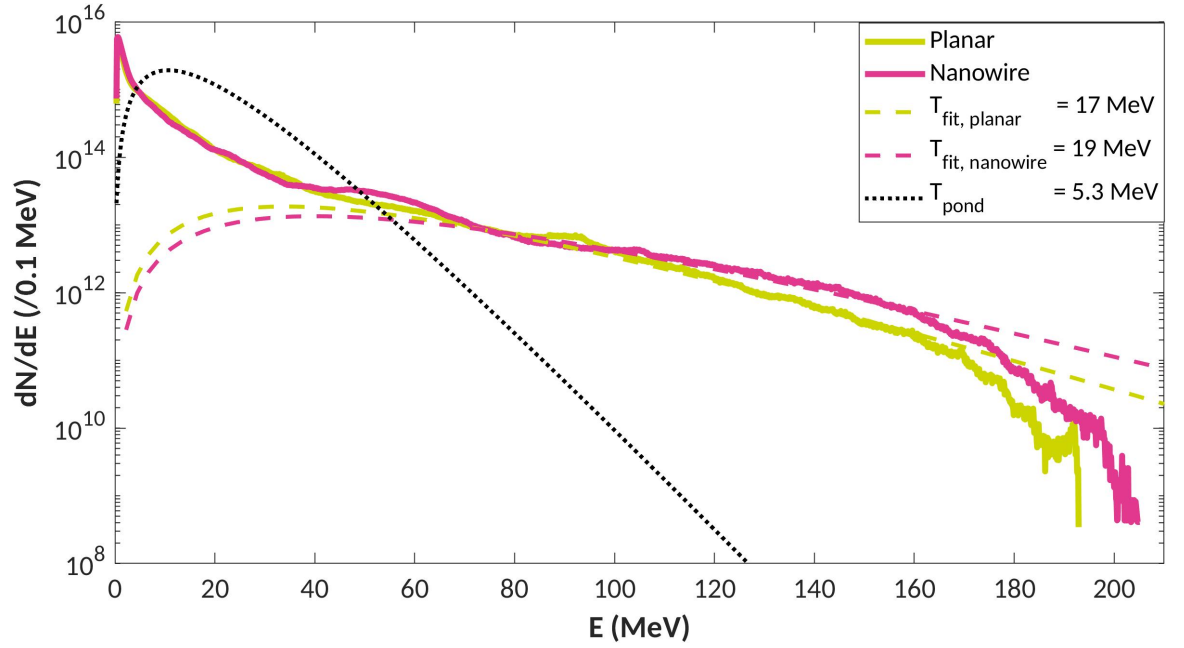


Figure 5.16: Fast electron energy spectra from the interactions of the main laser pulse with the planar pre-plasma and the nanowire pre-plasma.

the nanowire pre-plasma is found to be advantageous in generating greater numbers of high energy electrons that will be able to reach the rear target surface whilst more robustly retaining their bunched structure. The magnitude of CTR emission has a quadratic dependence on the electron number, so one would expect a more intense emission is possible from the electrons predicted to be produced from the nanowire pre-plasma modelled here compared to the planar pre-plasma.

5.7 Summary and Conclusions

In an experimental campaign the performance of nanowire-coated targets was assessed through measurements of optical transition radiation emission from the rear target surface. It was discovered that whilst some laser shots yielded a comparable OTR intensity from the nanowires with respect to planar targets of similar thickness, there existed a subset of shots that produced a much more intense OTR emission. This result is particularly remarkable when we remind ourselves of the intense, 10^{17} W/cm^2 pre-pulse in the experiment that will surely have impacted the nanostructures by the time of the main pulse irradiation.

Hydrodynamic simulations revealed a longer scale length pre-plasma is predicted to be

formed from the nanowires, under the assumption an equivalent energy deposition to the planar targets. PIC simulations and previous literature suggest an enhanced laser coupling is expected into the nanowires, but we possess no experimental measurements to confirm or quantify this for the pre-pulse conditions.¹ The nanowires are also seen to experience shock breakout at the rear surface of the substrate, producing targets with an extended effective target thickness.

The interaction of the main laser pulse with the pre-plasma formed from the planar and nanowire target pre-pulse irradiation are modelled in EPOCH. It is found that the pre-plasma produced from the nanowires is preferential for producing a greater number of high energy, DLA-generated electrons. Since these highest-energy electrons are least sensitive to dephasing during propagation through a target, the high-energy electrons are thought be responsible for the most efficient CTR production at the rear surface: the greater numbers predicted means we can infer a greater magnitude of CTR intensity.

The energy spectra of electrons accelerated via a direct laser acceleration mechanism is sensitive to the properties of the pre-plasma. The variation in the measured CTR intensities could be related to a variation in the pre-plasma formation from the irradiated nanowires. As mentioned, we are uncertain of the degree of laser absorption achieved in the pre-pulse - nanowire interaction. Moreover, the dimensions and spacing of the nanostructures were variable on the front surface. As seen in Figure 5.1, there are areas where the wires are more closely packed together on the front surface, and others where the wire filling density is much less. This could also impact the pre-plasma formation, influencing the fast electron production and consequently the efficiency of coherent OTR production.

¹Numerous attempts were made by the author to produce an example hydrodynamic case for the nanowires with higher energy deposition also, but the simulations would fail to run to completion.

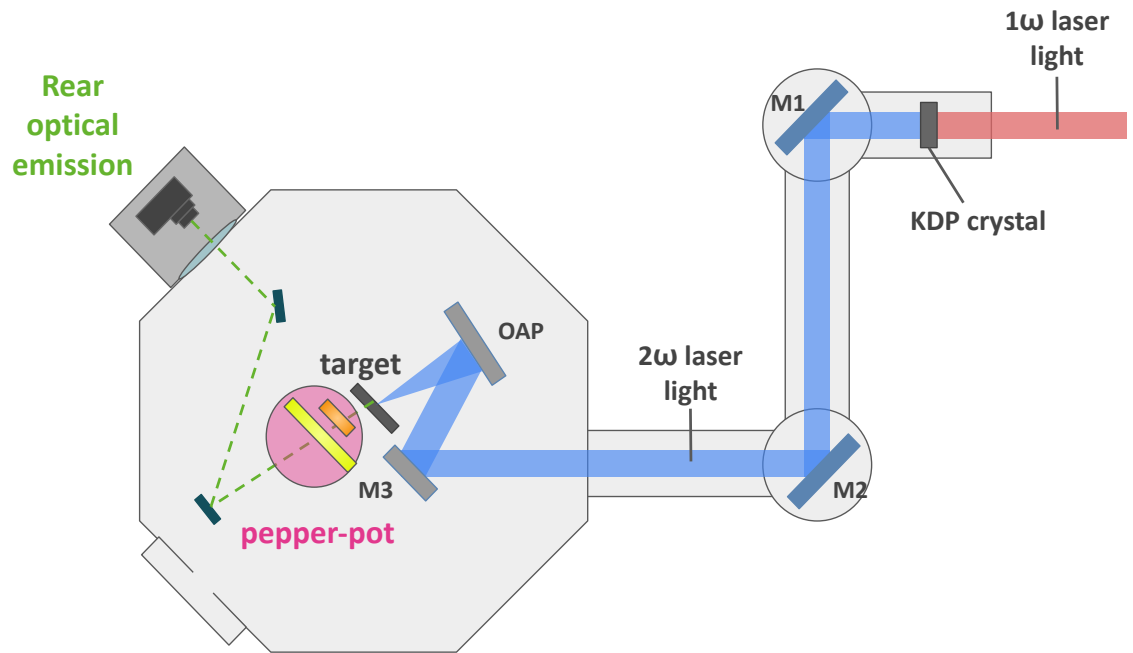
Chapter 6

Frequency Doubled Interactions with Nanowire Targets

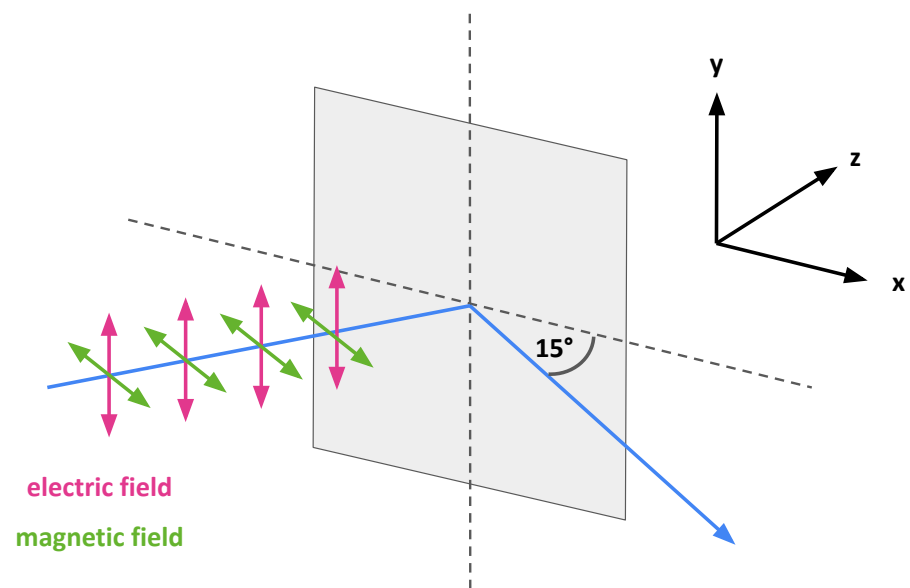
Following the detection of the significant pre-pulse in the previous campaign and the subsequent simulation work, it is clear we did not achieve the intended aim of investigating ultra-intense laser interactions with nanowire targets. A long scale length pre-plasma environment was created instead; whilst this can be of interest in other applications, this has made the presence of the nanostructures almost redundant. An additional experiment was required without the intense prepulse encountered in the previous experiment, to start exploring the interaction with the nanostructures via the fast electrons generated.

6.1 Experimental Layout

A follow-up experiment was carried out at ILIL, with an emphasis on producing a high-contrast laser interaction using their Ti:Sapphire laser. The Pockels cell misalignment was corrected, preventing the leakage of pulses every round-trip of the regenerative amplifier and removing the high intensity prepulse. To reduce contributions from the pedestal or any remaining prepulses, the pulse is frequency doubled using a KDP crystal placed after the compressor. The pulse then reflects off two blue turning mirrors and one metallic mirror before striking a silver-coated $f / \sim 4.5$ focusing parabola. The setup of the target chamber for this is depicted in Figure 6.1(a). The conversion efficiency of the laser pulse into 2ω is estimated to be $\sim 20\%$, resulting in an estimated 2ω energy of ~ 0.4 J contained inside an el-



(a)



(b)

Figure 6.1: (a) Layout of the target chamber with positioning of the relevant diagnostics indicated. The pepper-pot diagnostic was only in place for a small number of shots and was moved out the way of the optical emission imaging line when not in use. (b) Orientation of the laser fields with respect to the target.

liptical focal spot of size $3.5 \times 4.2 \mu\text{m}^2$. The duration of the pulse after propagation through the crystal is 80 fs, resulting in an estimated on-target intensity of $\sim 3.7 \times 10^{19} \text{ W/cm}^2$. The use of the KDP crystal means the polarisation of the laser field is rotated 90° such that the laser electric field oscillation is in the vertical direction in the target chamber. The laser pulse irradiates the targets at an incidence angle of 15° in the horizontal plane, meaning the laser is *s*-polarised in this interaction. The geometry of the laser-target interaction is illustrated in Figure 6.1(b); for consistency this co-ordinate system is used throughout this Chapter.

To explore the properties of the fast electrons generated from the irradiated targets, we again implement imaging of the optical emission from the rear target surface. The setup was unchanged from the previous experiment (see Section 4.1.1 for full details). In short, the rear emission from each shot is imaged using a digital Pentax K200D camera, capturing a wavelength range $\sim 350 - 750 \text{ nm}$, and is time-integrated over a period of 1 ms. In addition, spectral information on the emission was retrieved with a fibre spectrometer. This will be beneficial during analysis for characterising the source of the imaged emission.

The emittance of the exiting fast electron beam was estimated through the use of a novel pepper-pot diagnostic. This diagnostic consists of a pepper-pot mask, essentially a plate with a periodic grid array of holes drilled through it, placed in the path of the beam of fast electrons exiting through the rear target surface as described in Section 3.2.4. The pepper-pot mask implemented here has a spacing of 0.8 mm between each hole, and a hole diameter of 0.2 mm. A stack of 3 EBT3 films was placed behind the pepper-pot mask to detect the fast electrons propagating through. The pepper-pot set up was placed closely behind the target, with a distance of 17 mm between the target and the pepper-pot mask, and a distance of 51 mm between the pepper-pot mask and the EBT3 film. The orientation is shown in Figure 6.2.

6.2 Rear Optical Emission

The optical emission from the rear surface of the targets was imaged for each shot in an effort to measure coherent optical transition radiation (CTR) emission induced by the ex-

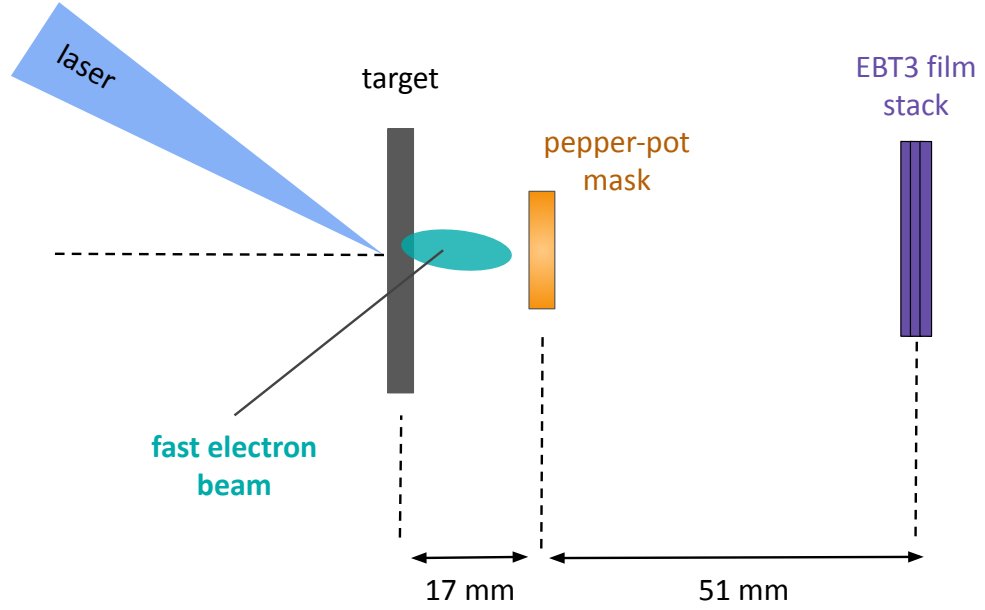


Figure 6.2: Pepper-pot diagnostic setup to estimate the emittance of the exiting, forward propagating fast electrons.

iting fast electrons. For some shots corresponding spectral information was obtained with a fibre spectrometer to complement the optical images. Since the laser pulse is frequency doubled the wavelength of the interacting laser is $\omega_L = 400$ nm, with $2\omega_L = 200$ nm. The detection range of the optical camera used in the experiment is $\sim 350 - 750$ nm; it is not possible to measure $2\omega_L$ with this setup. In the context of observing CTR, which is emitted at harmonics of the electron bunching frequency, only ω_L can be observed arising from the resonance absorption and/or vacuum heating mechanisms. It is not possible to observe CTR induced from ponderomotive accelerated fast electrons in this frequency doubled regime.

The results of two shots on Au $1 \mu\text{m}$ are shown in Figure 6.3: as the thinnest target used, the CTR emission should be most visible from these shots. The optical emission imaged from Shot 51 consists of a small, intense bright spot surrounded by a larger region of dimmer light. The corresponding recorded spectra shows an intense peak at $\lambda = 400$ nm and a lower intensity, broadband emission. CTR emission is known to peak at the electron bunching frequency; this could be an indication that electrons are injected at ω_L via vacuum heating. In contrast, the optical emission from Shot 52 shows a larger region of lower intensity emission, but no distinct smaller region of more intense emission as from

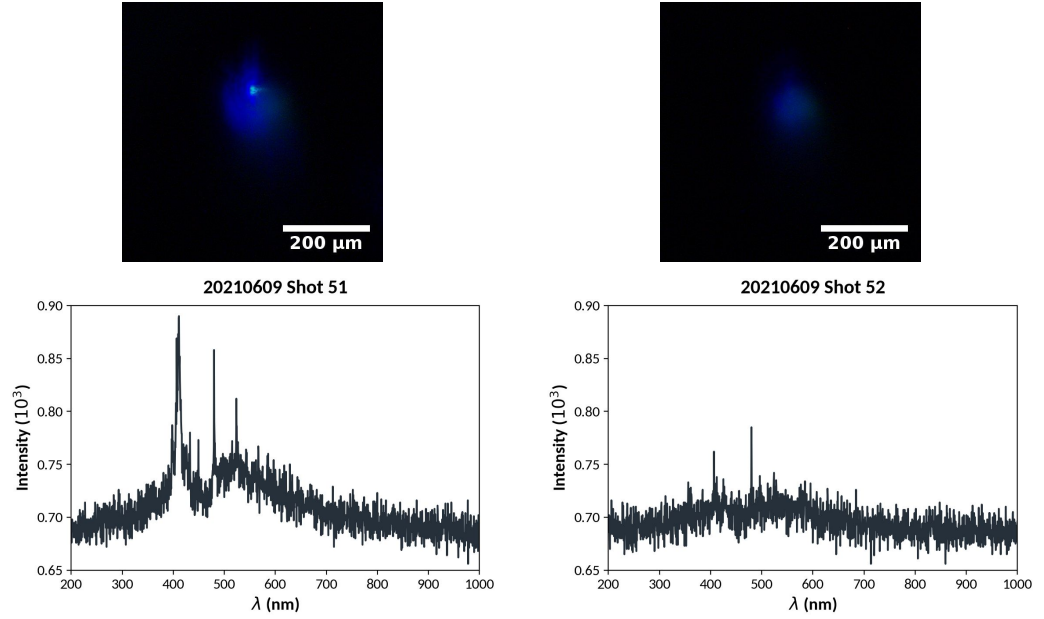


Figure 6.3: Image and spectra of optical emission measured from the rear surface of irradiated Au $1 \mu\text{m}$ targets.

Shot 51. The spectra does not present a clear peak at $\lambda = 400 \text{ nm}$ as before. This indicates that the smaller, intense region is $\lambda = 400 \text{ nm}$ light and we propose this is from CTR emission.

With the characteristics of CTR emission to look for in the optical images and spectra identified, we now address the data from shots on thicker planar targets and nanowire coated targets. Shown in Figure 6.4 are some typical images from shots on Ti $12.5 \mu\text{m}$ and nanowire coated targets with the corresponding spectra as measured by the fibre spectrometer. The characteristic bright spot we believe to be CTR emission is not present in the images, a result which is mirrored for all shots on nanostructured and thicker Ti targets. We believe the imaged broadband emission is from late time recombination of the plasma and/or from incoherent transition radiation. This is not to say that CTR was not produced at all, but we were unable to capture and isolate CTR emission in this instance. Consequently, in this experiment we were unable to attain optical data that could be used for CTR analysis and further our understanding of fast electron behaviour in the nanostructured targets.

In previous experiments we have been able to observe CTR emission from shots on tar-

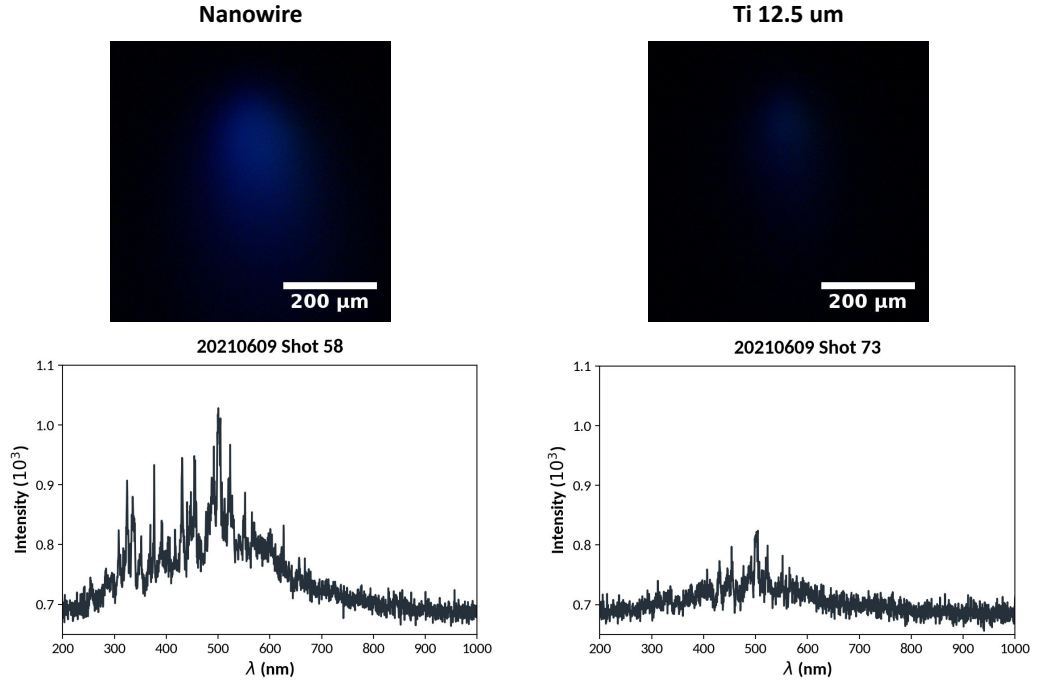


Figure 6.4: Image and spectra of optical emission measured from the rear surface of irradiated nanowire and Ti 12.5 μm targets.

gets of similar thickness at the fundamental frequency¹, but not from this frequency doubled interaction. As the intensity of CTR emission scales quadratically with electron number, the reduction in CTR intensity could also be a consequence of having less energy contained in the pulse to accelerate electrons since there is an energy loss during the frequency doubling conversion process. Particle-in-cell simulations were carried out using the code EPOCH to help support this argument and explain why it was not possible to see any CTR for the frequency doubled interaction compared to an interaction at the fundamental frequency. The goal is to model separately the interaction of the ω_L and $2\omega_L$ laser light with a planar target and study the interactions with respect to the laser coupling into fast electrons. The target consists of 2.5 μm thick Ti, with a 0.1 μm thick layer of pre-plasma on the front surface with a scale length of 15 nm. The average ionisation of the material is $Z_{bar} = 10$; electron density of the target is set to $20 n_{crit}$ to represent solid material. Initial target temperature is set to 1 keV. The target was placed in a simulation domain of size $17.5 \times 20 \mu\text{m}$ with a cell size of $2 \times 2 \text{ nm}$. Each cell with target material was populated with 4 pseudoparticles to represent Ti^{10+} ions, and 40 pseudoparticles to represent electrons. The properties of the

¹Private communication, Petra Koester, 2022

	ω_L	$2\omega_L$
Polarisation	p -polarised	s -polarised
λ (nm)	800	400
E_{tot} (J)	5.4	1.08
E_{spot} (J)	1.944	0.388
τ (fs)	27	80
FWHM focal spot size (μm)	4	4
I (W/cm^2)	5.7×10^{20}	3.9×10^{19}

Table 6.1: Summary of the properties of the fundamental and frequency doubled laser pulses employed in EPOCH.

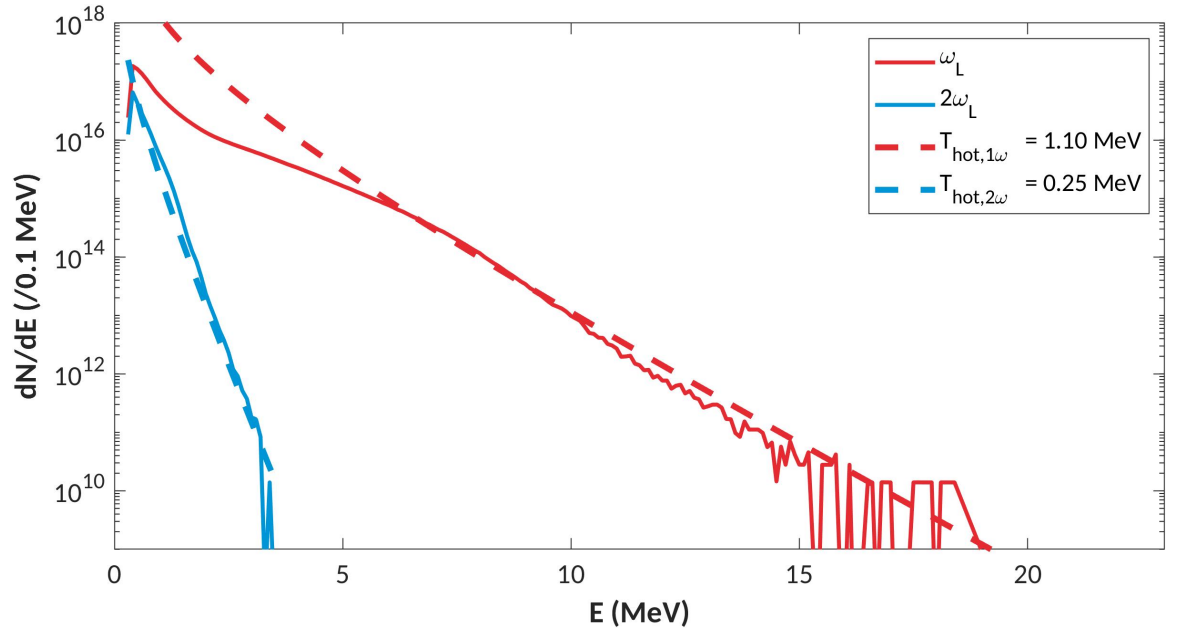


Figure 6.5: Energy spectrum of fast electrons recorded by the probe plane from a laser interaction at fundamental frequency, and a laser interaction with frequency doubled parameters.

laser pulse used to irradiate the target are given in Table 6.1. The energy contained in the $2\omega_L$ laser pulse is estimated assuming a 20% conversion efficiency from ω_L . Incidence angle of the laser is 15° , and the polarisations are set to p - and s - polarisation for the ω_L and $2\omega_L$ interactions respectively to replicate the experimental conditions. A probe plane is placed directly at the target rear surface edge to record the energies and numbers of injected fast electrons.

The energies of the exiting fast electrons are extracted from the probe plane with each energy determined from the momenta of the electron pseudoparticle. A histogram is created from these found energies to produce energy spectra as plotted in Figure 6.5. The temperature of the fast electrons generated from the ω_L interaction is greater than that generated from the $2\omega_L$ interaction; fitting to the spectra demonstrates a hot electron temperature of 1.1 MeV from the ω_L interaction compared to 0.25 MeV from the $2\omega_L$ interaction. For high intensity laser-plasma interactions the hot electron temperature has been shown to scale with laser irradiance as $(I\lambda^2)^{1/3}$ [178, 179]. Previous work has additionally reported a reduced laser to fast electron conversion efficiency for frequency doubled laser light compared to the fundamental frequency [180]. The use of frequency doubled light in the experiment is predicted to have produced a reduced flux of fast electrons and are described by a cooler temperature than for an interaction with the laser at fundamental frequency. As such, the frequency doubled interaction is expected to yield a lower number of fast electrons propagating through to the rear surface of target, and consequently a reduced intensity of transition radiation emission.

6.3 Electron Emittance

In this experiment a diagnostic was put in place to directly estimate the *emittance* of the fast electrons for shots on planar Ti foils and on the nanowire targets. Emittance is a measure of the area of phase-space occupied by a subset of particles; here, we are measuring the emittance of a subset of the exiting fast electron population. The priority of the experiment was to collect data on the rear optical emission - the positioning of the pepper-pot mask obstructed the rear imaging line and so the pepper-pot diagnostic was only in place for a limited number of shots. Integrated emittance data was collected over two shots on $12.5\ \mu\text{m}$ planar Ti, and for two shots on nanowire coated targets.

A stack of three EBT3 films is implemented to detect the electrons propagating through the pepper-pot mask. Due to the close positioning of the mask to the rear target surface, there is the potential that rear accelerated protons can contribute to the measured signal. The use of a stack is to ensure that any protons are restricted predominantly to the first

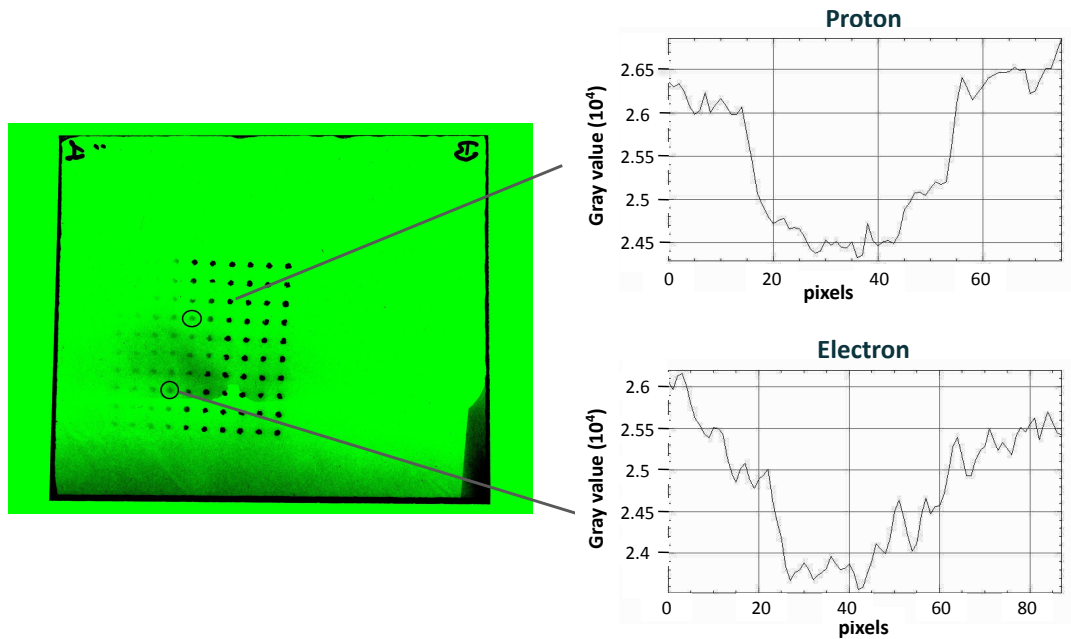


Figure 6.6: Difference in measured signal from proton versus electron deposition in EBT3 film. This data was taken from a separate experiment at the ILIL facility, and is included for descriptive purposes only to demonstrate the different signatures of proton and electron deposition.

film, with proton contributions reduced for the following films. The drawback is the electron signal will also reduce as we go to deeper films. Upon inspection of the scanned films it appears that there is little signature of proton deposition. Proton deposition demonstrates a sharper, more abrupt deposition at the edge of the beamlet, whilst electron deposition demonstrates a smoother edge due to straggling through the plastic protective layer, as depicted in Figure 6.6 from a separate campaign². The beamlets measured in this experiment are more characteristic of electron deposition, leading us to believe that electron deposition dominates the signal. On balance it was decided to carry out analysis on the first film in each stack only, since we do not observe signs of significant proton deposition and the electron signal rapidly reduced at increased film depth.

Analysis of the images obtained from the use of the pepper-pot diagnostic is carried out using a *Python* script written by the author. The analysis process is based on the emittance formula presented by Zhang with the full derivation found in Ref. [132] and summarised in

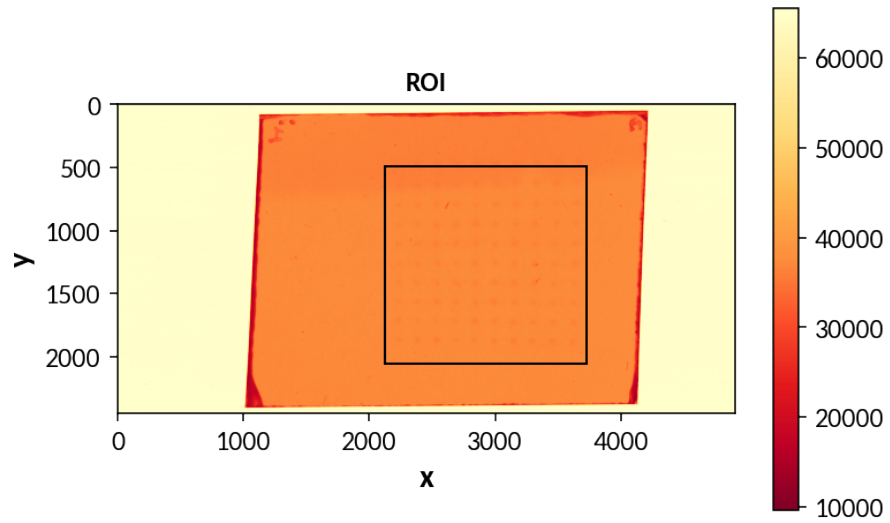
²Private communication, Petra Koester, 2023.

Section 3.2.4. The r.m.s. emittance, ϵ , is estimated as

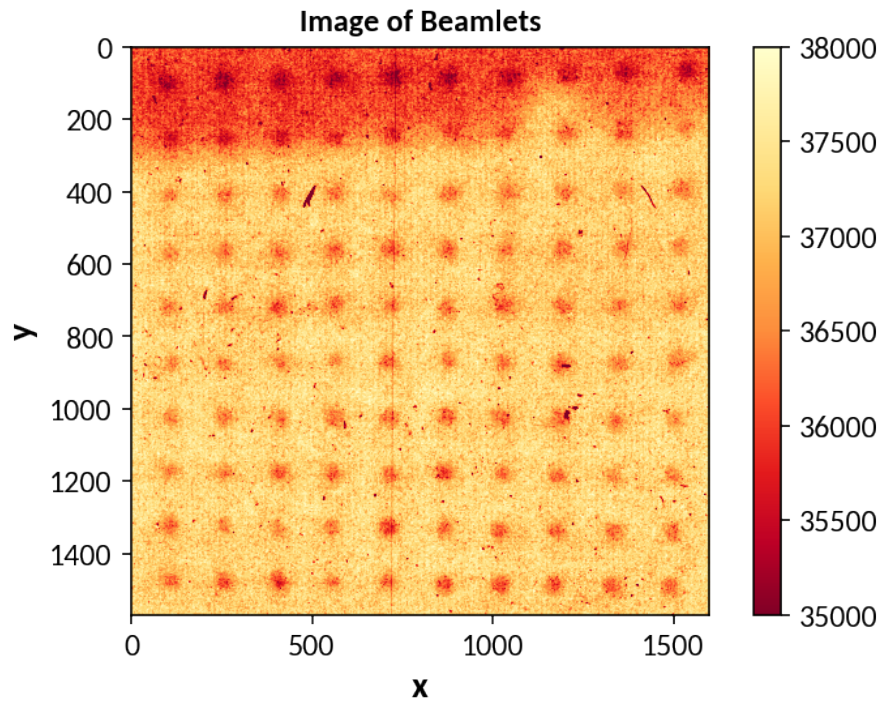
$$\epsilon^2 \approx \langle x^2 \rangle \langle x'^2 \rangle - \langle xx' \rangle^2 \quad (6.1)$$

where these values are calculated from information on the pepper-pot mask dimensions and from the properties of the *beamlets*. For clarity, in this context a ‘beamlet’ refers to the spot on the image created by the subset of electrons propagating through each hole in the pepper-pot mask. To explain how this information is extracted from our images in practice, the procedure implemented by the code is outlined as follows. The description applies to analysis of columns of beamlets to obtain an estimate of ϵ_y , but the process is identical to that applied to obtain an estimate of ϵ_x through analysis of the rows of beamlets.

1. Load the image of the beamlets and convert to RGB. Further analysis is carried out on the red channel only as this was found to produce the clearest images of the beamlets.
2. The user manually identifies a region of interest encompassing the 10×10 grid of beamlets. Crop image to this region.
3. Divide the region into 10 vertical ‘slices’ which are analysed on an individual basis. The following method details how one slice is analysed.
4. The user chooses x -limits within the slice to define a ‘beamlet region of interest’ that includes all beamlets as closely as possible. Intensity is integrated across x , and an average beamlet intensity calculated by dividing by the height of the beamlet region of interest. Note the beamlets are actually seen as local dips in intensity rather than peaks.
5. The user chooses an x -position to take the background intensity from. A ‘background region of interest’ with a thickness of 10 pixels is selected using the chosen x -position as the centre. Intensity is integrated across x , and an average background intensity calculated by dividing by the height of the background region of interest.
6. Imperfections in the film can form a large contribution to the measured intensities. For the background intensity, the effect of these deviations is mitigated by applying a



(a)



(b)

Figure 6.7: Identifying the region of interest from the pepper-pot image to analyse.

Savitzky-Golay filter to the data [181] using the *savgol_filter* subroutine from the SciPy module. This has the effect of smoothing the lineout.

7. Background correction is accomplished by subtracting the smoothed background intensity from the beamlet intensity. At this stage the intensity values are inverted so

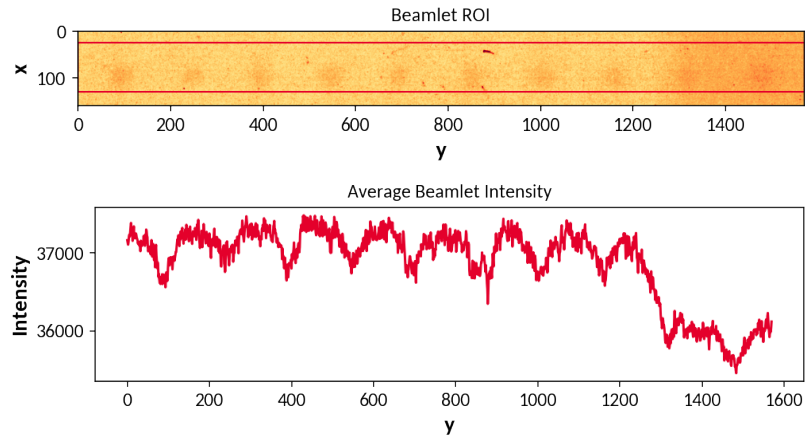


Figure 6.8: Identifying an region of interest around the beamlets for a horizontal slice.

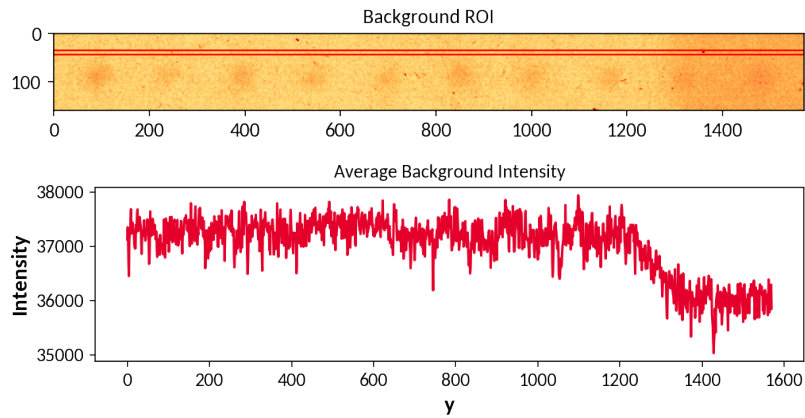


Figure 6.9: Identifying an region of interest to determine background intensity for a horizontal slice.

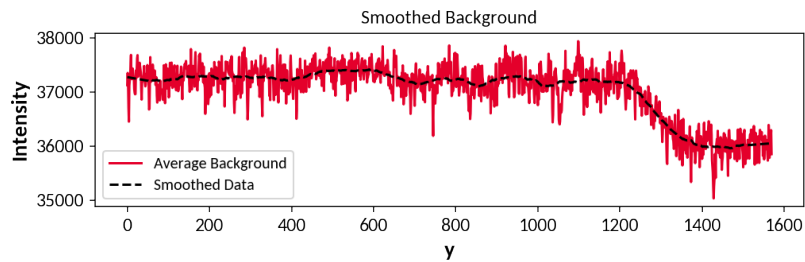


Figure 6.10: Background intensity after smoothing.

the beamlets are represented by intensity peaks.

8. Pixel values are converted into physical distance using the original image width (2448 pixels) and the measured width of the film (53 mm).

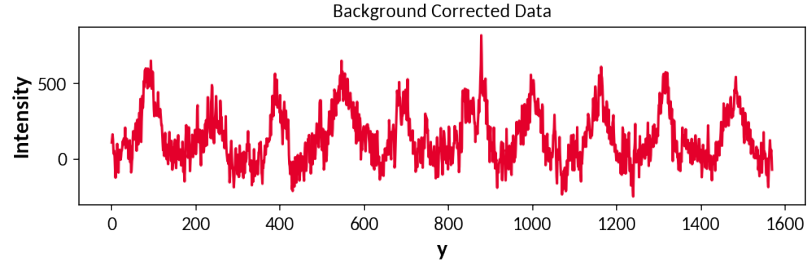


Figure 6.11: Background-corrected intensities across the beamlets.

9. Fitting to the beamlets is achieved using a 10-Gaussian fit of the form

$$I = h_1 \exp \left[- \left(\frac{y - y_{0,1}}{\sigma_1} \right)^2 \right] + h_2 \exp \left[- \left(\frac{y - y_{0,2}}{\sigma_2} \right)^2 \right] + \dots \\ \dots + h_{10} \exp \left[- \left(\frac{y - y_{0,10}}{\sigma_{10}} \right)^2 \right], \quad (6.2)$$

with optimal parameters determined using the *curve_fit* subroutine. It was found necessary to provide initial guesses and to set the bounds of the fitted parameters to within $\pm 50\%$ of the initial guess. Without the initial guess and the bounded conditions the *curve_fit* routine would instead fit to smaller localised peaks across the first couple of beamlets. In this example the initial guess was set to $h_{0-10} = 600$, $\sigma_{0-10} = 0.6$, and y_0 in increments of 3.07 mm.

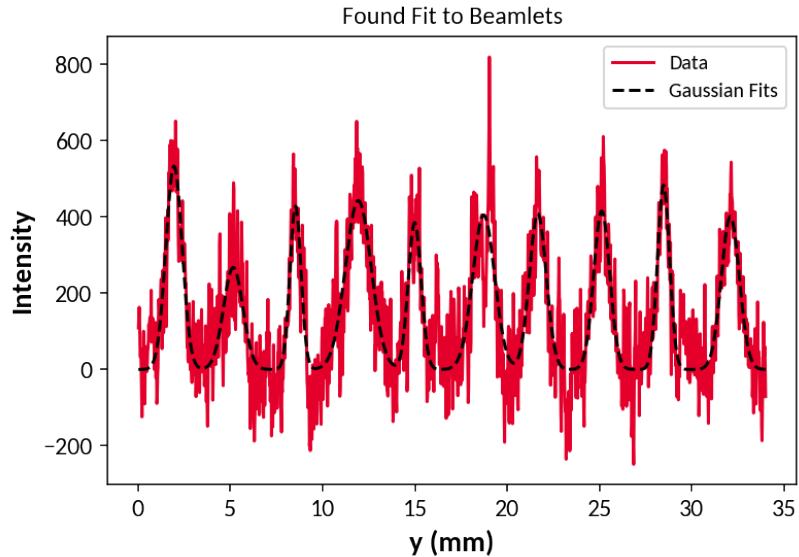


Figure 6.12: Found fit to the beamlet lineout.

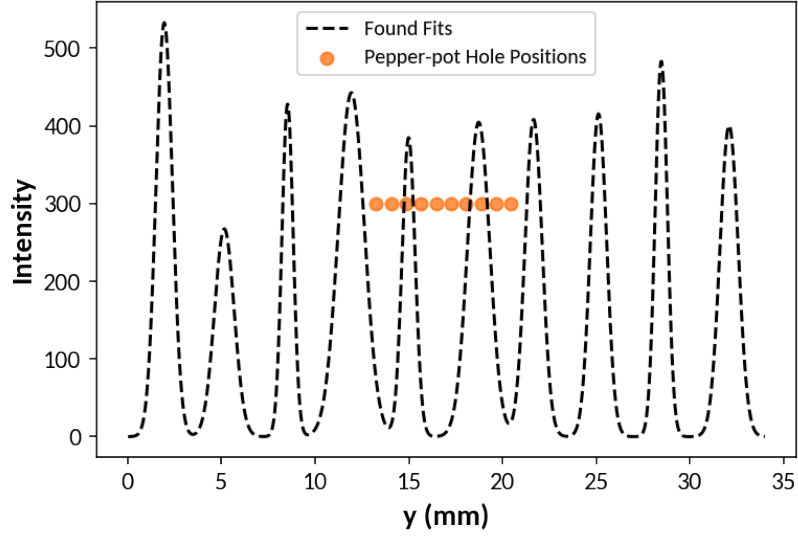


Figure 6.13: Transverse position of holes in the pepper-pot mask relative to the fitted beamlets.

10. The values of h , y_0 , and σ are saved in a dataframe. It is advised to check none of the found parameters are restricted by the initial guess, e.g. if a height is found to be 300.000, a lower height value is likely a better fit but has been limited by the $h = 600 \pm 50\%$ condition. In this case, the user is advised to go back to the fitting step and adjust the initial guesses accordingly.
11. The transverse positions of the pepper-pot holes are set, assuming the centre of the pepper-pot holes coincides with the centre of the 5th and 6th beamlets (see Figure 6.13). According to the Zhang derivation, the final value of the emittance should not be affected if there is an offset between the origin position of the pepper-pot holes and the beamlets. This was tested by setting the pepper-pot holes in different positions (e.g. centred between the 6th and 7th beamlets) and the final emittance value was found to be invariant under these applied offsets.

This processing has yielded all the necessary information to now calculate the emittance. The final formula to obtain the emittance is

$$\epsilon_y^2 \approx \frac{1}{N^2} \left\{ \left[\sum_{j=1}^p n_j (y_{hj} - \bar{y})^2 \right] \left[\sum_{j=1}^p \left[n_j \sigma_{y_j}^2 + n_j (\bar{y}_j - \bar{y})^2 \right] \right] - \left[\left(\sum_{j=1}^p n_j y_{hj} \bar{y}_j \right) - N \bar{y} \bar{y}' \right]^2 \right\} \quad (6.3)$$

as presented in Section 3.2.4 where p is the number of pepper-pot holes in each column. We

will now describe in the following table how the found fits are used to calculate the individual terms in this formula:

Term	Calculation Method	Reference
n_j	Number of electrons at each hole. Intensity on the image is proportional to the electron number, so the height h_j of the fitted peak is used.	-
N	Total number of electrons across all holes. This is taken as the sum of the heights of the fitted peaks, $\sum_{j=1}^p h_j$.	-
y_{hj}	Transverse hole position. Taken as the user-defined transverse hole positions in mm, assuming they are centred between beamlets 5 and 6 as explained in Step 11 of the code description.	-
\bar{y}	Average hole position. Taken as the intensity weighted average of the defined hole positions, $\frac{1}{N} \sum n_j y_{hj}$.	Eqn. 5
σ_j	The r.m.s. spot size of each beamlet. Taken as the standard deviation, σ , of the fitted peak.	Eqn. 22
σ'_{y_j}	The r.m.s. divergence of each beamlet. Calculated as $\frac{\sigma_j}{L}$, where L is the distance between the pepper-pot mask and the detector in mm.	Eqn. 21
\bar{Y}_j	Mean transverse position of each beamlet. Taken as the central position of the fitted peak, y_0 , in mm.	Eqn. 9
\bar{y}'_j	Mean divergence of the electrons passing through each beamlet. Calculated as $(\bar{Y}_j - y_{hj})/L$, equivalent to (transverse position at detector - transverse position at hole)/hole-detector distance. Given in radians.	Eqn. 10
\bar{y}'	Mean divergence of all beamlets. Taken as the intensity weighted average of the mean divergences for each beamlet, $\frac{1}{N} \sum n_j \bar{y}'_j$	Eqn. 11

Table 6.2: Description of how each term is calculated to determine an estimate of the emittance. Where applicable the number of the relevant equation in Zhang's Fermilab report is given, if the reader wishes to find more information on the derivation.

The calculated terms are input into Equation 6.3 to get an estimate of the emittance for the column. This process was repeated for each column in the recorded images to obtain ϵ_y as a function of x , and for each row to obtain ϵ_x as a function of y . The found emittance values are shown in Figure 6.14. It was found that the emittance value was sensitive to the position chosen to take the background lineout from (Step 5) due to regions of inhomogeneous background. Each emittance value given in Figure 6.14 is the average value of two measurements, one with the background lineout taken from the left of the beamlets and a second with the background taken from the right of the beamlets for ϵ_y ; an equivalent approach was taken for ϵ_x with the background being taken from above and from below the beamlets. The error on each point is determined from the variation of these two values. Error bars are noticeably larger for the ϵ_x dataset; this is due to larger variations in the background intensity in the y -direction (see for example the large shadowy region at the top of Figure 6.7(b), meaning the background profile changed drastically when taken from the top or bottom of the rows of beamlets in some instances.

The emittance values determined from the obtained data are in the range 20 - 40 mm mrad. Measurements of electron emittance in laser-solid interactions are scarce, but there are some examples in the literature to refer to when confirming if our values are reasonable. When measuring electron beams generated from the front surface of intense laser-irradiated solid targets, Ma *et al.* [182] states a normalised emittance can be estimated as $\epsilon_n \approx \gamma\theta\sigma$, where γ is the electron Lorentz factor, θ is the beam divergence angle and σ is the beam source size. We have a laser intensity $\sim 3.7 \times 10^{19}$ W/cm² contained within a FWHM focal spot of size 4 μ m, with the work by Green *et al.* [88] predicting a fast electron divergence angle $\sim 30^\circ$ (523 mrad) at this intensity. Since this a rough estimate we shall use $\gamma = 9.4$ as used in the Ma paper ($E_{avg} = 5.3$ MeV). For our experimental conditions this would yield an estimated emittance $\epsilon_n \approx (9.4)(523)(4 \times 10^{-3}) = 19.7$ mm mrad. An experiment by Cowan *et al.* [183] detected electrons accelerated by a 3×10^{20} W/cm² laser pulse ($\tau = 450$ fs); within the accelerated fast electron population a monoenergetic electron jet was identified with a normalised r.m.s. emittance $< 10\pi$ mm·mrad. Both of these emittance estimates suggest electron emittance values to the order of 10's mm mrad are not unreasonable from laser-solid interactions, particularly from our relatively thin targets of ~ 12.5 μ m thickness.

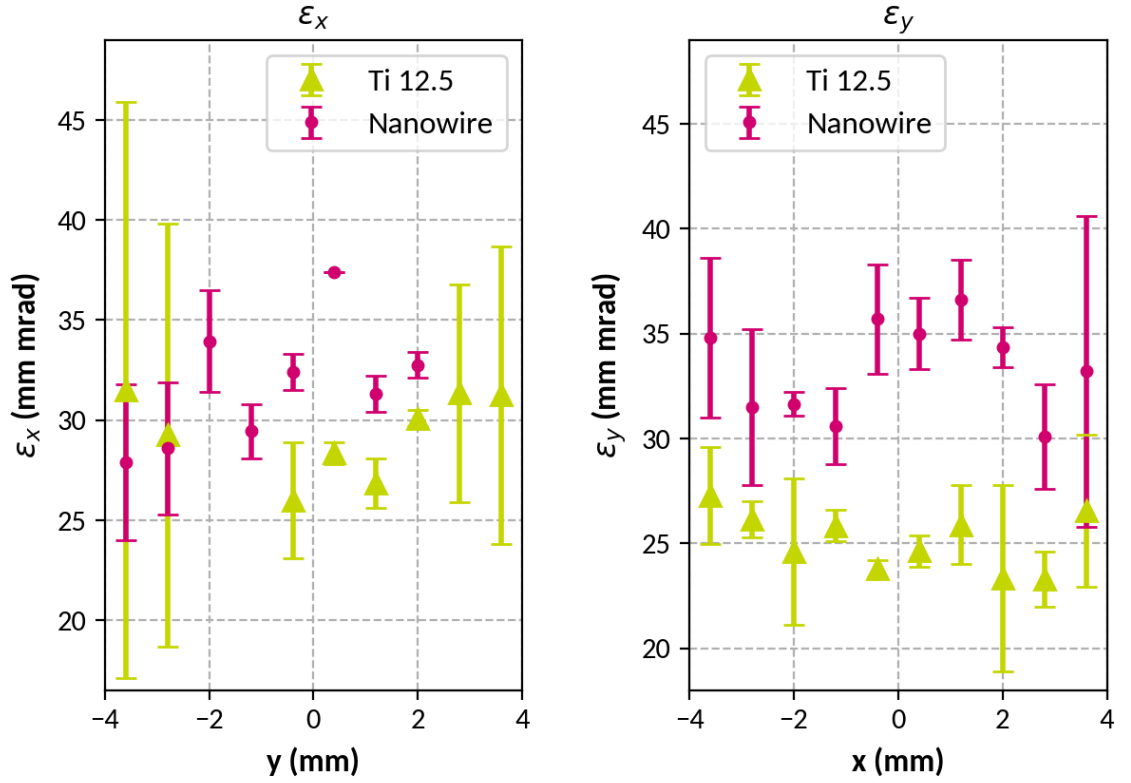


Figure 6.14: Calculated estimates of emittance of the exiting fast electron beam for shots on planar $12.5 \mu\text{m}$ and nanowire coated targets.

The average values of ϵ_x and ϵ_y values are 29.3 ± 20 and 25 ± 8 mm mrad for the planar targets, compared to average values of 32 ± 7 and 33 ± 10 mm mrad for the nanowire coated targets. The experimental pepper-pot measurements indicate a general trend of an *increased emittance* of exiting fast electrons from the nanowire coated targets compared to planar targets. There is a more distinct difference in the estimate of ϵ_y for the two target types; this correlates to the direction of the laser electric field polarisation. To understand whether these observations are to be expected, we look to model the interaction to explore the effect of presence of the wire structures, and the laser polarisation direction on the emittance of the fast electron population.

6.3.1 Particle-in-Cell Simulations

EPOCH is used to model the interaction of the frequency doubled laser pulse with both target types. A domain of size $20 \times 30 \mu\text{m}$ is established with a cell size 2×2 nm. The

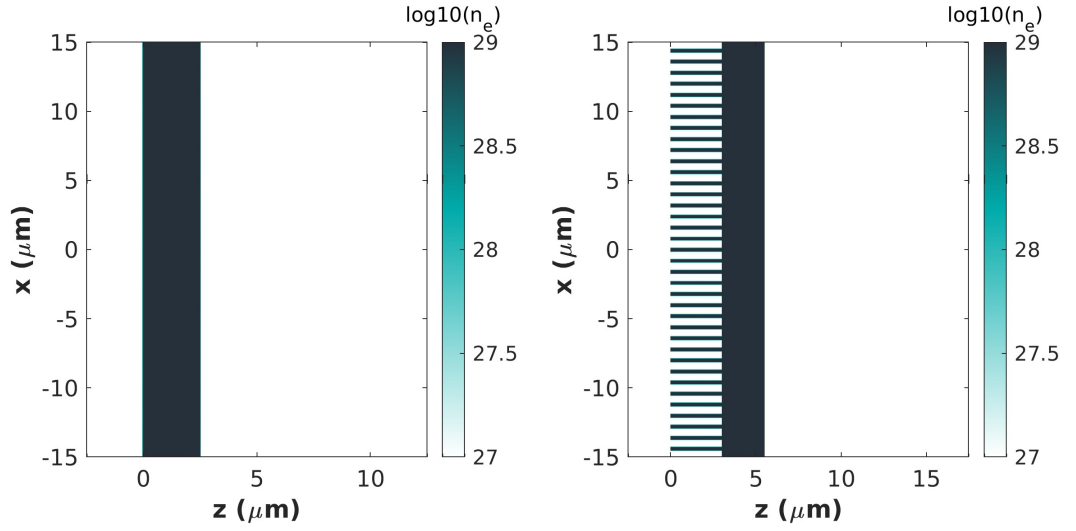


Figure 6.15: Initial target profiles modelled in EPOCH.

planar foil is modelled as a $2.5 \mu\text{m}$ thick Ti target, consisting of Ti^{10+} ions and $n_e = 20 n_{crit}$, and an initial temperature of 1 keV. The nanowires are modelled as the same planar target as a substrate, with wires of diameter and gap size of 400 nm and a length of $3 \mu\text{m}$ standing normal on the planar target, and an initial temperature of 10 eV. The resultant targets are shown in Figure 6.15. The laser is set to deliver 0.388 J contained in a focal spot of size $r_{FWHM} = 2 \mu\text{m}$ in a time $\tau_{FWHM} = 50$ fs, and has a wavelength $\lambda = 400$ nm. The laser enters the domain from the left-hand side and strikes the targets at an incidence angle of 15° . Simulations are carried out for s -polarised and p -polarised laser light. 2D EPOCH simulations are in the $z-x$ plane according to the coordinate system defined in Figure 6.1(b), more easily visualised if you imagine we are looking at the laser-target interaction in EPOCH from a “top-down” perspective. In this 2D simulation the s -polarisation case is realised with the laser electric field oscillating into/out of the page (y); for p -polarisation the electric field oscillates in the simulation plane ($z-x$), with the target thickness in the z -direction.

For each target the p_x-p_z phase space is extracted at a time of 75 fs, and is shown in Figure 6.16(a). The p_x-p_z phase space of the target electrons is first assessed for a s -polarised laser interaction, corresponding with the laser polarisation in the experiment. In this orientation p_z is the electron momenta in the direction of the target thickness, and p_x is the electron momenta perpendicular to the laser polarisation in y . We see an increased momenta

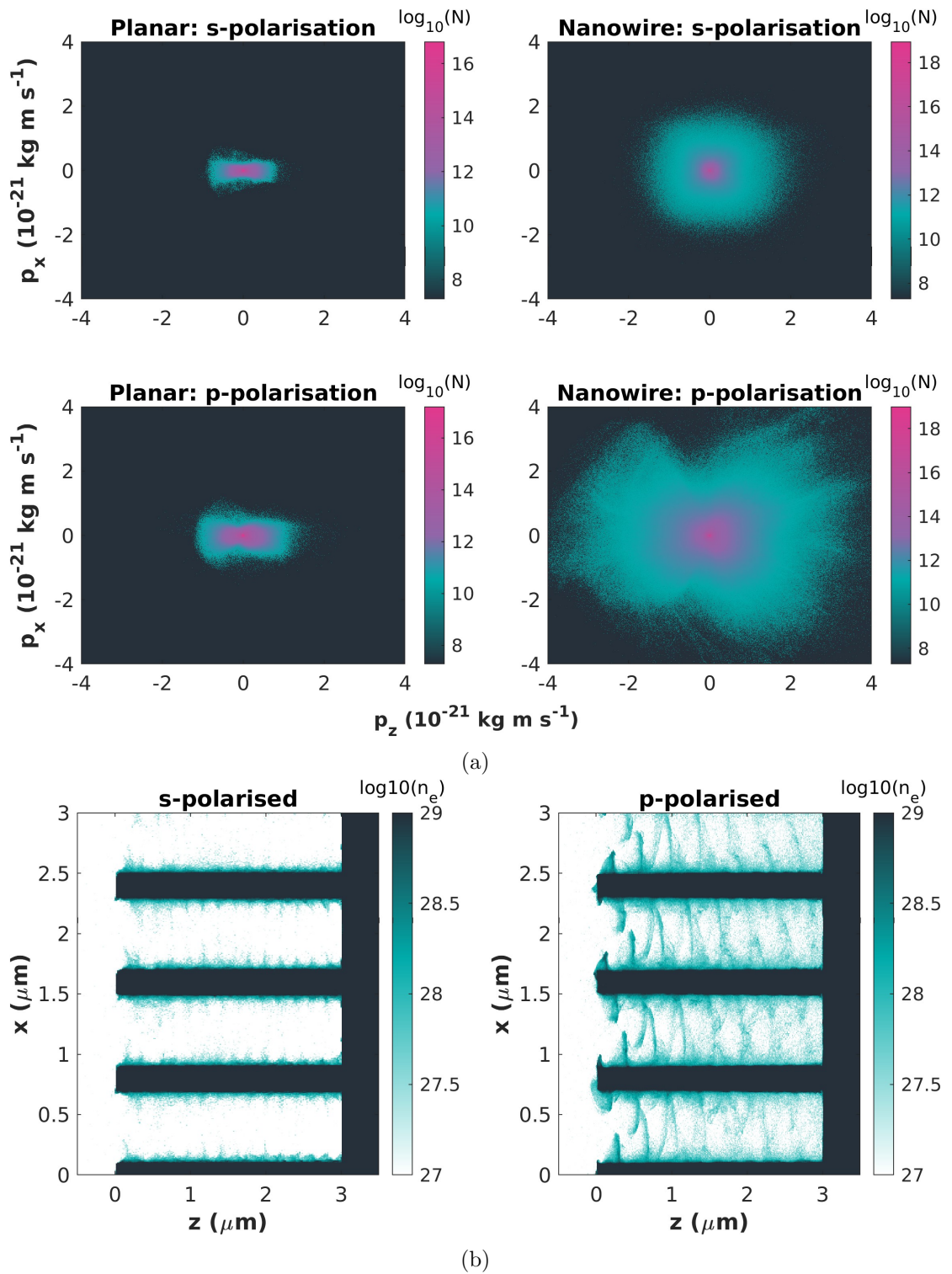


Figure 6.16: (a) $p_x - p_y$ phase space at $t = 75$ fs of electrons generated from s - and p -polarised interactions with planar and nanowire targets. (b) Number density of electrons in the wire region at $t = 45$ fs.

in the transverse (x) direction for the nanowire target compared to planar - this correlates with the ϵ_x emittance values estimated in the experiment, where a greater momenta from the nanowires was put forward. That being said, we must acknowledge an inherent issue with modelling in 2D in that we cannot capture the presence of wires in the y -direction. PIC simulation studies of intense laser interactions with nanowires by other groups (see e.g. Refs. [45, 51, 184]) propose the laser electric field directed into the density gradient along the lengths of the wires is capable of extracting electrons and pulling them into the vacuum, where they can then be accelerated in the forward direction by the $\mathbf{J} \times \mathbf{B}$ force. To this end a p -polarisation case is modelled as a substitute to explore the s -polarised laser with wires situated in the y -direction. The plot in Figure 6.16(a) shows the momenta range for the nanowire target is greatly increased in both the injected (z) and transverse (x) directions, highlighting the importance of the electric field component directed into the lengths of the wires for effective electron acceleration. This is illustrated in Figure 6.16(b), where the electron number density is shown around the wires at the time of peak laser irradiation. The electrons are more efficiently extracted from the wires for the p -polarised case, where a component of the laser electric field is able to be pointed in the x -direction.

Laser-electron coupling with nanowire targets has been reported elsewhere. A PIC study by Ji *et al.* [53] assessed the energy spectra of electrons generated in nanowire targets of diameter 0.5λ and vacuum gap size λ . The peak electron energy was comparable to a planar test case; however, a larger number of moderate energy electrons were generated, indicating a more stochastic regime of heating. In the work of Cristoforetti *et al.* [45] the importance of the dimensions of the wires on the final energy spectra of the electrons was emphasised. A difference in the heating of the population was distinguished as transitioning towards stochastic when the amplitude of the electron oscillation is greater than the gap size; in this situation the electron energy gain is limited by collisions with neighbouring wires, randomising their trajectories. The stochastic heating could result in a larger spread of transverse momenta of the electrons; this would be in agreement with the experimental measurements and result predicted by PIC simulation. Furthermore, in the experimental measurements we observed comparable estimates of electron emittance in the x - and y -directions for the nanowire targets; this could be evidence towards the argument of stochastic heating for these targets.

6.4 Summary and Conclusions

The experimental work presented in Chapters 4 and 5 was subject to an exceptional pre-pulse, likely resulting in the destruction of the nanowires prior to the arrival of the main laser pulse. A high contrast, frequency-doubled laser was implemented in a follow-up experiment in 2021 to explore a high intensity laser interaction with the nanowires whilst producing minimal pre-plasma. The exiting fast electrons were the focus of the investigation as a means of diagnosing the interaction.

Optical emission from the rear target surfaces of the nanowire targets and planar targets was imaged in an effort to observe and measure coherent optical transition radiation emission induced by the passage of the exiting fast electrons. In this experiment we did not yield any evidence of measurable CTR emission. PIC simulations of the ω_L and $2\omega_L$ interaction demonstrate frequency doubling the laser light produces a lower flux and a lower temperature of the fast electron population, following the $T_{hot} \propto (I\lambda^2)^{1/3}$ scaling by Beg *et al.* [178]. The frequency doubling process also reduces the laser energy by $\sim 80\%$, reducing the number of fast electrons generated. These effects mean the CTR production from the frequency-doubled interaction is greatly reduced compared to a fundamental frequency interaction, which can explain why we struggled to observe CTR for this particular campaign.

For a small number of shots a pepper-pot mask was used to estimate the emittance of the exiting fast electron beam. The use of the pepper-pot mask as a diagnostic is rare in laser-solid interactions, and is certainly novel for nanowire targets. Analysis of the pepper-pot data revealed a greater estimated electron emittance for the nanowire target in comparison to a planar target of comparable thickness. Since the fast electron beam encompassed the whole mask, we cannot comment on the spatial extent of the beam, but we can infer that a *greater transverse momenta* of electrons is realised with the use of nanowire targets. PIC simulations were carried out to confirm this argument for the targets employed in the experiment. To be able to model the laser field interaction with the wires more thoroughly the simulations were ran in both *s*- and *p*-polarisations. The *p*-polarisation case uncovered the importance of the ability of the laser *electric field* in oscillating electrons across the density gradient across the length of the wires. Plots of the $p_z - p_x$ phase space presented a greater spread in transverse momenta for the nanowires compared to the planar targets, in

agreement with the experimental conclusion. This finding marries well with previous work on nanowires of a similar geometry.

As part of the discussion on electron emittance from nanowires it should be noted that other work in the literature proposes a reduces emittance is possible from nanowires. For example, Jiang *et al.* [184] carried out 3D PIC simulations and found a collimation of the electrons with a narrow angular divergence for electrons with $E > 50$ MeV. In this study the wire dimensions were rather large with respect to the laser spot (gap size $2 \mu\text{m}$ and focal spot size $2.9 \mu\text{m}$) and the set-up was able to facilitate a direct laser acceleration scheme. An experiment reported by Zhao *et al.* [41] measured a comparable electron beam size at the front and rear side of irradiated nanobrush targets, and inferred guiding of the fast electrons was achieved by the wire structures. Since we did not capture the full spatial extent of the exiting fast electron beam in our experiment we cannot compare the result, but of course the spatial extent is the “second half” of the emittance measurement besides the momenta of the particles and this should be addressed in future work.

Chapter 7

Conclusions and Outlook

In this thesis the results of two distinct experimental campaigns irradiating nanowire targets have been presented. In this section the key findings from the experiments and their complementary computational studies are summarised and discussed the context of future work and relevance in the broader laser-plasma field.

7.1 Optical Transition Radiation from Preheated Planar and Nanowire Targets

The work described in Chapters 4 and 5 is centred around an experiment carried out in 2019 where measurements of coherent optical transition radiation (CTR) emission from the rear target surface were taken to characterise the performance of nanowire coated targets in ultra-intense laser interactions in comparison to planar foil targets. These measurements were implemented in an effort to investigate the exiting fast electrons at the rear surface of the targets. The brightness of CTR emission decreased when increasing the planar target thickness from $5\ \mu\text{m}$ to $12.5\ \mu\text{m}$, an expected result from the literature. Interestingly, when the planar target thickness was increased to $25\ \mu\text{m}$ the brightness of CTR emission was seen to increase where one would expect an appreciable decrease. Measurements of emission from the nanowire coated targets revealed a subset of shots where the CTR signal was significantly more intense with respect to planar targets of a comparable thickness.

An intense pre-pulse ($I \sim 10^{17}\ \text{W}/\text{cm}^2$) was discovered to have been present in this experiment. Particle-in-cell simulations were carried out to model the pre-pulse interaction

with the targets. It was found that the pre-pulse interaction was inefficient with respect to coupling into fast electrons. The number and temperature of the pre-pulse accelerated electrons was found to be too low to generate an observable amount of optical transition radiation, leading us to the conclusion that our experimental emission must originate from the main pulse interaction with the targets.

A computational study was undertaken to understand whether CTR emission was possible under the experimental conditions. The hydrodynamic simulations demonstrated the production of an extended pre-plasma at the front surface of the planar and nanowire targets. The results of EPOCH simulations propose that this pre-plasma facilitates the generation of super-ponderomotive electrons upon irradiation by a focused, ultra-intense laser pulse. Moreover, the nanowire-produced pre-plasma was predicted to be preferential for generating a greater yield of fast electrons described by a hotter electron temperature. This may explain the enhanced emission of CTR at the rear surface from the nanowire targets compared to planar targets. In both cases the fast electron population is favourable for efficient CTR emission from thicker (or expanded) targets, since fast electrons with a hotter temperature are less susceptible to bunch de-phasing.

The hydrodynamic simulations revealed the thinner planar and nanowire targets had a disrupted rear surface due to breakout of the shock-wave launched by the pre-pulse heating. Particle-in-cell simulations were carried out to explore the robustness of the coherent transition radiation mechanism under a disrupted rear surface. It was shown that emission in the optical region, around $2\omega_L$, remained at a comparable power relative to a steep density profile at the rear surface. In other words, the production of optical CTR is predicted to be insignificantly affected by the density scale length introduced by the shock break-out in our experiment.

One area for future work is a more detailed exploration of the hydrodynamic motion of the heated nanowires. This thesis presents one of the first instances of hydrodynamic modelling of the effect of a pre-pulse on nanostructures, and demonstrated a longer scale length pre-plasma is possible from nanowires relative to a comparable laser interaction with a planar target. However, due to computational restrictions the simulations were limited to considering an

equivalent energy deposition to planar targets, and to modelling the nanostructures in a 2D cylindrical geometry resulting in a ring-like representation instead of wires. We may therefore expect an enhanced absorption and a lower fill factor if the wires were modelled in a 3D geometry. This will impact the properties of the pre-plasma formed, and alter the properties of the fast electron produced from the main pulse interaction. Further modelling is unlikely to change the “net” result, in that the nanowires produce a lower density, longer scale length pre-plasma compared to planar targets. A more detailed study may however be useful as a predictive exercise in exploring nanostructured targets designed to produce an “optimal” pre-plasma for super-ponderomotive electrons. Whilst typically one would aim for a nanostructure interaction with as little pre-plasma as possible, this pre-plasma formation could be exploited to aid with generating a greater flux of high energy electrons at a lower laser energy and intensity.

7.2 Emittance of Fast Electrons Generated from Nanowire Targets

In Chapter 6 the details of an experimental campaign in 2021 with a frequency doubled laser pulse were presented, achieving a high-contrast intense laser interaction with nanowire targets. A pepper-pot diagnostic was implemented for the first time on nanowire targets to measure the exiting fast electrons. It is believed to also be a novel measurement from solid targets in general (the emittance of positrons as measured by a pepper-pot has been reported previously by Chen *et al.* [185]). The initial measurements indicate a larger emittance is realised for the exiting fast electrons produced from our nanowire targets compared to planar targets. EPOCH simulations demonstrated the interaction with nanowires is predicted to produce fast electrons with a larger spread in transverse momenta (i.e. in the radial direction), following a higher hot electron temperature compared to fast electrons generated from planar targets.

The scope for future progress on these emittance measurements from nanowire targets is plentiful and promising. The experimental campaign reported here implemented the pepper-pot diagnostic on two shots for nanowire targets, and two for planar targets. An obvious next step is to repeat the measurements on further shots and collect more statistics to confirm the

observations. An experiment was carried out recently at ILIL in March 2023 with a view of collecting more data with nanowire targets to validate our results of an increased emittance. Analysis on this experiment will begin in due course. In addition, it has been noted that there is a question as to whether we have captured the full fast electron beam size across the pepper-pot mask. In subsequent experiments a larger pepper-pot mask could be used as an approach to confirm the entire beam spot is sampled. Finally, these measurements can also be extended to nanowires with different dimensions. Previous literature has indicated a lower emittance is possible, e.g. Ref. [41], with other studies demonstrating a DLA-regime for certain wire dimensions which could be of interest in terms of guiding the fast electrons and reducing the emittance. Experimental measurements from nanowires with different dimensions could therefore be of importance to determine if there is an optimal parameter space for reduced electron emittance.

7.3 Future Prospects

The investigations of coherent transition radiation in preheated targets proved to be a fruitful avenue of research and hold relevance for the laser-plasma community going forwards. The experimental and simulation studies presented show that CTR emission in the optical regime is robust under the shock-breakout conditions experienced here. Future experiments with thin targets or with a laser profile with a low contrast may remain suitable for diagnosis via optical transition radiation emission. Careful characterisation of the shock breakout would be required to confirm this for each particular scenario. Ideally, a stronger shock would be preferred for retaining a steeper density profile at the rear surface. Overall, this work has demonstrated that optical CTR measurements remain possible for disrupted density profiles, and may help in guiding the choice of diagnostics implemented in future accelerated electron experiments.

In addition, the extended pre-plasma generated by the pre-pulse was determined to promote the production of super-ponderomotive electrons. It is suggested that these electrons are appropriate for propagation over thicker targets whilst retaining their bunching structure, rendering CTR emission possible when these electrons exit the target rear surface. It is proposed that an extended pre-plasma could be considered for the generation of high energy electrons; furthermore, since the bunching structures are retained a CTR diagnostic could

be implemented to investigate these electrons.

This thesis also reports on novel measurements using a pepper-pot diagnostic to estimate the emittance of the exiting fast electrons from planar and nanowire targets. A pepper-pot diagnostic is relatively simple to implement during an experiment, and can be extended to use on other laser-solid interactions as a means of diagnosing the exiting fast electrons. With respect to the measurements on nanowire targets, one proposed use of nanowire targets is as a fast electron source in fast ignition. These initial measurements suggest a higher emittance of nanowire-generated electrons, which is not beneficial when considering propagation over the distance of the generation to a hot spot. The emittance of the fast electron beam needs to be carefully controlled, and experimental pepper-pot measurements could play a key role in guiding future investigation and determining optimal structures.

List of References

- [1] D. Batani. Matter in extreme conditions produced by lasers. *EPL*, 114:65001, 2016.
- [2] T. H. Maiman. Stimulated optical radiation in ruby. *Nature*, 187:494, 1960.
- [3] A. L. Schawlow and C. H. Townes. Infrared and optical masers. *Physical Review*, 112:1940, 1958.
- [4] J. Nuckolls, L. Wood, A. Thiessen, and G. Zimmerman. Laser compression of matter to super-high densities: Thermonuclear (ctr) applications pressure: Implosion, ablation. *Nature*, 239:139, 1972.
- [5] N. G. Basov, I. Kertes, P. G. Kryukov, Y. A. Matveets, Y. V. Senatskif, and S. V. Chekalin. Nonlinear losses in generators and amplifiers of ultrashort light pulses. *Soviet Physics JETP*, 33:289, 1971.
- [6] D. Strickland and G. Mourou. Compression of amplified chirped optical pulses. *Optics Communications*, 56:219, 1985.
- [7] C. Danson, D. Hillier, N. Hopps, and D. Neely. Petawatt class lasers worldwide. *High Power Laser Science and Engineering*, 3:e3, 2015.
- [8] N. Booth, et al. Laboratory measurements of resistivity in warm dense plasmas relevant to the microphysics of brown dwarfs. *Nature Communications*, 6:8742, 2015.
- [9] D. Kraus, et al. Formation of diamonds in laser-compressed hydrocarbons at planetary interior conditions. *Nature Astronomy*, 1:606, 2017.
- [10] H. Terasaki, T. Sakaiya, K. Shigemori, K. Akimoto, H. Kato, Y. Hironaka, and T. Kondo. In situ observation of the rayleigh-taylor instability of liquid fe and fe-

- si alloys under extreme conditions: Implications for planetary core formation. *Matter and Radiation at Extremes*, 6:054403, 2021.
- [11] J. Meinecke, et al. Turbulent amplification of magnetic fields in laboratory laser-produced shock waves. *Nature Physics*, 10:520, 2014.
- [12] A. Macchi, M. Borghesi, and M. Passoni. Ion acceleration by superintense laser-plasma interaction. *Reviews of Modern Physics*, 85:751, 2013.
- [13] M. Roth and M. Schollmeier. Ion acceleration-target normal sheath acceleration. In *CAS-CERN Accelerator School: Plasma Wake Acceleration 2014, Proceedings*, pages 231–270. CERN, 2014.
- [14] C. Reich, P. Gibbon, I. Uschmann, and E. Förster. Yield optimization and time structure of femtosecond laser plasma ka sources. *Physical Review Letters*, 84:4846, 2000.
- [15] P. A. Norreys, et al. Observation of a highly directional γ -ray beam from ultrashort, ultraintense laser pulse interactions with solids. *Physics of Plasmas*, 6:2150, 1999.
- [16] A. B. Zylstra, et al. Burning plasma achieved in inertial fusion. *Nature*, 601:542, 2022.
- [17] A. L. Kritcher, et al. Design of inertial fusion implosions reaching the burning plasma regime. *Nature Physics*, 18:251, 2022.
- [18] H. Abu-Shawareb, et al. Lawson criterion for ignition exceeded in an inertial fusion experiment. *Physical Review Letters*, 129:075001, 2022.
- [19] K. B. Wharton, S. P. Hatchett, S. C. Wilks, M. H. Key, J. D. Moody, V. Yanovsky, A. A. Offenberger, B. A. Hammel, M. D. Perry, and C. Joshi. Experimental measurements of hot electrons generated by ultraintense ($\sim 10^{19}$ W/cm²) laser-plasma interactions on solid-density targets. *Physical Review Letters*, 81:822, 1998.
- [20] E. Martinolli, M. Koenig, F. Amiranoff, S. D. Baton, L. Gremillet, J. J. Santos, T. A. Hall, M. Rabec-Le-Gloahec, C. Rousseaux, and D. Batani. Fast electron heating of a solid target in ultrahigh-intensity laser pulse interaction. *Physical Review E - Statistical Physics, Plasmas, Fluids, and Related Interdisciplinary Topics*, 70:055402(R), 2004.

- [21] L. J. Bae, et al. Diagnosis of warm dense conditions in foil targets heated by intense femtosecond laser pulses using $k\alpha$ imaging spectroscopy. *Optics Express*, 26:6294, 2018.
- [22] M. Tabak, J. Hammer, M. E. Glinsky, W. L. Kruer, S. C. Wilks, J. Woodworth, E. M. Campbell, M. D. Perry, and R. J. Mason. Ignition and high gain with ultrapowerful lasers. *Physics of Plasmas*, 1:1626, 1994.
- [23] M. H. Key, et al. Hot electron production and heating by hot electrons in fast ignitor research. *Physics of Plasmas*, 5:1966, 2002.
- [24] J. J. Honrubia and J. Meyer-Ter-Vehn. Fast ignition of fusion targets by laser-driven electrons. *Plasma Physics and Controlled Fusion*, 51:014008, 2009.
- [25] C. Bellei, L. Divol, A. J. Kemp, M. H. Key, D. J. Larson, D. J. Strozzi, M. M. Marinak, M. Tabak, and P. K. Patel. Fast ignition: Dependence of the ignition energy on source and target parameters for particle-in-cell-modelled energy and angular distributions of the fast electrons. *Physics of Plasmas*, 20:052704, 2013.
- [26] A. J. Kemp, F. Fiuza, A. Debayle, T. Johzaki, W. B. Mori, P. K. Patel, Y. Sentoku, and L. O. Silva. Laser-plasma interactions for fast ignition. *Nuclear Fusion*, 54:054002, 2014.
- [27] R. A. Snavely, et al. Intense high-energy proton beams from petawatt-laser irradiation of solids. *Physical Review Letters*, 85:2945, 2000.
- [28] C. M. Brenner, et al. High energy conversion efficiency in laser-proton acceleration by controlling laser-energy deposition onto thin foil targets. *Applied Physics Letters*, 104:081123, 2014.
- [29] A. P. L. Robinson and M. Sherlock. Magnetic collimation of fast electrons produced by ultraintense laser irradiation by structuring the target composition. *Physics of Plasmas*, 14:083105, 2007.
- [30] S. Kar, A. P. L. Robinson, D. C. Carroll, O. Lundh, K. Markey, P. McKenna, P. Norreys, and M. Zepf. Guiding of relativistic electron beams in solid targets by resistively controlled magnetic fields. *Physical Review Letters*, 102:055001, 2009.

- [31] Y. Ji, G. Jiang, W. Wu, C. Wang, Y. Gu, and Y. Tang. Efficient generation and transportation of energetic electrons in a carbon nanotube array target. *Applied Physics Letters*, 96:041504, 2010.
- [32] G. Cristoforetti, et al. Laser-driven proton acceleration via excitation of surface plasmon polaritons into tio2 nanotube array targets. *Plasma Physics and Controlled Fusion*, 62:114001, 2020.
- [33] M. Passoni, et al. Toward high-energy laser-driven ion beams: Nanostructured double-layer targets. *Physical Review Accelerators and Beams*, 19:061301, 2016.
- [34] H. A. Sumeruk, et al. Hot electron and x-ray production from intense laser irradiation of wavelength-scale polystyrene spheres. *Physics of Plasmas*, 14:062704, 2007.
- [35] P. P. Rajeev, P. Taneja, P. Ayyub, A. S. Sandhu, and G. R. Kumar. Metal nanoplasmas as bright sources of hard x-ray pulses. *Physical Review Letters*, 90:4, 2003.
- [36] A. Zigler, et al. Enhanced proton acceleration by an ultrashort laser interaction with structured dynamic plasma targets. *Physical Review Letters*, 110:215004, 2013.
- [37] G. Kulcsár, D. Almawlawi, F. W. Budnik, P. R. Herman, M. Moskovits, L. Zhao, and R. S. Marjoribanks. Intense picosecond x-ray pulses from laser plasmas by use of nanostructured "velvet" targets. *Physical Review Letters*, 84:5149, 2000.
- [38] Z. Samsonova, et al. Hard x-ray generation from zno nanowire targets in a non-relativistic regime of laser-solid interactions. *Applied Sciences (Switzerland)*, 8:1728, 2018.
- [39] S. Mondal, et al. Highly enhanced hard x-ray emission from oriented metal nanorod arrays excited by intense femtosecond laser pulses. *Physical Review B - Condensed Matter and Materials Physics*, 83:035408, 2011.
- [40] M. A. Purvis, et al. Relativistic plasma nanophotonics for ultrahigh energy density physics. *Nature Photonics*, 7:796, 2013.
- [41] Z. Zhao, et al. Acceleration and guiding of fast electrons by a nanobrush target. *Physics of Plasmas*, 17:123108, 2010.

- [42] P. Singh, et al. Efficient generation and guiding of megaampere relativistic electron current by silicon nanowires. *Applied Physics Letters*, 100:244104, 2012.
- [43] S. Jiang, et al. Microengineering laser plasma interactions at relativistic intensities. *Physical Review Letters*, 116:085002, 2016.
- [44] A. Moreau, et al. Enhanced electron acceleration in aligned nanowire arrays irradiated at highly relativistic intensities. *Plasma Physics and Controlled Fusion*, 62:014013, 2020.
- [45] G. Cristoforetti, et al. Transition from coherent to stochastic electron heating in ultra-short relativistic laser interaction with structured targets. *Scientific Reports*, 7:1479, 2017.
- [46] D. Sarkar, et al. Silicon nanowire based high brightness, pulsed relativistic electron source. *APL Photonics*, 2:066105, 2017.
- [47] D. Khaghani, et al. Enhancing laser-driven proton acceleration by using micro-pillar arrays at high drive energy. *Scientific Reports*, 7:11366, 2017.
- [48] S. Vallières, et al. Enhanced laser-driven proton acceleration using nanowire targets. *Scientific Reports*, 11:2226, 2021.
- [49] A. Curtis, et al. Micro-scale fusion in dense relativistic nanowire array plasmas. *Nature Communications*, 9:1077, 2018.
- [50] S. Mondal, et al. Aligned copper nanorod arrays for highly efficient generation of intense ultra-broadband thz pulses. *Scientific Reports*, 7:40058, 2017.
- [51] L. Cao, Y. Gu, Z. Zhao, L. Cao, W. Huang, W. Zhou, X. T. He, W. Yu, and M. Y. Yu. Enhanced absorption of intense short-pulse laser light by subwavelength nanolayered target. *Physics of Plasmas*, 17:043103, 2010.
- [52] V. Kaymak, A. Pukhov, V. N. Shlyaptsev, and J. J. Rocca. Nanoscale ultradense z-pinch formation from laser-irradiated nanowire arrays. *Physical Review Letters*, 117:035004, 2016.

- [53] L. Ji, S. Jiang, A. Pukhov, R. Freeman, and K. Akli. Exploring novel target structures for manipulating relativistic laser-plasma interaction. *High Power Laser Science and Engineering*, 5:1, 2017.
- [54] G. Cristoforetti, et al. Investigation on laser-plasma coupling in intense, ultrashort irradiation of a nanostructured silicon target. *Plasma Physics and Controlled Fusion*, 56:095001, 2014.
- [55] E. Eftekhari-Zadeh, M. S. Blümcke, Z. Samsonova, R. Loetzsch, I. Uschmann, M. Zapf, C. Ronning, O. N. Rosmej, D. Kartashov, and C. Spielmann. Laser energy absorption and x-ray generation in nanowire arrays irradiated by relativistically intense ultra-high contrast femtosecond laser pulses. *Physics of Plasmas*, 29:013301, 2022.
- [56] Z. Samsonova, et al. Relativistic interaction of long-wavelength ultrashort laser pulses with nanowires. *Physical Review X*, 9:021029, 2019.
- [57] L. A. Gizzi, L. Labate, F. Baffigi, F. Brandi, G. Bussolino, L. Fulgentini, P. Köster, and D. Palla. Overview and specifications of laser and target areas at the intense laser irradiation laboratory. *High Power Laser Science and Engineering*, 9, 2021.
- [58] P. Gibbon. Introduction to plasma physics. In *CAS-CERN Accelerator School: Plasma Wake Acceleration 2014, Proceedings*, pages 51–65. 2014.
- [59] S. Keppler, A. Sävert, J. Körner, M. Hornung, H. Liebetrau, J. Hein, and M. C. Kaluza. The generation of amplified spontaneous emission in high-power cpa laser systems. *Laser and Photonics Reviews*, 10:264, 2016.
- [60] P. Agostini, F. Fabre, G. Mainfray, G. Petite, and N. K. Rahman. Free-free transitions following six-photon ionization of xenon atoms. *Physical Review Letters*, 42:281, 1977.
- [61] S. Augst, D. Strickland, D. D. Meyerhofer, S. L. Chin, and H. Eberly. Tunneling ionization of noble gases in a high-intensity laser field. *Physical Review Letters*, 63:2212, 1989.
- [62] L. V. Keldysh. Ionization in the field of a strong electromagnetic wave. *J. Exptl. Theoret. Phys. (U.S.S.R.)*, 20:1307, 1965.
- [63] N. B. Delone and V. P. Krainov. Tunneling and barrier-suppression ionization of atoms and ions in a laser radiation field. *Physics - Uspekhi*, 41:469, 1998.

- [64] T. Z. Esirkepov, et al. Prepulse and amplified spontaneous emission effects on the interaction of a petawatt class laser with thin solid targets. *Nuclear Instruments and Methods in Physics Research, Section A: Accelerators, Spectrometers, Detectors and Associated Equipment*, 745:150, 2014.
- [65] W. L. Kruer. *The Physics of Laser Plasma Interactions*. Westview Press, 1st edition, 2003.
- [66] P. Kaw and J. Dawson. Relativistic nonlinear propagation of laser beams in cold overdense plasmas. *The Physics of Fluids*, 13:472, 1970.
- [67] S. C. Wilks and W. L. Kruer. Absorption of ultrashort, ultra-intense laser light by solids and overdense plasmas. *IEEE Journal of Quantum Electronics*, 33:1954, 1997.
- [68] G. J. Tallents. *An introduction to the atomic and radiation physics of plasmas*. Cambridge University Press, 2018.
- [69] J. P. Freidberg, R. W. Mitchell, R. L. Morse, and L. I. Rudinski. Resonant absorption of laser light by plasma targets. *Phys. Rev. Lett*, 28:795, 1972.
- [70] G. J. Pert. The analytic theory of linear resonant absorption. *Plasma Physics*, 20:175, 1978.
- [71] D. W. Forslund, J. M. Kindel, and K. Lee. Theory of hot-electron spectra at high laser intensity. *Physical Review Letters*, 39:284, 1977.
- [72] F. Brunel. Not-so-resonant, resonant absorption. *Physical Review Letters*, 59:52, 1987.
- [73] P. Gibbon and A. R. Bell. Collisionless absorption in sharp-edged plasmas. *Physical Review Letters*, 68:1535, 1992.
- [74] H. Hora. *Laser Plasma Physics: Forces and the Nonlinearity Principle*. SPIE Press, second edition edition, 2014.
- [75] W. L. Kruer and K. Estabrook. Jxb heating by very intense laser light. *Physics of Fluids*, 28:430, 1985.
- [76] S. C. Wilks, W. L. Kruer, M. Tabak, and A. B. Langdon. Absorption of ultra-intense laser pulses. *Physical Review Letters*, 69:1383, 1992.

- [77] M. Sherlock. Universal scaling of the electron distribution function in one-dimensional simulations of relativistic laser-plasma interactions. *Physics of Plasmas*, 16, 2009.
- [78] A. Pukhov, Z. M. Sheng, and J. M. ter Vehn. Particle acceleration in relativistic laser channels. *Physics of Plasmas*, 6:2847, 1999.
- [79] S. P. Mangles, et al. Electron acceleration in cavitated channels formed by a petawatt laser in low-density plasma. *Physical Review Letters*, 94:245001, 2005.
- [80] L. Willingale, et al. Surface waves and electron acceleration from high-power, kilojoule-class laser interactions with underdense plasma. *New Journal of Physics*, 15:025023, 2013.
- [81] A. V. Arefiev, B. N. Breizman, M. Schollmeier, and V. N. Khudik. Parametric amplification of laser-driven electron acceleration in underdense plasma. *Physical Review Letters*, 108:145004, 2012.
- [82] A. P. Robinson, A. V. Arefiev, and D. Neely. Generating "superponderomotive" electrons due to a non-wake-field interaction between a laser pulse and a longitudinal electric field. *Physical Review Letters*, 111:065002, 2013.
- [83] A. R. Bell, J. R. Davies, S. Guerin, and H. Ruhl. Fast-electron transport in high-intensity short-pulse laser–solid experiments. *Plasma Physics and Controlled Fusion*, 39:653, 1997.
- [84] J. R. Davies. Electric and magnetic field generation and target heating by laser-generated fast electrons. *Physical Review E - Statistical Physics, Plasmas, Fluids, and Related Interdisciplinary Topics*, 68:056404, 2003.
- [85] M. S. Wei, et al. Observations of the filamentation of high-intensity laser-produced electron beams. *Physical Review E - Statistical Physics, Plasmas, Fluids, and Related Interdisciplinary Topics*, 70:056412, 2004.
- [86] E. S. Weibel. Spontaneously growing transverse waves in a plasma due to an anisotropic velocity distribution. *Physical Review Letters*, 2:83, 1959.
- [87] A. Bret, M. C. Firpo, and C. Deutsch. Characterization of the initial filamentation of a relativistic electron beam passing through a plasma. *Physical Review Letters*, 94:1, 2005.

- [88] J. S. Green, et al. Effect of laser intensity on fast-electron-beam divergence in solid-density plasmas. *Physical Review Letters*, 100:015003, 2008.
- [89] K. L. Lancaster, et al. Measurements of energy transport patterns in solid density laser plasma interactions at intensities of 5×10^{20} wcm⁻². *Physical Review Letters*, 98:125002, 2007.
- [90] R. B. Stephens, et al. Ka fluorescence measurement of relativistic electron transport in the context of fast ignition. *Physical Review E - Statistical Physics, Plasmas, Fluids, and Related Interdisciplinary Topics*, 69:066414, 2004.
- [91] M. Storm, et al. High-current, relativistic electron-beam transport in metals and the role of magnetic collimation. *Physical Review Letters*, 102:235004, 2009.
- [92] J. C. Adam, A. Héron, and G. Laval. Dispersion and transport of energetic particles due to the interaction of intense laser pulses with overdense plasmas. *Physical Review Letters*, 97:205006, 2006.
- [93] A. Debayle, J. J. Honrubia, E. D'Humières, and V. T. Tikhonchuk. Divergence of laser-driven relativistic electron beams. *Physical Review E - Statistical, Nonlinear, and Soft Matter Physics*, 82:036405, 2010.
- [94] C. D. Armstrong, et al. Bremsstrahlung emission profile from intense laser-solid interactions as a function of laser focal spot size. *Plasma Physics and Controlled Fusion*, 61:034001, 2019.
- [95] C. B. Schroeder, E. Esarey, J. van Tilborg, and W. P. Leemans. Theory of coherent transition radiation generated at a plasma-vacuum interface. *Physical Review E - Statistical Physics, Plasmas, Fluids, and Related Interdisciplinary Topics*, 69:016501, 2004.
- [96] A. P. Kobzev. On the radiation mechanism of a uniformly moving charge. *Physics of Particles and Nuclei*, 45:628, 2014.
- [97] C. Bellei, J. R. Davies, P. K. Chauhan, and Z. Najmudin. Coherent transition radiation in relativistic lasersolid interactions. *Plasma Physics and Controlled Fusion*, 54:035011, 2012.

- [98] J. Zheng, K. A. Tanaka, T. Miyakoshi, Y. Kitagawa, R. Kodama, T. Kurahashi, and T. Yamanaka. Theoretical study of transition radiation from hot electrons generated in the laser-solid interaction. *Physics of Plasmas*, 10:2994, 2003.
- [99] U. Happek, A. J. Siever, and E. B. Blum. Observation of coherent transition radiation. *Physical Review Letters*, 67:2962, 1991.
- [100] H. Popescu, et al. Subfemtosecond, coherent, relativistic, and ballistic electron bunches generated at ω_0 and $2\omega_0$ in high intensity laser-matter interaction. *Physics of Plasmas*, 12:063106, 2005.
- [101] S. D. Baton, et al. Evidence of ultrashort electron bunches in laser-plasma interactions at relativistic intensities. *Physical Review Letters*, 91:105001, 2003.
- [102] M. Manclossi, J. J. Santos, D. Batani, J. Faure, A. Debayle, V. T. Tikhonchuk, and V. Malka. Study of ultraintense laser-produced fast-electron propagation and filamentation in insulator and metal foil targets by optical emission diagnostics. *Physical Review Letters*, 96:125002, 2006.
- [103] L. C. L. Yuan, C. L. Wang, H. Uto, and S. Prunster. Formation-zone effect in transition radiation due to ultrarelativistic particles. *Physical Review Letters*, 25:1513, 1970.
- [104] C. Bellei. *Measurements of Optical Radiation from High-Intensity Laser-Plasma Interactions*. Ph.D. thesis, Imperial College London, 2009.
- [105] S. Buffechoux, et al. Hot electrons transverse refluxing in ultraintense laser-solid interactions. *Physical Review Letters*, 105, 2010.
- [106] C. P. Ridgers, M. Sherlock, R. G. Evans, A. P. Robinson, and R. J. Kingham. Superluminal sheath-field expansion and fast-electron-beam divergence measurements in laser-solid interactions. *Physical Review E - Statistical, Nonlinear, and Soft Matter Physics*, 83:036404, 2011.
- [107] S. C. Wilks, A. B. Langdon, T. E. Cowan, M. Roth, M. Singh, S. Hatchett, M. H. Key, D. Pennington, A. MacKinnon, and R. A. Snavely. Energetic proton generation in ultra-intense laser-solid interactions. *Physics of Plasmas*, 8:542, 2001.
- [108] H. Schmitz. Target normal sheath acceleration sheath fields for arbitrary electron energy distribution. *Physics of Plasmas*, 19:083115, 2012.

- [109] Y. Sentoku, T. E. Cowan, A. Kemp, and H. Ruhl. High energy proton acceleration in interaction of short laser pulse with dense plasma target. *Physics of Plasmas*, 10:2009, 2003.
- [110] K. L. Lancaster, et al. Observation of extremely strong shock waves in solids launched by petawatt laser heating. *Physics of Plasmas*, 24, 2017.
- [111] A. J. Mackinnon, M. Borghesi, S. Hatchett, M. H. Key, P. K. Patel, H. Campbell, A. Schiavi, R. Snavely, S. C. Wilks, and O. Willi. Effect of plasma scale length on multi-mev proton production by intense laser pulses. *Physical Review Letters*, 86:1769, 2001.
- [112] M. Kaluza, J. Schreiber, M. I. Santala, G. D. Tsakiris, K. Eidmann, J. Meyer-Ter-Vehn, and K. J. Witte. Influence of the laser prepulse on proton acceleration in thin-foil experiments. *Physical Review Letters*, 93:045003, 2004.
- [113] P. Tournois. Acousto-optic programmable dispersive filter for adaptive compensation of group delay time dispersion in laser systems. *Optics Communications*, 140:245, 1997.
- [114] B. Dromey, S. Kar, M. Zepf, and P. Foster. The plasma mirror - a subpicosecond optical switch for ultrahigh power lasers. *Review of Scientific Instruments*, 75:645, 2004.
- [115] V. Krylov, A. Rebane, A. G. Kalintsev, H. Schworer, and U. P. Wild. Second-harmonic generation of amplified femtosecond ti:sapphire laser pulses. *Optics Letters*, 20:198, 1995.
- [116] M. Aoyama, T. Harimoto, J. Ma, Y. Akahane, and K. Yamakawa. Second-harmonic generation of ultra-high intensity femtosecond pulses with a kdp crystal. *Optics Express*, 9:579, 2001.
- [117] R. Boyd. *Nonlinear Optics*. Academic Press, 3rd edition, 2008.
- [118] P. D. Maker, R. Terhune, M. Nisenoff, and C. M. Savage. Effects of dispersion and focusing on the production of optical harmonics. *Physical Review Letters*, 8:21, 1962.
- [119] J. Blakeney, H. Quevedo, G. M. Dyer, and T. Ditmire. Characterization of laser produced hot electron propagation via coherent transition radiation in cold and warm dense aluminum. *Physics of Plasmas*, 27:123105, 2020.

- [120] C. Bellei, et al. Micron-scale fast electron filaments and recirculation determined from rear-side optical emission in high-intensity laser-solid interactions. *New Journal of Physics*, 12:073016, 2010.
- [121] J. J. Santos, A. Debayle, P. Nicolai, V. Tikhonchuk, M. Manclossi, D. Batani, A. Guemnie-Tafo, J. Faure, V. Malka, and J. J. Honrubia. Fast electron transport and induced heating in aluminium foils. *Physics of Plasmas*, 14:103107, 2007.
- [122] Y. Ping, et al. Absorption of short laser pulses on solid targets in the ultrarelativistic regime. *Physical Review Letters*, 100, 2008.
- [123] L. Veisz, W. Theobald, T. Feurer, H. Schillinger, P. Gibbon, R. Sauerbrey, and M. S. Jovanović. Three-halves harmonic emission from femtosecond laser produced plasmas. *Physics of Plasmas*, 9:3197, 2002.
- [124] A. Tarasevitch, C. Dietrich, C. Blome, K. Sokolowski-Tinten, and D. von der Linde. 3/2 harmonic generation by femtosecond laser pulses in steep-gradient plasmas. *Physical Review E - Statistical Physics, Plasmas, Fluids, and Related Interdisciplinary Topics*, 68:026410, 2003.
- [125] M. Salvadori, et al. Accurate spectra for high energy ions by advanced time-of-flight diamond-detector schemes in experiments with high energy and intensity lasers. *Scientific Reports*, 11:3071, 2021.
- [126] G. Milluzzo, et al. A new energy spectrum reconstruction method for time-of-flight diagnostics of high-energy laser-driven protons. *Review of Scientific Instruments*, 90:083303, 2019.
- [127] M. Marinelli, et al. Analysis of laser-generated plasma ionizing radiation by synthetic single crystal diamond detectors. *Applied Surface Science*, 272:104, 2013.
- [128] G. Bertuccio, D. Puglisi, L. Torrisi, and C. Lanzieri. Silicon carbide detector for laser-generated plasma radiation. *Applied Surface Science*, 272:128, 2013.
- [129] S. Nakamura, et al. Real-time optimization of proton production by intense short-pulse laser with time-of-flight measurement. *Japanese Journal of Applied Physics, Part 2: Letters*, 45:L913, 2006.

- [130] V. Shpakov, et al. First emittance measurement of the beam-driven plasma wakefield accelerated electron beam. *Physical Review Accelerators and Beams*, 24, 2021.
- [131] R. Pompili, et al. Energy spread minimization in a beam-driven plasma wakefield accelerator. *Nature Physics*, 17:499, 2021.
- [132] M. Zhang. Emittance formula for slits and pepper-pot measurement. Technical report, Fermi-lab-TM-1988, 1996.
- [133] T. D. Arber, et al. Contemporary particle-in-cell approach to laser-plasma modelling. *Plasma Physics and Controlled Fusion*, 57, 2015.
- [134] T. Esirkepov. Exact charge conservation scheme for particle-in-cell simulation with an arbitrary form-factor. *Computer Physics Communications*, 135:144, 2001.
- [135] R. Courant, K. Friedrichs, and H. Lewy. On the partial difference equations of mathematical physics. *IBM Journal of Research and Development*, 11:215, 1967.
- [136] A. B. Langdon. Effects of the spatial grid in simulation plasmas. *Journal of Computational Physics*, 6:247, 1970.
- [137] H. Okuda. Nonphysical noises and instabilities in plasma simulation due to a spatial grid. *Journal of Computational Physics*, 10:475, 1972.
- [138] W. J. Ding and Z. M. Sheng. Sub gv/cm terahertz radiation from relativistic laser-solid interactions via coherent transition radiation. *Physical Review E*, 93, 2016.
- [139] J. R. Angus, A. Link, A. Friedman, D. Ghosh, and J. D. Johnson. On numerical energy conservation for an implicit particle-in-cell method coupled with a binary monte-carlo algorithm for coulomb collisions. *Journal of Computational Physics*, 456:111030, 2022.
- [140] B. Fryxell, K. Olson, P. Ricker, F. X. Timmes, M. Zingale, D. Q. Lamb, P. Macneice, R. Rosner, J. W. Truran, and H. Tufo2. Flash: An adaptive mesh hydrodynamics code for modeling astrophysical thermonuclear flashes. *The Astrophysical Journal Supplement Series*, 131:273, 2000.
- [141] J. J. MacFarlane, I. E. Golovkin, and P. R. Woodruff. Helios-cr - a 1-d radiation-magnetohydrodynamics code with inline atomic kinetics modeling. *Journal of Quantitative Spectroscopy and Radiative Transfer*, 99:381, 2006.

- [142] M. R. Zaghoul. Rosseland and planck mean and multi-group opacities of weakly non-ideal fibre plasma. *Plasma Physics and Controlled Fusion*, 49:1129, 2007.
- [143] R. P. Drake. *High-Energy-Density Physics*. Springer, 2006.
- [144] P. Macneice, K. M. Olson, C. Mobarri, R. D. Fainchtein, and C. Packer. Paramesh: A parallel adaptive mesh refinement community toolkit program summary. *Computer Physics Communications*, 126:330, 2000.
- [145] R. Löhner. An adaptive finite element scheme for transient problems in cfd. *Computer Methods in Applied Mechanics and Engineering*, 61:323, 1987.
- [146] J. T. Larsen and S. M. Lane. Hyades - a plasma hydrodynamics code for dense plasma studies. *J Quant. Spectrosc. Radiat. Transfer*, 51:179, 1994.
- [147] A. M. Rubenchik, M. D. Feit, M. D. Perry, and J. T. Larsen. Numerical simulation of ultra-short laser pulse energy deposition and bulk transport for material processing 1. *Applied Surface Science*, 127:193, 1998.
- [148] D. Turnbull, A. V. Maximov, D. H. Edgell, W. Seka, R. K. Follett, J. P. Palastro, D. Cao, V. N. Goncharov, C. Stoeckl, and D. H. Froula. Anomalous absorption by the two-plasmon decay instability. *Physical Review Letters*, 124:185001, 2020.
- [149] D. S. Montgomery. Two decades of progress in understanding and control of laser plasma instabilities in indirect drive inertial fusion. *Physics of Plasmas*, 23:055601, 2016.
- [150] L. Veisz, W. Theobald, T. Feurer, H. Schwoerer, I. Uschmann, O. Renner, and R. Sauerbrey. Three-halves harmonic emission from femtosecond laser produced plasmas with steep density gradients. *Physics of Plasmas*, 11:3311, 2004.
- [151] J. Zheng, K. A. Tanaka, T. Sato, T. Yabuuchi, T. Kurahashi, Y. Kitagawa, R. Kodama, T. Norimatsu, and T. Yamanaka. Study of hot electrons by measurement of optical emission from the rear surface of a metallic foil irradiated with ultraintense laser pulse. *Physical Review Letters*, 92:165001, 2004.
- [152] J. J. Santos, et al. Fast electron transport in ultraintense laser pulse interaction with solid targets by rear-side self-radiation diagnostics. *Physical Review Letters*, 89:025001, 2002.

- [153] A. J. Mackinnon, Y. Sentoku, P. K. Patel, D. W. Price, S. Hatchett, M. H. Key, C. Andersen, R. Snavely, and R. R. Freeman. Enhancement of proton acceleration by hot-electron recirculation in thin foils irradiated by ultraintense laser pulses. *Physical Review Letters*, 88:2150061, 2002.
- [154] L. A. Gizzi, et al. Enhanced laser-driven proton acceleration via improved fast electron heating in a controlled pre-plasma. *Scientific Reports*, 11, 2021.
- [155] Y. Takagi, N. Iwata, E. D’Humieres, and Y. Sentoku. Multivariate scaling of maximum proton energy in intense laser driven ion acceleration. *Physical Review Research*, 3:043140, 2021.
- [156] M. Shaikh, K. Jana, A. D. Lad, I. Dey, S. L. Roy, D. Sarkar, Y. M. Ved, A. P. Robinson, J. Pasley, and G. R. Kumar. Tracking ultrafast dynamics of intense shock generation and breakout at target rear. *Physics of Plasmas*, 25, 2018.
- [157] P. K. Singh, Y. Q. Cui, A. Adak, A. D. Lad, G. Chatterjee, P. Brijesh, Z. M. Sheng, and G. R. Kumar. Contrasting levels of absorption of intense femtosecond laser pulses by solids. *Scientific Reports*, 5:17870, 2015.
- [158] R. H. Scott, et al. A study of fast electron energy transport in relativistically intense laser-plasma interactions with large density scalelengths. *Physics of Plasmas*, 19, 2012.
- [159] S. M. Osipov, K. Y. Platonov, and A. A. Andreev. Influence of an ambipolar field and target boundary blurring on transition radiation from fast electrons of laser plasma. *Optics and Spectroscopy (English translation of Optika i Spektroskopiya)*, 104:337, 2008.
- [160] G. J. Pert. Two-dimensional hydrodynamic models of laser-produced plasmas. *Journal of Plasma Physics*, 41:263, 1989.
- [161] J. R. Davies, A. R. Bell, M. G. Haines, and S. M. Gué. Short-pulse high-intensity laser-generated fast electron transport into thick solid targets. *Physical Review E - Statistical Physics, Plasmas, Fluids, and Related Interdisciplinary Topics*, 56, 1997.
- [162] J. J. Honrubia, M. Kaluza, J. Schreiber, G. D. Tsakiris, and J. Meyer-Ter-Vehn. Laser-driven fast-electron transport in preheated foil targets. *Physics of Plasmas*, 12:1, 2005.

- [163] J. S. Green, et al. Time-resolved measurements of fast electron recirculation for relativistically intense femtosecond scale laser-plasma interactions. *Scientific Reports*, 8:4525, 2018.
- [164] S. V. Bulanov, T. Z. Esirkepov, M. Kando, A. S. Pirozhkov, and N. N. Rosanov. Relativistic mirrors in plasmas — novel results and perspectives. *Uspekhi Fizicheskikh Nauk*, 183:449, 2013.
- [165] F. Quéré, C. Thauray, P. Monot, S. Dobosz, P. Martin, J. P. Geindre, and P. Audebert. Coherent wake emission of high-order harmonics from overdense plasmas. *Physical Review Letters*, 96:125004, 2006.
- [166] B. Dromey, et al. Coherent synchrotron emission from electron nanobunches formed in relativistic laser-plasma interactions. *Nature Physics*, 8:804, 2012.
- [167] D. R. Rusby, C. D. Armstrong, G. G. Scott, M. King, P. McKenna, and D. Neely. Effect of rear surface fields on hot, refluxing and escaping electron populations via numerical simulations. *High Power Laser Science and Engineering*, 7:e45, 2019.
- [168] J. L. Shaw, N. Lemos, K. A. Marsh, F. S. Tsung, W. B. Mori, and C. Joshi. Estimation of direct laser acceleration in laser wakefield accelerators using particle-in-cell simulations. *Plasma Physics and Controlled Fusion*, 58:034008, 2016.
- [169] D. Levy, X. Davoine, A. Debayle, L. Gremillet, and V. Malka. Enhanced laser-driven proton acceleration with gas-foil targets. *Journal of Plasma Physics*, 86:905860608, 2020.
- [170] A. Poyé, et al. Dynamic model of target charging by short laser pulse interactions. *Physical Review E - Statistical, Nonlinear, and Soft Matter Physics*, 92:043107, 2015.
- [171] J. Peebles, et al. Impact of pre-plasma on fast electron generation and transport from short pulse, high intensity lasers. *Nuclear Fusion*, 56:016007, 2016.
- [172] D. Calestani, M. Villani, G. Cristoforetti, F. Brandi, P. Koester, L. Labate, and L. A. Gizzi. Fabrication of zno-nanowire-coated thin-foil targets for ultra-high intensity laser interaction experiments. *Matter and Radiation at Extremes*, 6:046903, 2021.

- [173] M. Sedov, et al. Features of the generation of fast particles from microstructured targets irradiated by high intensity, picosecond laser pulses. *Laser and Particle Beams*, 37:176, 2019.
- [174] M. Bailly-Grandvaux, et al. Ion acceleration from microstructured targets irradiated by high-intensity picosecond laser pulses. *Physical Review E*, 102:021201(R), 2020.
- [175] A. Ovchinnikov, O. Kostenko, O. Chefonov, O. Rosmej, N. Andreev, M. Agranat, J. Duan, J. Liu, and V. Fortov. Characteristic x-rays generation under the action of femtosecond laser pulses on nano-structured targets. *Laser and Particle Beams*, 29:249, 2011.
- [176] D. P. Higginson, et al. High-contrast laser acceleration of relativistic electrons in solid cone-wire targets. *Physical Review E - Statistical, Nonlinear, and Soft Matter Physics*, 92, 2015.
- [177] A. E. Hussein, et al. Towards the optimisation of direct laser acceleration. *New Journal of Physics*, 23:023031, 2021.
- [178] F. N. Beg, A. R. Bell, A. E. Dangor, C. N. Danson, A. P. Fews, M. E. Glinsky, B. A. Hammel, P. Lee, P. A. Norreys, and M. Tatarakis. A study of picosecond laser-solid interactions up to 1019 wcm⁻². *Physics of Plasmas*, 4:447, 1997.
- [179] H. Chen, S. C. Wilks, W. L. Kruer, P. K. Patel, and R. Shepherd. Hot electron energy distributions from ultraintense laser solid interactions. *Physics of Plasmas*, 16:020705, 2009.
- [180] R. H. Scott, et al. Fast electron beam measurements from relativistically intense, frequency-doubled laser-solid interactions. *New Journal of Physics*, 15:093021, 2013.
- [181] A. Savitzky and M. J. E. Golay. Smoothing and differentiation of data by simplified least squares procedures. *Analytical Chemistry*, 36:1627, 1964.
- [182] Y. Ma, et al. Ultrahigh-charge electron beams from laser-irradiated solid surface. *Proceedings of the National Academy of Sciences of the United States of America*, 115:6980, 2018.

- [183] T. E. Cowan, M. Roth, M. M. Allen, J. Johnson, S. Hatchett, and G. L. S. and S. C. Wilks. Low-emittance monoenergetic electron and ion beams from ultra-intense laser-solid interactions. *The Physics of High Brightness Beams*, pages 418–438, 2000.
- [184] S. Jiang, A. G. Krygier, D. W. Schumacher, K. U. Akli, and R. R. Freeman. Effects of front-surface target structures on properties of relativistic laser-plasma electrons. *Physical Review E - Statistical, Nonlinear, and Soft Matter Physics*, 89:013106, 2014.
- [185] H. Chen, et al. Emittance of positron beams produced in intense laser plasma interaction. *Physics of Plasmas*, 20:013111, 2013.